Magnetic resonance microscopy of Aplysia neurons : studying neurotransmitter-modulated transport and response to stress

Ileana O. Jelescu

UNIVERSITE PARIS SUD XI

ECOLE DOCTORALE: Sciences et Technologies de l'Information des Télécommunications et des Systèmes

LABORATOIRE: Unité d'Imagerie RMN et de Spectroscopie, NeuroSpin, CEA

DISCIPLINE: Physique

THESE DE DOCTORAT

Soutenue le 2 octobre 2013

par

Ileana O. JELESCU

Magnetic resonance microscopy of *Aplysia* neurons: studying neurotransmitter-modulated transport and response to stress.

Composition du jury:

Directeur de thèse :	**Denis LE BIHAN**	**Directeur, NeuroSpin, CEA**
Encadrante :	**Luisa CIOBANU**	**Chercheur, NeuroSpin, CEA**
Président du jury :	**Jean-Christophe GINEFRI**	**MCF, Univ. Paris-Sud**
Rapporteurs :	**Paul GLOVER**	**Prof., Univ. of Nottingham**
	Markus WEIGER	**Chercheur, ETH Zürich**
Examinateur :	**Romuald NARGEOT**	**MCF, Univ. Bordeaux 2**

This thesis is submitted in partial fulfillment of the requirements for the degree of Doctor of Philosophy by Université Paris Sud.

Contents

Acknowledgments

My adventure at NeuroSpin started in October 2010, and in the – short – three years that have gone by, I have benefitted from a wonderful working and learning environment, where seniors became mentors and juniors became friends.

I would like to express my gratitude to Denis Le Bihan for taking a chance on my unsolicited Ph.D. application and granting me an interview over the phone – a call from Kyoto, where he was working, to Montreal, where I was completing my master degree. I also wish to thank him for his guidance throughout the project, for sharing his extensive knowledge on so many matters and for pushing me to aim ever higher.

Very warm thanks to Luisa Ciobanu, for her wonderful daily supervision. I measure how lucky I was to be able to knock on your door whenever necessary (and there *has* been a lot of knocking…). Thank you for your ever ultrafast feedback/corrections, and for sharing your knowledge and outstanding expertise in physics, microcoils, scanner hardware, troubleshooting, guessing artifacts… I truly appreciated your intellectual honesty, enthusiasm and concern for your students.

I would like to thank Drs. Paul Glover and Markus Weiger for accepting to review this manuscript (over the summer!) and Drs. Jean-Christophe Ginefri and Romuald Nargeot for being part of the jury.

I am also grateful to Romuald for teaching me everything I know about *Aplysia* and for bringing an indispensable biological expertise to our studies on living tissue. Thank you for your kindness and patience, and for encouraging me to trust my physicist hands and perform meticulous biological tasks. I have fond memories of our trips to Arcachon, picking up *Aplysia* at low tide.

Françoise Geffroy is the person who took over when my dissection skills reached their limits: thank you for your help with isolating single cells and for your enthusiasm to image them under your microscope and watch them "talk to their neighbors"! Thank you also for your indefectible good mood, sounding laughter, kindness to everyone and excellent "macarons"!

Another remarkable collaboration I would like to mention is that with Nicolas Boulant, who knows the physics of selective excitation inside out and wrote the code to design the DESIRE pulses. Thank you for encouraging me whenever I was

depressed with my experiments (the physics cannot be questioned, so “it should work”) and for providing me with precious advice on numerous matters.

I would like to thank Pierre Marquet for spending several months at NeuroSpin to perform DHM experiments in parallel with my diffusion MRI ones. I learned a lot about your technique and very much appreciated all of our conversations. Switzerland sounds like a wonderful place!

My gratitude also goes to the electronics team – Eric Giacomini and Marie-France Hang – for getting me started on coil design and building, as well as to Jérémy Bernard for fabricating numerous stands and supports for my – otherwise shaky – experimental set-ups. Many thanks also to Boucif for his help with *Aplysia* tending (it’s a lot of work!), and to Denis F, Maryline, Emmanuelle, Elisabeth and Nathalie for their help with purchasing substances and gizmos, and other organizational matters.

Thank you to all the temporary residents of the open space 1025A who made every day enjoyable and with whom I have shared so many joyful coffee breaks, lab beers and conference outings: Benjamin, Julien F, Céline, Nadya, Alfredo, Guillaume, Rémi and Marianne. The first four are now safe, happy and sound; good luck to the remaining four in the completion of your PhDs! I hope the museum of horrors will keep expanding. I would also like to thank Ioana and Dominique, who kept our open space clean and could tell from a distance whether I was having a good or a bad day.

I would like to mention all the people with whom I have had highly entertaining scientific and less-scientific conversations at lunch breaks, lab and scientific meetings, or on the train to Paris: Benoît L, Sébastien, Fawzi, Julien V, Franck, Aurélie, Alexandre, Cyril, Fabrice, Alexis, Tom, Mami, Shun, Chris, Karl, Jing, Béchir, Aurélien, Martijn, Alice, Clarisse, Delphine, Véronique, Benoît S and Chloé.

Very special thanks go to Olivier, for getting me started with the scanner and programming in ParaVision, then gradually putting up with me every day and eventually becoming the best life sidekick – I look forward to our forthcoming adventures!

I am finally very grateful to my family and friends, for letting me be who I am and do what I love, and accepting that I have chosen to spend three years studying a sea slug instead of getting “a proper job”.

I dedicate this thesis to my father, an engineer, who would have been very happy to know I am still doing science.

General Introduction

Recent advances in the life sciences have had a tremendous impact on our understanding of physiology and pathology, and eventually on our life comfort. However, faithful to the popular wisdom that the more you know, the less you understand, new findings raise ever more questions. This is particularly applicable to the study of living systems, which appear under many aspects to be anything but deterministic. One natural way of trying to explain the unexplained is to take a closer look – a microscopic look. This is roughly the philosophy behind this thesis.

While the advent of magnetic resonance imaging (MRI) in the clinic has irreversibly transformed many fields such as radiology, medical research and neurosciences, there are observations which currently have no definite explanation. For instance, cerebral ischemia has been known to cause a decrease in water diffusion in the brain, likely related to the membrane depolarization and cell swelling caused by ischemia. The exact mechanism has however not been established, yet diffusion MRI is used routinely in the clinic for the diagnosis of acute ischemia. Similarly, the manganese ion (Mn^{2+}), used as an MR contrast agent in animal studies, is known to be transported along neural pathways, up to distant regions with brain activation. However, the exact mechanisms of its transport, whether synaptic or non-specific, have not been fully elucidated.

One drawback of MRI is its poor sensitivity, which is translated into relatively low spatial resolution images. Yet one feels that truly useful insight could be brought into the questions raised above if one could image what happens in the brain at a cellular scale. This is where magnetic resonance microscopy comes in. This technique consists in acquiring MR images of small samples at much higher resolution than usually typical for MRI, e.g. 20 µm versus 1 mm. Yet 20 µm is perhaps still too coarse for the human brain, with its 4 µm neuronal bodies and hundreds of trillions of synapses. So let us then take a microscopic look at a nervous system with larger structures: that of *Aplysia californica*, with its neuronal bodies several hundred microns in diameter and some 20,000 neurons in total.

The global objective of this thesis was therefore to use magnetic resonance microscopy techniques for the study of fundamental aspects of the nervous system at the level of individual neurons and their networks. The strength of combining MR microscopy with the *Aplysia* model is the potential to exploit all the richness of MR

contrast mechanisms for the study of an almost fully determined neuronal network. Two approaches were chosen, corresponding to the two questions raised earlier. On the one hand, the study of Mn^{2+} transport inside a neuronal network, tracked with manganese enhanced MRI, and its ability to accurately trace axonal projections and neurotransmitter-modulated communication. On the other hand, the diffusion changes induced by membrane depolarization and cell swelling, tracked with diffusion-weighted MRI at two structural scales: at the level of overall nervous tissue and inside the neuronal body.

For these biological experiments to be possible, important MR hardware and methodology needed to be developed. These include the design, building and testing of dedicated transceiver coils, and the development and implementation of appropriate sequences, in particular for diffusion measurements. (This is not to mention the setup from scratch of an aquaria section in the animal house of NeuroSpin and daily tending for the *Aplysia*.)

This thesis is organized into three parts. The first part serves as an introduction to the basic principles of MRI (Chapter 1) and to the main challenges and achievements of magnetic resonance microscopy (Chapter 2). It also deals with what the author has called "materials": a description of both the animal model and the hardware used for the experiments, in particular the design and performance of the micro-coils (Chapter 3). The second part provides an introduction to MR contrast agents and to manganese enhanced MRI (Chapter 4) and covers the study performed on neurotransmitter modulated Mn^{2+} transport in the *Aplysia* (Chapter 5). The third part is dedicated to diffusion MRI. Chapter 6 reviews the principles of diffusion weighted MRI, its main applications and challenges. Chapters 7 and 8 deal with the implementation and phantom validation of two diffusion sequences particularly suited for microscopy: 2D DESIRE (Diffusion Enhancement of SIgnal and REsolution) and 3D DP-FISP (Diffusion-Prepared Fast Imaging with Steady-state free Precession). Chapter 9 makes extensive use of the DP-FISP sequence to carry out the study on tissue and cellular diffusion changes in response to stress.

Part I

MR microscopy: General concepts and methodology

When medical and biological applications of MRI started developing in the 1970s, the aim was to achieve whole body imaging in humans. Within hospitals and research centers, this new modality quickly became very popular, as it was non-invasive and allowed the visualization of tissues with an unprecedented variety of contrasts.

The idea behind magnetic resonance microscopy (MRM) is to apply the potentiality of MRI – tissue preservation and diversity of contrasts – to small, living, biological samples. The first achievement of this was the publication of an MR image of an ovum from *Xenopus laevis* (Aguayo et al., 1986). This first MR image of a single cell allowed the visualization of the nucleus and of the vegetal and animal poles within the cytoplasm. The spatial resolution of the image was 10x13 μm in-plane with a 250 μm thick slice. MRM has since developed into a full-fledged field, with its very own requirements, limitations and specificities.

The scale boundary between MRI and MRM is not clear-cut. It is generally accepted that images with spatial resolution below 100 μm pertain to microscopy. However, it would perhaps be more appropriate to refer to such a "boundary" in terms of voxel volume, because reported high in-plane spatial resolutions (< 10 μm) usually come with thicker slices. Let us then say that MRM images are generally associated with voxel volumes on the order of the nanoliter, which corresponds to a 100 μm cubic voxel.

Compared to optical imaging or even more so to atomic force microscopy, the spatial resolution achievable with MRM might seem unworthy of the term "microscopy". However, MRM should always be regarded as complementing other microscopy techniques. Its major advantages are the non-invasiveness and the variety of information it can provide, while its major drawback is the poor inherent sensitivity.

1. MRI

The development of magnetic resonance imaging (MRI) was a two-step process: the first step was the discovery of the nuclear magnetic resonance (NMR) phenomenon and its application to the spectroscopy of liquids and solids, separately by Bloch and Purcell in 1946. The second step was taken in 1973 by Lauterbur and later Mansfield, who developed the idea of using magnetic field gradients to spatially encode the NMR signal and produce an NMR image (Lauterbur, 1973).

This chapter will very briefly present the concepts behind MRI, in particular those needed to understand the challenges of MRM. For a more detailed description of MRI, one can refer to specialized literature (Haacke et al., 1999; Nishimura, 1996).

1.1 NMR

NMR is a quantum phenomenon that can be observed in nuclei with an odd number of protons and/or neutrons. These nuclei possess a non-zero spin angular momentum **S**, usually simply referred to as "spin". In biological tissue, the most common elements with a non-zero nuclear spin are hydrogen (^{1}H), sodium (^{23}Na) and phosphorus (^{31}P). Hydrogen nuclei (or simply "protons") are by far the most abundant, given the large proportion of water in tissue. All of the experiments performed in this work pertain to proton imaging.

A charged particle with a non-zero spin also possesses a small magnetic moment **μ**:

$$\vec{\mu} = \gamma \vec{S} \tag{1.1}$$

where γ is the gyromagnetic ratio and is nuclei dependent. For protons, $\gamma/2\pi = 42.58\ MHz/T$.

In the presence of an external magnetic field $\mathbf{B_0} = B_0\mathbf{z}$, the magnetic moment **μ** is endowed with a potential energy equal to:

$$E = -\vec{\mu} \cdot \vec{B}_0 = -\mu_z B_0 = -\gamma m_s \hbar B_0 \tag{1.2}$$

where ħ is Planck's reduced constant and m_s are the magnetic quantum numbers which take on discrete values: $\pm\frac{1}{2}$ in the case of the proton. This results in a splitting of the nuclear energy levels known as the Zeeman effect. In other words, for protons, two energy states are available: a lower one (also referred to as "parallel' or "spin-up" state) corresponding to $m_s = 1/2$ and a higher one (also referred to as "anti-parallel" or "spin-down" state) corresponding to $m_s = -1/2$.

Because the "parallel" state corresponds to a lower energy state, its population n_+ slightly exceeds that in the "anti-parallel" state (n_-), in a ratio given by the Boltzmann distribution:

$$\frac{n_-}{n_+} = \exp\left(-\frac{\Delta E}{kT}\right) = \exp\left(-\frac{\gamma\hbar B_0}{kT}\right) \tag{1.3}$$

where k is Boltzmann's constant and T is the absolute temperature. In practice, at room temperature, nuclear magnetic energies are much smaller than thermal energies and therefore the excess of the parallel population is very small, typically 1 to 10 out of 10^6. Nonetheless, it is sufficient to produce a net macroscopic magnetization **M** in a sample, which is aligned along $\mathbf{B_0}$ at equilibrium. The intensity of the equilibrium magnetization $\mathbf{M_0}$ in the Curie regime (i.e. $\gamma\hbar B_0 \ll kT$) is proportional to the applied static field and to the proton density ρ_0 in the sample, and inversely proportional to the temperature:

$$M_0 = \frac{1}{4}\rho_0 \frac{\gamma^2\hbar^2}{kT} B_0 \tag{1.4}$$

Transitions between the two quantum states occur when the spins are excited by an electromagnetic wave with photon energy ħω equal to the energy gap between the parallel/anti-parallel states $\Delta E = \gamma\hbar B_0$. The corresponding frequency of the electromagnetic wave, called resonant (or Larmor) frequency, is therefore equal to γB_0. With current magnetic field strengths comprised between 1.5 T and 21 T, Larmor frequencies fall within the radiofrequency (RF) range (64 –900 MHz).

NMR is by nature a quantum phenomenon and all its theory can be derived from quantum mechanics. However, a classical mechanics description of a magnetic moment in a magnetic field is often adopted for simplicity. This classical standpoint is justified by the fact the expectation values for the proton magnetic moment derived from quantum mechanics are eventually governed by classical equations. For convenience, a classical description of NMR will also be adopted in this thesis.

From a classical standpoint, the application of a resonant electromagnetic field $\mathbf{B_1}$, perpendicular to $\mathbf{B_0}$, results in the tipping of the macroscopic magnetization **M** away from its equilibrium orientation (i.e. away from the axis of $\mathbf{B_0}$, traditionally labeled **z**). The flip angle α, by which the magnetization is tipped away from **z,** is dependent on B_1 amplitude and duration τ through:

$$\alpha = \int_0^\tau \gamma B_1(t) dt \tag{1.5}$$

When $\mathbf{B_1}$ is switched off, the out-of-equilibrium magnetization **M** will keep precessing around the z-axis at the Larmor frequency. A receiver coil oriented transversally to **z** will pick up changes of magnetic flux generated by the rotating magnetization in the form of induced current. This current is the NMR received signal, which comes solely from the transverse component of **M**.

Once the system is out-of-equilibrium and not supplied with energy ($\mathbf{B_1}$ is off), it will also relax back to its equilibrium orientation (along $\mathbf{B_0}$) while precessing. In NMR, there are two separate relaxation processes, one for each of the two projections of **M**: the "longitudinal" component along the z-axis, and the "transverse" component in the xy-plane.

The first process is referred to as spin-lattice, longitudinal or T_1 relaxation. It consists in the gradual increase of the longitudinal component M_z of **M** up to its equilibrium value M_0, a growth empirically described by an exponential recovery with a time constant T_1. This process stems from the interaction between a spin with its surrounding atomic and nuclear lattice. The energy involved in the transition between two proton spin states is compensated by an opposite transition (requiring the same amount of energy) between lattice states. Because it is related to energy exchanges between the spins and the lattice, T_1 depends on the chemical and physical properties of the spins' environment. T_1 also increases with B_0.

The second process is referred to as spin-spin, transverse or T_2 relaxation. It consists in the gradual decrease of the transverse component M_{xy} of **M**, empirically described by an exponential decay with a time constant T_2. This relaxation is caused both by spin-lattice and spin-spin interactions, and therefore $T_2 \leq T_1$. Spin-spin interactions refer to a collective dephasing effect. The local field experienced by a spin is indeed modified by the fields of its neighbors, resulting in a modified local precessional frequency and global dephasing between spins in time. In biological tissue, spin-spin interactions typically dominate the transverse relaxation process and therefore

$T_2 << T_1$. T_2 also depends on the chemical and physical properties of the spins' environment, but is less dependent on B_0.

The behavior of the nuclear magnetization **M** is therefore described by the following phenomenological relationship, known as the Bloch equation:

$$\frac{d\vec{M}}{dt} = \vec{M} \times \gamma\vec{B} - \frac{M_x\vec{x} + M_y\vec{y}}{T_2} - \frac{(M_z - M_0)\vec{z}}{T_1} \tag{1.6}$$

In this equation, **B** is the sum of the various magnetic fields ($\mathbf{B_0}$, $\mathbf{B_1}$…) applied at a given time t, and **x**, **y**, **z** are the unit vectors in the x, y, z directions, respectively. The cross-product term describes a precessional behavior at a frequency γB, while the second and third terms describe the exponential relaxation of the transverse and longitudinal components, respectively.

Using a complex formalism, the solution for the transverse component of **M** in the presence of $\mathbf{B_0}$ only is:

$$M_{xy}(t) = M_{xy}(0)e^{-\frac{t}{T_2}}e^{-i\omega_0 t} \tag{1.7}$$

Assuming a receiver coil that is uniformly sensitive over the sample, the NMR signal s(t) picked up will be proportional to the volume integral of $M_{xy}(t)$.

Considering a homogeneous sample (e.g. a water phantom), the signal recorded from a simple NMR experiment – excitation / reception – oscillates at a frequency ω_0 within an envelope that decays with time constant T_2. This signal is called free-induction decay (FID). If the magnetic field throughout the sample is not perfectly homogeneous, the magnetizations at different spatial locations will precess at different frequencies, leading to a global loss of coherence when adding up, and to a more rapid decay of the overall measured signal. This new time constant is referred to as T_2^*, with $T_2^* \leq T_2$.

In practice, the static magnetic field throughout a sample is never perfectly homogeneous. Although the homogeneity of an unloaded magnet is a crucial specification of MR systems, placing a sample and a coil inside the magnet will necessarily produce additional distortions in the field. This effect is enhanced at ultra-high fields and at interfaces (e.g. air/water), because of magnetic susceptibility mismatches. In an attempt to minimize static field inhomogeneities specific to each experimental setup (i.e. sample and probe dependent), magnets come with sets of "shim" coils. To improve homogeneity in a given volume of interest, the current in

each shim coil is adjusted to counteract part of the B_0 variations in that volume. The complexity of the shimming process is well described in (Chmurny and Hoult, 1990).

Briefly, the behavior of the static field inside a magnet through which no current flows is governed by the Laplace equation:

$$\Delta B_0 = 0 \tag{1.8}$$

In traditional polar spherical coordinates (r, θ, φ), the solution to Equation (1.8) can be expressed as an expansion in spherical harmonics:

$$B_0 = \sum_{n=0}^{\infty} \sum_{m=0}^{n} C_{nm} \left(\frac{r}{a}\right)^n P_{nm}(\cos\theta) cos[m(\varphi - \psi_{nm})] \tag{1.9}$$

where a is the average magnet radius, C_{nm} and ψ_{nm} are constants, and P_{nm} are associated Legendre polynomials. The only harmonic that represents a homogeneous field is the one for n = 0 and m = 0. All the other harmonics are error terms that must be set to zero. Although there is an infinity of them, in practice only harmonics of order n up to 5 (and in fact most often 2) are considered, because beyond that the factor $(r/a)^n$ becomes negligible for a small volume ($r << a$). The idea behind shimming is to introduce additional fields that cancel all unwanted harmonics (Golay, 1958).

Ideally, each shim coil should generate a single harmonic, the amplitude of which is meant to cancel the one in the main static field. In practice, the current in each shim coil also generates lower and higher order harmonics, hence the complexity of the problem. The current in each shim coil can be manually adjusted by the operator at the magnet console but most frequently automatic algorithms are provided for shimming at various levels: in the global sensitive volume of the coil (usually first order shims, n = 1), or within a particular region of interest (usually involving second order shim, $n \leq 2$) (Gruetter, 1993; Kanayama et al., 1996). The main pitfall of shimming is finding a local, rather than the global optimum solution. Good practice for successful shimming begins with centering the probe with respect to the origin of the shim coils.

1.2 Magnetic field gradients and imaging

In the case of a non-uniform sample, such as biological tissue, it is interesting to differentiate the contributions of protons at different locations in the sample to the overall signal, as they may have different properties (e.g. proton density, T_1, T_2…). The idea behind this achievement was hinted at in the previous section: if experiencing different magnetic field strengths, local magnetizations will precess at different frequencies.

Following excitation (i.e. $\mathbf{B_1}$ is off) and ignoring inhomogeneities, if a magnetic field gradient $\mathbf{G}(t)$ is added to the main field $\mathbf{B_0}$, the Bloch equation becomes:

$$\frac{\partial \vec{M}(\vec{r},t)}{\partial t} = \vec{M}(\vec{r},t) \times \gamma(B_0 + \vec{G}(t)\cdot\vec{r})\vec{z} - \frac{M_x(\vec{r},t)\vec{x} + M_y(\vec{r},t)\vec{y}}{T_2} - \frac{(M_z(\vec{r},t) - M_0)\vec{z}}{T_1} \quad (1.10)$$

Using the complex formalism, the solution for the transverse component of the magnetization, starting from any initial condition $m(\mathbf{r})$, is therefore:

$$M_{xy}(\vec{r},t) = m(\vec{r})e^{-\frac{t}{T_2(\vec{r})}}e^{-i\omega_0 t}\exp\left(-i\gamma\int_0^t \vec{G}(\tau)\cdot\vec{r}\,d\tau\right) \quad (1.11)$$

In the interest of clarity, we will ignore T_2 relaxation for now and consider the signal demodulated by ω_0. The received NMR signal is:

$$s(t) = \int_V m(\vec{r})\exp\left(-i\gamma\int_0^t \vec{G}(\tau)\cdot\vec{r}\,d\tau\right)d\vec{r} \quad (1.12)$$

We define a space of spatial frequencies, or k-space, in which the location is given by the time integral of the gradient waveforms. If i refers to either dimension x, y or z, the k-space location at a given moment during the acquisition is given by:

$$k_i(t) = \frac{\gamma}{2\pi}\int_0^t G_i(\tau)d\tau \quad (1.13)$$

Hence Equation (1.12) becomes:

$$s(t) = \int_V m(\vec{r})e^{-i2\pi\vec{k}\cdot\vec{r}}\,d\vec{r} \quad (1.14)$$

In this form, it appears that the NMR signal measured at a given time t is the 3D Fourier transform (FT) of the sought magnetization map m(**r**), evaluated at spatial frequency coordinates **k**(t). Once this FT is evaluated over a sufficient range of k-space, the inverse FT can provide a reasonable estimate of m(**r**).

In Cartesian sampling, there are two dedicated paths for acquiring information from a given coordinate in k-space. One way is to apply a constant gradient while the signal is being acquired, thus "moving" along one direction in k-space. This gradient is referred to as "frequency encoding" or "read-out" (ro) gradient and its direction is traditionally labeled "x". The successive signals recorded by the analog-to-digital (A/D) converter in the reception pipeline will thus map one line in k-space along k_x. The second way is to apply a gradient in-between the excitation and the reception blocks. This gradient is referred to as "phase-encoding" (pe) gradient and its direction is traditionally labeled "y" for the second dimension and "z" for the third. The phase-encoding gradients bring the system at a given coordinate along k_y (and k_z) prior to read-out, but this coordinate remains constant during signal reception.

In two dimensions, if the sought image is an NxN matrix, then the typical MR imaging scheme will be the repetition of excitation/encoding/acquisition with N phase-encoding steps, and the acquisition of N samples during each signal read-out. The extension to 3D acquisitions (mainly used in this work) is straightforward by introducing a third gradient G_z and taking the 3D inverse FT of the cuboid k-space thus filled.

In order to retrieve m(**r**) through inverse FT, the k-space should be covered and sampled "sufficiently". Let us specify what this means. Relationships between position **r** and spatial phase **k** will allow us to define crucial imaging parameters.

The spatial resolution of the MR image along dimension i (δ_i) is determined by the maximum position attained in k-space along i, which in turn is governed by the maximum gradient areas attained by the read-out or phase-encoding gradients:

$$\delta_i = \frac{1}{2k_{i,max}} \tag{1.15}$$

The field-of-view (FOV) covered by the image is determined by the spacing between samples in k-space along i:

$$FOV_i = \frac{1}{\Delta k_i} \tag{1.16}$$

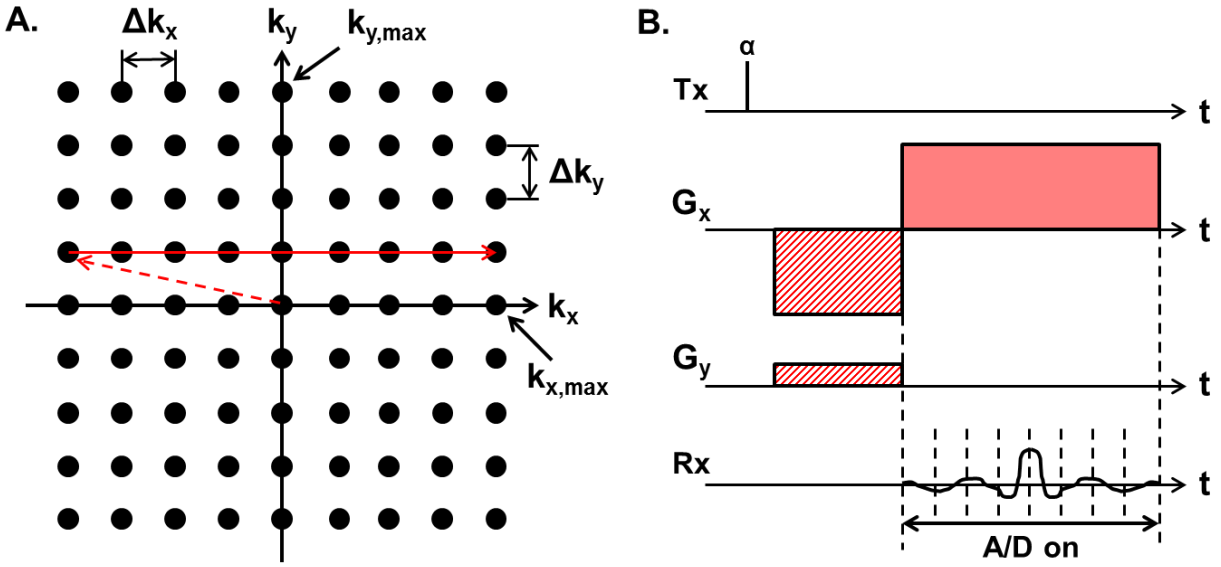

Figure 1. A: Cartesian sampling of 2D k-space. The furthest position reached and the spacing between points determine the image resolution and FOV, respectively (see Equations (1.15) and (1.16)). The gradients played to produce the trajectory outlined in red are represented in B. The relative gradient intensities and durations are to scale. The phase-encoding time is also used to reach $-k_{x,max}$ in the read-out direction by applying a dephasing lobe of half-area and opposite polarity. During "read-out", the analog-to-digital converter is on and the signal is sampled at an appropriate rate to fill the matching points in k-space. *Tx: transmission / Rx: reception.*

For the read-out direction, this is dictated by the product of G_x and the dwell time of the A/D converter. For the phase-encoding directions, this is dictated by the product of the incremental gradient amplitude step and phase-encoding duration.

For simplicity, we have described the protocol for a line-by-line Cartesian filling of k-space, illustrated in Figure 1. If the successive lines are acquired starting from one edge of k-space (e.g. $-k_{y,max}$) and gradually moving towards the furthest opposite position ($k_{y,max}$) then the encoding is referred to as linear. If the first line acquired is the central k-space line ($k_y = 0$) and the successive encoding steps allow the acquisition of lines for increasing $|k_y|$, then the encoding is referred to as centric.

An extremely popular accelerated version of the Cartesian scheme is the echo-planar imaging (EPI), which consists in acquiring all (single-shot) or a subset of (multi-shot) the lines in k-space following a single excitation (Stehling et al., 1991). Now that the relationship between k-space and image space is clear, it is also important to mention that different k-space sampling strategies, such as radial or spiral (Ahn et al., 1986), are also possible by simultaneously applying appropriate gradient waveforms on two or three axes. However, such data need to be re-gridded before applying the FT to obtain the image.

1.3 Echoes, timings and sequences

As mentioned earlier, the FID following excitation will decay with a time constant T_2* due to magnetic field inhomogeneities. Let us concentrate on the acquisition of the central k-space line. The introduction of the dephasing read-out gradient lobe (see Figure 1) translates into additional dephasing and even more rapid signal decay. However, the position-dependent phase thus accumulated by the spins is undone when the read-out gradient is switched on, with an opposite polarity to that of the dephasing lobe. When the gradient areas are compensated (i.e. the center of k-space is reached), the signal is restored to the level of the T_2* decay envelope: this signal resurrection is referred to as a gradient echo.

The effect of constant field inhomogeneities can also be undone and the amplitude of the echo restored to the level of the T_2 decay envelope. This signal resurrection is then referred to as a spin echo, and is typically achieved by introducing a refocusing RF pulse before the read-out. Spin-echo sequences are based on 90° excitations pulses and 180° refocusing pulses. Figure 2 illustrates the effect of a 180° refocusing pulse on the dephased magnetization: the "faster" spins are given a negative phase advance and the "slower" spins a positive one, so that at echo time they are all in phase again.

Spin-echo sequences are typically slower than gradient echo ones and deposit more RF energy. However, they are by design insensitive to magnetic susceptibility artifacts and produce higher signal levels. Figure 3 shows basic timing diagrams for

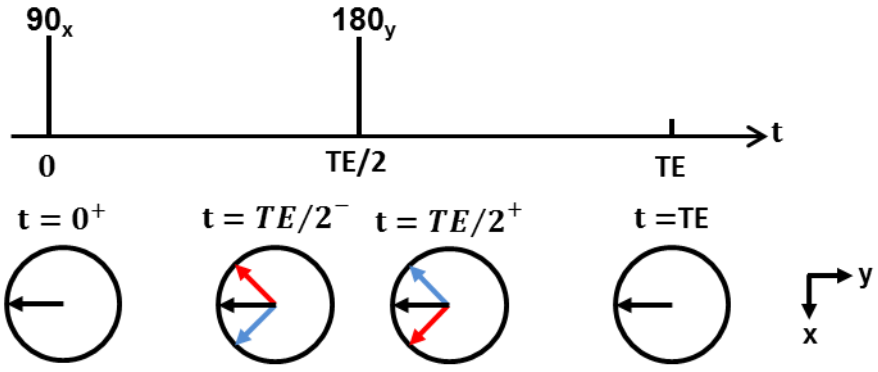

Figure 2. Schematic of the effect of a refocusing pulse. Following a 90° excitation, the spins gradually dephase due to local magnetic field inhomogeneities. The "blue" spin has a phase advance and the "red" spin a phase delay. By applying a 180° flip angle at TE/2, the magnetization configuration is flipped such that the "faster" blue spin has a phase delay and the "slower" red one has a phase advance. At TE they will thus all come into phase again and the overall signal will be at its strongest. *TE: echo time. The pulse subscript gives the axis around which the magnetization is flipped.*

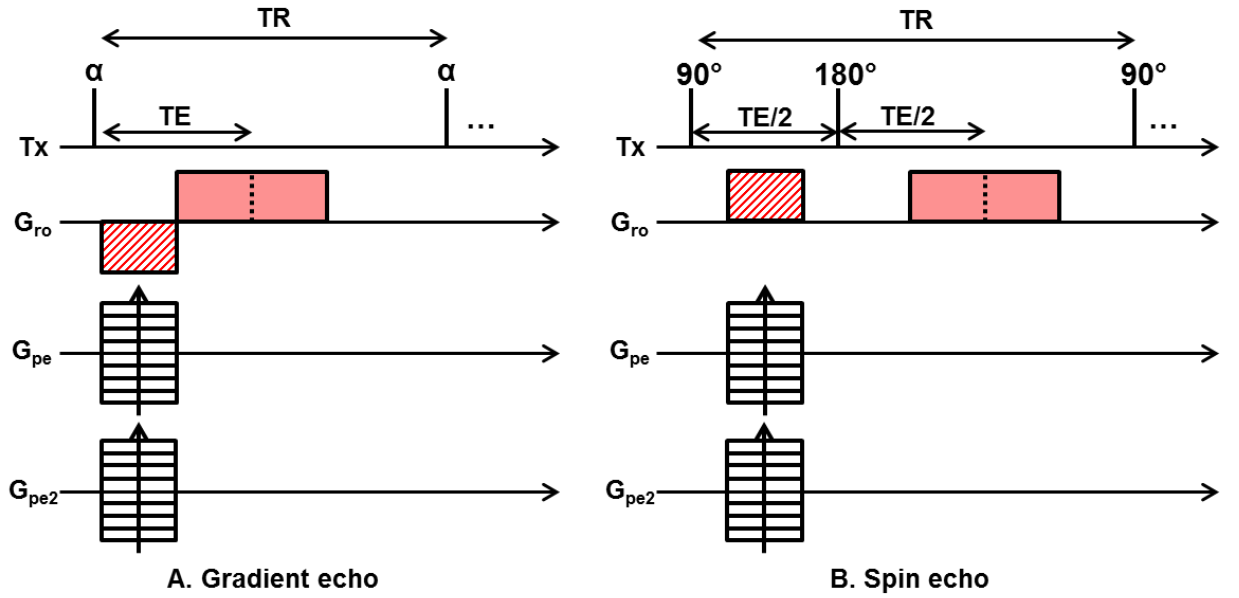

Figure 3. Timeline of events for basic gradient echo (A) and spin echo (B) acquisitions. A 3D Cartesian acquisition scheme is represented, with phase-encoding gradients on two axes. The A/D converter (not shown) is on concomitantly with the read-out gradient.

gradient echo and spin echo. Echo time (TE) and repetition time (TR) are crucial sequence parameters that influence signal-to-noise ratio (SNR), acquisition time (TA) and most importantly image contrast.

Indeed, the richness of MRI comes from the fact that the signal level in the image is a function of many parameters, intrinsic and extrinsic. The extrinsic parameters are related to sequence design, such as excitation flip angle α, TR or TE. The intrinsic parameters are for example free water proton density (PD) or relaxation times T_1, T_2 and T_2*. The extrinsic parameters can be chosen so that the signal is more or less weighted by each of the intrinsic parameters. For example, a long TE produces T_2 weighting in spin-echo sequences and T_2* weighting in gradient echo sequences. T_1 weighted images can be obtained from gradient echo sequences with short TR and TE. This feature of MRI is important because proton density for instance varies little across biological tissue, but T_1 and T_2 weighted images allow to differentiate between structures at many different levels (between gray and white matter in the brain, between healthy or cancerous tissue, between cytoplasm and nucleus within a cell…).

From the basic gradient echo and spin echo sequence blocks described above, a certain number of important sequence-types emerged. We will briefly describe the concepts behind the ones that have turned out to be of interest in this thesis work.

FLASH (Fast Low Angle SHot) and TurboFLASH

The FLASH sequence is a basic gradient-echo sequence with two typical features (Frahm et al., 1986). The TR is generally shorter than the T_1 of the sample, meaning the longitudinal magnetization has not fully recovered between two successive excitation pulses. After a given number of pulse repetitions, the longitudinal magnetization available before each pulse reaches a steady-state level. The transverse magnetization remaining at the end of the read-out block is "spoiled" by a gradient, ensuring that $M_{xy} = 0$ before the following excitation pulse. Thus no coherent magnetization will be tipped from the transverse plane onto the longitudinal axis by the next RF pulse. This spoiling is required for instance if $TR < 5T_2$. Combining these conditions on M_z and M_{xy}, the FLASH signal equation in steady-state is:

$$S = M_0 \frac{\left(1 - e^{-\frac{TR}{T_1}}\right) \sin(\alpha)\, e^{-\frac{TE}{T_2^*}}}{1 - \cos(\alpha) e^{-\frac{TR}{T_1}}} \tag{1.17}$$

The steady-state therefore depends on the choice of TE, TR and flip angle (usually 5 – 30°). Ideally, all of the data in k-space should be acquired when the system is in steady-state, hence the need for "dummy scans" (all the pulses and gradients are played but the data is not acquired) to reach steady-state prior to the actual acquisition start. In practice, if k-space is acquired linearly starting from the edge, dummy scans are less crucial since steady-state will likely be reached before the center of k-space (which determines the main signal level) is acquired. The advantage of the FLASH sequence is a short acquisition time via a short TR. The short TR will generally introduce T_1 weighting, although T_2* weighting is also possible through a choice of relatively long TE.

A very rapid version of FLASH using extremely short TRs (~10 ms) and small flip angles is called TurboFLASH (Chien and Edelman, 1991). At such short repetition times, the T_1 contrast in FLASH is lost (the TR is much shorter than all the T_1s in the sample…). To recover T_1 contrast, the sequence uses an inversion 180° pulse prior to acquisition start.

FSE (Fast Spin Echo) or RARE (Rapid Acquisition with Refocused Echoes)

Spin-echo based sequences also have their acceleration "tricks". The idea is to acquire multiple lines in k-space following a single 90° excitation, by repeatedly playing 180° refocusing pulses at TE intervals. However, the amplitude of the

successive echoes naturally decays with T_2. This implies that each line in k-space has a different T_2 weighting from the other lines acquired within the same echo train. The effective echo time of such acquisitions depends on the time when the central line in k-space is acquired, hence a very important choice of phase-encoding steps ordering. FSE (or RARE) typically provides excellent T_2-weighted (T2w) images in a short time but is improper for T_2 quantification because of the mixed T_2 weighting within a single k-space plane (Hennig et al., 1986). FSE acquisitions can sometimes be used to acquire several images with various PD/T2w at once, if only the echoes in the same train position are used to form each image.

SSFP (Steady-state free precession) and FISP (Fast Imaging with SSFP)

SSFP sequences generate a complex image contrast. The difference with FLASH lies in that the transverse magnetization is not spoiled prior to each new excitation pulse and therefore also reaches a non-zero steady-state after a certain number of pulse repetitions (Carr, 1958). For that purpose, the TR should also be shorter than the T_2 in the sample. Once dynamic equilibrium is reached for both the transverse and longitudinal magnetization, three types of images can be formed, depending on how the gradients are distributed. Figure 4 shows a diagram of the three types of SSFP acquisitions.

In balanced SSFP, the net gradient moment over TR is zero. This makes the sequence less sensitive to T_2* effects than other gradient echo sequences. Contrast in the images depends on T_2/T_1 ratio. FISP-FID is somewhat similar to FLASH but their behavior diverges at very short TRs. The contrast of FISP-FID depends on T_2/T_1 ratio, just like balanced SSFP, but it is more sensitive to T_2* effects. FISP-Echo displays heavy T_2 weighting, since the effective TE is longer than TR (TE = TR + τ using notations in Figure 4C). Its contrast is also highly dependent on flip angle.

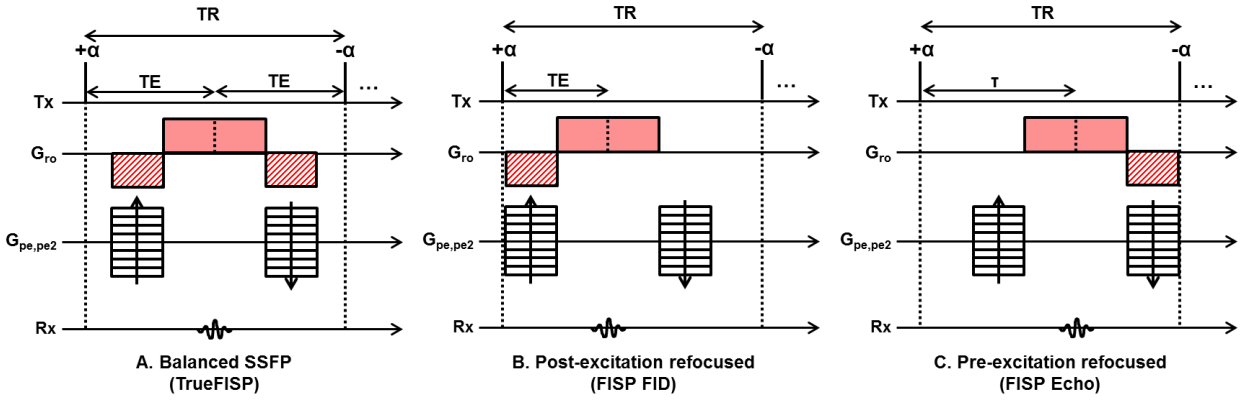

Figure 4. Simplified sequence diagrams for 3D SSFP acquisitions.

1.4 Excitation schemes

3D versus 2D acquisitions

In the previous sections, we have described a non-selective acquisition scheme to cover a 3D volume of interest. This strategy implies that the whole volume within the coil sensitivity range is excited before encoding and acquisition. As a result, a 3D k-space needs to be filled, with one read-out direction and two phase-encoding directions. However, the most common approach is in fact the selective excitation of a single (thin) slice prior to 2D imaging. Stacking adjacent slices then allows the reconstruction of the 3D volume of interest.

The main advantages of 3D acquisitions are high SNR, as the whole volume contributes to signal, and the possibility of achieving isotropic resolution. Indeed, in multi-slice 2D mode, the slice thickness (or "thinness") is limited by gradient strength and excitation duration, and the thinner the slice, the lower the signal as well. For these reasons, the 3D scheme was chosen for the experiments described in Chapters 5, 8 and 9.

However, being able to excite and image only a part of the attainable volume also presents clear advantages. One may not be interested in imaging the totality of the volume, and selecting only a given spatial location leads to considerable gain in scan time while removing aliasing concerns in the selection direction. Spatial selection in one direction (also known as slice/slab selection) is very commonplace in MRI protocols. Spatial selection in two directions (i.e. selecting an infinite prism, cylinder, etc…) is used for further reduction in imaging time or for localized spectroscopy (Keevil, 2006). Multidimensional selective excitation is also at the heart of the 2D implementation of the DESIRE sequence (Diffusion Enhancement of SIgnal and REsolution (Lauterbur et al., 1992)), presented in Chapter 7. The next paragraph therefore explains the underlying theory of selective excitation.

Selective excitation

The literature on this topic is abundant, but the current section is essentially based on two works: (Pauly et al., 1989) and (Nishimura, 1996).

First, let us describe an intuitive approach to 1D selective excitation. In the absence of gradients, the protons in the entire coil volume are supposed to have a common resonant frequency, which is determined by B_0. An RF pulse on this resonant frequency will therefore excite all spins. If a linear gradient G_z is applied while the pulse is played, the pulse will only have an effect on spins whose resonant frequency

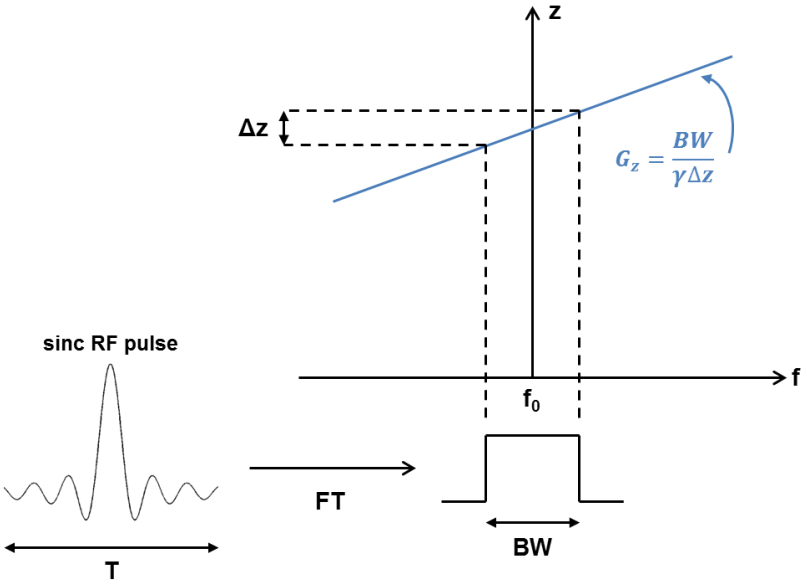

Figure 5. Selective excitation of a plane perpendicular to z, of thickness Δz. An RF pulse with a central frequency f_0 and a sinc envelope is played for a duration T. Its Fourier transform is a rectangle centered on f_0 with a bandwidth BW proportional to the inverse of the pulse duration. The pulse is played while a gradient G_z is on, affecting only spins within a thickness $\Delta z = BW/\gamma G_z$.

(now $\gamma(B_0+z.G_z)$) is comprised within the limited bandwidth of the pulse. The effect of the RF pulse on spins at various locations is therefore determined by the spectral components of the pulse, i.e. by its Fourier transform. For a "clean" slice selection, i.e. a uniform selection over a thickness Δz and none outside, the ideal pulse envelope is a sinc, because its Fourier transform is a rectangle. Figure 5 illustrates this simple but important concept.

In the general case – with any B_1 shape and time-varying gradients on multiple axes, the resultant magnetization can be determined in the small flip angle approximation by solving the Bloch equation.

If the signal is demodulated at ω_0 and relaxation effects are neglected (which implies that under all circumstances pulse duration should be short compared to T_2), the Bloch equation can be written as follows:

$$\frac{\partial \vec{M}(\vec{r},t)}{\partial t} = \gamma \begin{pmatrix} 0 & \vec{G}\cdot\vec{r} & -B_{1,y} \\ -\vec{G}\cdot\vec{r} & 0 & B_{1,x} \\ B_{1,y} & -B_{1,x} & 0 \end{pmatrix} \vec{M}(\vec{r},t) \qquad (1.18)$$

where **G** and $\mathbf{B_1}$ are both functions of time. In the small flip angle approximation, we consider that $M_z \approx M_0$ = constant, which is valid for flip angles up to about 30°. Under this assumption, the transverse magnetization can be decoupled from the longitudinal one. Using once again the complex formalism, Equation (1.18) becomes a single differential equation:

$$\frac{\partial M_{xy}}{\partial t} + i\gamma \vec{G} \cdot \vec{r} M_{xy} = i\gamma B_1 M_0 \tag{1.19}$$

Assuming a relaxed initial condition ($\vec{M} = M_0 \vec{z}$), the solution of this equation for the final magnetization at time T is explicit:

$$M_{xy}(\vec{r}) = i\gamma M_0 \int_0^T B_1(t) e^{i\vec{r}\cdot\vec{k}(t)} dt \tag{1.20}$$

where $\vec{k}(t) = -\gamma \int_t^T \vec{G}(s) ds$ parametrically describes a path through spatial frequency space. Using a change of variable from t to k, the solution can be rewritten as:

$$M_{xy}(\vec{r}) = i\gamma M_0 \int_K p(\vec{k}) e^{i\vec{r}\cdot\vec{k}} dk \tag{1.21}$$

where $p(\vec{k})$ is a path that scans k-space weighted by $B_1(t)/\left|\gamma \vec{G}(t)\right|$. The resulting transverse magnetization is therefore none other than the FT of the weighted k-space trajectory.

For two-dimensional selective excitation, what is therefore required is a gradient waveform that produces 2D k-space coverage in one shot, such as echo-planar or spiral. While these gradients are played, an RF field is applied to produce the required weighting in k-space. The simplest approach then for designing such an excitation is to take the 2D FT of the desired excitation pattern, which provides the weighting in excitation k-space, and to apply it via a trajectory that ensures uniform coverage and sufficient density.

If a solution for an excitation pattern is found at a small angle (e.g. 30°), then it has been shown that it still performs reasonably well when the RF is scaled to produce a 90° excitation instead, although this is way beyond the small flip angle limit.

1.5 Chapter summary

In this chapter, we described the nuclear magnetic resonance phenomenon and introduced basic concepts of main magnetic field, excitation field and relaxation processes. We then explained how magnetic field gradients can be used to spatially encode the signal and obtain an MR image. We described the correspondence between physical space and k-space in terms of Fourier transform relationship, spatial resolution and field-of-view. We underlined that in our studies we will mainly make use of 3D Cartesian sampling of k-space. The concepts of gradient echo and spin echo were introduced, along with typical sequence parameters. From there, the main "classical" sequences used in this thesis (FLASH, RARE and FISP) were briefly presented. Lastly, in the perspective of our work on the DESIRE sequence, we introduced the theory behind multi-dimensional selective excitation.

All experiments performed in this work will involve imaging at spatial resolutions below $(100\ \mu m)^3$. In the following chapter, we will therefore introduce the field of MR microscopy and its associated challenges.

2. Magnetic Resonance Microscopy

Bringing MRI from the clinical scale (~1 mm cubic voxel) to the cellular scale represents a tremendous achievement in terms of hardware. The main acceptability criterion behind any type of imaging is eventually the SNR: if the signal falls within the noise level, there can be no possible interpretation of what is "seen". The minimum acceptable SNR in an image depends on what is sought, but a general acceptability threshold is 5 (Minard and Wind, 2002). There are 1000 times less protons (and therefore signal) in a 100 μm cubic voxel than there are in a 1 mm cubic voxel, and it only gets "cubically" worse as resolution is increased. How do we achieve high spatial resolution while compensating for the associated loss of signal?

The goal of this chapter is to provide an introduction to MRM, focused on its applications in liquids and living tissue in particular. The main objectives, limitations and developments of the field will be explained. Extensive information can be found in books (Callaghan, 1993) and reviews (Glover and Mansfield, 2002; Tyszka et al., 2005). We will first discuss the main factors that influence spatial resolution and SNR in an MRI experiment and describe the three hardware components that made MRM possible: strong gradients, strong main magnetic field and small dedicated coils. We will then review the current achievements of MRM in small biological samples.

2.1 Achieving high spatial resolution

In this section, we will assume for a start that we have "lots of signal" and focus on physical requirements to highly resolve this signal spatially.

Physical limitations to spatial resolution

Combining the information from Equations (1.13) and (1.15) (pages 19-20), it appears that the theoretical spatial resolution of an MRI experiment is a function of the accumulated gradient area, i.e. the product of gradient amplitude and time of application. However, once the system has been excited, the time t available for

acquisition is limited by two phenomena: T_2 relaxation, which attenuates the signal by $\exp(-t/T_2)$, and molecular diffusion.

Indeed, when discussing the dephasing and rephasing effect of magnetic field gradients on the magnetization, the underlying assumption was that individual protons remain in the same position during the experiment, such that if they accumulate a phase $\varphi = \gamma G_x x \tau$ while the G_x gradient is on for duration τ, they will accumulate the exact opposite phase $-\varphi$ after application of $-G_x$ for duration τ, resulting in a net null phase. However, this is obviously a coarse approximation since molecules in fluids are mobile: their thermal energy translates into a random translational motion, or diffusion. This motion obeys the following distribution in a free medium:

$$< x^2 >= 2d\ D\ t \tag{2.1}$$

where $<x^2>$ is the average mean-square distance travelled, d is the number of spatial dimensions available, D is the diffusion coefficient and t is the time imparted for the molecule to travel (Einstein, 1905). Diffusion in the presence of a gradient G applied for a duration t produces irreversible dephasing and thus signal attenuation by $\exp(-\gamma^2 G^2 D\ t^3/3)$ (Callaghan and Eccles, 1988).

It therefore appears clearly that the better approach to reach high spatial resolution is to increase the gradient amplitude and slew rate (rate of switching from 0 to 90% of maximum), rather than the time of application.

When considering very high spatial resolution, the self-diffusion of water molecules poses an additional limit. Indeed, during the time of acquisition (or encoding) T, the displacement of a water molecule should not exceed the size of a voxel. Assuming pure water at room temperature ($D \approx 2\text{x}10^{-3}$ mm²/s) and T = 1 ms, this limits for instance the resolution to $\sqrt{\langle r^2 \rangle} = \sqrt{6DT} \sim 3.5\ \mu m$. In practice, diffusion in biological structures is slower than in pure water, and higher resolutions can therefore theoretically be attained. Nonetheless, short encoding and read-out times (achievable by using strong gradients) are also beneficial for reducing this diffusion-related blurring.

Magnetic field gradients

Considerable improvement of gradient capabilities was therefore necessary to make MRM possible. While clinical systems use gradient sets of 30 – 80 mT/m, lately developed microscopy gradients – albeit effective over a smaller volume on the order

of millimeters – can go up to 10 T/m. The important drawback of strong and rapidly switching gradients is the induction of eddy currents in the vicinity of the sample, which produce an unwanted and uncontrolled additional magnetic field and cause severe artifacts in the image (Ahn and Cho, 1991). Other consequences are the much increased acoustic noise and mechanical vibration. While the first is of no relevance on *ex vivo* biological samples, the latter imposes a robust experimental set-up which does not transmit the vibration to the object of interest, especially when seeking spatial resolutions of a few microns.

2.2 SNR considerations: how do we get it back?

In this section, we will examine the SNR dependencies on imaging parameters and on physical and hardware parameters. We will show how the dramatic loss in SNR that accompanies high spatial resolution can be compensated by improvements in magnet and coil design.

First, let us specify that the definition we take of SNR is:

$$SNR = \frac{signal\ amplitude}{standard\ deviation\ of\ noise} \tag{2.2}$$

The raw MR signal is a complex quantity, measured with a quadrature detector to obtain its real and imaginary components. The noise in each of these components has a Gaussian probability distribution with zero mean and standard deviation σ. The Fourier transform is a linear operation that preserves these noise characteristics in the image voxel that still contains complex information on magnitude and phase. However, what is usually observed is a magnitude image $\sqrt{Re^2 + Im^2}$. The noise of this magnitude image is no longer characterized by a Gaussian distribution, but by a Rician one (Gudbjartsson and Patz, 1995). If the SNR in the complex image is higher than 3, the Rician distribution approximates a Gaussian one fairly well and the bias in the magnitude image is not important. However, care must be taken when examining regions of low SNR (≤ 3) since the mean of the Rician noise distribution in the magnitude image is shifted with respect to the Gaussian one in the complex image. Typically, in regions of no signal, the mean is not zero but $\sigma\sqrt{\pi/2}$.

In the following paragraphs, we will focus on the SNR of the raw MR signal.

SNR and imaging parameters

The SNR dependencies on imaging parameters can be summarized by the following relationship:

$$SNR \propto \Delta x \Delta y \Delta z \sqrt{NA \cdot N_{PE} \cdot T_{RO}} f(\rho, T_1, T_2) \tag{2.3}$$

where Δx, Δy and Δz are the voxel sizes in each dimension. The dramatic decrease in SNR with increased spatial resolution is obvious. SNR also varies with the square root of the total signal acquisition time, which is the product of number of averages (NA), number of phase-encoding steps (N_{PE}) and read-out time (T_{RO}). $f(\rho,T_1,T_2)$ is a function that represents the available signal depending on sequence timings and tissue properties. Several points are worth discussing.

First of all, this relationship shows the inefficiency of using experiment averaging to win back what is lost through high spatial resolution: if the spatial resolution is doubled in a single direction, the number of averages (and thus the acquisition time) needs to be multiplied by four to maintain the SNR level.

Second, although lengthier, 3D acquisitions versus 2D bring high benefits in terms of SNR, since N_{PE} becomes $N_{PE}*N_{PE2}$.

The read-out time T_{RO} is often expressed as 1/BW, where BW is the receiving bandwidth of the A/D converter. Longer read-out times are therefore associated with shorter bandwidths that introduce less noise and improve the SNR (Edelstein et al., 1986). This aspect is in direct competition with the benefits reaped from short read-out times, which help reduce T_2- and diffusion-related losses.

SNR and physical parameters

Let us now focus on the physical and hardware parameters that impact SNR, and see what steps must be taken to obtain high spatial resolution images with sufficient SNR.

As a very general description, if all other conditions are fixed (i.e. sample, sequence and temperature), the SNR depends on three parameters (Minard and Wind, 2001a):

$$SNR \propto \frac{B_0^2 B_{xy}}{\sqrt{R_{total}}} \tag{2.4}$$

The numerator refers to signal dependencies, in terms of main magnetic field strength B_0 and coil sensitivity B_{xy}, defined as the strength of the RF field produced at the center of the sensitive volume when a unit current flows in the coil. The denominator refers to noise dependencies via the effective resistance of the receiver circuit R_{total}. Equation (2.4) is already a hint that one crucial element in the pathway of maximizing SNR in an MRM experiment is the coil performance, via its sensitivity and resistance. Indeed, the efficiency of a coil is defined as:

$$\eta = \frac{B_{xy}}{\sqrt{P}} = \frac{\sqrt{2}B_{xy}}{\sqrt{R_{total}}} \tag{2.5}$$

where P is the supplied power to produce the B_{xy} field. Maximizing the efficiency of the coil is then synonymous of maximizing the SNR.

The solenoid design gives the best efficiency (Hoult and Richards, 1976). Solenoid-shaped coils have thus been extensively used in MRM experiments and all parameter dependencies introduced below are based on a solenoid model. Figure 6 shows a schematic of a solenoid, with notations of typical features. In the following paragraphs, we will detail the origins and implications of each of the factors introduced in Equation (2.4).

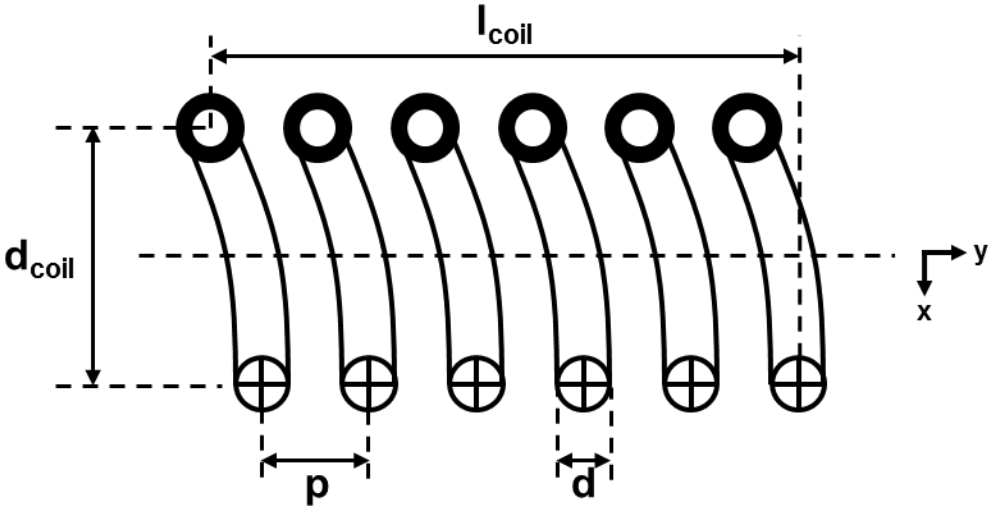

Figure 6. Cutaway schematic of a solenoid, showing the main geometric characteristics. The current flows into the page at the bottom and out of the page at the top. The number of turns is n = 6. The solenoid axis is along y. The coil diameter and length are defined from wire center to wire center and are labeled d_{coil} and l_{coil}, respectively. The wire diameter is d, and the total wire length is approximately $l = n\pi d_{coil} + l_{coil}$. The spacing between turns, or pitch, is also defined from wire center to wire center and is labeled p.

Signal dependencies

Let us go back to the origin of the received NMR signal and consider the transverse (i.e. rotating) component of the magnetization, $M_{xy}(\mathbf{r})$, in an elementary volume δV. According to Faraday's law, the changing magnetic flux associated with the magnetic moment ($M_{xy}(\mathbf{r})*\delta V$) will induce a voltage δU across the receiver coil. The principle of reciprocity relates δU directly to the strength of the magnetic field produced in the transverse plane $B_{xy}(\mathbf{r})$ by a unit current flowing in the coil at the Larmor frequency (Hoult and Richards, 1976). Thus:

$$\delta U = \omega_0 M_{xy}(\vec{r}) B_{xy}(\vec{r}) \delta V \tag{2.6}$$

As seen in the introductory part on MRI, the nuclear polarization fraction M_0, and therefore $M_{xy}(\mathbf{r})$, scale linearly with the magnetic field strength B_0. The Larmor frequency ω_0 is also proportional to B_0. Thus the voltage induced and thereby the signal received are proportional to the square of the field strength.

$$S_{received}(t) \propto B_0^2 \tag{2.7}$$

Equation (2.6) shows that the signal received is also proportional to the sensitivity of the receiver coil, and using the derivation of the magnetic field inside a solenoid, it has been demonstrated that the field in the very center depends on the geometrical characteristics of the coil via:

$$B_{xy} = \frac{n\mu_0}{d_{coil}\sqrt{1 + \left(\frac{l_{coil}}{d_{coil}}\right)^2}} \tag{2.8}$$

where μ_0 is the vacuum permeability and coil parameters are as defined in Figure 6 (Minard and Wind, 2001b). Since the geometric characteristics of the coil also impact the coil resistance and the uniformity of the RF field inside the coil, global recommendations for coil geometry will be provided in more detail in the forthcoming "microcoil" section.

Noise dependencies

Noise in MRI is mainly of thermal origin, arising from Brownian motion of electrons in a conductor, which causes random electrical fluctuations. The corresponding noise power spectral density is $4k_BTR$, where k_B is Boltzmann's constant, T the absolute temperature and R the conductor resistance. The proposed analysis of the elements

contributing to thermal noise in an NMR experiment is based on work by (Minard and Wind, 2001a). In a "receiver + sample" system, the various elements in which dissipation mechanisms occur are the coil, the leads, the tuning capacitor and the sample. They can each be represented by a separate resistor. Losses in the matching capacitor are negligible when operating near the circuit's resonant frequency. Thus:

$$R_{total} = R_{coil} + R_{leads} + R_{cap} + R_{sample} \tag{2.9}$$

For microscopy size coils ($d_{coil} < 2$ mm), noise from the coil is considered to dominate if loaded with biological samples of normal conductivity (Cho et al., 1988; Glover and Mansfield, 2002). However, losses in the tuning capacitor and in the sample increase more rapidly with frequency than losses in the coil, and at frequencies higher than 500 MHz (11.7 T for proton), they cannot be fully neglected.

A solenoid dissipates energy through two processes: eddy currents in the core of the wire that effectively only allow conduction at the wire surface (skin effect), and eddy currents induced in each turn by neighboring turns once the wire is coiled (proximity effect). The skin effect is more pronounced with increasing frequency f, since the current is only carried within a skin depth $\delta = \sqrt{\rho/(\pi\mu_0\mu_r f)}$, where ρ is the electrical resistivity and μ_r the relative permeability of the conductor (Jackson, 1975). Considering copper at room temperature, the skin depth is for example about 3 μm at 500 MHz and ever thinner with higher frequencies. In this high frequency regime, δ is therefore much smaller than the wire diameter d, so the resistance of the solenoid due to its sole wire length l can be approximated by:

$$R_{wire} = \frac{l}{d}\sqrt{\frac{\mu_0\mu_r\rho f}{\pi}} \tag{2.10}$$

In the high frequency regime ($d >> \delta$), the proximity effect results in a coil resistance which is the product of R_{wire} and an enhancement factor ξ (Butterworth, 1926). The enhancement factor depends on the ratios of coil length to coil diameter and wire diameter to wire spacing. Values of ξ for solenoids with many turns ($n > 30$) are reported in a table by (Medhurst, 1947) and the enhancement for coils with a lower number of turns n can be approximated by $\xi_n \sim 1 + (\xi - 1)(1 - 1/n)$. Eventually, at the resonance frequency:

$$R_{coil} = \xi_n \frac{l}{d}\sqrt{\frac{\mu_0\mu_r\rho\omega_0}{\pi}} \tag{2.11}$$

$$R_{leads} = \frac{l_{leads}}{d}\sqrt{\frac{\mu_0\mu_r\rho\omega_0}{\pi}} \tag{2.12}$$

The dependencies of the solenoid inductance on geometry are dominated by:

$$L_{coil} \propto d_{coil}n^2 \tag{2.13}$$

Moving on to the tuning capacitor, its resistance can be written as:

$$R_{cap} = \frac{1}{\omega_0 C_{tune} Q_{cap}(\omega_0)} \tag{2.14}$$

where C_{tune} is its capacitance and Q_{cap} its quality factor. The latter typically has a frequency dependence that varies with capacitor design. Overall, for a fixed capacitance, capacitor losses can increase with frequency faster than coil losses.

Last but not least, a conducting sample will dissipate additional electromagnetic energy in the form of magnetic (m) and dielectric (e) losses: $R_{sample} = R_m + R_e$.

Magnetic losses result from the eddy currents induced in the sample by the alternating RF field. Using previous notations and introducing a cylindrical conducting sample of direct current conductivity σ, the effective resistance associated with magnetic losses is described as follows (Cho et al., 1988):

$$R_m = \frac{\pi\omega_0^2\mu_0^2 n^2 d_{sample}^4 l_{sample}\sigma}{128(d_{coil}^2 + l_{sample}^2)} \tag{2.15}$$

For samples of large diameter, the total resistance in the system is considered to be dominated by R_m. For the small objects of interest in MRM, the latter is on the contrary usually negligible.

Dielectric losses in aqueous solutions arise from two effects of the alternating electric field: the first is realigning the electric dipoles of water molecules, and the second is moving ions back and forth in the fluid. The latter is a function of sample conductivity and is the dominating source of dielectric losses in biological samples for frequencies below 2 GHz. The exact estimation of R_e is not straightforward, with required experimental measurement of certain factors. However, in terms of relative weight compared to other sources of noise, dielectric losses can be quite severe and should not be neglected unless counteracted by special designs (Faraday screen or

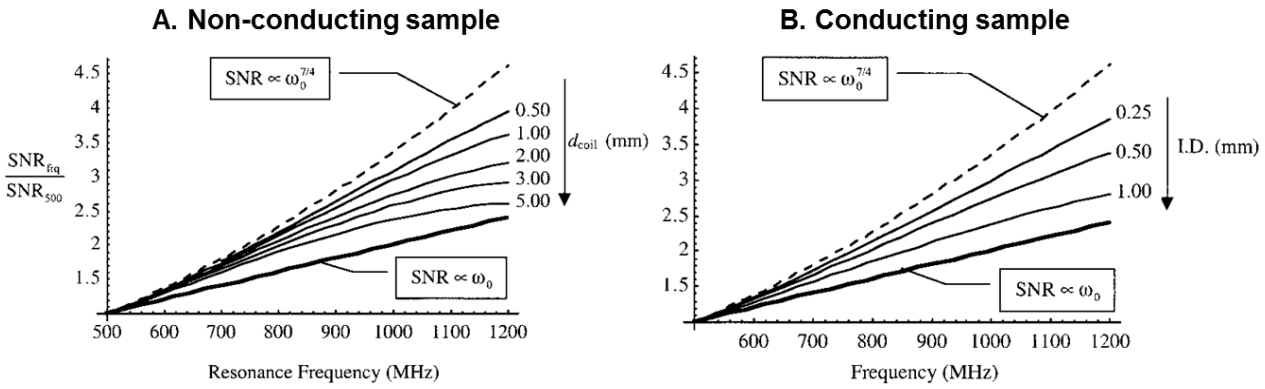

Figure 7. Relative SNR per unit sample volume as a function of frequency and coil size. The dashed line represents the ideal $\omega_0^{7/4}$ response if coil losses dominate, the bold line shows the limit when either capacitor losses (A) or dielectric sample losses (B: σ = 1 S/m) dominate. Overall, the SNR performance is significantly degraded by dielectric losses in the sample, and the degradation increases with coil size. *From (Minard and Wind, 2001a).*

distribution of the tuning capacitance throughout the coil structure). For high frequencies:

$$R_e \propto \omega_0^2 L_{coil}^2 <=> R_e \propto \omega_0^2 n^4 \tag{2.16}$$

Overall, if a, b and c are the relative weights of each source of noise (coil+leads, capacitor and sample, respectively) defined by circuit design, temperature and sample conductivity and size, the frequency (and therefore static field) dependence of the equivalent system resistance is:

$$R_{total} = aB_0^{1/2} + bB_0^x + cB_0^2 \tag{2.17}$$

where x depends specifically on capacitor model but can be larger than unity. Combining Equations (2.7) and (2.17), the overall impact of magnetic field strength on SNR can be expressed as follows:

$$SNR \propto \frac{B_0^2}{\sqrt{aB_0^{1/2} + bB_0^x + cB_0^2}} \tag{2.18}$$

In MRI of large samples, the noise is usually dominated by magnetic losses in the sample, hence SNR α B_0. In MRM, there is great incentive in designing the coil and circuit such that the noise is dominated by resistive losses in the coil (SNR α $B_0^{7/4}$) but the effective dependence is usually somewhere between B_0 and $B_0^{7/4}$ due to unavoidable capacitor losses and dielectric losses in the sample. Figure 7 illustrates

the evolution of the relative SNR between the two limits depending on coil diameter and sample conductivity. Nonetheless, there is great benefit in terms of SNR to work at high field strength, and the latter is the first step in achieving successful MRM experiments.

Ultra-high magnetic field

The development of super-conducting magnets opened the way for MR systems of several teslas. The technological constraints of magnet building are higher on large-bore versus small-bore magnets, and on horizontal versus vertical designs. In MRM, small bores are largely acceptable as the sample size rarely exceeds the centimeter. Horizontal magnets are often more convenient for small animal imaging, but vertical magnets are common use in MRM. While in clinical MRI, standard field strengths range from 1.5 to 7 T, MRM makes use of horizontal systems up to 17.2 T (730 MHz) and vertical systems up to 21 T (900 MHz).

Unfortunately, working at ultra-high field does not only come with advantages. The increase in T_1 with field strength often leads to longer scan times because repetition times need to be increased. Variations in magnetic susceptibility produce larger unwanted field inhomogeneity, especially at interfaces, resulting in very short T_2* and overall image degradation. Last but not least, increasing the field strength means working at higher radio-frequencies for excitation and reception. Some of these downsides can however be minimized to a certain extent by the coil design.

In the next section, we will provide general guidelines for coil design in MRM in order to achieve high sensitivity, minimal losses and RF homogeneity.

2.3 Microcoil design

One crucial element in the pathway of obtaining high quality MRM images is the coil performance. We will focus on volume microcoils, since they are better suited than surface coils to obtain homogeneous RF coverage of an entire biological sample. Surface microcoils have important applications nonetheless, when direct access to the sample is needed for instance (Eroglu et al., 2003). The analysis and recommendations presented in this section are mainly inspired by (Minard and Wind, 2001a, b).

For a fixed sample volume, the SNR increases with decreasing coil dimension, meaning that the coil should be closely fitted around the sample. Again, the simplest

and most effective volume coil shape for microscopy has proven to be the solenoid (with a diameter typically < 2 mm) (Mohmmadzadeh et al., 2011; Peck et al., 1995). There are three factors that limit the minimal size one can choose for a solenoid: the size of the sample, B_0 homogeneity and B_1 homogeneity. Once the diameter and length of the solenoid are determined by these requirements, additional geometric parameters such as number of turns, spacing and wire diameter can be chosen to optimize the SNR for the sought application. The rest of the circuit characteristics follow.

B_0 homogeneity

At ultra-high field, the variations in magnetic susceptibility at interfaces cause large static field distortions, especially at the copper/air interface around the coil's wire. One way to reduce this source of B_0 inhomogeneity is to replace the air around the coil with a medium that has a magnetic susceptibility comparable to that of copper: for instance D_2O or perfluorinated fluids (Olson et al., 1995).

Nonetheless, some line broadening due to the presence of the coil remains, and it is worsened with decreasing distance between the coil and the sample. This distance is usually quantified by the filling factor, which is the sample-to-coil volume ratio. Experiments on a sample of deionized water showed that the linewidth of the spectrum, which is a measurement of B_0 inhomogeneity, was increased from 0.005 parts-per-million (ppm) to 0.013 ppm when the filling factor varied from 2% to 51%. Concomitantly, the relative SNR also increased from 1.0 to 22.3 (Webb and Grant, 1996). The considerable gain in SNR associated with high filling factors encourages the design of close fitting coils for applications where high spectral resolution is not required. Additionally, when heterogeneous samples are examined, the line broadening is typically dominated by variations of magnetic susceptibility inside the sample itself rather than by the proximity of the coil. For MR microscopy using solenoid coils, filling factors of up to 90% are recommended (Glover and Mansfield, 2002).

B_1 homogeneity

Equations (2.4) and (2.8) (pages 33 and 35) have already shown how the SNR is affected by the coil sensitivity B_{xy}, and how the latter in turn depends on solenoid characteristics. The main feature than stands out is that the sensitivity increases as the coil diameter decreases and the number of turns increases. However, the homogeneity of the transmission and reception RF fields is also of importance to ensure an image with no artifactual intensity variations.

Competing with sensitivity, RF homogeneity is improved for larger coils. One solution then consists in using a larger transmit coil and a smaller close-fitted receiver coil. This improves the uniformity of the excitation but not of the reception. Moreover, this solution is accompanied by complicated coil design, and imperfect decoupling between the two coils can eventually have detrimental impacts on SNR and image quality. The more common approach in MRM is to use the same coil for transmission and reception (i.e. a transceiver), the minimal size of the latter being dictated by the amount of RF heterogeneity deemed acceptable.

Equation (2.6) (page 35) illustrated the double impact of spatial variations in the transmit RF field on the received signal: via B_{xy} directly and also via variations in the magnetization M_{xy} induced by non-uniform flip angles. When looking at the RF field produced not just at the coil center but also along the coil length (axis y in Figure 6), a theoretical derivation gives:

$$B_y(y) = n\mu_0 \left[\frac{\frac{1}{2} + \frac{y}{l_{coil}}}{\sqrt{d_{coil}^2 + (l_{coil} + 2y)^2}} + \frac{\frac{1}{2} - \frac{y}{l_{coil}}}{\sqrt{d_{coil}^2 + (l_{coil} - 2y)^2}} \right] \tag{2.19}$$

The total magnetic field per unit current in the transverse plane is in fact $B_{xy} = \sqrt{B_x^2 + B_y^2}$. However, $B_x/B_y \sim l_{coil}/(nd_{coil}\pi)$ such that, unless the coil is loosely wound, the contribution of $B_x(y)$ is small and $B_{xy}(y)$ is well approximated by $B_y(y)$.

Assuming a sample of length l_{sample} and centered in the coil, the amount of deviation of the RF field at the sample edges can be calculated by computing $\left(B_{xy}(0) - B_{xy}\left(l_{sample}/2\right)\right)/B_{xy}(0)$ from Equation (2.19). In practice, for coil design, this maximum acceptable RF deviation can be set as an input criterion (e.g. 10%) along with sample size and coil diameter, and the minimum coil length and number of turns chosen accordingly.

Minimal noise

From the perspective of RF sensitivity, the solenoid diameter should be as small as possible to fit the sample. Moreover, assuming a somewhat spherical sample, the coil length should roughly be at least 1 – 1.5 times the coil diameter for proper RF homogeneity in the sample. Let us then assume that d_{coil} and l_{coil} are set from these RF sensitivity and homogeneity considerations. Resistive losses can further guide us to choose the remaining parameters, such as wire diameter and spacing.

In Section (2.2), we have detailed the main contributors to thermal noise in the NMR experiment and assessed their dependence on frequency and circuit characteristics. The name of the game in solenoid and circuit design is naturally to minimize all losses, and also ensure that the noise is – whenever possible – dominated by resistive losses in the coil, which ensures optimal SNR gain from working at high field.

For a given number of turns n, there exists an optimal thickness of wire that maximizes SNR. This can be understood as an optimum between two competing phenomena: increasing the wire diameter decreases the resistance in the wire, but also decreases the effective distance between adjacent turns, which leads to more pronounced proximity effects (see Equation (2.11) page 36). A rough guideline which is independent of the number of turns is to set the spacing between turns to approximately 1.5 times the wire thickness (Hoult and Richards, 1976).

For non-conducting samples ($R_{sample} = 0$), (Minard and Wind, 2001a) showed that the SNR per unit sample volume is increased for a coil with thinner wire and larger number of turns. Indeed, in such a configuration, both R_{coil} and R_{cap} are increased, the former because of increased wire length and thinness and the latter because C_{tune} needs to be decreased to accommodate the increased coil inductance L_{coil}. However, R_{coil} increases proportionally more than R_{cap} and becomes the primary source of noise: the SNR increases (Equation (2.18)). The proportionality between B_{xy} and n also serves the SNR (Equation (2.8) page 35).

On the contrary, for conducting samples, Minard and Wind showed that the SNR is improved for coils with fewer turns and thicker wire. The main reason for this behavior is that dielectric losses are proportional to n^4 (Equation (2.16)) and can therefore quickly become the dominating source of noise for coils with many turns, thus causing the SNR to plummet.

Miscellaneous considerations

The resonant frequency of an LC circuit is defined by:

$$\omega_0^2 = \frac{1}{LC} \tag{2.20}$$

At very high frequencies, a relatively large circuit inductance (to which the coil is the primary contributor) will require an exceedingly small overall capacitance. Surprising as it may sound, one has to ensure that such low capacitance is feasible with available capacitors. Also, for very low capacitor values, the equivalent

capacitance of the other elements in the circuit could eventually dominate, a configuration hardly desirable for matching and tuning purposes. As a consequence, the maximum inductance, and thereby solenoid diameter and number of turns are usually limited. This proves the usefulness of the solenoid for microimaging but its impracticality for imaging larger objects.

In an effort to further reduce the overall circuit inductance and resistance, the length of the coil leads and of the copper tracks in the circuit should also be minimized within feasibility limits.

The performance of a resonating circuit can be partially evaluated via its quality factor Q, which is an indicator of the rate of resistive losses in the system. The quality factor is typically defined and measured as:

$$Q = \frac{f_0}{\Delta f} \tag{2.21}$$

where f_0 is the frequency of interest (usually the resonance frequency) and Δf the bandwidth for which the energy falls to half its peak value, i.e. an attenuation of 3 dB. When building the circuit, capacitors should be chosen to achieve a high quality factor Q. Nonetheless, it should be noted that Q is not an indicator of the actual coil efficiency. Large probes for MRI usually display quality factors of 50 – 500. However, the smaller the probe the lower the Q and microcoils are usually characterized by quality factors between 20 and 100 (Massin et al., 2002).

The quality factor can be influenced by the presence or absence of a load (sample), depending on the relative importance of resistive losses in the sample. There are two implications to this. First, it is important to build the resonating circuit while the coil is loaded with a representative sample. Second, if the resonating frequency shifts and/or Q is altered when a load is introduced in the coil, it can be assumed resistive losses in the sample will be non-negligible during the MR experiment. If there is no shift or significant change in Q, the equivalent resistance of the system is likely dominated by the resistance of the coil.

In terms of RF penetration, the shorter wavelength associated with high frequencies is not limiting in microscopy as it is in clinical applications because the sample size itself is much smaller too. Similarly, the increase of RF power deposition with the square of the frequency is not an issue in microscopy because the power deposited by micro-coils is very low to start with.

Special designs of the ground plane are necessary to prevent the circulation of eddy currents induced by the gradients, especially since the latter are particularly strong for microscopy (Jin, 1999). Such a design will turn out necessary for our microcoils and will be described in Chapter 3.

Overall, improvements in the design of magnets, gradients and transceiver coils have made magnetic resonance microscopy "feasible". Eventually, the spatial resolution of MRM images is dictated by the interplay between sample size, structure size (i.e. what size of detail is needed?), diffusion, critical SNR and available acquisition time. The next section presents the main experimental achievements in magnetic resonance microscopy of liquids (structured phantoms and biological samples).

2.4 Current imaging achievements

The primary interest of MRM for biology and medicine is the visualization of small biological structures – possibly single cells – weighted by various MR contrasts. Access to high resolution information on MR relaxation times or other MR measurable quantities (e.g. an apparent diffusion coefficient – ADC[1]) inside microscopic structures appears of great interest, especially if such measurements can be performed within the timeframe of sample viability. The dynamic study of microscopic biological processes with MRM is the aim of current work in the field.

As mentioned earlier, the first MR image of a single cell was reported in 1986: a T_2-weighted image of a *Xenopus* oocyte (Aguayo et al., 1986). Because of time limitations, imaging consisted in the acquisition of a single thick slice (250 µm) across the ovum, with 10x13 µm² in-plane resolution. Since 2D multi-slice acquisitions are much more time efficient than 3D acquisitions, the former were often preferred, and subsequent works usually quoted much higher in-plane than through-plane resolution. In order to overcome the problem of partial volume effects (PVE) in the slice direction, MRM experimentalists therefore turned to imaging biological objects with an intrinsic cylindrical structure, such as geranium stems, human hair or fixed spinal cords from lamprey, rat and human (Bowtell et al., 1990; Cho et al., 1988; Flint et al., 2012; Flint et al., 2009; Lee et al., 2001; Wright et al., 2002).

[1] Formally defined in Chapter 6

In parallel, the limits of new and highly performing gradients and RF coils were tested on phantoms. One group reported 1 µm in-plane resolution (the highest ever achieved) and 75 μm^3 voxel volume on a hydrocarbon oil phantom containing thin-wall glass capillaries (Lee et al., 2001). The low diffusion coefficient of the oil dramatically reduced diffusion-related attenuation during their half-Fourier space spin-echo acquisition. Later, 3.7x3.3x3.3 μm^3 resolution was demonstrated in a phantom containing water and polymer beads, using 3D phase-encoding (i.e. no gradient is played during the read-out) (Ciobanu et al., 2002). Similarly, 3.0 µm isotropic resolution was achieved in a phantom of glass fiber fleece in water (Weiger et al., 2008a).

Single cell imaging has not been abandoned nonetheless. Figure 8 shows highlights of MR single cell imaging from the literature. Following the 1986 initial publication, subsequent works on *Xenopus* oocytes reported 20 µm isotropic images of water and lipids (Wind et al., 2000) or 60 µm isotropic parametric maps of T_1, T_2 and ADC (Sehy et al., 2001). With technological improvements, the object of interest could evolve towards a single cell somewhat smaller than the toad's egg (300 µm vs 1 mm): the isolated L7 neuron from *Aplysia californica* (Aiken et al., 1996; Bowtell et al., 1995; Grant et al., 2001; Hsu et al., 1996; Schoeniger et al., 1994). In these sets of studies, MRM started going beyond the sole aim of achieving high spatial resolution, by addressing issues of true T_2 relaxation differences between nucleus and cytoplasm, evolution of T_2 and ADC with neuron maturation or hypotonic stress, and even non Gaussian diffusion in cytoplasm and nucleus.

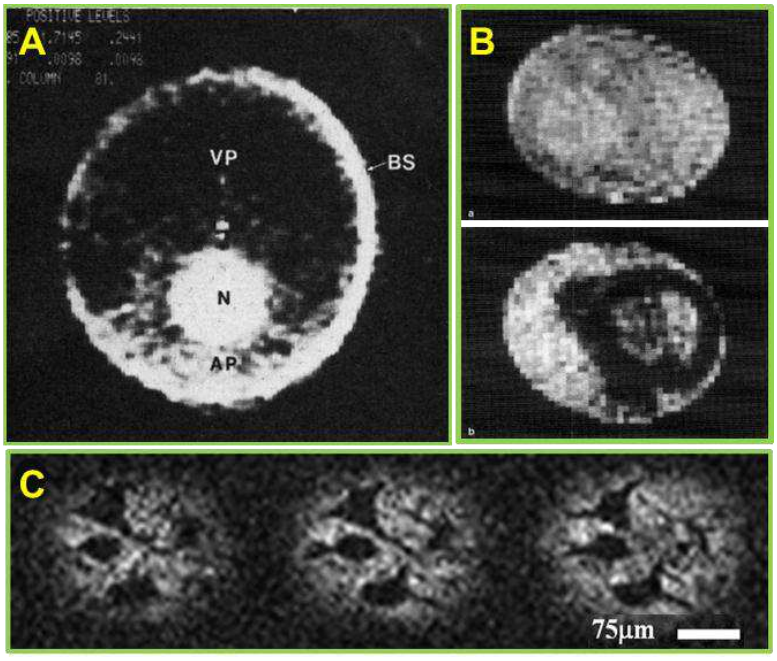

Figure 8. A. (Aguayo et al., 1986) NMR image of a *X. laevis* ovum; spatial resolution: 10x13 µm²; slice width: 250 µm. The differences between the cell nucleus and different zones of the cytoplasm are easily discerned. B. (Schoeniger et al., 1994) Spin density (top) and T_2-weighted (bottom) images of isolated *Aplysia* neurons. In the latter the cell cytoplasm appears as a dark annulus surrounding a lighter nucleus. C. (Flint et al., 2012) T_2-weighted images of neuronal processes in the pig; 6.25 µm isotropic resolution. Adjacent slices show the hypointense projections emanating from the cell bodies of α-motor neurons.

Recently, the first MR images of cell bodies and projections of α-motor neurons from human and porcine fixed spinal cord were reported, with an isotropic resolution of 6.25 μm for 64 hours of acquisition (Flint et al., 2012). Thus mammalian neuron imaging slowly comes within reach, although the step from fixed to living tissue remains a challenge.

Table 1 summarizes the important achievements in MRM of biological samples since 1986 (see also the review by (Ciobanu et al., 2003)).

As mentioned earlier, the choice of spatial resolution is governed by a trade-off between the detail size required, the sample size and the acquisition time. It is today still out-of-reach to image a large volume (e.g. a mouse brain) at very high spatial resolution (~10 μm) *in vivo*. Because *in vivo* imaging is nonetheless of the greatest interest, there has been a steady development of MRM at lower-end resolutions (~100 μm) for studies on genetically engineered mouse models of human pathologies (Badea and Johnson, 2012; Benveniste and Blackband, 2006).

In the current work, this is however not the path that was followed. The objectives of this thesis relied on the possibility of imaging single neurons in small *ex vivo*, yet living, samples. Perhaps it would be more appropriate today to refer to such methods as MR "micro-imaging", rather than MR microscopy.

Ref.	Object	Resolution (µm)	Field (T)	Gradient (mT/m)
(Aguayo et al., 1986)	*Xenopus* oocyte	10x13x250 in 32 min	9.5	200
(Cho et al., 1988)	Plant stem / human hair	4x4x300 in 1h	7	8,000
(Schoeniger et al., 1994)	*Aplysia* L7	20x20x100 parametric maps in 2h	8.5	Not specified
(Wind et al., 2000)	*Xenopus* oocyte	20 isotropic in 2h20	11.7	Not specified
(Lee et al., 2001)	Capillaries in hydrocarbon oil	1x1x75 in 1h	14.1	10,000
(Ciobanu et al., 2002)	Polymer beads in water	3.7x3.3x3.3 in 30h	9	5,800
(Weiger et al., 2008a)	Glass fibers in water	3.0 isotropic in 58h	18.8	65,000
(Flint et al., 2009)	Fixed rat striatum	4.7 isotropic in 22h	14	3,000
(Flint et al., 2012)	Fixed human spinal cord	6.25 isotropic in 64h	14	3,000
(Meme et al., 2013)	*Drosophila*	10x10x80 in 1h30	9.4	950

Table 1. Landmarks in MRM of biological samples, since 1986.

2.5 Chapter summary

In this chapter, the challenges associated with acquiring high spatial resolution images with sufficient SNR in a reasonable amount of time were put forward and the need for strong magnetic field gradients, high magnetic field and dedicated coils was discussed in that perspective. Guidelines for building optimized solenoids and transceiver circuits were provided. Additionally, issues associated with ultra-high field and strong rapidly switching gradients were raised, along with experimental consequences and recommendations. To-date achievements in MRM of biological samples and phantoms were also reviewed.

In the next chapter, we will present the characteristics of the biological samples used in the context of this work (single cells and ganglia from *Aplysia californica*) and describe the hardware used to image these samples.

3. "Materials": big neurons and small coils

The main objective of this thesis was to perform magnetic resonance microscopy measurements on isolated neurons and ganglia from *Aplysia*, in order to study both the transport of the manganese ion within a neuronal network and the changes in diffusion coefficient induced by various challenges, at a scale that allowed individual cell visualization. This chapter will provide a description of the nervous system of the animal model *Aplysia californica*. As explained in the previous chapter, MRM experiments require a strong magnetic field, a strong gradient set with high slew rates and dedicated micro-coils. This chapter will therefore also present the hardware available at NeuroSpin and more importantly the specific coils that were built for the experiments.

3.1 Larger and simpler is better: *A. californica*

Neurons are cells that allow information to be transported and processed. They are therefore organized in networks. Each neuron is constituted of a cell body (soma), an axon and multiple dendrites. Transfer of information from one neuron to the next occurs at synapses, which in most cases are located between the axon terminal of the pre-synaptic neuron and one dendrite from the post-synaptic neuron.

The study of the nervous system in mammals is challenging due to the small size of neuron bodies and to the complexity of the network as a whole. In humans, the soma diameter is about 4 μm for some 100 billion estimated neurons (Williams and Herrup, 1988), and 100 – 500 trillion synapses.

Luckily, other species present a nervous system that is easier to study (larger cell size and fewer neurons), with nonetheless comparable cellular and network properties. For instance, much of the current knowledge on axonal function (e.g. ionic mechanism of action potentials) was obtained from studies on the squid giant axon, which is 0.5 – 1 mm diameter (Hodgkin and Huxley, 1952).

Similarly, the sea slug *Aplysia californica* has become a widespread model in neuroscience, thanks to its very simple nervous system. *Aplysia* studies, led by

neuropsychiatrist Eric Kandel, permitted crucial advances in the understanding of short- and long-term memory formation (Carew et al., 1981; Kupfermann and Kandel, 1969). More importantly, most of these mechanisms were found to be present in vertebrates as well (Kandel, 2001). The description of the nervous system of the *Aplysia* presented below is taken from (Kandel and Kupfermann, 1970).

The nervous system of *Aplysia* is constituted of around 20,000 neurons, distributed among five pairs of bilateral ganglia with specific functions. Each ganglion is connected to its symmetrical counterpart through a commissure, to other ganglia through connectives, and to the periphery through nerves. The abdominal ganglia fused to form a single unit. Figure 9 shows a picture of *A. californica* at NeuroSpin and a schematic of its nervous system.

Each ganglion is organized into three easily identifiable constituents: a surrounding sheath, a region of cell bodies and a region of neuropil (axons and dendrites). The sheath is known to mainly provide structural support and does not represent a strong barrier to the diffusion of small molecules. As with all invertebrates, the regions of cell bodies and neuropil are separated within the ganglion: the former are located in a rind under the sheath and the latter are in the core of the ganglion. This separation is of great experimental interest, as will be highlighted later on. The neuronal cell bodies are large (up to 1 mm diameter in adults) and most of them are individually identifiable. Their functions, axonal projections and synapses have been extensively studied using optical imaging and electrophysiology techniques (Morton et al., 1991; Nargeot and Simmers, 2012; Quicke and Brace, 1979).

Moreover, *Aplysia* neurons are easier to manipulate experimentally: their ideal temperature is 4 – 15°C and they are generally more resistant to non-ideal experimental conditions (temperature, osmotic stress…) than mammalian neurons.

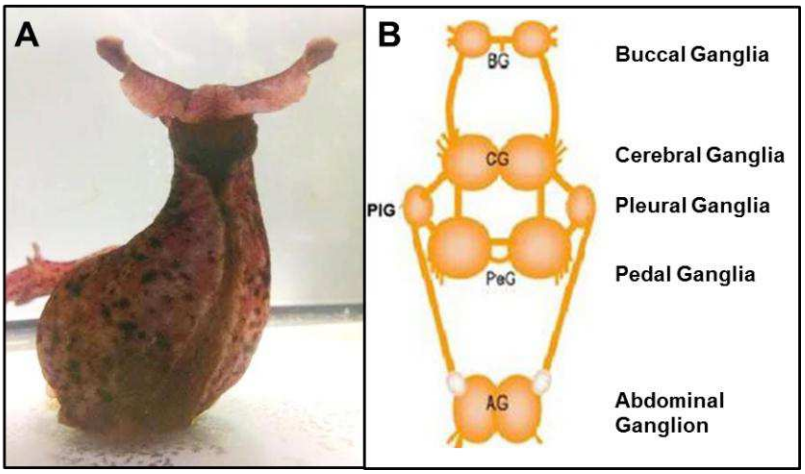

Figure 9. A: Ventral view of *Aplysia californica*. (*Courtesy of G. Radecki).*
B: Schematic of ganglia layout in the animal, from head (top) to tail (bottom). Also shown are commissures and connectives to other ganglia.

For the experiments pertaining to the imaging of neural networks with manganese enhanced MRI, the buccal ganglia were chosen because the cellular network is very well determined in terms of neuron, axonal projection and synapse identifications (see Figure 10A). This pair of ganglia was also used for diffusion measurements at tissue scale. The MR imaging protocol involves inserting the ganglia into glass capillaries. The overall small size and stretched out shape of the buccal ganglia also made this insertion safer and easier.

For diffusion measurements in single cells, notoriously large neurons of up to 500 µm in diameter were individually extracted from the abdominal and left pleural ganglia (see Figure 10, B and C).

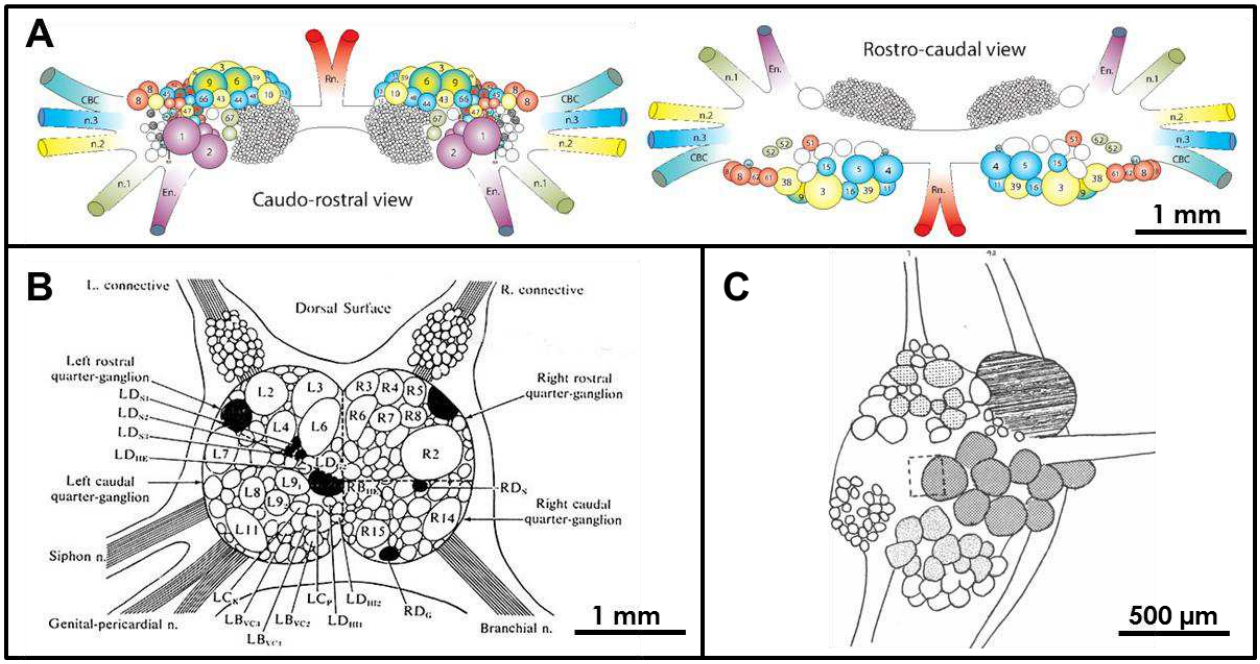

Figure 10. Schematics of three ganglia. A: Buccal ganglia. Two views (front and back) are represented. The color code indicates which neurons have axonal projections into which peripheral nerves. n.1-3: nerve 1-3; E.n.: esophageal nerve; R.n.: radular nerve; CBC: cerebro-buccal connective. C*ourtesy of R. Nargeot*. B. Abdominal ganglion, showing some of the largest cells in the animal: R2, L3 to L7 and L11. *Diagram taken from (Kupfermann et al., 1974)*. C: Left pleural ganglion. The giant cell LPl1 is in the upper right-hand corner. *Diagram taken from (Kehoe, 1972)*. The length scales give an indication of the cell sizes involved. The actual sizes vary with animal age and weight.

3.2 Hardware

This section provides details on the magnet and gradients available for microscopy experiments, and on the design of the micro-coils. The latter were built specifically to match the needs of imaging *Aplysia* cells and ganglia.

3.2.1 Magnet and gradients

All experiments in this thesis work were performed on a 17.16 Tesla horizontal magnet developed by Bruker BioSpin (Ettlingen, Germany) – see Figure 11. It is currently the strongest horizontal magnet in the world. The operating frequency for proton imaging is 730.2 MHz, with an associated wavelength in vacuum of 41 cm. The magnet bore diameter is 25 cm.

Figure 11. 17.2 Tesla system at NeuroSpin.

The magnet is equipped with a gradient set of 1000 mT/m on each axis (X, Y, Z), withstanding slew rates of up to 9000 T/(m.s) – i.e. gradients can switch from 5% to 95% of their maximum in 100 µs. Gradient linearity is within 3% over 3.5 cm. The bore diameter of the gradient set is 8.5 cm. This corresponds to the physical space available for coil and sample insertion.

The magnet is also equipped with five second order shim coils (the first order shim coils are the gradients). Loaded with a 3 cm spherical water phantom and shimmed, the magnetic field displays an inhomogeneity of 2.5 Hz (0.003 ppm) over 1 cm^3. The main field fluctuates by less than 5.5 Hz (0.008 ppm) per hour.

3.2.2 Micro-coils

Because of the unusual high frequency and the very specific applications considered, transmission and reception coils were not readily available commercially. Coils were therefore custom-designed and built for the experiments presented. However, the main goal of this thesis project was not coil optimization *per se*. The theory of micro-solenoid design presented in Chapter 2 was used as a guideline.

Coil design

A schematic of the transceiver design is represented in Figure 12. Each of the design elements is described within this section.

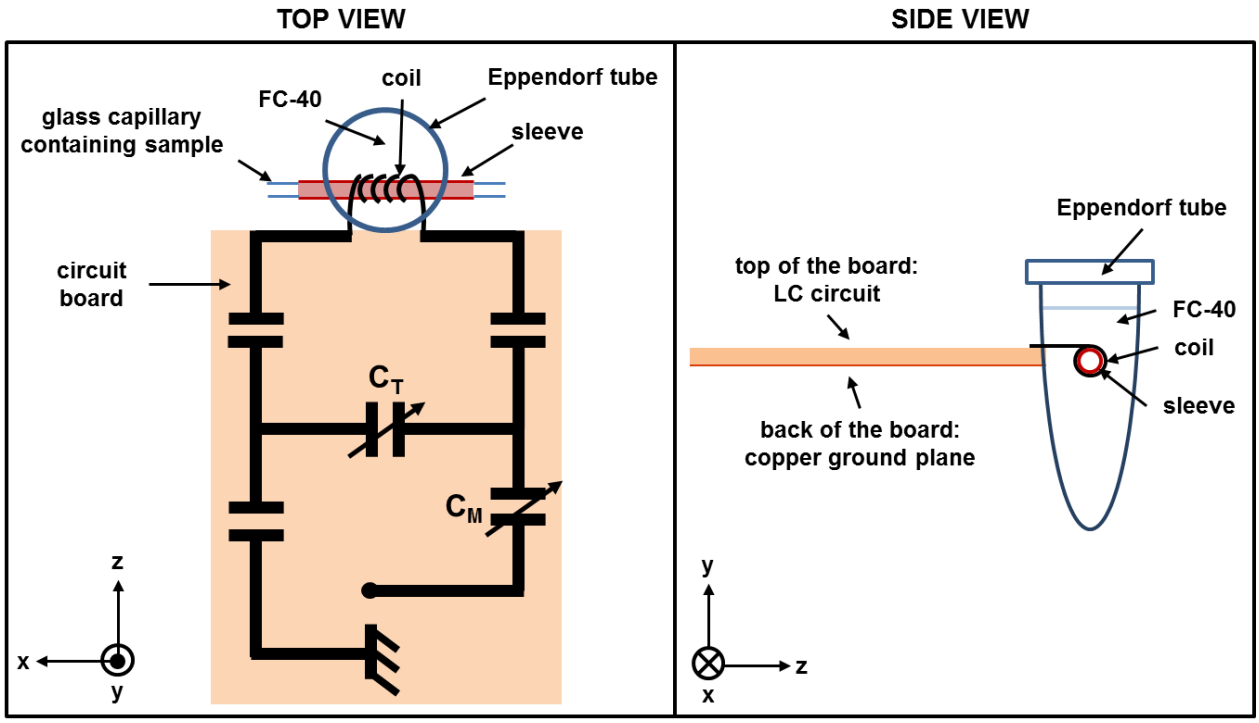

Figure 12. Schematic of the transceiver, from the top and the side. The z direction is that of the main magnetic field. The coil is part of a circuit with fixed and variable capacitors used for tuning (C_T) and matching (C_M). Fixed capacitors are sometimes added in series to bring down the equivalent capacitance and thus bring up the resonating frequency. The coil is contained in an Eppendorf tube and immersed in FC-40, for improved B_0 homogeneity. A polyimide sleeve passes through the coil and comes out on each side of the tube. Glass capillaries containing the sample of interest can be easily slid in and out of the coil through the sleeve. The back of the circuit board is covered with a thin copper foil for shielding purposes.

To optimize the excitation/reception homogeneity in the volume of interest, the chosen coil shape was a solenoid, with a diameter matching the sample size as closely as possible. Two sizes of solenoids were considered: one to image the buccal ganglia, and one to image single cells.

Each coil was manually wound on a thin polyimide sleeve (MicroLumen, Oldsmar, FL) containing a glass capillary (VitroCom, Mountain Lakes, NJ). Two sizes of capillaries were chosen: 2.0/2.4 mm (ID/OD[2]) for the ganglia coil and 0.5/0.7 mm for the single cell coil. The sleeve sizes were chosen accordingly. The wire was made of

[2] Inner/Outer diameter

copper with a polyurethane coating (RS, United Kingdom). The coil was wound on the sleeve such that the capillary could still be easily slid in and out. Geometric specifications of the two solenoid sizes produced are collected in Table 2. Notations are consistent with those of Chapter 2.

Application	Capillary ID/OD (mm)	d_{coil} (mm)	l_{coil} (mm)	Wire thickness (mm)	Turns n	Pitch (mm)
Ganglia	2.0/2.4	2.9	4.5	0.5	5	0.88
Single cell	0.5/0.7	0.95	2.5	0.25	5	0.50

Table 2. Geometric characteristics of the coils developed for each application. The OD of the glass capillary matches the ID of the coil (the sleeve thickness is 25 – 30 µm, assumed negligible).

The length of the coil was in both cases approximately 1.5 times the coil diameter. Using the IDs of the capillary and of the coil, the filling factors were 58% for the ganglia coil and 36% for the single cell coil.

At a frequency of 750 MHz (thus similar to ours) and with a sample conductivity of 1 S/m, the optimal number of turns and wire thickness were reported to be (n_{opt} = 8 ; d_{opt} = 86 µm) for a coil ID = 0.5 mm, and (n_{opt} = 4 ; d_{opt} = 244 µm) for a coil ID = 1 mm (Minard and Wind, 2001a)[3]. The sample conductivity considered was representative of mammalian tissues with plasma osmolarity of around 300 mM, whereas *Aplysia* tissues and their survival medium are characterized by an osmolarity of 1090 mM. The *Aplysia* samples to be imaged therefore have higher conductivity, and magnetic and dielectric losses are potentially greater. The general recommendation to use thicker wire and fewer turns for conducting samples was therefore followed and our choice leant towards the use of even thicker wire than prescribed above (also accounting for the actual IDs of our coils): 250 µm for the cell coil and 500 µm for the ganglia coil. At 730.2 MHz, the skin depth in copper at room temperature is about 2.5 µm. Both wire diameters used ensure that resistive losses occur in the anticipated high-frequency regime ($d >> \delta$).

The recommended pitch to wire thickness ratio of 1.5 was approximately respected, allowing for uncertainties of manual coil winding. This resulted in five-turn solenoids in both cases.

[3] These values were calculated for a circuit with a specific type of capacitors and allowing for 4% RF inhomogeneity over a length of 90% the coil ID.

Solenoids were incorporated into a circuit, along with non-magnetic matching and tuning capacitors. Fixed capacitor values ranged between 0.1 and 47 pF with a quality factor Q_c > 10,000 at 1 MHz (Dalian Dalicap Technology, Harbin, China). Variable capacitors for load-dependent tuning and matching spanned 0.4 – 2.5 pF with a quality factor Q_c > 4000 at 200 MHz (Alfred Tronser, Engelsbrand, Germany). The frequency dependence of Q_c was not specified. The overall circuit size was kept to a minimum and measured 16x32 mm.

Appropriate capacitor values were chosen empirically to produce a circuit resonating at 730.2 MHz, with the highest possible quality factor (defined as $Q = f_0/\Delta f$, see Equation (2.21) page 43) and sufficient tuning and matching range. The probes were tuned and matched while loaded with phantoms of artificial sea water (ASW) (NaCl: 450 mM; KCl: 10 mM; $MgCl_2$: 30 mM; $MgSO_4$: 20 mM; $CaCl_2$: 10 mM; HEPES: 10 mM; pH = 7.5 – Sigma-Aldrich, Saint-Quentin Fallavier, France). ASW is the survival medium for *Aplysia* ganglia and isolated cells, hence a pertinent load. The ganglia coil displayed a resonant frequency and quality factor that were sensitive to the presence of the load, indicating as expected that sample losses would not be negligible given the sample conductivity and size. On the other hand, the single cell coil was found to be insensitive to the load due to its smaller size.

The quality factor was measured on the workbench (i.e. outside the magnet) by connecting the coil directly to a network analyzer (Rohde&Schwar, Munich, Germany). This method does not provide a measurement of the true Q value of the coil, which should be measured using a coupling method with a small loop. However, the workbench Q estimate is a useful parameter for assessing coil losses, as long as the coil is impedance-matched. The coil spectrum was examined in reflection mode (S11) and the bandwidth at -3 dB from baseline measured. The attenuation at the resonant frequency was sufficient to assume zero reflection (< -20 dB). Figure 13 shows screen captures of the reflection spectrum for each coil, as measured with the network analyzer. The spectra display a dual resonance, the second one most likely stemming from the circuit board tracks which form a loop. This additional resonance somewhat compromises the measurement of the Q value for the coil: the actual value is underestimated. The measured quality factors of the loaded ganglia and cell coils were 26 and 47, respectively. These values, although underestimated, were satisfactory. However, the quality factor of the ganglia coil was expected to be higher than the cell coil due to its larger size. The lower Q value for the ganglia coil could be explained by two factors. The first is a more pronounced bias of the measurement by the second parasite resonance. The second is an overall large equivalent resistance in the system which could not be easily decreased. One

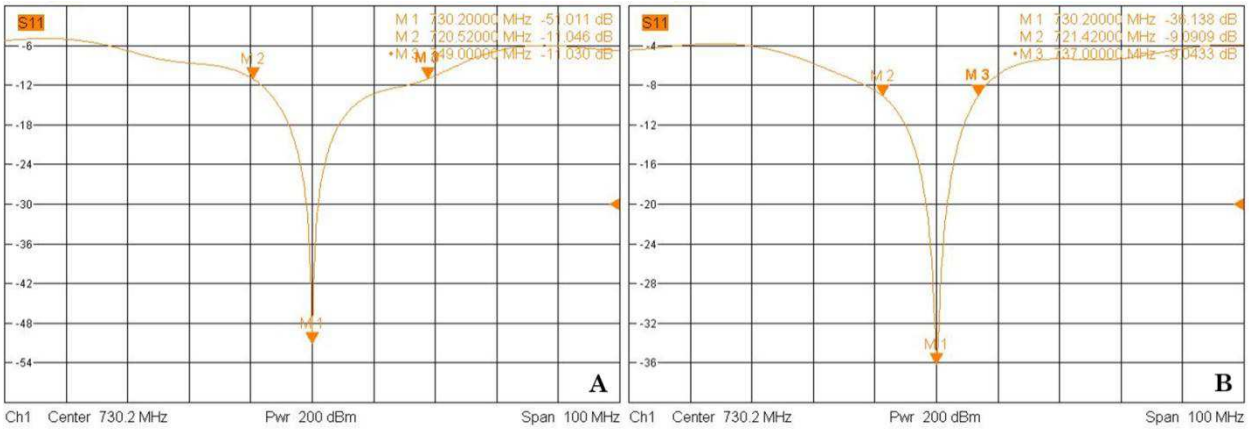

Figure 13. Reflection spectra of the ganglia coil (A) and of the cell coil (B) circuits. The attenuation at the resonant frequency (730.2 MHz) is sufficient to assume zero reflection (> 20 dB from baseline). The quality factor is determined by measuring the bandwidth at half reflection (-3 dB from baseline), but the measurement is somewhat biased by the presence of a second resonance, likely originating from the circuit board tracks forming a loop.

solution would have been to increase the coil inductance (by increasing the number of turns for instance). However, the current coil size was already relatively large and placed the circuit at the borderline of "tunability". Further increasing the number of turns did therefore not constitute a good option.

To avoid severe field inhomogeneities produced by the very near proximity of a copper – air interface, the coil was immersed in FC-40 Fluorinert (3M, Cergy-Pontoise, France), which matches the magnetic susceptibility of copper and is MR invisible (Olson et al., 1995). For this purpose, the solenoids were enclosed in a plastic tube (Eppendorf, Le Pecq, France), with the leads coming out trough small holes and soldered on the circuit board and the polyimide sleeves passing inside the coil and coming out through larger holes on each side of the tube. The tube impermeability was restored around the leads and sleeve with glue. This design imposed a minimum length for the coil leads of about 4 mm.

The circuit was shielded by covering the back of the circuit board with a 5-µm thin copper foil connected to the ground. An oscilloscope and a small loop close to the circuit were used for initial inside-magnet measurements of the eddy currents induced by a demanding gradient sequence (oscillations at the maximum slew rate for ~10 ms). This type of gradient waveform will be required for the DESIRE sequence, detailed in Chapter 7. The experiment revealed that unwanted eddy currents were induced. As these currents most likely circulated within the copper ground plane, the initial design was modified to split the foil surface into 2 mm-wide

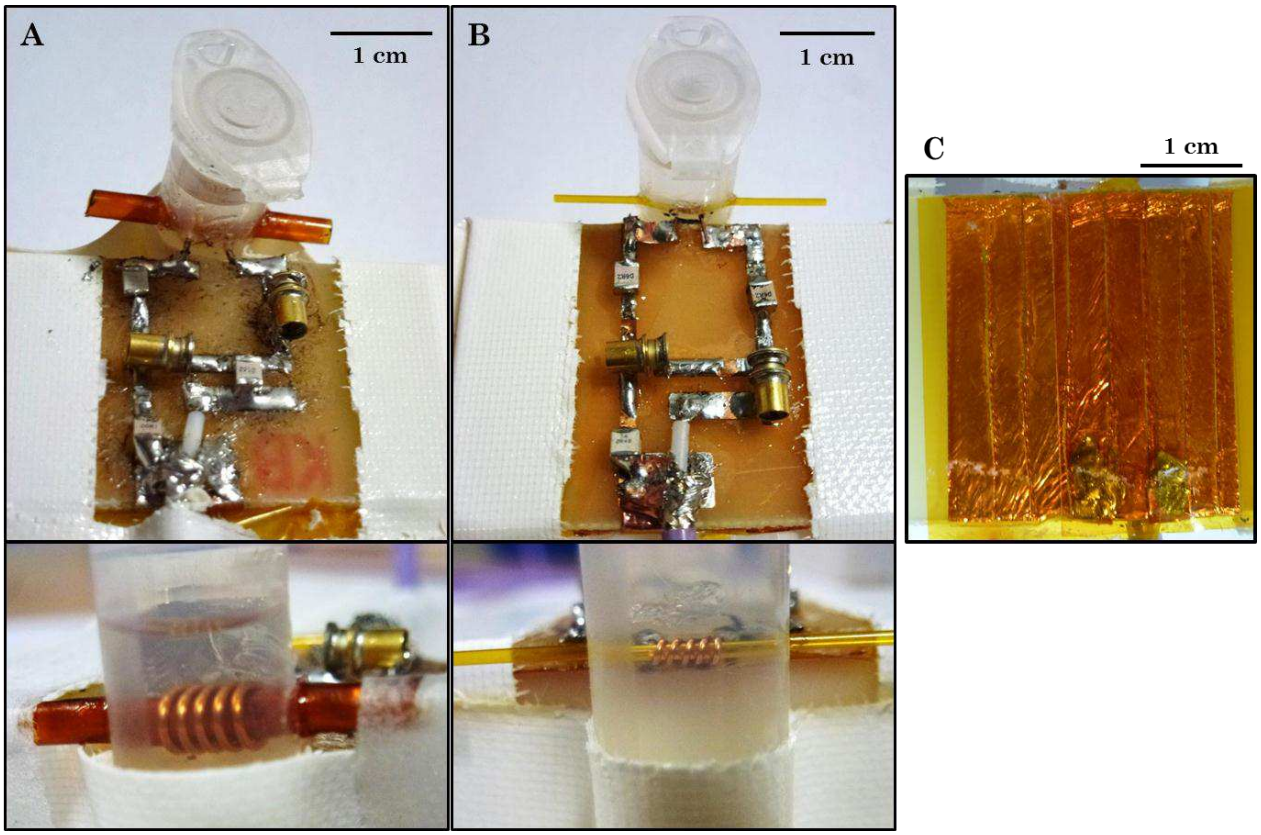

Figure 14. Micro-coils for ganglia and single cell imaging. A. Ganglia-dedicated coil – Length: 4.5 mm; ID = 2.4 mm. B. Single cell-dedicated coil – Length: 2.5 mm; ID = 0.7 mm. C. Ground plane at the back of the circuit boards. The 5-µm thin copper foil is split into 2 mm-wide parallel strips to avoid eddy current circulation.

strips parallel to the magnetic field (Jin, 1999). The strip separation avoided eddy current circulation while maintaining shielding properties.

Figure 14 shows representative pictures of the two types of coils fabricated. A double-shielded coaxial cable finally connected the coils to the line leading to a low power amplifier (100 W) for transmission and to a preamplifier for reception. Although all the elements are supposed to be impedance-matched (50 Ω), in practice the match is never perfect. The length of the cable was therefore chosen to be a multiple of half the wavelength for minimal losses (Fukushima and Roeder, 1993):

$$\frac{\lambda_c}{2} = \frac{v_c}{2f} = \frac{c \cdot 0.695}{2f} = 14.3\ cm \qquad (3.1)$$

where λ_c and v_c are the wavelength and propagation speed, respectively, in the cable, f is the operating frequency (730.2 MHz), c is the speed in vacuum and 69.5% is the speed in the cable relative to vacuum.

Coil performance

The MRI performance of the two types of coils was tested on phantoms. For each coil, the phantom was a glass capillary of the appropriate size (ID/OD: 2.0/2.4 mm for the ganglia coil and 0.5/0.7 mm for the single cell coil) filled with ASW and sealed with wax. Table 3 presents the main performance characteristics of each coil.

Application	Quality factor	Typical power (mW)	Linewidth at half-maximum in 1 mm³ (Hz)	Linewidth at half-maximum in VOI (Hz)
Ganglia	26	230	2.5	6.0
Single cell	47	70	6.0	5.0

Table 3. Main characteristics of the two types of coils built. Quoted values are indicative and can vary slightly from experiment to experiment.

The typical power quoted (70 and 230 mW for the cell and ganglia coil, respectively) is that required to produce a 90° flip angle with a 1 millisecond square pulse. It was determined following an automatic power calibration procedure provided by the Bruker software for scanner control (ParaVision). Using Equation (2.5) (page 34), we can estimate a mean efficiency for these coils: $\eta_{ggl} = 12.5\ \mu T/\sqrt{W}$ for the ganglia coil and $\eta_{cell} = 22.7\ \mu T/\sqrt{W}$ for the cell coil. In comparison, the efficiency of a commercial headcoil for the Siemens wide-bore 7 T system at NeuroSpin is $0.34\ \mu T/\sqrt{W}$. Therefore, these micro-coils are characterized by a high efficiency, required to achieve high SNR, compared to standard size coils.

The linewidths at half-maximum were estimated using a PRESS (Point RESolved Spectroscopy) sequence (Bottomley, 1987). Briefly, the PRESS sequences uses a series of 3 orthogonally selective pulses (90° – 180° – 180°) to acquire signal from a cuboid volume of the sample and obtain the corresponding spectrum. If the sample is homogeneous, the linewidth of the spectrum is an indicator of the extent of B_0 inhomogeneity stemming from the magnet itself and the presence of the coil. The shimming procedure and linewidth measurement were performed for two different cube sizes for each coil: first the typical 1 mm³ and then a more pertinent "volume of interest" (VOI) – (2 mm)³ for the ganglia coil and (0.5 mm)³ for the cell coil, respectively. The linewidths in these VOIs were 5 Hz for the cell coil and 6 Hz for the ganglia coil. The field inhomogeneity in a (2 mm)³ VOI was also measured on the ganglia coil while loaded with buccal ganglia. The linewidth was broadened to 26 Hz by the presence of the biological sample. This confirmed that the B_0 inhomogeneity would be eventually dominated by the sample and not by the proximity of the coil.

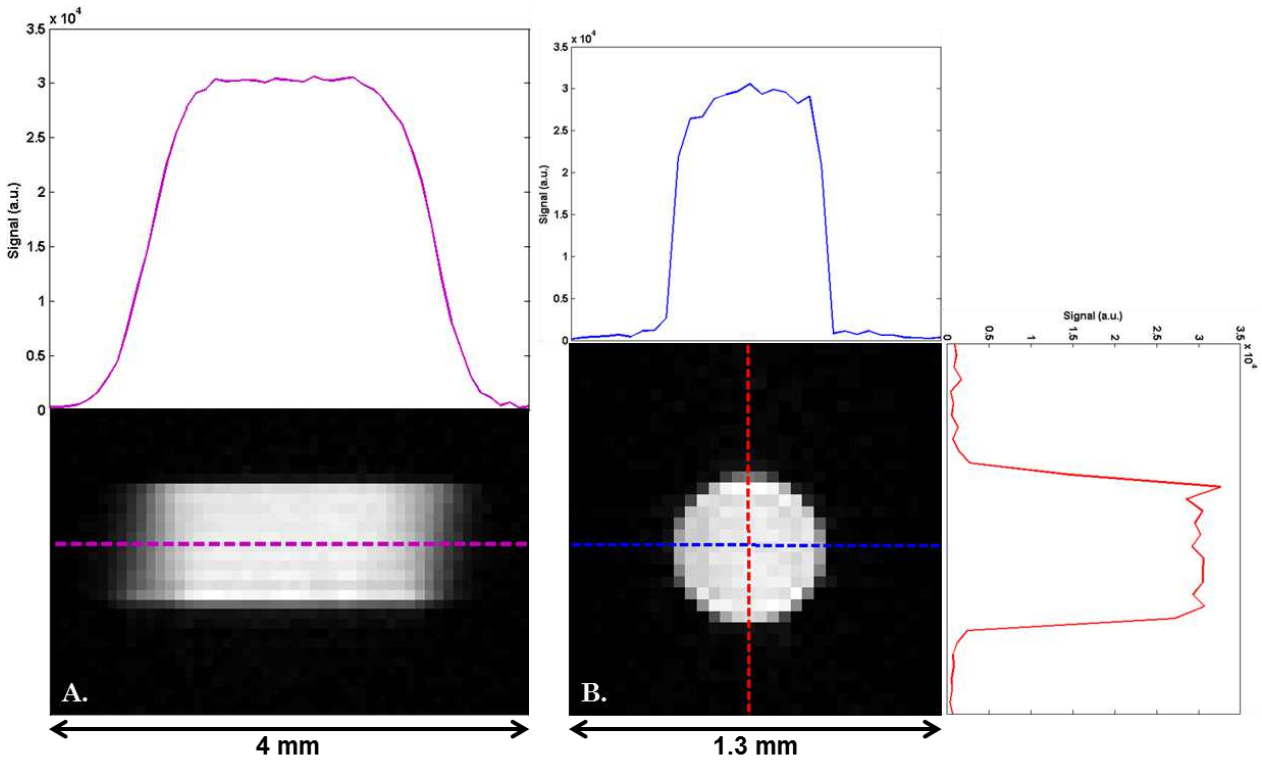

Figure 15. Spin-echo images and corresponding profiles of an ASW phantom, acquired with the cell-dedicated coil. Imaging parameters for A: Resolution: 80x41 µm² / Slice thickness: 150 µm / FOV: 4x1.3 mm² / TE = 7.9 ms / TR = 2.5 s / TA = 1min20s. Imaging parameters for B: Resolution: 41x41 µm² / Slice thickness: 500 µm / FOV: 1.3x1.3 mm² / TE = 6.8 ms / TR = 2.5 s / TA = 1min20s. The coil volume within 90% of maximum signal is 0.5x0.5x1.75 mm³.

These reported linewidths should be smaller than the frequency span necessary to resolve two locations in imaging. This span is governed by the quantity $\gamma G_x \Delta x$, where G_x is the read-out gradient and Δx the resolution. For our upcoming experiments, if we chose $\Delta x = 25\ \mu m$ and $G_x = 0.1 - 1\ T \cdot m^{-1}$, this would result in a frequency span of 100 – 1000 Hz. The linewidths were therefore largely acceptable for imaging purposes.

Figure 15 and Figure 16 show signal profiles along the three main axes of each coil. The profiles display good homogeneity in the axial plane and a satisfactory coverage along the coil length. In these spin-echo images, the signal is within 90% of its maximum value over a length of 1.75 mm along the cell-dedicated coil and 2.1 mm along the ganglia-dedicated coil. The former clearly provides sufficient coverage for spherical cells of 500 µm at most. The latter provides tight but sufficient coverage for ganglia about 2 mm in length. Ideally the ganglia coil should have been longer but this was not possible for reasons detailed earlier. In the ganglia experiments, the coil longitudinal profile will be taken into account whenever necessary.

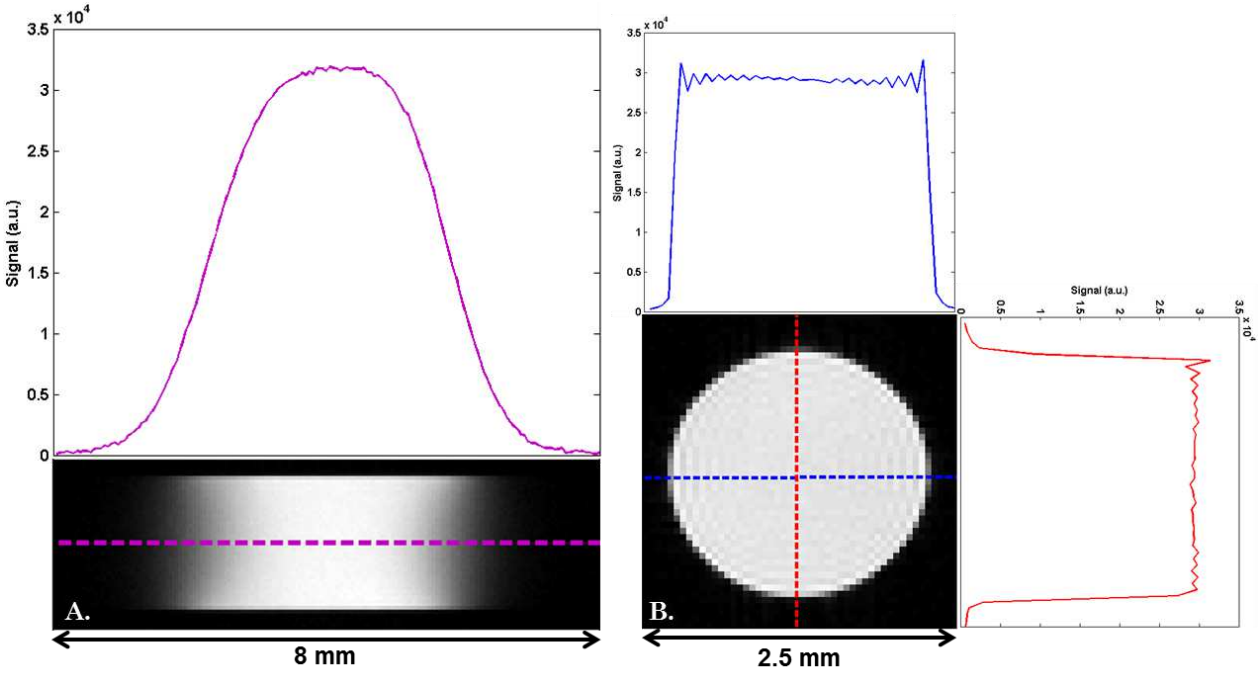

Figure 16. Spin-echo images and corresponding profiles of an ASW phantom, acquired with the ganglia-dedicated coil. Imaging parameters for A: Resolution: 50x50 µm² / Slice thickness: 500 µm / FOV: 8x2.5 mm² / TE = 25 ms / TR = 2.5 s / TA = 2 min. Imaging parameters for B: Resolution: 50x50 µm² / Slice thickness: 500 µm / FOV: 2.5x2.5 mm² / TE = 7.5 ms / TR = 2.5 s / TA = 2 min. The coil volume within 90% of maximum signal is 2.0x2.0x2.1 mm³.

3.3 Chapter summary

In this chapter, we presented the organization and specificities of the nervous system of the animal model *Aplysia californica*. This model has several experimental advantages: the neuronal bodies are very large, they are spatially separated from the neuropil, and the neurons have individually identified functions, projections and synapses. The hardware used for MR microscopy was also introduced, with special attention given to the in-house built microcoils, adapted to the biological samples of interest (ganglia and single cells). The coil design partially solves eddy current and susceptibility mismatch issues raised by strong gradients and ultra-high magnetic field. The coils were tested on phantoms of artificial sea water and showed good performance in terms of B_0 and signal homogeneity.

With all the hardware required for MRM experiments now available (magnet, gradients and micro-coils), let us proceed with the two experimental axes of this project: manganese enhanced MRI (MEMRI) of the buccal ganglia and diffusion MRI in single cells and in ganglia.

Part II

Neurotransmitter-modulated transport in *Aplysia* revealed by manganese enhanced MR microscopy

4. MEMRI

In this chapter, we will explain the main physical principles behind MR contrast agents. The role of Ca^{2+} (of which Mn^{2+} is an analog) in synaptic transmission and the development of manganese-enhanced MRI (MEMRI) will be reviewed, along with major current applications, advantages and pitfalls.

4.1 MR contrast agents

Although proton MRI is a very flexible yet non-invasive imaging modality, for some purposes the addition of a contrast agent is necessary to enhance T_1 or T_2 contrast. These contrast agents can be administered through intravenous, intraperitoneal or topical injection. MR contrast agents are usually indirect because they are not visible themselves, but rather through their effect on water relaxation times: they are mainly paramagnetic and superparamagnetic compounds that locally modify the magnetic environment of the protons and thus change their longitudinal and transverse relaxation rates (Mendonca-Dias et al., 1983).

Paramagnetic atoms or molecules are characterized by a permanent magnetic moment, or dipole, resulting from the spin of unpaired electrons. Their electronic magnetic moment is at least two orders of magnitude higher than the proton magnetic moment. In the absence of an external magnetic field, the dipoles are oriented randomly due to thermal motion and produce an effective zero magnetic moment. When placed in a magnetic field, the dipoles of paramagnetic compounds tend to align with the magnetic field: their magnetic susceptibility is positive ($\chi > 0$). This response is opposite to that of diamagnetic compounds that are repelled by a magnetic field ($\chi < 0$). The magnetic susceptibility of paramagnets is low, resulting in a weak attraction. Unlike ferromagnets, they do not retain any magnetization once they are removed from the magnetic field. Superparamagnets behave similarly, only their magnetic susceptibility is 100 to 1000 times greater than that of paramagnets (Hashemi et al., 2012).

The superparamagnetic contrast agents used in MRI usually consist of iron oxides. Their predominant effect is to shorten T_2 and T_2^*, which results in reduced signal intensity. These contrast agents are therefore referred to as negative contrast media.

The effect of paramagnetic contrast agents is predominantly to shorten T_1. The accelerated recovery of longitudinal magnetization results in higher signal intensity (or "enhancement") on T_1-weighted (T1w) images. These compounds are therefore referred to as positive contrast media.

The dipolar interactions between the unpaired electrons of the paramagnetic compound and the water molecules are responsible for the shortened relaxation time of the water protons. The effective relaxation rate can be expressed as the sum of a diamagnetic rate (d), in the absence of the paramagnetic compound, and a paramagnetic rate (p), proportional to the contrast agent concentration (Solomon, 1955):

$$\frac{1}{T_i} = \left(\frac{1}{T_i}\right)_d + \left(\frac{1}{T_i}\right)_p = \frac{1}{T_{i,0}} + r_i \cdot [CA] \tag{4.1}$$

where i = 1 or 2, $T_{i,0}$ is the initial relaxation time (diamagnetic), [CA] is the contrast agent concentration, and r_1/r_2 are the longitudinal/transverse relaxivities of the contrast agent, respectively, which quantify its efficiency to locally alter the T_1/T_2 of protons.

The paramagnetic relaxation mechanisms are classically explained as the added contributions from two spheres of influence of the paramagnetic center on neighboring protons: an "inner sphere" involving water molecules directly coordinated with the paramagnetic core, and an "outer sphere" involving long-distance dipolar interactions of bulk water (Muller, 1996). The various interactions are illustrated in Figure 17. The relaxivity is a function of the solvent in which the contrast agent is diluted, the magnetic field strength, the temperature, the pH...

Dedicated MR sequences allow the quantification of T_1 or T_2, by acquiring data with various TR or TE values, respectively, and fitting the exponential recovery/decay curves. Using multiple buffer solutions of known contrast agent concentrations, the value for the relaxivity (r_1 or r_2) can be measured experimentally by performing quantitative T_1 or T_2 measurements in the buffer solutions and injecting the values into Equation (4.1). Inversely, if the relaxivity is known, T_1 or T_2 measurements permit the quantification of the contrast agent concentration.

The gadolinium (Gd^{3+}) and manganese (Mn^{2+}) ions are powerful paramagnetic ions with 7 and 5 unpaired electrons, respectively. Their properties have been exploited very early in MRI (Carr, 1984; Mendonca-Dias et al., 1983). Most paramagnetic contrast agents today are complexes of gadolinium (Gd^{3+}) and they are largely used

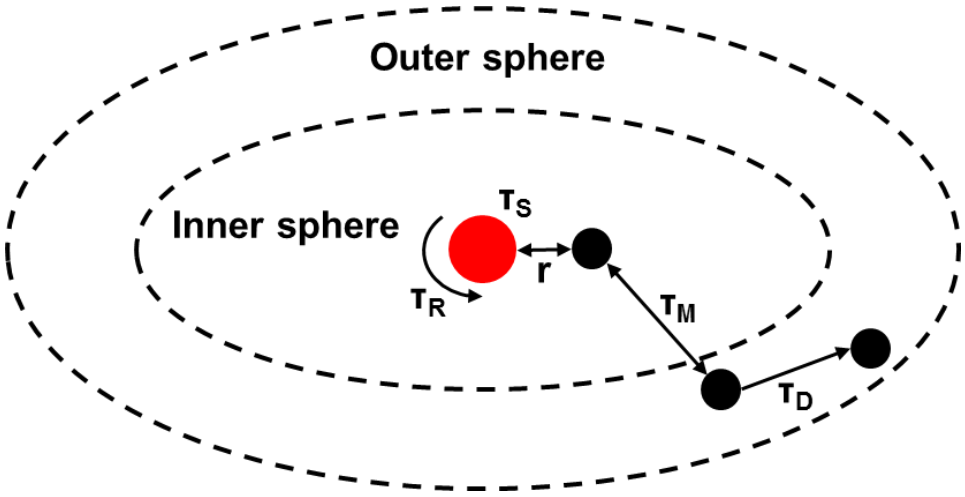

Figure 17. Schematic of the inner and outer spheres of interaction of a paramagnetic core (red) with surrounding water molecules (black). The inner sphere interactions depend on the distance r between the paramagnetic compound and the water proton, and on the electronic relaxation time τ_S, the molecule rotation time τ_R and exchange time of protons τ_M. The outer sphere interactions depend on the diffusional correlation time τ_D.

for instance in the detection of regions of blood-brain barrier disruption – in tumors or multiple sclerosis inflammation – which allows the local passage of the contrast agent from the circulatory system into brain tissue.

MEMRI developed around two properties of the manganese ion: on the one hand its paramagnetism, and on the other hand its ability to enter neurons via voltage-gated Ca^{2+} channels (Yamashita, 1982) and to be further transported both anterogradely and retrogradely in the nervous system. Mn^{2+} is not used as an MR contrast agent in humans because chronic exposure to manganese can lead to a toxic condition referred to as "manganism". The exact mechanism of Mn^{2+} neurotoxicity is not clear but some involvement with the disruption of the iron metabolism in neurons has been demonstrated (Zheng et al., 1998). Nonetheless, manganese is commonly used in animal studies as an efficient contrast agent for the nervous system.

4.2 Ca^{2+} and synaptic transmission

In order to understand the usefulness of Mn^{2+} as an MR contrast agent, let us first briefly describe how Ca^{2+} is transported and used in the nervous system. More information can be found in the (Lodish, 2003) textbook.

As with any cell, the neuronal membrane – a phospholipid bilayer – is essentially impermeable to most soluble molecules, ions, and somewhat to water. Most

transport across the membrane is then mediated by proteins, in the form of adenosine triphosphate (ATP)-powered pumps or gated channels. An electric potential is maintained across the membrane, resulting from a controlled imbalance between negatively and positively charged ions on each side.

The specificity of neurons is their electrical excitability. An "action potential" is a sudden membrane depolarization and repolarization, resulting from a large influx of Na^+ ions followed by a rapid efflux of K^+ ions via voltage-gated channels. This event generates a wave of depolarization, which moves down the axon towards the terminals (Lodish, 2003).

Transfer of information from one neuron to the next occurs at synapses. There are two types of synapses: chemical and electrical. In electrical synapses, the gap junction is very small (3 – 4 nm) and there are ion channels that cross both cellular membranes, thus allowing the direct transmission of the action potential. In chemical synapses, cells are separated by a 20 – 40 nm gap. The synaptic cleft is crossed by neurotransmitters packed inside vesicles. The arrival of a wave of depolarization at the axon terminal opens local voltage-gated Ca^{2+} channels, allowing extracellular Ca^{2+} to enter the cell. The local increase of cytosolic Ca^{2+} concentration triggers the fusion of neurotransmitter-packed vesicles with the membrane and the exocytosis of neurotransmitters into the synaptic cleft. The neurotransmitters further bind on receptors of the post-synaptic cell, changing the membrane potential of the latter. Return to resting state is produced by the export of the Ca^{2+} back to the extracellular space through ATP-powered Ca^{2+} pumps and recycling of the neurotransmitters by the axon terminal that released them. Figure 18 illustrates the process of information transmission through chemical synapses. The advantage of electrical synapses is their speed of operation. The advantage of chemical synapses is the flexibility of operation: the action potential can be enhanced or on the contrary inhibited in the post-synaptic neuron.

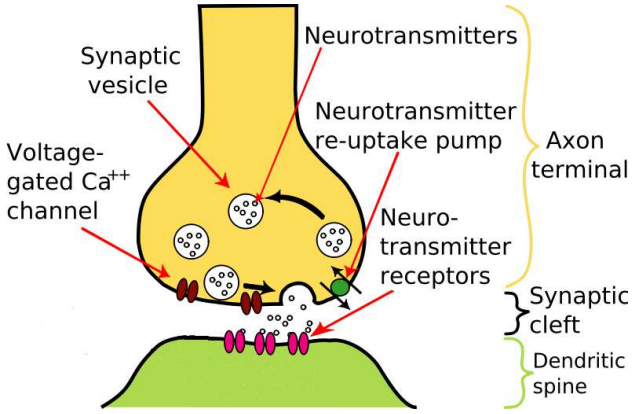

Figure 18. Main actors of a chemical synapse. The arrival of an action potential at the axon terminal causes Ca^{2+} inflow through voltage-gated channels, which in turn triggers vesicle fusion with the membrane and release of neurotransmitters in the cleft. Neurotransmitters bind on specific receptors of the post-synaptic neuron to further convey the information (either transmission or inhibition).

These pathways of Ca^{2+} cellular import and export can be traced with MEMRI, thus obtaining valuable information on transport and connections in the nervous system.

4.3 Applications of manganese-enhanced MRI

As mentioned, MEMRI is confined to animal studies. So far, it has been used for three types of applications (Silva et al., 2004). The first is global enhancement of brain contrast after systemic administration of $MnCl_2$, which improves the visualization of the neuroarchitecture (Aoki et al., 2004; Watanabe et al., 2002). The second is the tracing of specific neuronal connections in the brain (Murayama et al., 2006; Pautler et al., 1998). The third application, closely related to tract-tracing, is the study of differential Mn^{2+} accumulation in active/inactive areas of the brain (Duong et al., 2000; Lin and Koretsky, 1997) and heart (Hu et al., 2001; Krombach et al., 2004), referred to as activation-induced MEMRI.

The potential of manganese chloride injections to be used concomitantly with MRI for *in vivo* neural tract tracing was first introduced by (Pautler et al., 1998). This study focused on the visualization of the olfactory and visual pathways in mice, following $MnCl_2$ administration in the naris and in the cavity of the eye, respectively. MEMRI came with the advantage of performing tract tracing *in vivo*, without necessary sacrifice of the animal (unlike tracers such as biotinylated dextran, horseradish peroxidase or herpes simplex virus) or recourse to radioactive Mn^{2+}. This study hypothesized the crossing of synapses due to the enhancement pattern detected in the secondary olfactory neurons and primary olfactory cortex. However, it was acknowledged that the high resolution of light microscopy would be needed to bring a definite answer about Mn^{2+} synapse crossing. In subsequent studies in rodents, MEMRI was also utilized to trace connections from various brain regions such as striatum and amygdala (Pautler et al., 2003), or to validate results from diffusion tensor imaging[4] (DTI) in the optic tract of rats (Lin et al., 2001). Assumed synaptic transport was shown to require neural activity, while axonal transport did not. Indeed axonal transport is micro-tubule based, although the exact motors involved have not been fully identified yet (Bearer et al., 2007). The specificity of MEMRI tract tracing was also validated in non-human primates against a standard tracer (wheat germ agglutinin with horseradish peroxidase), both producing similar patterns in the basal ganglia (Saleem et al., 2002), with evidence of transport up to the cortex, and hypothesized crossing of three synapses

[4] See Chapter 6

(Murayama et al., 2006). Tract-tracing studies can be naturally combined with activation-induced MEMRI. Studies on songbirds revealed not only the sex-dependent volume of the song-control nuclei (Van der Linden et al., 2002), but also their seasonal plasticity (Van der Linden et al., 2004).

The only MEMRI experiments on non-vertebrates had so far been performed on crayfish. These studies focused on the enhancement of the anatomy after $MnCl_2$ injection (Brinkley et al., 2005; Herberholz et al., 2004) and more recently on highlighting neural activation through differential Mn^{2+} uptake following electrical shocks (Herberholz et al., 2011).

These animal studies were all performed at spatial resolutions that only allowed the detection of Mn^{2+} in "areas" of the brain. With manganese-enhanced magnetic resonance microscopy, the motivation is to detect the accumulation and transport of Mn^{2+} at cellular level (i.e. from neuron to neuron), as well as modifications of accumulation and transport following different forms of stimulation. In this context, *Aplysia californica* constituted an excellent model for studying Mn^{2+} transport in the nervous system at cellular level.

4.4 Chapter summary

In this chapter, we presented the first main MR technique that will be used for the current work: MEMRI. We introduced the general concept of MR contrast agent, along with the relationship between contrast agent concentration and relaxation times. We described the role of Ca^{2+} in synaptic transmission. We stressed that the specificity of the manganese ion as both paramagnetic and a Ca^{2+} analog has made it a valuable neural contrast agent for animal imaging, with applications in global enhancement of brain contrast, neural tract-tracing and tracking of activation-induced accumulation. We reviewed the use of Mn^{2+} combined with MRI as neural tract-tracer in the nervous system of rodents, non-human primates, birds and crayfish. In all these studies, Mn^{2+} accumulation and transport were detected at the spatial scale of brain "regions". In the next chapter, we will use manganese enhanced MR microscopy to track Mn^{2+} transport within a network of identified neurons.

5. Manganese dynamics in the nervous system of *Aplysia*

In this chapter, we will study Mn^{2+} transport in a neuronal network (the buccal ganglia of *Aplysia californica*) with manganese enhanced MR microscopy. Using retrograde transport of Mn^{2+} along the peripheral nerves of the ganglia, we will produce a map of axonal projections from identified neurons into the buccal nerves, and compare it to the one previously obtained with Co^{2+} or Ni^{2+} migration and optical techniques (Morton et al., 1991; Quicke and Brace, 1979). Due to notorious Mn^{2+} toxicity, the functionality of the neural network following this labeling experiment will be assessed. A second study will then be presented, which focuses on the dynamics of Mn^{2+} inside the buccal ganglia following stimulation with the neurotransmitter dopamine (DA). The identification of individual neurons on MR images, and the *a priori* knowledge of synaptic connections between them (Nargeot and Simmers, 2012) provide a solid starting point for the study of Mn^{2+} transport mechanisms inside the nervous system (and could potentially lead to a direct proof of Mn^{2+} specific synaptic transport), as well as for functional MEMRI studies on a DA-modulated neuronal network.

The study presented in this chapter was published as: Jelescu IO, Nargeot R, Le Bihan D, Ciobanu L. *Highlighting manganese dynamics in the nervous system of Aplysia californica using MEMRI at ultra-high field*. NeuroImage 2013;76:264-271.

5.1 Confirming axonal projections

Methods

Animal preparation

Three late juvenile *Aplysia californica* (National Resource for Aplysia, Miami, FL) were anesthetized by injection of an isotonic magnesium chloride solution ($MgCl_2$: 360 mM; HEPES: 10 mM; pH = 7.5 – Sigma Aldrich). $MgCl_2$ is a neuromuscular blocking agent commonly used for anesthetizing invertebrates (Kohn et al., 1997). The bilateral buccal ganglia were isolated and placed in a Sylgard-coated (Dow

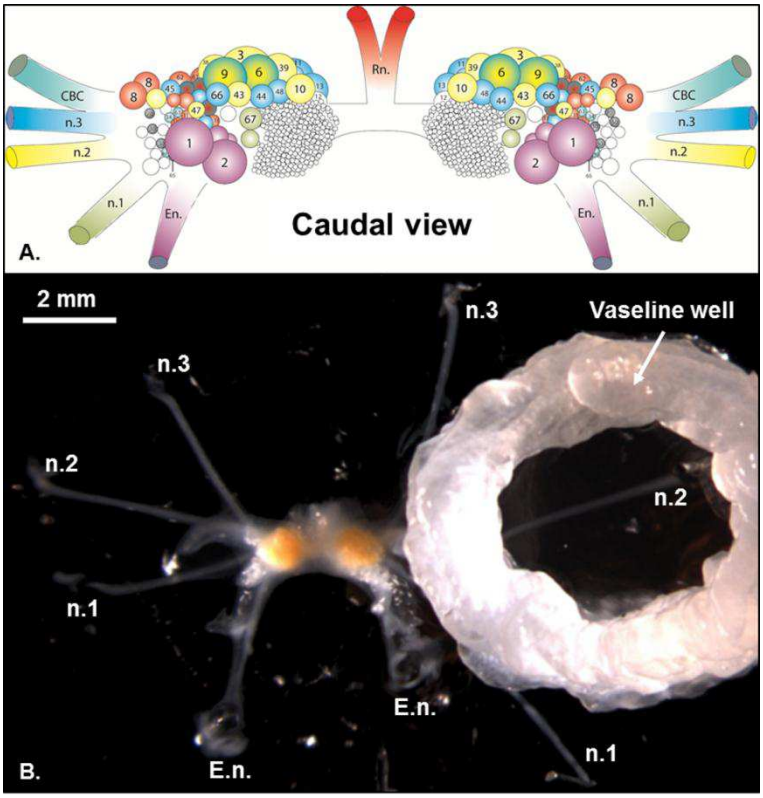

Figure 19. Caudal views of the buccal ganglia in *Aplysia*. A. Color-coded schematic of neurons' axonal projections into peripheral nerves, established using Co^{2+} migration and optical imaging. Colored circles indicate the cell bodies identified by individual numbers. *Courtesy of R. Nargeot.* B. Isolation of a single nerve 2 (n.2) into a Vaseline well. The well is filled with a $MnCl_2$ solution, while the rest of the ganglia bathe in ASW. *Digital microscope camera (World Precision Instruments, Hitchin, UK) image.*

Corning, Midland, MI) Petri dish, filled with ASW. The three pairs of buccal ganglia were used for unilateral Mn^{2+} migration along one peripheral nerve: nerve 2 (n.2), 3 (n.3) or esophageal (E.n.). The ending of the selected nerve was isolated in a well of petroleum jelly (Vaseline), as illustrated in Figure 19. The well was filled with a solution of manganese chloride mimicking intracellular medium ($MnCl_2$: 25 mM; NaCl: 50 mM; KCl: 440 mM; $MgCl_2$: 10 mM; Hepes: 10 mM; pH = 7.2). The ganglia were stored at 4°C and the manganese was allowed to migrate for 18 hours before imaging.

MR Imaging

The ganglia were inserted into a 2.0 mm ID glass capillary filled with ASW. MR imaging was performed at room temperature (19°C), using the ganglia-dedicated coil as RF transceiver.

Three dimensional acquisition schemes were chosen because they can more easily produce isotropic spatial resolution and have higher SNR. Acquisition time had to be short compared with ganglion viability, so rapid schemes for T_1 weighting and T_2 weighting were required. For T_1 contrast, the FLASH sequence was chosen. For T_2 contrast, the RARE sequence produces good contrast in a reasonable time, provided no T_2 quantification is sought. This sequence was therefore chosen for our purposes.

Imaging therefore consisted of a 3D FLASH (TE = 2.4 ms / TR = 150 ms / FA = 40° / 25 µm isotropic / NA = 10 / TA = 2h40) and of a 3D RARE (TE_{Eff} = 18.4 ms / TR = 3 s / 25 µm isotropic / TA = 1h20). During the first experiment, the repetition time of the FLASH sequence was optimized empirically on lower resolution scans (25x50x50 μm^3; NA = 1) to provide the best contrast between regions with and without Mn^{2+}. The cell bodies displayed a natural T_2 contrast with respect to ASW, making them all visible on T2w images, but hardly any T_1 contrast on FLASH images at TR = 150 ms. T1w images therefore revealed regions of Mn^{2+} uptake only.

The combined information from T1w and T2w images allowed the precise identification of neurons filled with Mn^{2+} following the exposure of n.2, n.3 or E.n. to a source of $MnCl_2$ at 25 mM for 18 hours. This identification was based on the relative position and size of the cells in the ganglion as described by Church and Lloyd (Church and Lloyd, 1991, 1994).

Results and discussion

In each of the three experiments, all cell bodies that were enhanced in the T1w images were identified as motor neurons with axonal projections into the nerve dipped in $MnCl_2$, as shown in Figure 20. Reciprocally, all ipsilateral motor neurons with known axonal projections into the nerve in contact with $MnCl_2$ were found to be unambiguously hyperintense in the T1w images. Indeed, according to previously established schematics (see Figure 19A or Figure 20A for example), n.2 receives projections from eight identified (i.e. numbered) neurons and one unidentified (but known) ipsilateral neuron. Following $MnCl_2$ migration along n.2, all eight identified neurons and two unidentified ones were labeled. Comparison with RARE confirmed that the additional enhanced area corresponded to an unidentified neuron with no projections in n.2, but this appeared as an exception. Nerve 3 is known to receive projections from 13 identified and 5 unidentified ipsilateral neurons. All of those and only those were labeled with Mn^{2+}. E.n. receives projections from two identified and two unidentified ipsilateral neurons, which correspond exactly to the enhancement regions obtained.

We note nonetheless that according to the projections' map established using 1 M cobalt chloride or nickel chloride, some contralateral neurons should also have been labeled (Morton et al., 1991). This difference could be explained by the migration time we allowed, which was shorter than in Morton *et al.*'s experiment (18h vs. 24–72h), and our $MnCl_2$ concentration which was much lower, both preventing remote cells from accumulating sufficient Mn^{2+}. Smaller neurons than those labeled in our experiments also project into the peripheral nerves. They are thought to be sensory,

rather than motor neurons, and are reported to be 20 – 30 µm in diameter (Walters et al., 2004). These were not visible with our technique most likely because of PVE in $(25\ \mu m)^3$ voxels.

These results confirmed, for the first time using MEMRI and retrograde transport along a single nerve (also referred to as "backfilling"), the mapping of motor neurons' axonal projections into the peripheral nerves of the buccal ganglia in *Aplysia*. Compared to light microscopy, MEMRI presents the advantage of mapping these projections while maintaining the ganglia alive, whereas Co^{2+} or Ni^{2+} backfillings are revealed by chemical treatments which alter the viability of the ganglia. Although the in-plane spatial resolution of light microscopy is far better (the small sensory neurons are resolved), resolution in the z direction remains an issue, while the tomographic approach of MR acquisition allows 3D imaging of the ganglia.

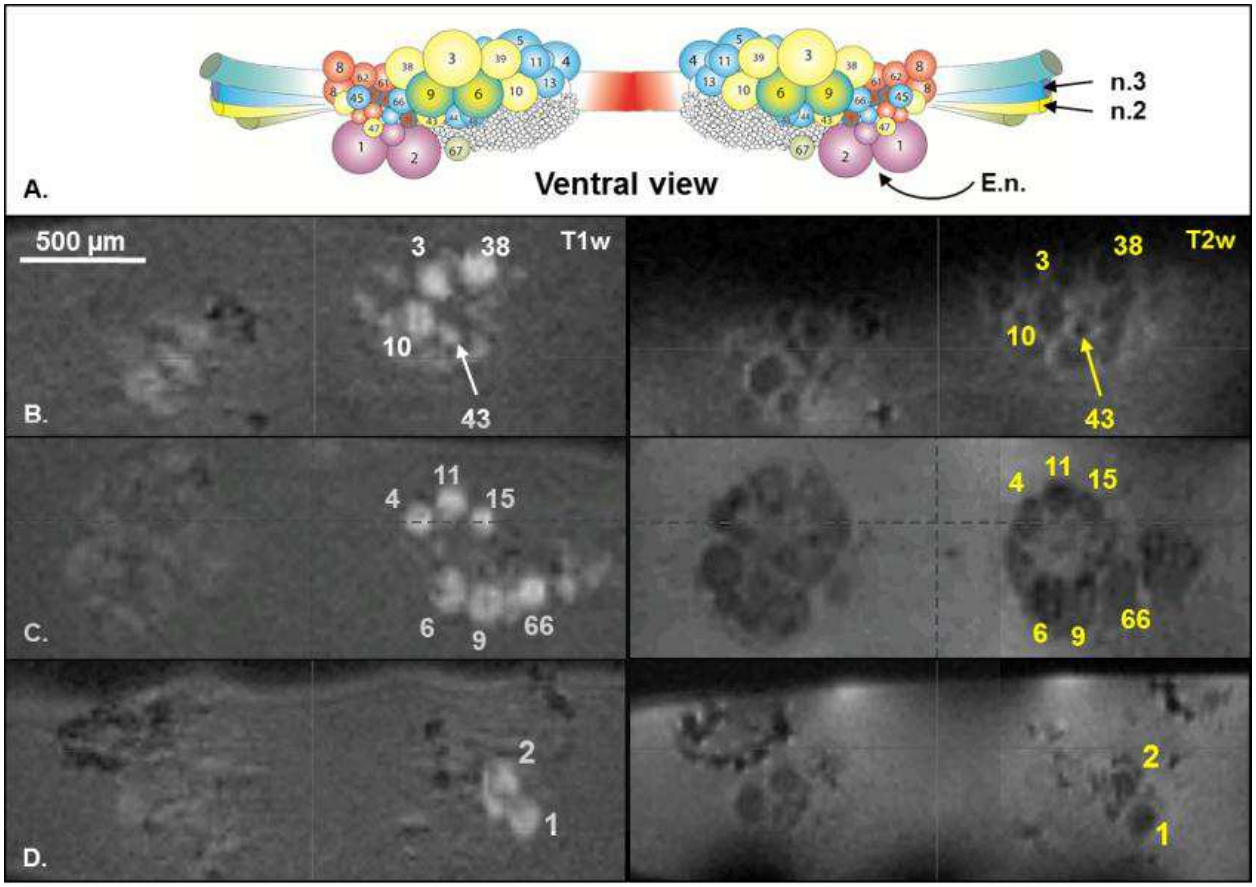

Figure 20. A. Schematic of the ventral side of the buccal ganglia. The arrows point to the nerves used for retrograde Mn^{2+} transport. B-D. MR images showing accumulation of Mn^{2+} following retrograde transport along n.2 (B), n.3 (C) and E.n. (D). The enhanced cells are indicated on the T1w (left column) and T2w (right column) images, and can also be found on the schematic (A). They are all cells with known axonal projections in the corresponding nerve.

Other optical techniques, such as the use of voltage-sensitive dyes and a photodiode array to map optical spikes in response to stimulation of the esophageal nerve, allow the differentiation between motor neurons and interneurons, but on the other hand suffer from poor spatial resolution and low SNR (Morton et al., 1991).

5.1 Toxicity of the backfilling technique

As mentioned earlier, Mn^{2+} accumulation can potentially damage the neuronal function. Given that the visualization of Mn^{2+} in living, functional structures is a major issue in MEMRI, we next investigated the intracellular concentration of Mn^{2+} resulting from backfilling and its potential toxicity for the neurons.

Mn^{2+} relaxivity at 17.2 T

In order to link MR measurable relaxation times to Mn^{2+} concentration in the ganglia, Mn^{2+} longitudinal relaxivity r_1 was first evaluated at 17.2 T and room temperature from T_1 measurements in six ASW phantoms. The phantoms contained $[Mn^{2+}]$ = 0 / 0.125 / 0.25 / 0.5 / 1.0 / 2.0 mM, respectively. T_1 maps were obtained using a multi-TR RARE acquisition (17 TR values ranging from 20 to 15000 ms; TE = 7 ms; slice thickness: 1.5 mm; 150x150 µm in-plane resolution).

Relaxation times measured in the ASW phantoms containing 0 to 2 mM $MnCl_2$ are presented in Table 4. A linear fit on $1/T_1 = f([Mn^{2+}])$ produced an estimate of $r_1 = 5.1 \pm 0.3$ $(mM.s)^{-1}$. This relaxivity was consistent with reported literature values of 6.3 ± 0.1 $(mM.s)^{-1}$ in water and 8.6 ± 0.6 $(mM.s)^{-1}$ in *ex vivo* brains at comparable field strength (14 T) (Huang et al., 2009). In the absence of information on relaxivity in ganglia tissue, the relaxivity in ASW was therefore used in the following section in order to estimate Mn^{2+} concentrations reached in the cells.

$[Mn^{2+}]$ (mM)	0	0.125	0.25	0.5	1.0	2.0
T_1 (ms)	2800 ± 140	1005 ± 35	569 ± 6	349 ± 2	171 ± 4	95 ± 3

Table 4. Mean relaxation times ± SD measured at 17.2 T and room temperature, in ASW containing different concentrations of $MnCl_2$.

Estimation of [Mn^{2+}] and associated toxicity

Methods

In order to assess Mn^{2+} concentration levels inside cell bodies and determine the toxicity level of the backfilling technique described in Section 5.1, one *Aplysia* was sacrificed and the Mn^{2+} migration experiment was performed along n.3. The MRI session consisted in the acquisition of a T_1 map (multi-TR RARE: 15 TR values ranging from 20 ms to 6000 ms; TE = 7 ms; 50 µm isotropic resolution) and a 3D FLASH (as in 5.1) post-migration. Two types of cells were manually segmented: cells with axonal projections in the ipsilateral n.3, clearly labeled by Mn^{2+}, and cells with no axonal projections in the nerve, on the far contralateral side, assumed to contain no Mn^{2+} (neuronal activity is suspended at 4°C, thereby preventing any activity-dependent transport of Mn^{2+}). T_1s were thus determined inside cells with and without Mn^{2+}. T_1 measurements in the cells, combined with the r_1 value at 17.2 T gave access to Mn^{2+} concentration in the labeled cells following 18h retrograde migration along a nerve from a 25 mM $MnCl_2$ source.

Results

T_1 measurements in the ganglia after $MnCl_2$ backfilling through n.3 produced estimates of T_1 = 1460 ± 22 ms in unlabeled and T_1 = 640 ± 130 ms in labeled cells. The high T_1 variability in the labeled cells comes from the non-uniform Mn^{2+} uptake across this pool (probably due to variability in the distance to $MnCl_2$ source, axon diameter, etc). Taking the two extreme values, 510 and 770 ms, the Mn^{2+} concentration in the cell bodies after backfilling was found to be comprised between 0.12 and 0.25 mM, which is very low compared to concentrations injected locally in the brain in other species, > 5 mM (Silva and Bock, 2008). Moreover, since relaxivity is expected to be somewhat higher in tissue than in ASW due to macromolecule binding of Mn^{2+} (Huang et al., 2009), the actual Mn^{2+} concentrations in the cells are expected to be lower than our estimates.

Neuronal functioning after backfilling

Methods

In order to test the integrity of neuronal functioning in the presence of Mn^{2+}, three *Aplysia* were sacrificed and the migration experiment along n.3 was performed under identical conditions, with the MR imaging session replaced by electrophysiological recordings. Extracellular recordings of the bilateral nerves 3, one targeted by the Mn^{2+} (e.g. ipsilateral to the source of Mn^{2+}), one non-targeted

(contralateral), were performed simultaneously with intracellular recordings of the two bilateral B4 cells which send their axon into the ipsilateral or contralateral n.3, respectively. Extracellular recordings were made using wire pin electrodes placed against selected nerves and insulated from the bath with Vaseline. Intracellular recordings were made from connective tissue-desheathed ganglia with glass microelectrodes filled with 2 M KCH_3CO_2 (tip resistance 10-20 MΩ). Recorded bioelectrical signals were amplified by an Axoclamp-2B electrometer (Molecular Devices, Palo Alto, CA), digitized by an analog to digital converter (CED 1401, Cambridge Electronic Design, UK) and analyzed with Spike2 software (Cambridge Electronic Design, UK).

Results

At such low intracellular Mn^{2+} concentrations, the bioelectrical properties of the neurons and of the neuronal network were not altered. All the recordings showed that the neuronal network remained spontaneously active and generated a characteristic motor pattern. Figure 21 reproduces the simultaneous intracellular recordings of the membrane potential of both B4 neurons (Mn^{2+} loaded and contralateral unloaded – see Figure 20, A and C) and extracellular recordings of the peripheral buccal nerves 3 during the emission of a spontaneous burst of action potentials, in one pair of ganglia. The resting membrane potentials measured in the three ganglia sets were -60.6 ± 8.8 mV for the loaded B4 neuron and -62.7 ± 9.7 mV for the unloaded, respectively. The resting membrane potential and the intrinsic bursting properties of the loaded B4 neurons were thus unaltered as compared to the contralateral unloaded B4 cells.

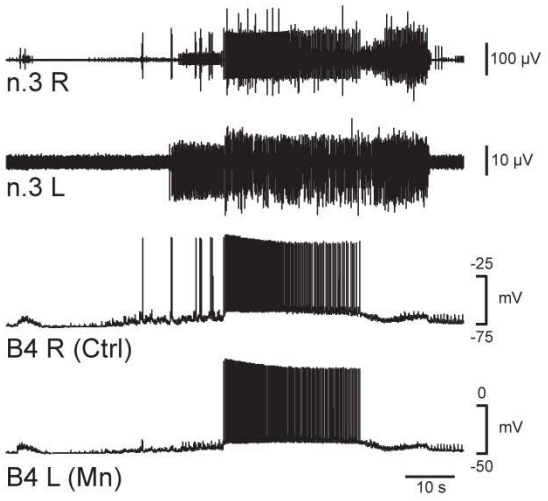

Figure 21. Recording of a spontaneous pattern of action potentials on the right (R) and left (L) n.3 and in the bilateral neurons B4 after a retrograde Mn^{2+} migration along the left n.3. The bioelectrical activity was not altered in the nerve and cell targeted by Mn^{2+} as compared to the non-targeted ones. The amplitude of the electrical signals recorded extracellularly in the nerves is dependent on the electrode position and its insulation with Vaseline therefore the difference in signal amplitude between n.3 R and L is not meaningful. The intrinsic strength of electrical signals should be inferred from the intracellular recordings.

From these experiments combined, it is reasonable to consider that backfilling from a 25 mM $MnCl_2$ source at nerve terminal results in Mn^{2+} concentrations below the toxicity threshold inside cell bodies, and does not impair the network's functional properties.

5.2 Response to dopamine stimulation

In this part of the study we aimed to highlight potential synaptic transfer (or extracellular release) of Mn^{2+} due to activation of the neuronal network by a modulatory transmitter. The results presented in the two previous sections highlighted the possibility of selectively labeling an identified pool of cells in the buccal ganglia using non-toxic concentrations of Mn^{2+}. This technique was therefore used as the starting point for this part of the study: the investigation of Mn^{2+} transport from these initially loaded cells into new cells (possibly post-synaptic cells) during activation. Bath application of DA was used for its ability to strongly stimulate the electrical activity in the buccal ganglia (Kabotyanski et al., 2000). Given the strong connectivity of B4-B5 cells with neighboring neurons (Gardner, 1971, 1977), the nerve into which they send their axon (n.3) was chosen as a source for retrograde migration for the entire set of experiments.

Methods

Experimental protocol

Ganglia from seven animals were used in these experiments.

Six sets of buccal ganglia underwent backfilling through n.3 followed by an imaging session as described in Section 5.1.

Following this initial imaging session, the ganglia were pinned back inside a Petri dish and perfused for two hours at a rate of 60 mL/h using a peristaltic pump (Watson Marlow, La Queue Lez Yvelines, France). Three ganglia were perfused with a solution of ASW containing 50 µM of dopamine hydrochloride (Sigma Aldrich). Oxidation of DA was prevented by adding an equimolar concentration of ascorbic acid (Sigma Aldrich) and maintaining the perfusate in an ice-chilled balloon, sheltered from light. The other three ganglia were perfused with a solution of ASW containing ascorbic acid only ("dummy" perfusate).

All six ganglia then underwent a "post-perfusion" imaging session, identical to the "pre-perfusion" one.

Given the overall duration of this protocol – two scanning sessions and two hours of perfusion in-between – the FLASH acquisitions were reduced from 10 to 6 averages, in order to increase cell viability chances and fit within available scanner time. Once isolated, the ganglia are expected to survive for 48h in a Petri dish with ASW, at 4°C. The overall duration of our experiments added up to 27h from isolation, with only 2x3h30 of scanning at room temperature. Inspection of cell contrast on the final T2w images allowed us to test for the presence of dead cells (change from hypointensity to hyperintensity compared to ASW).

One pair of ganglia underwent a single imaging session using identical FLASH and RARE protocols, in the absence of manganese.

Data analysis

Because the ganglia were positioned differently between the "pre-" and "post-" sessions, images were not comparable on a voxel-by-voxel basis, and the non-rigid transformation made registration difficult. However, within each session, the T2w image allowed the identification of regions of Mn^{2+} uptake seen on the T1w image. All processing was performed using Matlab (The MathWorks, MA, USA).

A region of interest (ROI), covering the full length of the coil, was drawn in ASW, and the signal intensity profile for ASW in the T1w dataset was determined as a function of position x along the coil axis, as illustrated in Figure 22.

For each set of T1w-T2w images, the ganglia were manually segmented on the T2w dataset. The masks were applied to the T1w images and segmented voxels in the ganglia at a particular position along x were normalized to ASW signal at the same position (Figure 22). Voxels with signal intensities below or equal to that of ASW were discarded, thus eliminating ASW or air bubbles from manually drawn masks.

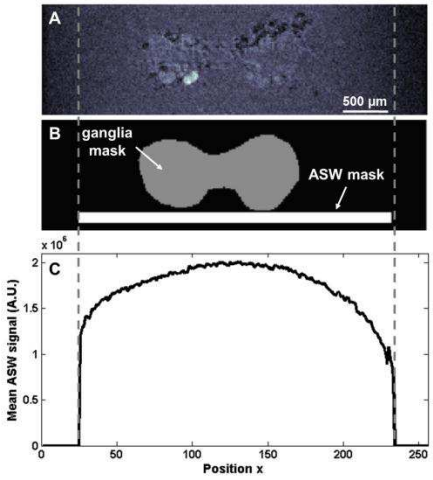

Figure 22. Procedure for signal normalization to ASW. A. T1w image. B. Manually drawn masks for the ganglia and ASW, the latter fully covering the extent of positions x occupied by the ganglia. C. Mean signal in the ASW mask at each position x along the solenoid axis. The profile obtained is typical of a solenoid transceiver. Voxels in the ganglia at each position x were normalized to mean ASW signal for the same position.

The remaining voxels were grouped into 11 bins, depending on their normalized signal level R: $1.0 < R \leq 1.1$; $1.1 < R \leq 1.2$; … ; $1.9 < R \leq 2.0$ and $R > 2.0$. Voxel counts in each bin produced the overall distribution of signal enhancement throughout the ganglia. We evaluated the changes in this distribution between "pre-" and "post-" perfusion, in the presence and absence of DA. Maps of normalized signal in the ganglia were also produced.

Results and discussion

First of all, visual inspection of post-perfusion T2w images did not lead to the identification of any bright (i.e. dying) cell. This allowed us to conclude that the ganglia had survived the full experimental protocol: 18h of migration at 4°C and two 3h30-scanning sessions with two hours of perfusion in-between.

Figure 23 shows selected slices and corresponding Mn^{2+} distribution from two perfusion experiments. With DA, the resulting signal ratio map presents more regions of intermediate enhancement ($1.3 < R < 1.6$), in the shape of tracts or cells.

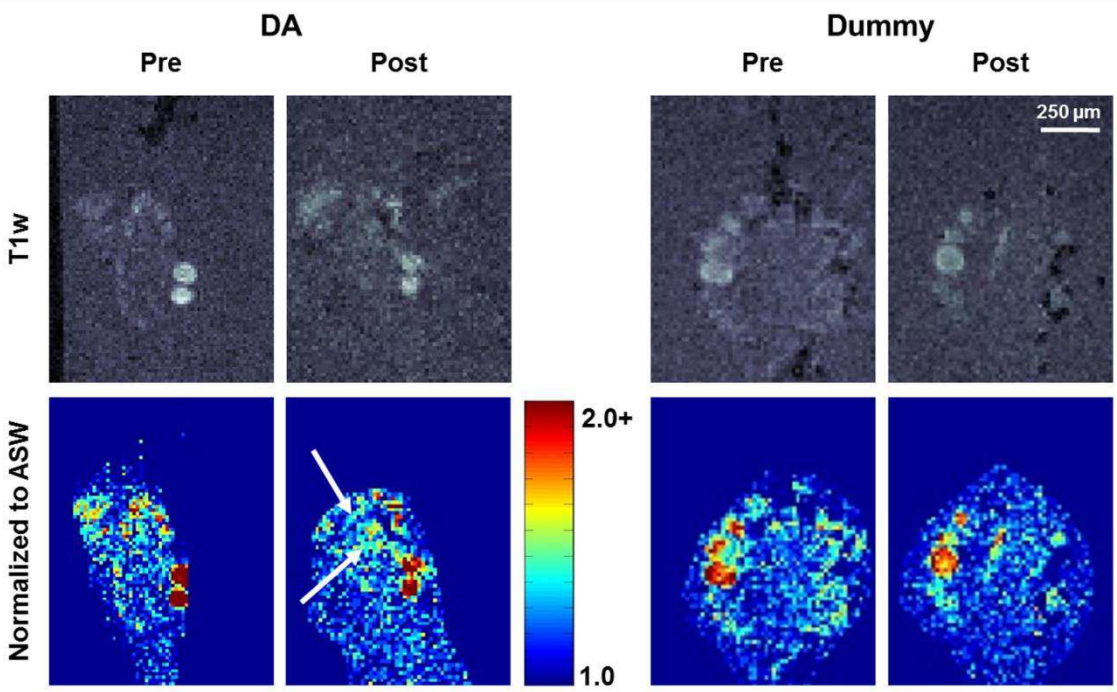

Figure 23. Selected slices showing Mn^{2+} distribution before and after perfusion, with and without dopamine. In each case, the pre- and post- slices, although not identical, were chosen as similar as possible – major common cells are identifiable. In the post-DA normalized image, intermediate enhancement (R~1.4) is detectable in the shape of tracts or extended areas (indicated by the arrows). In the post-dummy normalized image, the distribution shows a uniform decrease of enhancement compared to the pre-dummy.

Figure 24 shows histograms of typical voxel counts in each bin, expressed as fractions (%) of all retained voxels, in the absence of Mn^{2+} and following backfilling. In the absence of Mn^{2+}, the large majority of voxels (70%) falls within $1.0 < R < 1.2$. Following our backfilling technique, the upper bins ($R > 1.8$) become populated (~2000 voxels, 3% of total).

Starting from the Mn^{2+}-backfilled state, Figure 25 illustrates the pre/post change in the fraction size of each bin in DA and dummy experiments. Three "groups" were delineated: the first group is referred to as "weakly hyperintense", with $1.0 < R \leq 1.2$, the second as "intermediately hyperintense", with $1.2 < R \leq 1.8$, and the third one as "strongly hyperintense", with $R > 1.8$. Following DA perfusion, the size of the first and third groups decreased, while that of the second group increased. Following dummy perfusion, both second and third groups decreased in size while the first group increased, the hyperintensity distribution thus evolving towards that of the Mn^{2+}-free ganglia shown in Figure 24A.

Table 5 (page 84) provides exact voxel counts and percentages in each of these three groups for all six perfusion experiments. Between pre- and post-perfusion imaging sessions, the relative size of the weakly hyperintense group decreased by -3.1 ± 1.4 points in the DA perfusion experiments. The same group increased by 5.8 ± 2.0 points in the dummy experiments. The relative size of the intermediate group increased by 3.8 ± 0.8 points in the DA perfusion experiments, while

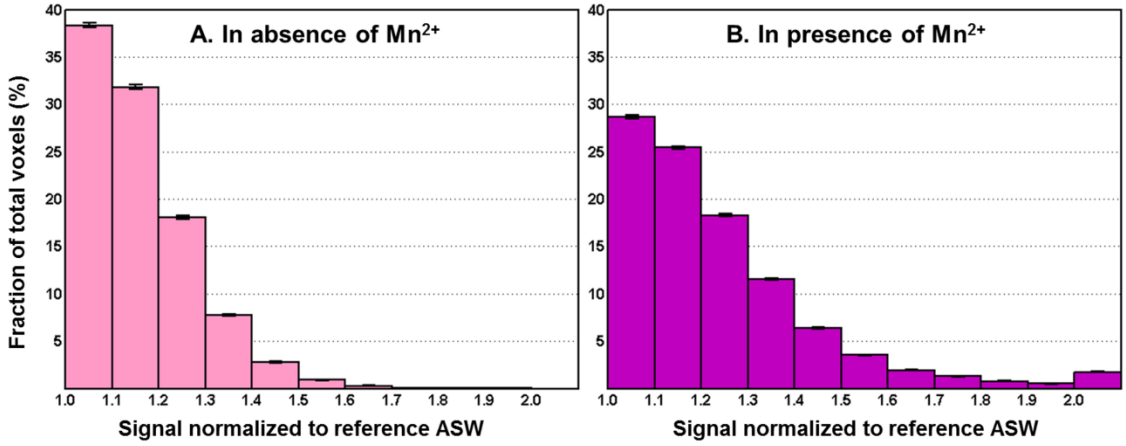

Figure 24. Distributions of voxel intensities (as % of all voxels hyperintense compared to ASW) in two pairs of ganglia, one in the absence of $MnCl_2$ exposure (A), and one following 18h $MnCl_2$ (25 mM) unilateral migration along n.3 (B). The error bars represent standard errors within each bin, calculated as $\sqrt{(f(1-f)/N)}$, where f is the fraction and N the total number of voxels segmented. In the absence of Mn^{2+}, the large majority of voxels (70%) is within R < 1.2, and the counts fall to quasi-zero for R > 1.7. Following our backfilling technique, the upper bins (R > 1.8) become populated (~2000 voxels, 3% of total).

decreasing by -5.4 ± 1.8 points after the dummy perfusions. The fraction size of the third group was always very small compared to that of the other two (0.1 – 3%), therefore we considered that its change with perfusion (either DA or dummy) was not meaningful if expressed as difference in percentage change. Instead, the change in terms of exact voxel counts was calculated. For the six perfusion cases, its final size compared to the initial one decreased in proportions ranging from -16 to -98%.

In the case of dummy experiments, the changes in the group sizes following perfusion can be interpreted as a natural washout of Mn^{2+} from the loaded cells, with the intermediately and strongly hyperintense groups emptying in favor of the weakly hyperintense one. However, in the conditions of the present experiments, it was described that the buccal ganglia spontaneously generate repeated patterns of electrical activity (Nargeot and Simmers, 2012) – see Figure 21. The Mn^{2+} dynamics presented should therefore be interpreted as a mixture of natural washout and effects of some spontaneous neuronal activity.

In the case of DA perfusions, results can be interpreted as Mn^{2+} transport dominated by the intensification of the neuronal activity induced by the modulatory transmitter. Indeed, the size of the intermediately hyperintense group increases,

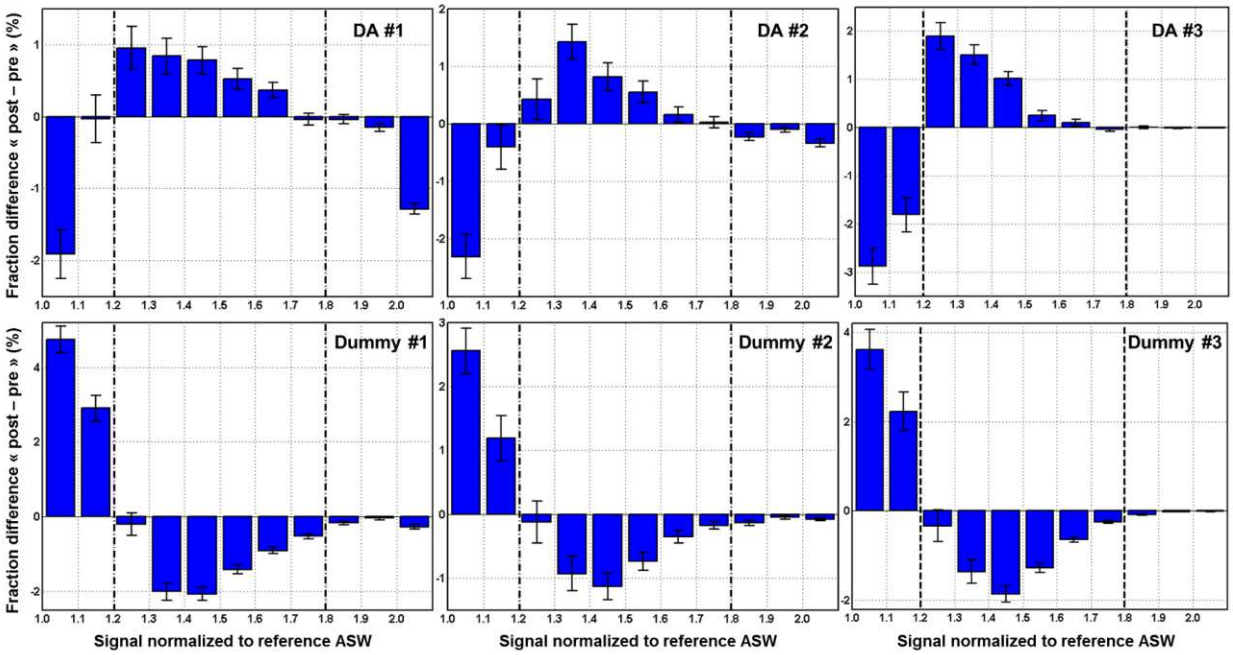

<u>Figure 25.</u> Absolute changes in size of each bin, following perfusion with DA (top row), or perfusion without DA (bottom row). The vertical dotted lines delimitate regions where the population of voxels evolves differently between pre- and post- in the presence or absence of DA. The error bars were calculated by adding the absolute values of the standard errors for pre- and post- distributions.

likely as a result of the weakly hyperintense cells capturing Mn^{2+}, and the strongly hyperintense ones releasing it. Thus, under DA some Mn^{2+} appeared to be transferred from cell to cell.

This set of experiments shows that Mn^{2+} distribution inside the ganglia is altered by DA-induced activity, versus natural washout. Following chemical stimulation with DA, regions of the ganglia displaying intermediate enhancement are extended, at the loss of regions of low or very high enhancement. In the absence of DA, the size of regions of both high and intermediate enhancement is reduced, at the profit of regions of low enhancement. These results are consistent with previous rodent studies which demonstrated Mn^{2+} release was correlated with that of neurotransmitters (Serrano et al., 2008; Takeda et al., 1998).

We note however that we were unable to identify specific neurons that were not labeled initially but accumulated Mn^{2+} after DA perfusion. Such identification, along with known synapses between neurons, would allow one to obtain direct proof of Mn^{2+} synaptic transfer (or, on the contrary, of extracellular release upon activation and recapture by any neighboring activated neuron). It is possible that the Mn^{2+} concentrations in post-synaptic neurons were below the detection threshold of our current protocol. In order to optimize the contrast-to-noise ratio in the T1w images for lower Mn^{2+} concentrations, the TR and flip angle should be adjusted accordingly. Moreover, the backfilling technique has the disadvantage of labeling a large number of cells (all those with axonal projections in the chosen nerve), thus leaving many pathways for Mn^{2+} to travel with chemical activation, and making post-perfusion results confounding in terms of tracking Mn^{2+} movement precisely. One way of overcoming this problem would be to replace backfilling with direct Mn^{2+} intracellular injection into a chosen identified neuron (e.g. B4). However, the issue of sensitivity to lower Mn^{2+} concentrations in post-DA images would still need to be addressed.

5.3 Conclusion

We have demonstrated the feasibility of tracking axonal projections with MEMRI in the buccal ganglia of *Aplysia californica*. At ultra-high magnetic field, high spatial resolutions allow the identification of most motor neurons in the network at low, non-toxic, Mn^{2+} concentrations. Although optical techniques can provide complementary information, the strength of MEMRI lies in its capability to obtain fully three-dimensional images and in the possibility to work with living specimens at non-toxic contrast agent concentrations.

This study opens the way for tracking Mn^{2+} flux from and to identified cells (possibly pre- and post-synaptic neurons) using chemical stimulation. We have established that chemical stimulation with DA alters the dynamics of Mn^{2+} inside the ganglia, namely that the natural washout in time becomes dominated by Mn^{2+} transfer from initially loaded cells to unloaded cells. For clear identification of cells capturing Mn^{2+} upon activation by DA, $MnCl_2$ intracellular injections should be used rather than backfilling through a motor nerve.

By injecting $MnCl_2$ into the living *Aplysia*, one can also study the Mn^{2+} uptake by identified neurons under various stimulation conditions (Radecki et al., 2013). Moreover, such studies are not limited to the buccal ganglia but can be extended to other neural circuits (other ganglia).

		R > 1.0 (Total)	1.0 < R ≤ 1.2	1.2 < R ≤ 1.8	1.8 < R
DA #1	**pre**	65052	35189	27918	1945
		100 %	54 %	43 %	3.0 %
	post	73310	38230	33971	1109
		100 %	52 %	46 %	1.5 %
DA #2	**pre**	50715	25447	24380	888
		100 %	50 %	48 %	1.8 %
	post	49692	23584	25571	537
		100 %	47 %	51 %	1.1 %
DA #3	**pre**	68975	49498	19371	106
		100%	72%	28%	0.2%
	post	68600	46008	22503	89
		100%	67%	33%	0.1%
Dummy #1	**pre**	68368	38111	29157	1100
		100 %	56 %	43 %	1.6 %
	post	68747	43571	24410	766
		100 %	63 %	36 %	1.1 %
Dummy #2	**pre**	62415	31656	30395	364
		100 %	51 %	49 %	0.6 %
	post	62323	33941	28191	191
		100 %	54 %	45 %	0.3 %
Dummy #3	**pre**	47331	30036	17237	58
		100%	64%	36%	0.1%
	post	46093	31940	14152	1
		100%	69%	31%	0.0%

Table 5. Voxel counts in the overall masks (the signal intensity was normalized to ASW signal) and in each of the three groups: weak (1.0 < R ≤ 1.2), intermediate (1.2 < R ≤ 1.8) and strong hyperintensity (1.8 < R). In the first three experiments (DA), the ganglia were perfused with 50 µM DA + ascorbic acid between "pre" and "post" conditions, in the other three (Dummy) they were perfused with 50 µM ascorbic acid only. The volume of one voxel is 15.6 pL.

5.4 Chapter summary

In this chapter, we presented a study where we performed for the first time MEMRI on the buccal ganglia of *Aplysia californica*. The presence of Mn^{2+} was detected in visible and identifiable neurons. Using retrograde transport (backfilling) from nerve end into neuronal body, we confirmed the mapping of motor neurons' axonal projections into the peripheral nerves of the buccal ganglia. This backfilling technique resulted in low cellular Mn^{2+} concentrations that did not impair the functionality of the network, while still permitting clear Mn^{2+} localization through enhancement. Following backfilling, the ganglia were perfused with either a dopamine or a control solution. The presence of dopamine, and thus chemical stimulation, was found to trigger inter-neuronal Mn^{2+} transport inside the ganglia. Possible continuations of this study include the visualization of Mn^{2+} transport from identified pre-synaptic to post-synaptic neurons (by injecting $MnCl_2$ intracellularly) and the study of *in vivo* Mn^{2+} uptake under various stimulations (by injecting $MnCl_2$ in the living animal).

In Part III, we will cover the second main axis of this thesis work: implementing methods for diffusion-weighted MR microscopy and using them to evaluate the changes in apparent diffusion coefficient with membrane depolarization and cell swelling in the *Aplysia* buccal ganglia and isolated cells.

Part III

Response to hypotonic and ouabain challenges in *Aplysia* revealed by diffusion MR microscopy

6 Diffusion-weighted MRI

It has been known for a long time that the diffusion process introduces additional attenuation of the NMR signal when gradients are played and this was used as early as 1954 to estimate the self-diffusion coefficient of water (Carr and Purcell, 1954). NMR is still today the only tool capable of measuring diffusion coefficients non invasively. Diffusion MRI, i.e. the incorporation of diffusion gradients additionally to the imaging gradients within an MRI sequence, was implemented in the mid-80s and soon yielded the first *in vivo* map of the so-called "apparent diffusion coefficient" (ADC) in healthy and diseased human brain (Le Bihan et al., 1986).

6.1 The physics behind the DW MR signal

In order to account for the effect of diffusion in the presence of a gradient **G**, the Bloch equation can be modified to incorporate an additional diffusion term. In the interest of clarity, we neglect the relaxation terms. The expression of this equation, referred to as Bloch-Torrey, is:

$$\frac{\partial \vec{M}(\vec{r},t)}{\partial t} = \vec{M}(\vec{r},t) \times \gamma\left(B_0 + \vec{G}(t)\cdot\vec{r}\right)\vec{z} + D\Delta\vec{M}(\vec{r},t) \tag{6.1}$$

where D is the diffusion coefficient. Using the complex formalism and a signal demodulated at ω_0, the evolution of the transverse component $M_{xy}(\mathbf{r},t)$ is governed by:

$$\frac{\partial M_{xy}(\vec{r},t)}{\partial t} = -i\gamma\left(\vec{G}(t)\cdot\vec{r}\right)M_{xy}(\vec{r},t) + D\Delta M_{xy}(\vec{r},t) \tag{6.2}$$

The solution for unrestricted diffusion

We assume an unrestricted homogeneous medium (e.g. plain water far from any wall) and therefore a spatially invariant diffusion coefficient. We will come back on the implications of this model. In this case, the solution of Equation (6.2) can be written in its general form as:

$$M_{xy}(\vec{r},t) = A(t)\exp\left(-i\gamma\int_0^t \vec{G}(\tau)\cdot\vec{r}\,d\tau\right) \tag{6.3}$$

Reinjecting Equation (6.3) into Equation (6.2), a solution for A(t) is of the form:

$$\ln A(t) = -D\gamma^2\int_0^t\left[\left(\int_0^\tau \vec{G}(s)ds\right)\cdot\left(\int_0^\tau \vec{G}(s)ds\right)\right]d\tau + \ln A(0) \tag{6.4}$$

For convenience, we refer to the diffusion weighting introduced by the gradients as the b-value. For an arbitrary diffusion gradient waveform:

$$\mathrm{b} = \gamma^2\int_0^t\left[\left(\int_0^\tau \vec{G}(s)ds\right)\cdot\left(\int_0^\tau \vec{G}(s)ds\right)\right]d\tau \tag{6.5}$$

Hence for a gradient waveform with net zero integral after time t:

$$M_{xy}(\mathrm{t}) = \mathrm{A}(0)\exp(-bD) \qquad \text{and} \qquad \frac{S}{S_0} = exp(-bD) \tag{6.6}$$

where S and S_0 are the MR signals in a sequence with and without diffusion gradients, respectively.

The pulsed-gradient spin-echo (PGSE) sequence

The basic diffusion-weighted MR sequence is based on the addition of two pulsed field gradients (referred to as diffusion gradients) on either side of the refocusing pulse in a spin-echo sequence (Stejskal and Tanner, 1965). This sequence is often referred to as PGSE (for Pulsed Gradient Spin Echo). The timeline of the sequence is sketched in Figure 26, illustrating its main parameters. For this pair of gradients, the b-value is explicitly equal to:

$$b = \gamma^2\left(\int_0^\delta G_d^2\tau^2 d\tau + \int_\delta^\Delta G_d^2\delta^2 d\tau + \int_\Delta^{\Delta+\delta} G_d^2(\tau-(\Delta+\delta))^2 d\tau\right) = \gamma^2 G_d^2\delta^2\left(\Delta-\frac{\delta}{3}\right) \tag{6.7}$$

If diffusion gradients are present on multiple axes, $G_d^2 = G_{dx}^2 + G_{dy}^2 + G_{dz}^2$.

Rectangular pulses are an approximation because the gradient rise time cannot be infinitely short. To account for the actual trapezoidal shape of the gradients, the correct formula to compensate for gradient rise time ε is (Mattiello et al., 1994):

$$b = \gamma^2 G_d^2\left[\delta^2\left(\Delta-\frac{\delta}{3}\right)+\frac{\varepsilon^3}{30}-\frac{\delta\varepsilon^2}{6}\right] \tag{6.8}$$

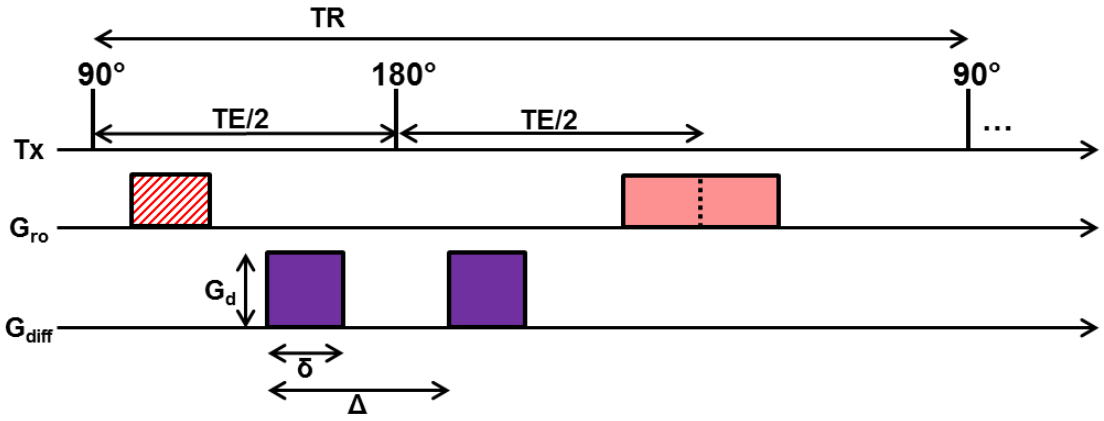

Figure 26. Timeline of a standard diffusion-weighted spin-echo sequence with pulsed field gradients. For simplicity, the phase-encoding and/or slice selection gradients are not shown. The diffusion gradients can be played on any one axis or on multiple axes at once. The relative weight of each axis determines the direction of diffusion sensitization. The duration of each pulse is labeled δ and the separation of pulses Δ.

Naturally, the imaging gradients contribute to diffusion weighting as well. While in most standard sequences their amplitudes are very low compared to those of the diffusion gradients and are therefore neglected, some configurations require the incorporation of the imaging gradients into the calculation of the b-value. This is the case for instance in MR microscopy, where imaging gradients are very strong. For a correct and complete assessment of the effective diffusion weighting of a sequence (or effective b-value, b_{eff}), there are analytical formulae that allow this calculation based on sequence parameters: (Mattiello et al., 1997; Mattiello et al., 1994). The most important aspect to bear in mind is that the various gradient pulses do not only contribute through a simple additive effect but also via cross-terms with other gradient pulses in the sequence.

On a simple diffusion weighted image (typically with b = 1000 s/mm²), media of higher diffusion appear hypointense because the irreversible dephasing caused by diffusion is more important. Using just two diffusion weightings, b_1 and b_2, one can already extract a quantitative estimate of D using Equation (6.6).

Narrow pulse approximation

If we assume that the gradient pulse duration δ in PGSE is short enough for diffusion to be ignored during the pulse, each proton accumulates the phase corresponding to its location at the time the pulses are played. Without any assumption on the diffusion regime, the transverse magnetization at the end of the paired pulses can be expressed as:

$$M_{xy}(\vec{r},\Delta) = \exp(-i\gamma\vec{G}_d \cdot \vec{r}\delta) \int_V \rho(\vec{r}_0)P(\vec{r},\vec{r}_0,\Delta)\exp\left(i\gamma\vec{G}_d \cdot \vec{r}_0\delta\right)d\vec{r}_0 \quad (6.9)$$

where P is a diffusion propagator that describes the probability for a molecule initially at $\mathbf{r_0}$ to be in location $\mathbf{r}$ after time Δ.

In the case of an unrestricted homogeneous medium, the diffusion propagator has a Gaussian expression:

$$P(\vec{r},\vec{r}_0,\Delta) = \frac{1}{(4\pi D\Delta)^{3/2}} exp\left[-\frac{(\vec{r}-\vec{r}_0)^2}{4D\Delta}\right] \quad (6.10)$$

where D is the free self-diffusion coefficient. Using this approach, the derivation of the MR signal also leads to the expression presented in Equation (6.6).

6.2 Gaussian phase approximation and ADC

In the presence of restrictions and inhomogeneities, the diffusion propagator in Equation (6.9) is in general not Gaussian. However, it can sometimes be approximated by a Gaussian function, which means the signal attenuation can eventually still be modeled as:

$$\frac{S}{S_0} = exp(-b \cdot ADC) \quad (6.11)$$

where the free diffusion coefficient D has been replaced by an apparent diffusion coefficient (ADC). The condition for the Gaussian phase approximation to be valid is that the ADC be independent of the strength of the diffusion gradients (Yablonskiy and Sukstanskii, 2010). This approximation is usually valid if the phase accumulated by the spins is small: $\varphi << 1$, i.e. at short diffusion times or low diffusion weightings.

The ADC is a practical phenomenological parameter to quantify diffusion in living tissue (and more specifically in nervous tissue, since this is the object of study of this work) where proton diffusion is neither homogeneous nor free. First of all, the attenuation measured at the voxel scale is the averaged effect of several heterogeneous media and viscosities encountered by protons at microscopic scale. Second, the tissue structure is such that during the diffusion time imparted by the MR experiment, the water molecules are likely to encounter some form of hindrance

to their movement, principally in the form of cellular or sub-cellular membranes (Le Bihan, 2007). The ADC is then a reflection not only of the various viscosities in the voxel but also of the size of the compartments in which the molecules can roam. There are several consequences to this.

One implication is that the diffusion time of the experiment will affect the ADC measured in the tissue (Niendorf et al., 1994). Indeed, it seems reasonable that the shorter the diffusion time, the fewer the barriers the molecules are likely to encounter and the higher the ADC. For infinitely short diffusion times, the ADC approaches the value of the free diffusion coefficient. Inversely, for very long diffusion times, water molecules encounter many hindrances, hence a lower ADC that depends essentially on compartment size rather than on medium viscosity. The effective diffusion time for PGSE sequences is $t_{diff} = \Delta - \delta/3$. Because of gradient hardware limitations, the diffusion times associated with this sequence remain quite long, in the range 10 – 100 ms. Shorter diffusion times, in the range 400 μs – 10 ms, are beginning to be probed using an Oscillating Gradient Spin Echo (or OGSE) sequence (Does et al., 2003; Schachter et al., 2000). The principle behind OGSE is to replace the diffusion gradient pulse (of single polarity) with a sinusoidal gradient. Because of the alternate switch in polarity, the effective diffusion time is dominated by the sinusoid period rather than by its entire duration, while the diffusion weighting effect (via the b-value) can still achieve relatively high values.

Another important consequence of tissue microstructure is diffusion anisotropy. As mentioned earlier, the direction of diffusion sensitization is determined by the resultant vector of diffusion gradients applied on each axis. Depending on the orientation of this vector with respect to tissue structure, the ADC can also vary. One of the most striking examples is provided by brain white matter, where diffusion perpendicular to the axon fibers is a lot lower than along the axons, due to the very low permeability of myelin to water. This property has paved the way for the development of a fascinating field of fiber tracking and connectomics in the brain using diffusion tensor imaging (DTI) (Conturo et al., 1999). This approach estimates the ADC in each voxel for a large number of orientations and determines the principal direction of the white matter tracts in each voxel based on the calculated direction of highest diffusion. More elaborate algorithms have been developed since, for reliable mapping of white matter tracts in healthy and diseased brain. More details can be found in a recent review (Le Bihan and Johansen-Berg, 2012).

6.3 Non Gaussian diffusion

Eventually, the complexity of the diffusion path followed by water molecules within a voxel of brain tissue becomes manifest in the deviation of the signal attenuation curve from a mono-exponential for high b-values (Assaf and Cohen, 1998; Niendorf et al., 1996). An illustration of this phenomenon is provided in Figure 27. This finding was only possible with improved gradient hardware which gave access to higher b-values (2000 – 10,000 s/mm², when the clinical standard is around 1000 s/mm²). The origin of this behavior is still under debate and multiple models have been proposed and tested to fit and explain the data. This section is based on reviews by (Mulkern et al., 2009) and (Yablonskiy and Sukstanskii, 2010).

The biexponential model

One popular view is the existence of two pools of water, assumed to be in slow or intermediate exchange over the duration of the MR experiment. The origin of this model is the empirical observation that the data are well fit by a biexponential function. If within the same imaging voxel coexist two pools of water that are characterized by different diffusion coefficients (one slow and one fast) and if these "compartments" are in slow (or intermediate) exchange, then the resulting signal will not take the monoexponential form (with an ADC that is the weighted average of the two diffusion coefficients), but indeed take the form of a biexponential decay, modeled by the following equation:

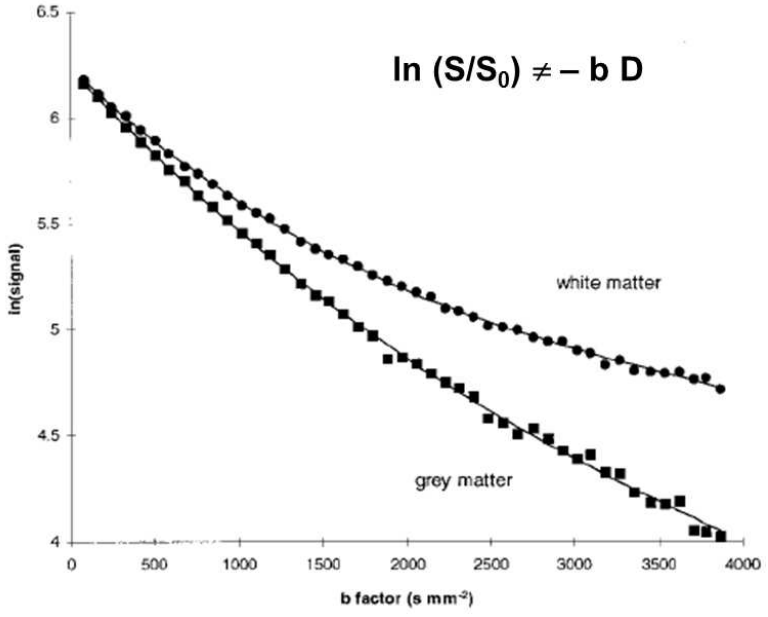

Figure 27. Evidence that the diffusion signal in the human white and gray matter deviates from a monoexponential decay. Plotting the natural logarithm of the signal against b-value, a linear shape is expected. The linear behavior does not hold for b-values > 1000 s/mm². *Data from (Clark and Le Bihan, 2000).*

$$\frac{S}{S_0} = f_{slow} \exp(-bD_{slow}) + (1 - f_{slow})\exp(-bD_{fast}) \quad (6.12)$$

where f_{slow} is the volumetric fraction of the slow pool, and D_{slow} and D_{fast} are the specific diffusion coefficients in each compartment. Note that if the pools are in intermediate rather than slow exchange, the fractions measured no longer mirror the physical sizes of the pools, but rather a mixture of physical sizes and acquisition parameters. The issue with this model is that all attempts at associating the two pools at stake with a biological reality remain unconvincing or doubtful. The different hypotheses which exist will be presented in great detail in Chapter 9, when they will be brought to the test of our diffusion measurements in the *Aplysia*.

Other phenomenological models

One argument against the biexponential model is that it involves fitting relatively noisy data to a model with a large number of parameters (three), which constitutes an ill-conditioned problem. There are at least three other functions with only two fit parameters that have been proposed to model the data.

The kurtosis model quantifies the deviation from a Gaussian process in the form of a Taylor expansion (Jensen et al., 2005). Truncated at the second term, the expression gives:

$$\ln S = \ln S_0 - b\overline{D} + \frac{K}{6}(b\overline{D})^2 \quad (6.13)$$

where K is the so-called kurtosis. Elements of tissue microstructure contributing to a non-Gaussian behavior are quantified by K, and for Gaussian diffusion, K = 0.

The statistical model (Yablonskiy et al., 2003) assumes a Gaussian distribution of diffusion coefficients centered around a mean ADC, with a given distribution width σ. The probability distribution of diffusion values P(D) can be chosen among various distribution functions. Assuming the voxel contains a large number of similar cells, the distribution is expected to be peaked around the mean ADC and fall off rapidly, such that it can be modeled by a Gaussian distribution. For D > 0:

$$P(D) = A \exp\left[-\frac{(D - ADC)^2}{2\sigma^2}\right] \quad (6.14)$$

where A is a fixed normalization constant. Results an MR signal expressed as:

$$\frac{S}{S_0} = \frac{1 + \Phi(ADC/\sigma\sqrt{2} - b\sigma/\sqrt{2})}{1 + \Phi(ADC/\sigma\sqrt{2})} \exp\left(-b \cdot ADC + \frac{b^2\sigma^2}{2}\right) \quad (6.15)$$

where Φ is the error function. For small b-values, the signal tends to a monoexponential decay and for large b-values the attenuation rate is slowed down by the second term in the exponential.

The stretched exponential model (Bennett et al., 2003) describes diffusion-related signal decay as a continuous distribution of sources decaying at different rates, with no assumptions made about the number of participating sources:

$$\frac{S}{S_0} = \exp[(-bD)^{\alpha}] \quad (6.16)$$

where α takes values between 0 and 1.

However, no clear relationship between the parameters of these models and tissue properties has been established so far either. Moreover, the ability of these models to fit the data for b-values larger than 2500 s/mm² remains doubtful compared with the biexponential model (Mulkern et al., 2009). Access to ever extended b-values might even encourage one to resort to multiexponential fitting, where "multi" is at least three (Pfeuffer et al., 1999).

Mathematical models

Aside from these empirical approaches, two types of theoretical approaches can be adopted.

One approach consists in evaluating the behavior of the MR signal in very simple – purely ideal – structures. For example, (Sukstanskii et al., 2003) assumed a single compartment model with impermeable barriers and showed that at short diffusion times, the reduced diffusivity near the membranes leads to an edge enhancement effect that translates into an MR signal that can be fit very well by a biexponential function. In this case, the non-Gaussian behavior is generated by the sole presence of a restrictive barrier. Although the distribution of diffusion values is not exactly composed of two delta-functions, the spins can nonetheless be divided into two pools: those close to the barrier, and those far from the barrier. The authors stress that this behavior is only valid if the diffusion time Δ is much shorter than the characteristic diffusion time a^2/D where a is the size of the compartment. Using typical values for biological tissue ($D \sim 10^{-3}$ mm²/s; $a \sim 1$ μm), the characteristic diffusion time is on the order of 1 ms, hence Δ should be at most 0.1 ms. This is not

achievable with the current hardware, and much larger cells should therefore be used for this "pooling" caused by the barrier to be measurable. This would be typically feasible on *Aplysia* neurons, but the model should incorporate the membrane non-zero permeability, as well as hindrance from intracellular structure. Indeed, the correct incorporation of the features of the medium is crucial. In a similar study on a 1D periodic structure with permeable membranes (Sukstanskii et al., 2004), the authors showed that the permeability of membranes has a critical impact on the MR signal and can lead to erroneous conclusions on compartment size distributions if not accounted for.

Other theoretical approaches consist in modeling the tissue in a realistic, though simplified manner, and parameterizing the various geometric features introduced. The MR diffusion signal in the model environment is calculated by numerical or analytical methods and then used to fit experimental data. This approach can potentially give access to physically meaningful quantities that characterize the tissue. Myelinated axon bundles for example can be modeled as impermeable infinite cylinders with characteristic parallel and transverse diffusion coefficients. Additional refinements can then be added, such as hindrance in the longitudinal direction, variations in axon diameters or the presence of non-cylindrical structures such as cell bodies (Assaf et al., 2004; Chin et al., 2004). Models for gray matter also include an additional compartment representing the glial cells with high membrane permeability and the extracellular space, where diffusion is assumed to be isotropic (Jespersen et al., 2007). However, the larger the refinement of the model, the higher the data quality and quantity required to fit a large number of parameters reliably. It should be mentioned that the theoretical diffusion decay curve generated by these models does deviate from a monoexponential behavior, and interestingly resembles a pseudo-biexponential function.

All of these considerations show the richness contained within the MR diffusion weighted signal and its potential for revealing tissue microstructure. Whether empirical or theoretical, all models presented are associated with parameters that can potentially be used as biomarkers of physiological and pathological change in tissue. However, MR microscopy could drastically reduce the impact of PVE and thus the confounding effects of heterogeneity on diffusion measurements, for a more straightforward approach to microstructure.

We stress once again that non Gaussian diffusion is manifest in brain tissue for b-values approximately above 1000 s/mm². Below this limit, the Gaussian phase approximation is usually valid.

6.4 Main applications of diffusion MRI

Since its introduction in the mid-1980s, diffusion MRI has quickly become very popular in the clinic, with many diagnostic applications. The most successful one is the early detection of acute brain ischemia, with an example given in Figure 28. Indeed, the ADC was found to drop by about 30 – 60% in the ischemic region within 45 minutes of onset, whereas T_2 modifications occured several hours later (Moseley et al., 1990). It is known that stroke leads to large cell swelling (cytotoxic edema) in the tissue and it is therefore believed that the decrease in ADC is a consequence of cell swelling. This hypothesis is supported by the fact that other physiological and pathological conditions, known to cause transient or durable cell swelling, have also been found to lead to a transient or durable decrease in ADC. This is the case for instance of epilepsy, which is associated with cell swelling but where blood flow is actually increased (as opposed to ischemia). Bicuculline-induced *status epilepticus* has been shown to produce a 15 – 20% ADC decrease in rat brain (Zhong et al., 1993). Cortical spreading depression has also been shown to cause a transient decrease in ADC which closely follows the wave of depolarization in the brain (Latour et al., 1994a). Last but not least, transient ADC decreases have been measured in the cortex upon activation (Darquie et al., 2001; Le Bihan et al., 2006), opening the way for a potential use of diffusion in functional MRI.

However, the exact mechanism that links cell swelling to tissue ADC decrease has not been established yet. This constitutes an ongoing field of research, which meets certain aspects of the discussion on multiple water "pools". A thorough review and discussion of the biochemistry of cell swelling and its impact on compartmentalization and diffusion measurements will therefore be presented in Chapter 9. Once again, it appears determining to understand diffusion mechanisms at the cellular level, and MR microscopy could be a great means of unveiling diffusion changes at tissue, cellular and sub-cellular levels during events leading to membrane depolarization and cell swelling.

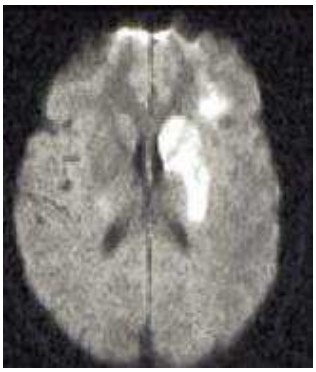

Figure 28. Diffusion weighted image of human brain affected by stroke in the left hemisphere. The hyperintense region characterized by reduced diffusion coincides with the ischemic area. *Image from (Østergaard et al., 2000).*

Aside from ischemia, the use of diffusion MRI has also become widespread for the study of white matter tracts (Chenevert et al., 1990) and therefore of numerous pathologies that lead to the alteration of the latter: multiple sclerosis, schizophrenia, dyslexia, epilepsy, Alzheimer's disease… (Le Bihan et al., 2001; Sundgren et al., 2004). More recently, diffusion MRI has also shown capability of assessing the evolution of tumor response to treatment (Colvin et al., 2011).

The extended use of diffusion MRI in the clinical context posed great challenges in terms of hardware and sequence improvement. The following section will discuss part of these aspects.

6.5 Strong gradients and rapid acquisition, please

Highly diffusion weighted images (i.e. acquired at high b-values) are precious as they reveal new features of diffusion in tissue, such as the earlier mentioned non Gaussian behavior. From Equation (6.7) (page 88), it appears clearly that in order to achieve high diffusion weighting, either the gradient amplitude, or duration, or separation need to be increased. Increasing gradient duration δ brings the experiment away from the "pulsed gradient" approximation, where δ needs to be short relative to Δ. Increasing the gradient separation Δ leads to prolonged echo times, hence a significant loss in signal from T_2 decay and longer acquisition times. Moreover, Δ and δ also dramatically impact the diffusion time in the experiment. Ideally we would like to choose the amount of diffusion weighting (b) and the diffusion time (t_{diff}) independently, as both parameters play important parts in data interpretation. The best option by far is therefore to increase the gradient amplitude. Unfortunately, strong gradients are a great hardware challenge on clinical scanners, with current typical values reaching 40 mT/m. On the pre-clinical side, the situation is better, with small-bore systems now usually equipped with gradient sets between 300 and 700 mT/m.

Another important limitation of diffusion measurements is the long acquisition time. The classical diffusion-weighted spin-echo sequence (Figure 26 page 89) is characterized by long TRs (on the order of T_1) in order to allow for sufficient T_1 relaxation between excitations. More importantly, quantitative diffusion experiments require the acquisition of data at multiple b-values (at least two for basic ADC estimation, and sometimes up to 50 for the analysis of non Gaussian diffusion) and/or for multiple directions of diffusion sensitization (for studies of anisotropy). Prolonged acquisition times are detrimental in the clinical setup under

several aspects. Images are more likely to be corrupted by macroscopic motion artifacts. More importantly, the study of acute pathologies such as stroke is biased by a low temporal resolution, as the tissue condition can evolve significantly over the timescale of a single acquisition. Available scan time can also be an issue on busy clinical scanners. These factors led to a strong motivation for developing more time efficient diffusion sequences.

The sequence that is by far the most widespread today is diffusion-weighted EPI. This consists in taking the DW-SE sequence illustrated in Figure 26 and replacing the single line read-out by an EPI read-out of an entire k-space plane, as explained in Chapter 1. Single shot EPI is essentially free of any motion artifacts, but on the other hand it is corrupted by geometric distortion artifacts caused by magnetic inhomogeneities, and displays significantly lower signal due to longer echo times (Farzaneh et al., 1990). A reasonable trade-off is then the acquisition of multi-shot DW-EPI. Other k-space sampling techniques such as spiral MRI (Li et al., 2005) have also been tested but have not become of standard use because of the gradient performance accuracy required by such k-space trajectories.

Another possibility that has been explored is the incorporation of a diffusion gradient within an SSFP (FISP-Echo) imaging scheme. While this constitutes a reasonable choice for rapid diffusion weighted images free from the artifacts of EPI, the technique is unsuitable for diffusion quantification because the diffusion weighting is tangled up with T_1 and T_2 weighting (Deoni et al., 2004; Le Bihan, 1988; McNab and Miller, 2010).

Sequences that offer a good alternative to EPI with comparable acquisition times commonly comprise a diffusion-preparation (DP) of the magnetization, followed by a fast acquisition that can be either spin-echo or gradient-echo based (Figure 29). In the spin-echo world, this translates into a preparation of the transverse magnetization prior to an FSE acquisition (Beaulieu et al., 1993; Norris et al., 1992). These sequences are far less sensitive to B_0 inhomogeneities than EPI. In the gradient-echo world, the longitudinal magnetization is diffusion weighted in the preparation module and then data is acquired using a fast spoiled gradient echo scheme. One such sequence is for instance diffusion-prepared TurboFLASH (Lee and Price, 1994; Thomas et al., 1998). Alternatively, SSFP acquisitions can also be used (Jeong et al., 2003; Lu et al., 2012). All of these methods have pros and cons and the choice among them is definitely application-dependent. They will therefore be discussed in more detail in Chapter 8, when the time will come to choose an appropriate sequence for ADC measurements in the *Aplysia* nervous system.

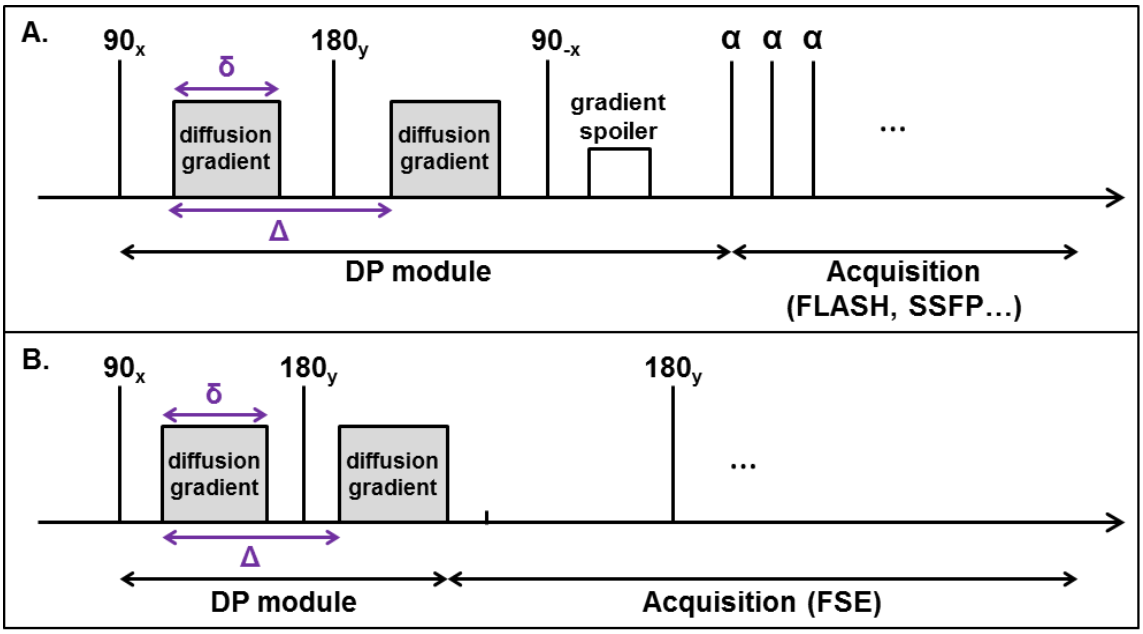

Figure 29. Schematic timelines of sequences that use a diffusion preparation of the longitudinal (A) or transverse (B) magnetization, prior to fast imaging schemes.

6.6 Chapter summary

In this chapter, we presented the physics behind DW-MRI, along with the most standard sequence, which is diffusion-weighted spin-echo. The difference between free diffusion in an unrestricted medium and diffusion in biological tissue was highlighted, and the dependencies of the "apparent diffusion coefficient" on the diffusion time imparted by the experiment, on the direction of diffusion sensitization and on the extent of diffusion weighting used were explained. Models of non-Gaussian diffusion were briefly presented. Stroke is one of the most successful applications of diffusion MRI, and the stakes of understanding how cell swelling leads to an ADC decrease in tissue are high. This question will be at the heart of our diffusion experiments on the *Aplysia*. Lastly, the challenges of diffusion MRI in terms of hardware (strong gradients to achieve high diffusion weighting) and sequence design (to speed up the acquisition time) were briefly described.

This introduction dealt with the development and applications of the technique for MR imaging, and not yet MR microscopy. In the following chapter, we will describe the theory and implementation of the DESIRE sequence, which uses a different mechanism to generate diffusion contrast and is particularly suited for microscopy.

7 Exploring 2D DESIRE for MR microscopy

In conventional diffusion weighted sequences, molecular self-diffusion leads to a loss of signal in the presence of gradients. A high diffusion coefficient translates into hypointensity and low SNR. Moreover, with Fourier encoding techniques, diffusion also limits the spatial resolution in MRM because diffusion distances within the acquisition time of a k-space line should be inferior to the voxel size (Callaghan and Eccles, 1988). On the contrary, DESIRE (Diffusion Enhancement of SIgnal and REsolution), first proposed by Lauterbur and co-workers (Lauterbur et al., 1992), is a technique by which images display strong signal enhancement in regions with a high diffusion coefficient. The technique relies on the measurement of the overall amount of spins affected by a highly localized saturation (a "hole") applied for a prolonged time (corresponding to the imparted diffusion time). The higher the diffusion coefficient at the saturation location is, the faster the spin renewal inside the area and the larger the number of spins effectively saturated. The DESIRE signal mirrors this amount of saturated spins and is therefore higher with higher diffusion. The voxel size and location in a DESIRE image are those of the initial saturation "hole".

This chapter will explain the principles behind the DESIRE method in detail, along with previous theoretical and experimental achievements. In this work, the first implementation of two-dimensional (2D) DESIRE was developed and tested on water and silicone oil phantoms, with a prospective application to single cell imaging with an unprecedented diffusion contrast.

The methods and results pertaining to this study were published as: Jelescu IO, Boulant N, Le Bihan D, Ciobanu L. *Experimental demonstration of diffusion signal enhancement in 2D DESIRE images*. Journal of magnetic resonance 2012;218:44-48.

7.1 The idea behind DESIRE

Starting from equilibrium, if the magnetization in a given region is selectively flipped to 90° and dephased before applying an overall 90° excitation to the whole

sample and acquiring signal, that specific region will not contribute to signal: this type of pre-excitation is therefore referred to as "saturation".

For DESIRE, the idea is to apply a highly localized saturation, repeated for a prolonged time, prior to a non-selective 90° excitation and acquisition of overall sample signal (with no imaging gradients). In its 1D, 2D and 3D declinations, the saturated area is a very thin plane, a very narrow cylinder or a very small sphere, respectively. As the saturation pulse is repeated N times for a total duration T, the diffusion process will cause spins to move in and out of the area of saturation: the number of spins affected by the saturation will therefore increase with diffusion for a given T, as illustrated in Figure 30.

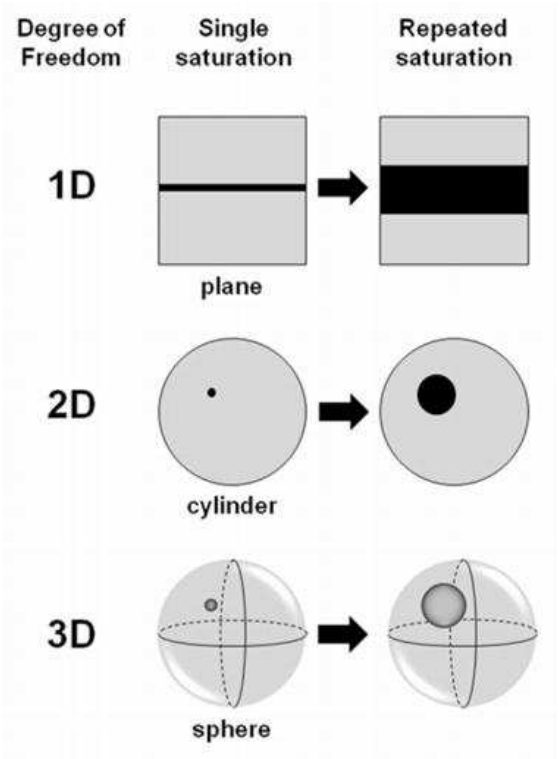

Figure 30. Growing saturation with diffusion. The saturation is a plane of thickness $2a$ in 1D, a cylinder of radius a in 2D, or a sphere of radius a in 3D. Due to diffusion, spins move in and out of the saturation region in the imparted time, increasing the effectively saturated volume.

The enhancement obtained experimentally with DESIRE is defined as:

$$E(\vec{r}) = \frac{S_0 - S(\vec{r})}{S_0} \times \frac{V}{\varepsilon} - 1 \tag{7.1}$$

with S_0 the overall signal from the volume of interest without saturation, $S(\mathbf{r})$ the overall signal after saturation at location $\mathbf{r}$, V the volume of interest (imaging volume) and ε the direct saturation volume (Pennington, 2003). In the absence of diffusion, $E(\mathbf{r}) = 0$. The enhancement is thus weighted by the diffusion coefficient at

the saturation location in a positive way: the higher the diffusion, the higher the signal difference (S_0-S(**r**)) and the higher the enhancement. This is opposite from the standard diffusion-weighted sequences where higher diffusion translates into lower signal.

The theoretical enhancement can be explicitly derived in the case of homogeneous unrestricted diffusion, as presented in (Pennington, 2003). Neglecting relaxation effects, the Bloch-Torrey equation gives the following relationship for the longitudinal magnetization:

$$\frac{\partial M_z(\vec{r},t)}{\partial t} = D\nabla^2 M_z(\vec{r},t) \tag{7.2}$$

This equation can be rewritten using adimensional variables, with length expressed in units of a and time in units of a^2/D:

$$\left(\nabla^2 - \frac{\partial}{\partial t}\right) M_z(\vec{r},t) = 0 \tag{7.3}$$

The initial conditions (t = 0) are:

- thermal equilibrium: $M_z = 1$ for all $r > a$,
- boundary condition: $M_z = 0$ at $r = a$.

In the 1D case, the analytical solution is $M_z(r,t) = \Phi\left[(r-1)/2\sqrt{t}\right]$, where Φ is the error function. The 2D and 3D cases can be solved numerically. From the solution $M_z(r,t)$, the theoretical enhancement E(t) can be computed using:

$$E(t) = \frac{1}{\varepsilon}\int_{r>a}\left(1 - \frac{M_z(r,t)}{M_0}\right)dV \tag{7.4}$$

where dV is the appropriate volume element (dr in 1D, $2\pi r dr$ in 2D and $4\pi r^2 dr$ in 3D).

This theoretical evaluation of DESIRE for MR microscopy predicts enhancements of one to two orders of magnitude with gradient strengths of 1 – 10 T/m (Pennington, 2003). Figure 31 reproduces theoretical enhancement curves. It is apparent that the enhancement is all the more pronounced with smaller saturation size a and longer time imparted for diffusion $\Delta T_{diffusion}$. The gain in signal is also all the more marked with increasing number of diffusion sensitization dimensions.

The quantification of the diffusion coefficient is not the primary objective of DESIRE, which mainly aims to achieve improved SNR and spatial resolution for MR microscopy compared to standard acquisition schemes. Nonetheless, the quantitative estimation of the diffusion coefficient D from known enhancement level E, saturation radius α and diffusion time $\Delta T_{diffusion}$ is possible using theoretical enhancement curves as "look-up graphs". In the case of samples with a heterogeneous proton density distribution, the proton density map should be accounted for in the initial conditions associated with Equation (7.3) prior to the calculation of theoretical enhancements curves.

Practical considerations on implementation and acquisition

The previous theoretical evaluation assumed an ideal saturation profile of characteristic size *a*, which could be maintained for duration $\Delta T_{diffusion}$. In practice, what are the limitations on minimum size, maximum duration and profile shape of the saturation?

The dimension (i.e. 1D, 2D or 3D) and size *a* of the saturation are typically limited by time and gradient capabilities. The duration of the pulse producing the saturation is limited by T_2 for relaxation processes to be negligible. In Chapter 1, we saw that selective excitation requires that a given k-space region be covered while the RF pulse is applied. The extent of k-space that can be covered in the duration imparted for the pulse is of course limited by gradient amplitude, slew rate and duty

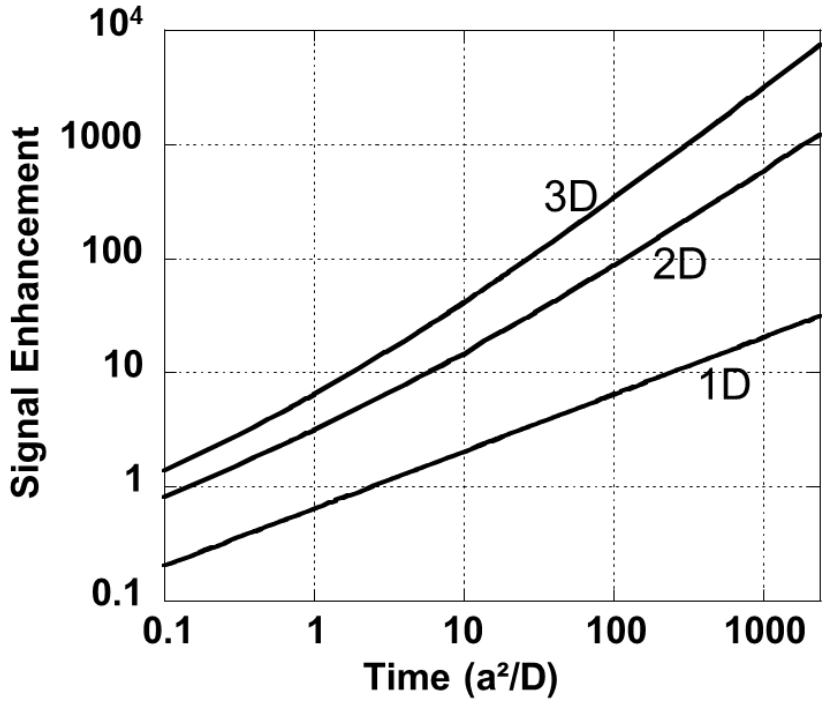

Figure 31. Calculated signal fractional enhancement vs. diffusion time T (in units of a^2/D, with *a* saturation radius and D diffusion coefficient), for 1D, 2D and 3D. ***From (Pennington, 2003).***

cycle. The combination of these effects eventually poses limits on the achievable saturation shape and size.

The total saturation time $\Delta T_{diffusion}$ (i.e. the duration for which the saturation pulse is repeatedly played) in turn is limited by T_1, to prevent saturated spins from restoring a longitudinal component.

DESIRE is inherently a "point-by-point" acquisition technique. The location of the saturation is the location of the pixel being imaged and the extent of the saturation gives the spatial resolution. For example, to construct an 8x8 2D enhancement map (or DESIRE image), the saturation needs to be moved at the 64 pixel locations, with signal $S(\mathbf{r})$ (Equation (7.1)) being acquired for each. S_0 need only be acquired once. Figure 32 illustrates the steps involved in the acquisition of a 2D DESIRE image.

DESIRE is thereby associated with long acquisition times, similarly to Fourier acquisitions with phase-encoding along all directions. The acquisition time is further

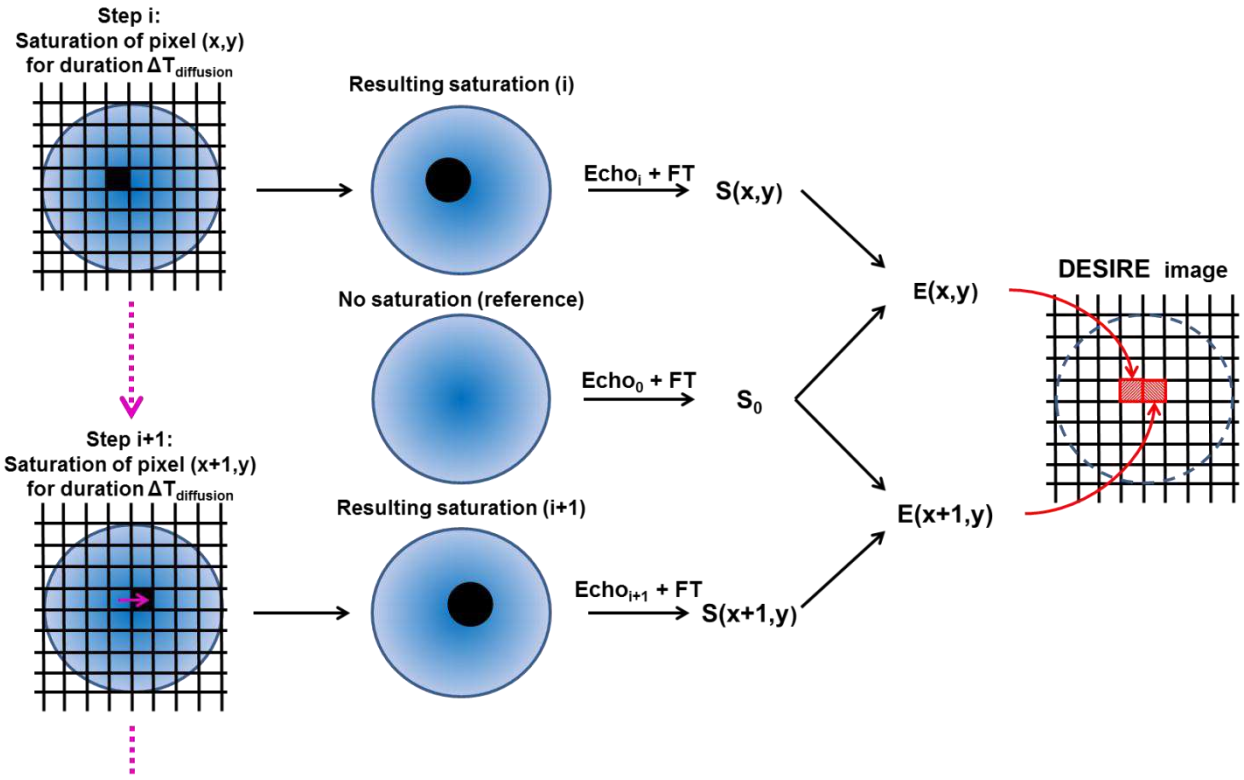

Figure 32. Schematic of the step-by-step acquisition of a 2D DESIRE image. Signal (either FID or echo) is collected from the entire imaged volume. The reference signal S_0 is acquired once. For each pixel (x,y) in the image, the signal is acquired following a saturation at location (x,y). The intended saturation size is the image spatial resolution. Enhancement E(x,y) is calculated from the signal difference (S_0 – S(x,y)) and is an indirect measurement of the diffusion coefficient at (x,y).

hampered by a long repetition time (> 5 T_1) to achieve full longitudinal recovery between the imaging of successive locations. Additionally, in slow real-space imaging, the voxel values in the image are directly affected by artifactual signal fluctuations (Weiger et al., 2008b). On the up side, the signal levels S_0 and $S(\mathbf{r})$ are high, because similarly to a 3D Fourier acquisition, they arise from the entire imaging volume. The signal difference $S_0 - S(\vec{r})$ can however be small, depending on the diffusion coefficient and the saturation size.

The true resolution of DESIRE images is not easy to assess experimentally. In practice, saturation profiles display imperfections that translate into a degraded full width at half maximum compared to the theoretical 2α. Moreover, in the absence of diffusion, the saturation profile obtained after N repetitions of the pulse (for duration $\Delta T_{diffusion}$) is altered compared to the single pulse case due to direct saturation effects. Indeed, in regions partially affected by the pulse (with an effective flip angle < 90°, e.g. side lobes in the sinc profile produced by a square pulse), the application of successive pulses will result in saturation build up unrelated to a spin renewal by diffusion. Luckily, this effect is greatly reduced in the presence of diffusion, but is nonetheless manifest. Figure 33 illustrates this phenomenon through simulation results for 1D saturation pulses, from (Weiger et al., 2008b). It appears clearly that the quality of the saturation profile via the choice of pulse shape is determining to achieve the sought spatial resolution and correctly interpret the enhancement levels measured.

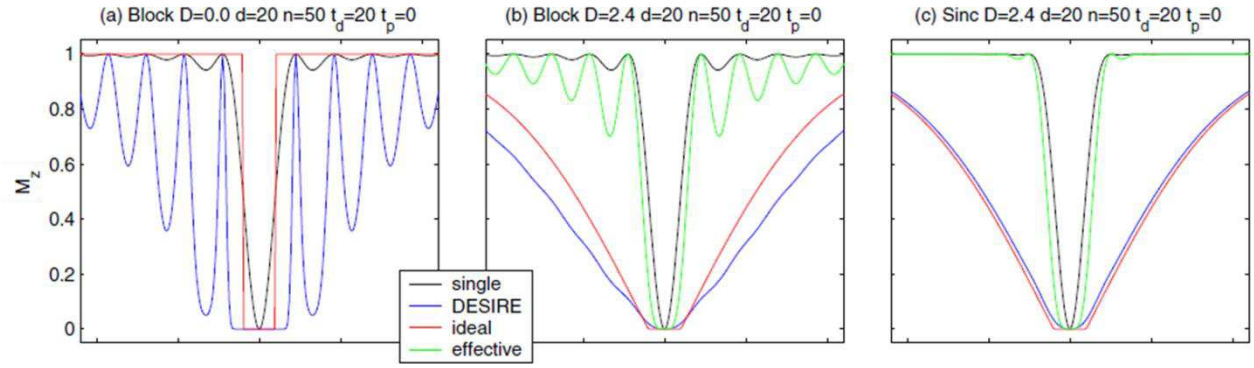

Figure 33. Simulated 1D magnetization profiles, for 20 µm aimed saturation size and 50 pulse repetitions with 20 ms inter-pulse delay. (a) Square pulse shape and no diffusion: the profile difference between the single pulse and the DESIRE pulse train (50 repetitions) is obvious on the sinc sidelobes. (b) With diffusion, the impact of direct saturation on effective resolution is attenuated but not eliminated. (c) The choice of a pulse shape will less intrinsic imperfections (sinc vs square) dramatically improves the agreement between ideal and effective profiles: direct saturation leads to an increase in the effective main lobe width only. *From (Weiger et al., 2008b).*

DESIRE has already been implemented in 1D (i.e. the saturation region is a thin infinite plane), achieving an enhancement of 8 on a plant stem, with a saturation thickness of 8 µm and gradient strength of 0.9 T/m (Ciobanu et al., 2004). Later an enhancement of 25 with a saturation thickness of 5 µm and gradient strength of 2.88 T/m was obtained on a water phantom (Weiger et al., 2008b). Similar methods for imaging diffusion along one direction, referred to as "hole burning", have also been reported (Sigmund and Halperin, 2003).

On small biological objects such as single cells, the use of the DESIRE sequence could be beneficial for achieving high resolution with heavy diffusion weighting while boosting the SNR. Given cell geometry, the implementation of DESIRE in at least two spatial dimensions was a pre-requisite. DESIRE images could thus provide 2D projections of the cell, weighted by diffusion. In this thesis work, the sequence was first implemented and tested on homogeneous phantoms.

7.2 Implementing 2D DESIRE – Methods

Materials

The RF transceiver was the 700 µm ID solenoid coil built for single cell imaging. Its design – including the immersion in FC-40 for improved B_0 homogeneity and the separation of the ground plane into thin strips to avoid eddy current circulation – proved to be critical to produce well localized saturation holes.

The phantoms were cylindrical glass capillaries (500 µm ID) filled with either distilled water ($D_{water} \approx 2.4 \times 10^{-3}$ mm²/s; $T_{1,water} \approx 3.0$ s) or silicone oils (Sigma Aldrich) ($D_{thin\ oil} \approx 1.5 \times 10^{-4}$ mm²/s; $T_{1,thin\ oil} \approx 1.7$ s and $D_{thick\ oil} \approx 2.1 \times 10^{-6}$ mm²/s; $T_{1,thick\ oil} \approx 1.4$ s). All measurements were performed at room temperature (19°C). The diffusion coefficients and T_1 relaxation times of the three media were measured separately on 3 cm diameter test tubes using a Bruker volume coil and standard methods: diffusion-weighted spin-echo (TE = 18 ms / TR = 3 s / resolution: 1.25x1.25x3 mm³ / TA = 16 min / 10 b-values ranging from 10 to 2000 s/mm² for water, from 10 to 4000 s/mm² for thin oil and from 20 to 9000 s/mm² for thick oil) and multi-TR RARE (TE = 7 ms / resolution: 1.25x1.25x3 mm³ / TA = 12 min / 15 TR values ranging from 20 to 15000 ms). The two silicone oils were chosen because their diffusion coefficients are very distinct from each other and from water, and because – unlike most other oils – they have a single resonance peak, which is crucial to avoid frequency shift artifacts at ultra-high field. The three chosen media thus

spanned a large range of diffusion coefficient values. Values for biological tissues (~ 0.2 – 1.0 x10^{-3} mm²/s) are expected to fall between that of pure water and thin silicone oil.

Design of the saturation pulse ("DESIRE pulse")

The DESIRE pulse had to meet several criteria: it had to produce a sharp cylindrical saturation, with a diameter ("hole" size) as small as possible. Relaxation effects should be negligible over the duration of the pulse, meaning it should not exceed T_2 ~ 40 ms.

Spiral-shaped k-space trajectories were generated using the code written by B. Hargreaves[5]. Field-of-view and hole size fixed the discretization step and extent of the spiral, respectively. The duration of this k-space trajectory at maximum gradient amplitude (1 T/m) and slew rate (9000 T/(m.s)) also set the minimum pulse duration. For example, a trajectory corresponding to a FOV of 1.2x1.2 mm² and 50 µm minimum hole size (i.e. $k_{max} = 1/(2 \cdot 50) = 0.01\,\mu m^{-1}$) lasted 10.19 ms. Square pulses were eventually chosen for our experiments because of their robustness. Other possibilities described below were however considered beforehand.

Custom-shaped RF pulses

Custom-shaped RF pulses were designed by using the small flip angle approximation (Boulant and Hoult, 2012; Pauly et al., 1989) and the additive flip angle method (Grissom et al., 2008).

The duration of the k-space trajectory t_{pulse} determined previously and the RF dwell time (Δt = 5 µs on our system) determined a time vector of N_t elements ($N_t = t_{pulse}/\Delta t$). The RF pulse was then characterized by $B_1(t)$, $1 \leq t \leq N_t$.

The FOV and hole size h determined a grid of N_s samples ($N_s = (FOV/h)^2$). The desired flip angle (FA) pattern was $FA^{des}(\mathbf{x}_s)$, $1 \leq s \leq N_s$. We started with a small target flip angle: $FA^{des30} = 30°$ for a single $\mathbf{x}_s$ position and 0 elsewhere.

In Chapter 1, we already introduced the expression for the transverse magnetization in the small flip angle approximation:

[5] http://www-mrsrl.stanford.edu/~brian/mritools.html

$$M_{xy}(\vec{r}) = i\gamma M_0 \int_0^T B_1(t) e^{i\vec{r}\cdot\vec{k}(t)} dt \tag{7.5}$$

Using the temporal and spatial discretization steps Δt and h, and approximating $\sin(FA) \approx FA$ (with FA in radians), the expression becomes:

$$FA(\vec{x}_s)\exp(i\varphi(M_{xy}(\vec{x}_s)) \approx i\gamma\Delta t \sum_{t=1}^{N_t} B_1(t) e^{i\vec{x}_s\cdot\vec{k}_t} \tag{7.6}$$

where $\varphi(M_{xy}(\mathbf{x}_s))$ is the phase of the transverse magnetization and $\mathbf{k}_t$ is the k-space trajectory obtained through reverse integration of the gradient waveforms. This expression assumes homogeneous B_0 and B_1 fields. Potential inhomogeneities can be accounted for by introducing spatially varying phase accumulation and RF sensitivity factors.

A first estimate of $B_1(t)$ was produced by a least squares minimization algorithm between $FA(\mathbf{x}_s)$ in Equation (7.6) and $FA^{des30}(\mathbf{x}_s)$. The amplitude of this first solution for a localized 30° flip angle was scaled (i.e. multiplied by 3) to produce a 90° flip angle: $B_1^0(t)$.

The actual flip angle pattern $FA^0(\mathbf{x}_s)$ produced by $B_1^0(t)$ over the FOV was simulated using the Bloch equations and naturally did not exactly match the ideal $FA^{des90}(\mathbf{x}_s)$. The error was quantified in terms of transverse magnetization pattern, between the sought one ($M^{des90}(\mathbf{x}_s) = 1$ at the hole location and 0 elsewhere) and the current one – $\sin(FA^0(\mathbf{x}_s))$:

$$RMSE = \sqrt{\frac{1}{N_s} \cdot \sum_{s=1}^{N_s} |M^{des90}(\vec{x}_s) - \sin(FA^0(\vec{x}_s))|^2} \tag{7.7}$$

The difference between $FA^0(\mathbf{x}_s)$ and $FA^{des90}(\mathbf{x}_s)$ fell within the small flip angle domain: $\widetilde{FA}(\vec{x}_s) = |FA^0(\vec{x}_s) - FA^{des90}(\vec{x}_s)| \leq 30°, 1 \leq s \leq N_s$. This difference could then be injected as a new target flip angle pattern into the least squares minimization algorithm and a new solution $B_1^1(t)$ produced.

The actual flip angle pattern $FA^1(\mathbf{x}_s)$ produced by $B_1^0(t) + B_1^1(t)$ over the FOV was again simulated using the Bloch equations and the RMSE calculated using Equation (7.7). The process was repeated until the RMSE was small enough (typically 1%).

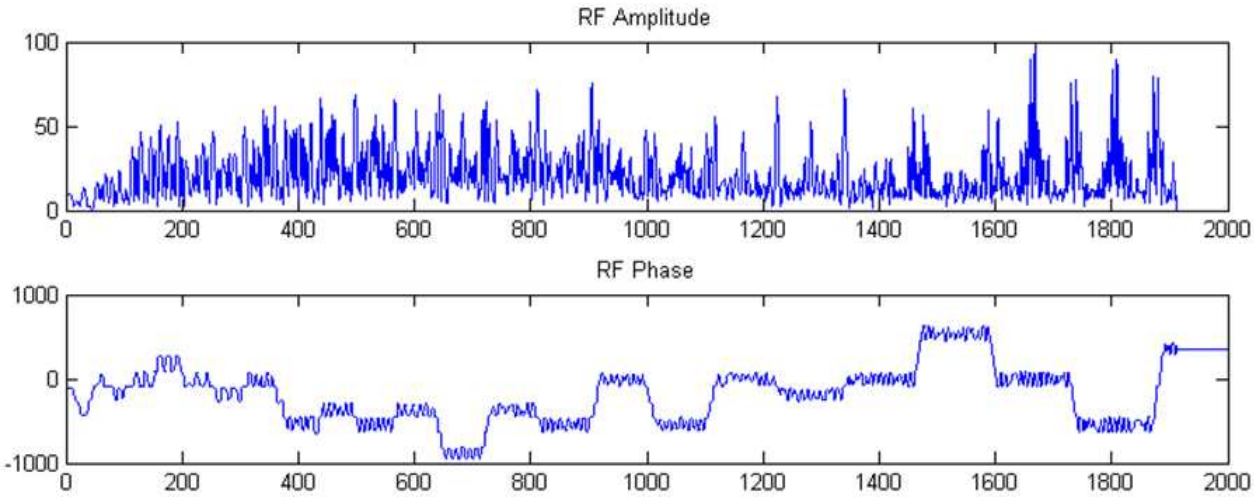

Figure 34. Custom RF pulse (top: amplitude (%); bottom: phase (°); Timestep: 5 µs) calculated for a 60 µm saturation hole, applied during a spiral trajectory in k-space.

A small number of iterations (~10) were found to be sufficient for our purposes. B_0 and B_1 corrections maps were also incorporated in the calculation. As successfully demonstrated in (Ciobanu et al., 2010), the excitation patterns arising from these RF pulses are not strongly affected by point-spread function effects. However, the demanding RF waveforms likely enhance the sensitivity to varying experimental conditions (mainly related to B_0 variations in space and time: position of the imaging volume with respect to magnet isocenter, shim, magnet fluctuations…), which compromises the reproducibility of the resulting saturation pattern. Figure 34 and Figure 35 show examples of a custom RF pulse for the saturation of a 60 µm hole and the resulting saturations on two different days…

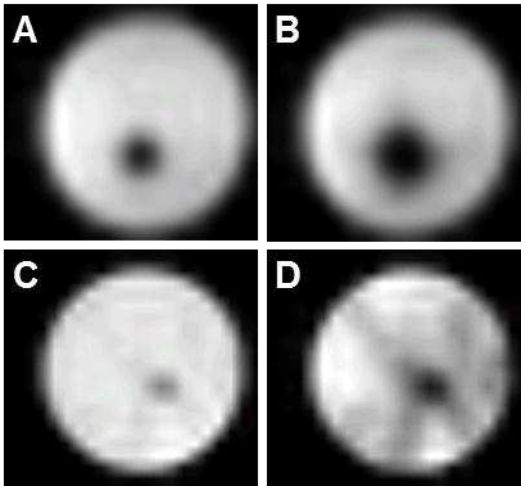

Figure 35. Saturation patterns in a water phantom, produced by the pulse shown in Figure 34 on two different days. Top row: day "X". Saturations after 1 (A) and 8 (B) pulse repetitions: the saturated region grows with diffusion and some direct saturation. Bottom row: day "Y". Saturations after 1 (C) and 8 (D) pulse repetitions: the saturation pattern is neither sharp nor clean, although the same pulse was used for all experiments.

Sinc and square pulses

Sinc-shaped pulses were also considered for the sharpness of the resulting saturation shape but their duration would have been too long, making them impractical for these applications.

As announced, square pulses were eventually used. Their main drawback is that the Fourier transform gives approximate sinc-function spatial profiles. Using square pulses, our gradient system enabled us to produce saturation holes down to 40 µm. However, the smaller the hole is, the shorter the separation between successive sinc oscillation rings around the aimed main lobe. With 40 µm, these rings were well within our sample. Holes of 60-micron diameter were eventually chosen as the best compromise between small size and saturation pattern accuracy.

The aimed saturation was therefore a 60 µm diameter infinite cylinder, and the FOV was 1.2x1.2 mm². The corresponding k-space trajectory lasted 10.19 ms using maximum gradient amplitude and slew rate. This was then also the duration of the DESIRE single pulse. The location of the hole was determined by using the Fourier shift theorem: an RF phase modulation by $e^{-i(k_x(t)x_0+k_y(t)y_0)}$ displaced the hole from the origin by x_0 and y_0 in the two orthogonal directions. Figure 36 shows RF waveform, gradient waveforms and resulting k-space trajectory for this DESIRE pulse.

Each pulse was followed by the application of gradient spoilers (2 ms at 400 mT/m in all 3 directions) to spoil remaining transverse magnetization. Radio-frequency

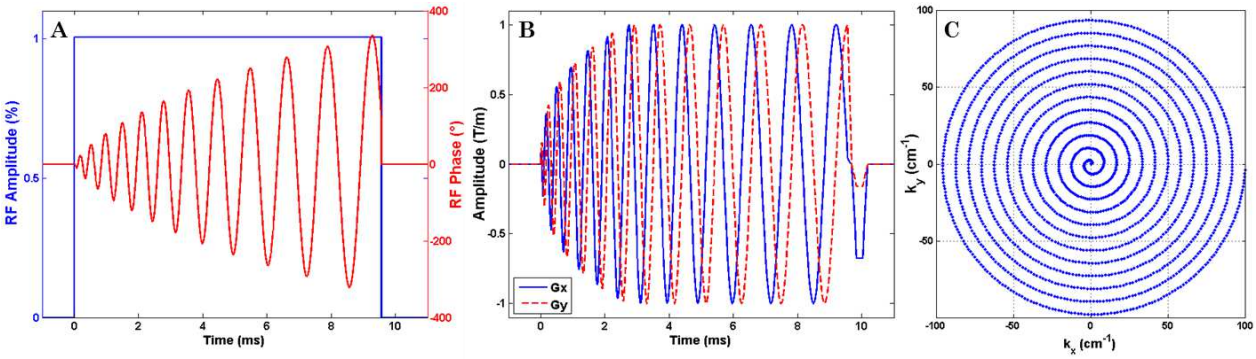

Figure 36. RF pulse amplitude and phase (A), gradient waveforms (B) and resulting k-space trajectory (C) played during the DESIRE saturation module. The phase of the RF pulse determines the location of the hole. Gradients are used to their maximum amplitude (1 T/m) to keep the pulse as short as possible. The coverage achieved in k-space determines the hole size (via k_{max}) and the FOV (via Δk in the radial direction). For an effective full width at half maximum (FWHM) of 60 µm of the main lobe, k_{max} was pushed to 100 cm^{-1} instead of 83 cm^{-1}. The overall duration of the module is 10.19 ms, including the time for gradient refocusing lobes.

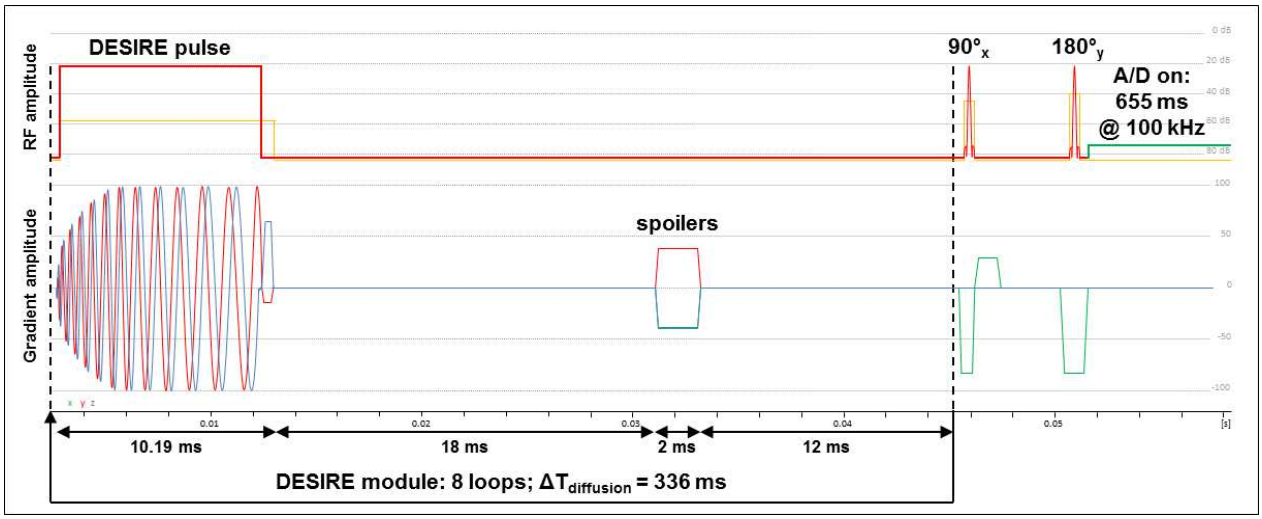

Figure 37. Timeline of DESIRE image acquisition. The sequence is repeated for each pixel in the image (i.e. each hole position), with TR = 15 s to allow for T_1 recovery. The reference signal S_0 is acquired after the same 336 ms block in which all the gradients are played, but not the RF. The physical axes for the gradients are as follows: x: slice selection; y and z: DESIRE selective excitation. Gradient amplitude in % of maximum (1 T/m) and RF amplitude in dB (0 dB ≡ 23.7 W).

spoiling was also employed, by giving the n^{th} pulse an additional phase $\varphi_n = n \cdot (n-1) \cdot 117/2$ (Zur et al., 1991). Given duty cycle limitations, we were able to repeat the DESIRE pulse block 8 times for a total saturation time (and hence diffusion time) $\Delta T_{diffusion}$ = 336 ms < T_1 (see Figure 37). This diffusion time translated into typical root mean square distances of 28 µm (0.47 voxel), 7.1 µm (0.12 voxel) and 0.8 µm (0.01 voxel) in the water, thin oil and thick oil samples, respectively.

Experiments

The selected image volume was a 250 µm-thick axial slice in the phantom, in which the saturation appeared as a 60 µm "hole". The resulting localized saturations were first imaged with a standard spin-echo sequence to ensure their compliance with theoretical position and size (TE = 10.4 ms/ TR = 5 s/ in-plane resolution: 20x20 µm²/ matrix: 60x60/ TA = 5 min). In order to produce DESIRE images – or enhancement maps – of the slice, the saturation "hole" was displaced over a 12 x 12 grid (720 x 720 µm²) in the cross-sectional plane of the phantoms (as illustrated previously in Figure 32). We acquired the echo from the slice for each hole position, as well as a reference echo without saturation (TE = 26 ms/ TR = 15 s/ BW = 100 kHz/ Acq size: 65536 points/ 144 + 1 scans). The signal level S was defined as the area under the peak of the FT.

Because we used square pulses, the first node, or "sinc-ring", was visible around the main hole on the spin-echo images of the resulting saturation. To account for this effect in the calculation of the directly saturated volume ε (see Equation (7.1)), we estimated an "equivalent" hole size using the thick oil phantom. Following the same procedure as for the acquisition of the DESIRE images, we displaced the saturation over a 12 x 12 grid and measured for each position the signal level S(x,y) following a single DESIRE loop (42 ms), as well as the reference signal S_0 without saturation. Given the very low diffusion coefficient of this oil, the signal enhancement over the duration of the pulse was considered to be zero. For each position, we calculated an equivalent hole size diameter *a(x,y)* using the formula:

$$a(x,y) = R\sqrt{\frac{S_0 - S(x,y)}{S_0}} \tag{7.8}$$

where R is the phantom diameter. The final equivalent hole size a was taken to be the average hole size measured in the central part of the phantom (4 x 4 pixels). The enhancement E was eventually calculated using $\varepsilon = \pi a^2/4$ and the formula in Equation (7.1).

The "enhancement-to-noise ratio" in the DESIRE images was estimated by calculating the ratio between the mean enhancement value in the central part of the object and the standard deviation of enhancement values outside the object.

The enhancement levels obtained experimentally were compared to numerical simulations using the 2D model presented earlier (Pennington, 2003). Input values for the simulations were the diffusion coefficients D of the considered media and the diameter a of the saturation cylinder. Equation (7.3) was solved using the partial differential equation solver in Matlab, and theoretical enhancement E was finally computed using Equation (7.4). Compared with notations used by Pennington, α in our case refers to hole diameter rather than radius. Proton density maps were not necessary for the theoretical computation given that the samples of interest were homogeneous phantoms.

7.3 Results

Based on the "hole" images obtained, the DESIRE pulse and gradient waveforms calculated proved to be satisfactory in terms of saturation localization and shape. Figure 38 shows the saturation produced by a single DESIRE loop (42 ms) in thick

oil. The FWHM of the main saturation region was 60 µm, consistent with theoretical saturation size. The first ring of the sinc saturation pattern was visible. The equivalent hole size map accounting for the saturation ring is shown in Figure 39. The average equivalent hole size was found to be a = 140 µm, much larger than the intended size, due to imperfections in the saturation pattern produced by the square pulse. The directly saturated volume used in the enhancement map calculation and simulation was therefore taken to be $\varepsilon = \pi * 70^2$ µm².

Figure 40 shows DESIRE images obtained in water and thin silicone oil. As expected, the higher the diffusion coefficient in the sample, the greater the enhancement obtained with DESIRE. The enhancement levels obtained in water are $E_{w,tot}$ = 1.01 overall and $E_{w,ctr}$ = 1.38 in the center (16 pixels, delimited by the red square in Figure 40). The variability, measured across the central 4 x 4 ROI as standard deviation / mean enhancement value, was found to be 17%. This value was fully consistent with the estimated enhancement-to-noise ratio of 6.6, corresponding to a variability of 15%. The additional 2% variability measured in the central ROI is attributable to B_0 and B_1 inhomogeneities. In oil the enhancements were $E_{o,tot}$ = 0.21 and $E_{o,ctr}$ = 0.56, respectively. The variability across the equivalent ROI was 37%, also consistent with an estimated enhancement-to-noise ratio of 3.0. The DESIRE image of oil was more impacted by noise because of the lower diffusion coefficient and therefore smaller signal differences (S_0-S(x,y)).

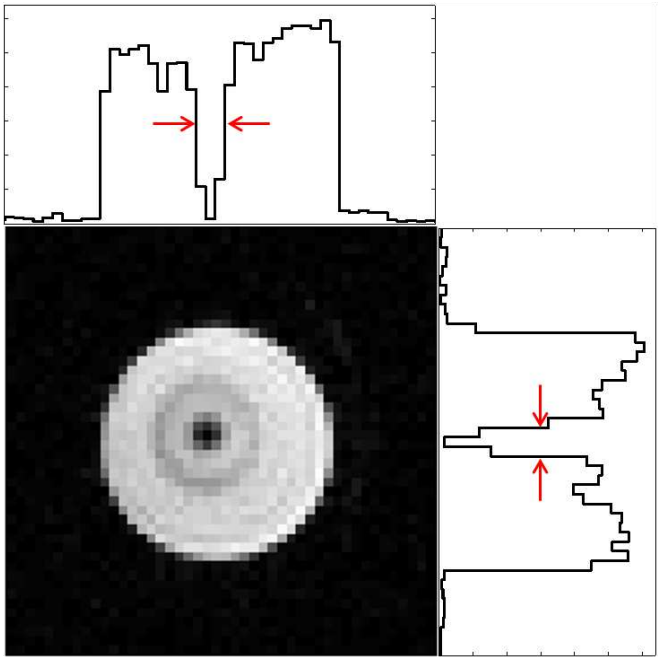

Figure 38. Spin-echo image of the saturation resulting from one DESIRE pulse application, in a thick oil phantom. In-plane resolution: 20x20 µm²; slice thickness: 250 µm. Top and right-hand side plots exhibit the image intensity profiles through the center of the hole, in each direction. The FWHM of the central saturation region (indicated by the arrows) is equivalent to 3 voxels, i.e. 60 µm, which is fully consistent with the desired hole size. The overall saturation pattern however shows imperfections related to the use of a square RF pulse, with a visible sinc-ring.

The theoretical enhancement as a function of total diffusion time $\Delta T_{diffusion}$ is plotted in Figure 41. For $\Delta T_{diffusion}$ = 336 ms, the simulated enhancements are $E_{w,sim}$ =1.08 and $E_{o,sim}$ = 0.24, which is approximately consistent with our measurements.

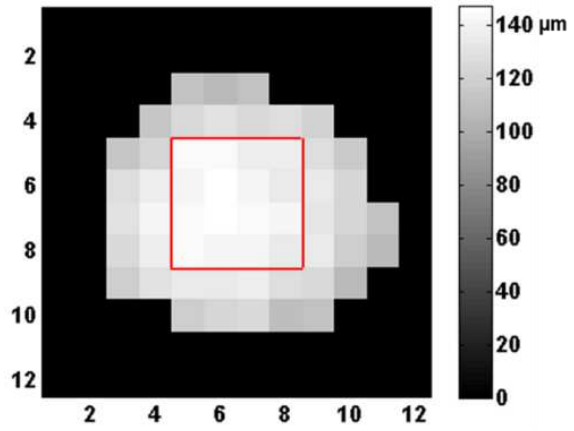

Figure 39. Map of equivalent hole sizes across the phantom, estimated as explained in Equation (7.8). The average hole size over the entire object slice (masked in the figure) is 128 µm, while the average size within the central region (delimited by the red square) is 141 µm.

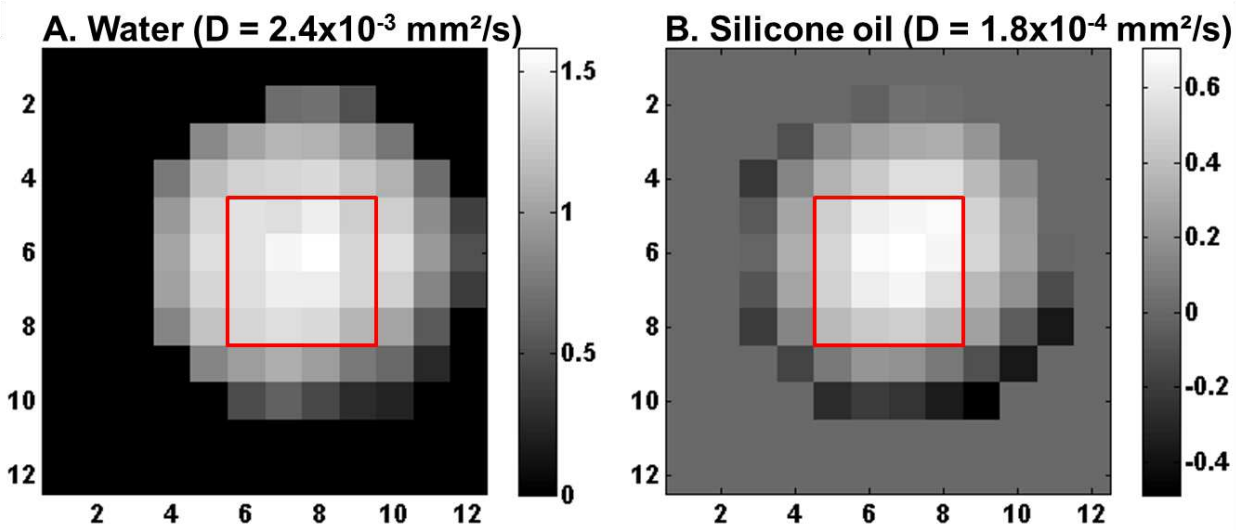

Figure 40. DESIRE images of (A) water and (B) thin silicone oil phantoms. The displacement of the saturation hole between two adjacent voxels is 60 µm. The grayscales are in units of enhancement. (A) The average enhancement over the entire slice (masked) is $E_{w,tot}$ = 1.01 and within the central region (delimited by the red square) $E_{w,ctr}$ = 1.38. (B) Likewise the average enhancement over the entire slice is $E_{o,tot}$ = 0.21 and within the central region $E_{o,ctr}$ = 0.56.

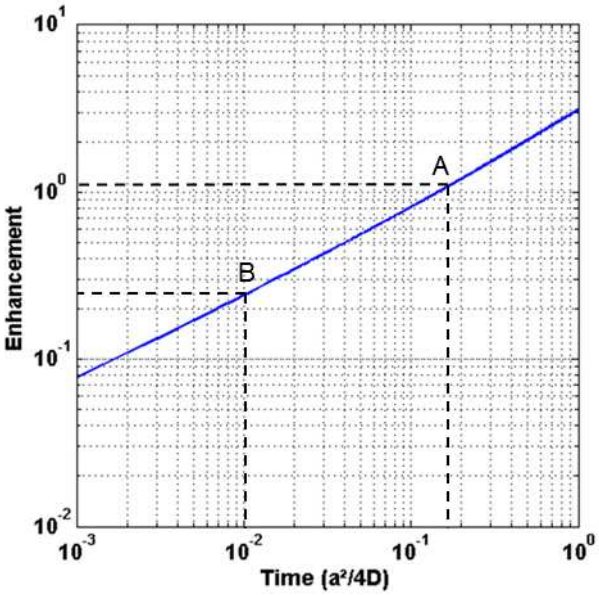

Figure 41. Simulated signal enhancement E vs. diffusion time $\Delta T_{diffusion}$ in units of $a^2/4D$, for two-dimensional DESIRE (a is the hole diameter rather than radius). Given $\Delta T_{diffusion}$ = 336 ms and a = 140 µm, the diffusion time in units of $a^2/4D$ is $\Delta T_{w,diffusion}$ = 0.165 for water (point A on the graph) and $\Delta T_{o,diffusion}$ = 0.0103 for oil (point B on the graph). Theoretical enhancements corresponding to our experimental parameters are therefore $E_{w,sim}$ = 1.08 and $E_{o,sim}$ = 0.24.

7.4 Discussion and conclusion

The DESIRE technique successfully produced 2D diffusion-weighted images in which stronger diffusion translated into larger signal.

The difference between experimental and simulated enhancement values in water and thin silicone oil has multiple explanations. First of all, the experimental enhancement in the center of the phantoms, where diffusion is unrestricted, was 28% higher than predictions in water, and 130% in oil. This enhancement overestimation was very likely the result of the imperfect saturation pattern produced by square pulses, leading to additional direct saturation which could not be fully suppressed through spoiling nor entirely accounted for by the use of an equivalent hole size. The spoiling could not be further increased because of duty cycle limitations. In oil, the effect of direct saturation was higher because diffusion is lower. Moreover, the contribution of noise was larger in the oil enhancement map, precisely because the diffusion and the enhancement are lower.

The average enhancement over the whole slice (rather than over the central ROI) on the other hand was slightly below the simulated enhancement (by 6% for water and 13% for thin oil). The lower enhancement on the edges compared to the center can be explained by two factors. On the one hand, the grid along which the hole was displaced could not perfectly match with the edges of the phantom: the directly saturated volume near the edges was likely smaller than the equivalent $\varepsilon = \pi * 70^2$ µm² calculated in the center. On the other hand, the simulation assumed

unrestricted diffusion, while diffusion is markedly restricted near the phantom walls. This effect is expected to play a larger role for the water phantom, where the mean diffusion distance was 28 µm over the duration of the DESIRE module, which represents half of the FWHM of the central saturation lobe. Our DESIRE images indeed displayed the expected decrease in enhancement from the center to the phantom walls, because of increasingly restricted diffusion. This phenomenon had been previously demonstrated experimentally in the 1D case, where the presence of an impermeable barrier produced a gradual decrease in enhancement starting from a distance to the barrier comparable to the diffusion distance covered during the DESIRE module (Weiger et al., 2008b).

Overall, the enhancement observed in our phantom experiments remained very limited, although non-zero even in a slowly diffusing medium such as silicone oil (diffusion coefficient ratio 1:16 compared to water). This resulted in very low enhancement-to-noise ratio in the DESIRE images. Averaging experiments would reduce the variability but would also further hamper the total acquisition time (already 36 minutes for a 12x12 grid and single slice). A more efficient way of proceeding would be to boost the enhancement via a prolonged diffusion time or smaller saturation hole. The gradient duty cycle prevented us from considering diffusion times longer than 336 ms. (Ciobanu et al., 2004) and (Weiger et al., 2008b) had set up DESIRE modules with diffusion times of 900 ms and up to 10 s respectively for their 1D experiments. However, while such long diffusion times are beneficial for proof of concept experiments on phantoms, parameters must be chosen carefully for imaging biological tissues. Indeed, because biological membranes are permeable, the mean water diffusion distance within the time imparted by the DESIRE module should not exceed the size of structures that are aimed to be differentiated (e.g. cell or nucleus diameter), otherwise diffusion contrast between these structures will be lost. In terms of saturation size, 60 µm holes are definitely larger than the size usually quoted for obtaining substantial enhancement with DESIRE (< 20 µm in 2D according to (Pennington, 2003)). The imperfect profile produced by the square pulses even precludes us from claiming an effective 60 µm resolution in our DESIRE images. The “effective” hole size was indeed estimated at 140 µm, which is very poor. RF pulse shapes that produce a saturation profile with fewer imperfections than square pulses should therefore be favored. Custom-shaped pulses are promising provided that the calculation of the waveforms is extended to take into account experimental variability. Stronger gradients, and/or a parallel transmission system in order to keep the pulse duration reasonably short, are also required to achieve smaller saturation holes.

Working at ultra-high field (17.2 T) has the double benefit of increasing SNR and providing longer T_1s for longer potential saturation times. The next validation step of 2D DESIRE would be to image a barrier or some form of structure inside a homogeneous phantom, in order to test the effective spatial resolution and demonstrate zero enhancement in a non-diffusing medium. However, attempts to image such small phantoms containing glass barriers or optic fiber rods at 17.2 T were fruitless due to enhanced magnetic susceptibility artifacts. The optimal combination for imaging barriers or structures with DESIRE should likely be a lower magnetic field system equipped with very strong field gradients (> 1 T/m).

Magnetic susceptibility mismatches are certainly less dramatic in biological samples such as single cells, for which DESIRE has the potential to generate a unique contrast of microscopic structures. The diffusion enhancement is expected to vary spatially with the diffusivity within the tissue according to the local microstructure (e.g. hindrance by membranes or fibers, tortuosity in narrow spaces or macromolecular crowding). It is likely that diffusing spins will instantaneously take on the native voxel diffusion properties, because they are imposed by the medium. For other parameters, such as relaxation rates, the time for equilibrium to be reached may depend on the type of diffusers and on the compartmentalization. The influence of this effect on the contrast in the DESIRE images remains to be investigated. However, the long diffusion times and distances required for high enhancement pose a true limitation to the generation of DESIRE contrast between subcellular structures for instance.

An additional limiting factor in generating DESIRE images in biological samples is that of magnetization transfer (MT). Briefly, protons in macromolecules have a different precession frequency from “free” protons in water. Their T_2 is also much shorter so these protons are typically not “seen” in an MR experiment. However, there is exchange of longitudinal magnetization (i.e. MT) between free and bound protons. In DESIRE, the frequency components of the spatially selective saturation pulse can affect bound protons at a different (unwanted) location, which can in turn transfer their magnetization to free protons at that same location. One possible strategy to tackle MT effects is to use an RF concatenation scheme (Golay et al., 1999), provided the B_0 field inhomogeneity is not important. In this scheme the 90° RF saturation pulses are replaced by pairs of two consecutive 45° pulses, while the reference sequence now contains the same RF pair with the second 45° pulse shifted by 180° in phase (effectively 45°/-45°). For free protons, the latter reference sequence produces a net zero flip angle. For bound protons however, the effect is the same for both the saturation and reference sequences. The amount of MT generated is then

the same in both signals and is eliminated by the subtraction, rendering the DESIRE enhancement map MT free.

In conclusion, enhancement maps in two homogeneous media were produced for the first time using a 2D DESIRE acquisition. The experimental results were approximately consistent with theoretical predictions and, in spite of limiting experimental conditions, the technique did demonstrate signal enhancement through diffusion. Higher enhancement levels could certainly be attained using more localized saturation, which requires stronger gradients, and/or a parallel transmission system. Custom-shaped RF pulses are promising provided that the calculation of the waveforms is extended to take into account experimental imperfections. While the imaging of structured phantoms appears as the next natural step for 2D DESIRE, these results suggest that it should be performed at lower field strength, where magnetic susceptibility differences at interfaces (e.g. oil/glass/oil) are less dramatic and therefore produce less distortion. Eventually, DESIRE could produce images of biological microscopic structures such as *Aplysia* neurons with a unique contrast. However, in order to achieve sufficient enhancement within a relatively limited overall diffusion time (< 100 ms), the size of the saturation should be reduced and its sharpness improved before cell experiments can be attempted with DESIRE.

7.5 Chapter summary

We have described the theory behind DESIRE, a "point-by-point" acquisition technique characterized by the measurement of saturation growth with diffusion. In this work, we have implemented 2D DESIRE (i.e. the growth takes place in two dimensions during prolonged saturation of a small cylinder) and tested it on water and silicone oil phantoms. The square pulse shape was chosen for its robustness but it comes with unwanted saturation of additional rings around the main lobe, bringing up the effective hole size from 60 μm to 140 μm and compromising spatial localization. Nonetheless, on homogeneous phantoms the experimental enhancement was consistent with theoretical predictions. Higher enhancement and spatial resolution could be achieved via stronger gradients and/or parallel transmission, as well as an improved pulse design. For imaging structured phantoms, a lower field than 17.2 T is recommended for reduced susceptibility differences at interfaces. For imaging small biological samples, an MT-free pulse scheme should be used and the total diffusion time reduced.

Little benefit is expected from using 2D DESIRE in its current form on *Aplysia* neurons to obtain diffusion contrast. Indeed, the resolution and enhancement level are likely insufficient to properly segment cells and cellular sub-structures and estimate any diffusion changes induced by cell swelling. For this reason, in the following chapter we explored a more standard approach to obtain diffusion information with MR microscopy.

8 Development of 3D DP-FISP for MR microscopy

This chapter serves as a methodological preparation for the study of diffusion changes at cellular and tissue levels induced by cell swelling. Indeed, MR microscopy is still in need of a sequence that allows rapid diffusion measurements with high spatial resolution. We will present a panel of possible sequences and motivate our choice for a DP-FISP (Diffusion Prepared Fast Imaging with Steady-state free Precession). The sequence design and its validation on phantoms will then be presented. Lastly, the sequence performance for ADC measurements in an isolated *Aplysia* neuron will be assessed.

The study presented in this chapter was published in the proceedings of the Annual Meeting of the International Society for Magnetic Resonance in Medicine 2013 as: Jelescu IO, Le Bihan D, Ciobanu L. *3D DP-FISP for diffusion measurements in MR microscopy at ultra-high field*.

8.1 Sequences for rapid diffusion measurements

Diffusion measurements in single cells reported so far consisted in 2D single slice acquisitions using a modified spin-echo sequence (Hsu et al., 1995), with typical slice thickness of 100 – 150 μm and 15 – 25 μm in-plane resolution. These images of *Aplysia californica* neurons were acquired in 13 minutes per b-value (Hsu et al., 1996, 1997; Schoeniger et al., 1994). One study reported ADC measurements on *Xenopus* oocytes using a standard 3D spin-echo sequence at 60 μm isotropic resolution in 35 minutes per b-value (Sehy et al., 2001). Given the cells' spherical geometry, 3D acquisitions with isotropic resolution are to be favored for segmentation purposes and for the possibility to measure potential cell and nucleus volume changes concomitantly with ADC changes. Nonetheless, the total scan time should be maintained as short as possible, since the lifetime of isolated cells or samples of excised biological tissue is generally a few hours in total.

As explained in Chapter 6, the acquisition time of diffusion sequences has also been a central issue for *in vivo* clinical and pre-clinical diffusion studies. Some of the accelerated quantitative techniques developed in that setting are therefore worth considering for microscopy.

The most widespread technique for clinical applications remains EPI, in spite of notorious artifacts related to off-resonance effects and eddy currents (Jezzard et al., 1998). With the ultra-high field and the strong fast-switching gradients required for microscopy, susceptibility leaps, frequency shifts and eddy currents are all enhanced, leading to severe artifacts with EPI read-outs. Subtle mechanical vibration from gradients also becomes an issue when the aimed resolution is a few tens of microns. Fast diffusion-prepared sequences could in that perspective offer a good alternative to EPI with comparable acquisition times.

Diffusion preparation of the longitudinal magnetization

The two main issues associated with a longitudinal preparation of the magnetization are the potential eddy currents generated by the diffusion gradients in the preparation, and the T_1 contamination of the diffusion-weighted magnetization via T_1 recovery between the end of the preparation and the start of the acquisition. Eddy currents are system (gradient and receiver coil) dependent, and their importance should be tested on each experimental setup before deciding on the need to correct for them. Modified preparation schemes have been proposed to counteract the effect of eddy currents. One solution is to introduce phase cycling on the second 90° pulse of the preparation in the fashion 90_{-x} / 90_{-y} (Thomas et al., 1998). The modified preparation scheme (90_x – 180_y – 90_{-y}) will tip up the magnetization component that was not properly rephased because of eddy currents. The recombination of the two image intensities in the form $I = \sqrt{(I_{90\_x})^2 + (I_{90\_y})^2}$ is free from eddy current artifacts. However, this results in a doubled acquisition time. Another solution explored consists in increasing the time between the diffusion preparation and the start of the image acquisition but the downside of this solution is the increased sensitivity to T_1 recovery (Sinha and Sinha, 1996). Multiple solutions have also been envisaged against the loss of diffusion weighting through T_1 regrowth of the stored magnetization. One efficient way is to keep the time between the end of the preparation and the acquisition of the central k-space line to a minimum. Centrically ordered encoding is therefore a simple means of eliminating most of the T_1 contamination. This solution however is in contradiction with eddy current reduction requirements.

Once the magnetization has been diffusion weighted and stored along the longitudinal axis, several rapid acquisition schemes can be considered. Balanced SSFP acquisitions have been successfully used previously on 1.5 T systems (Jeong et al., 2003) but off-resonance banding artifacts become a larger issue at ultra-high field (Nayak et al., 2007). A FISP-FID acquisition with diffusion preparation was

recently implemented at 7 T for single slice pre-clinical *in vivo* imaging, and produced artifact-free images as well as accurate and rapid ADC estimates (Lu et al., 2012).

Another possible candidate is TurboFLASH. The advantage is that for DP TurboFLASH, the T_1 contamination can theoretically be completely eliminated by acquiring two images with a phase cycling scheme on the second 90° pulse: 90_x / 90_{-x} as well as on the FLASH flip angle α/-α (Coremans et al., 1997). Their subtraction eliminates the diffusion independent contribution of T_1 recovery, but once again doubles the acquisition time. A post-processing method also investigated in the latter study is to fit the data to $S = A \cdot e^{-b \cdot ADC} + B$ rather than the standard $S = A \cdot e^{-b \cdot ADC}$ to account for the T_1 recovery term. Introducing additional fit parameters however usually compromises the precision of the fit. Another elegant approach proposed by (Sinha and Sinha, 1996) consists in introducing a crusher gradient that dephases the diffusion encoded magnetization prior to the tip up. A symmetrical rephasing gradient applied during the acquisition only rephases the diffusion labeled spins, while removing the contribution from those which have recovered in the meantime. The downside of this solution is the somewhat prolonged TE and overall acquisition time. Although TurboFLASH has shown good potential for diffusion measurements, with straightforward correction techniques for T_1 relaxation contamination described above, this method has intrinsically lower SNR than unspoiled sequences.

Diffusion preparation of the transverse magnetization

As already mentioned, fast spin-echo acquisitions are much less sensitive to B_0-related artifacts than EPI, thanks to the 180° refocusing pulses. They have already been combined with a DP module for initial microscopy studies (Beaulieu et al., 1993). Provided the central part of k-space is acquired in the earlier echoes, the varying diffusion weighting of successive echoes due to additional imaging gradients in the echo train does not seem to affect the accuracy of ADC estimation. However, FSE suffers from high sensitivity to phase changes and to imperfect refocusing. In particular, the ideal configuration between the phase of the magnetization and that of the refocusing pulses is no longer met when diffusion preparation is introduced. Corrections for this effect have been developed but they come with signal loss (Schick, 1997) or complicated reconstruction (Pipe et al., 2002). Moreover, spin-echo based sequences involve the preparation of the transverse magnetization. When performing MR microscopy at ultra-high field, it is in fact more appealing to take advantage of the prolonged T_1 relaxation times by storing the magnetization longitudinally.

For the purpose of this thesis work, we aimed to implement and test a 3D DP-FISP with suitable timings and resolution for MR microscopy at ultra-high field. The sequence was optimized and validated against a conventional spin-echo diffusion-weighted sequence (DW-SE) on phantoms with various diffusion coefficients and T_1 values. The impact of eddy currents and T_1 contamination was assessed. The following sections will present methods and results of the sequence validation step. Preliminary ADC measurements in isolated *Aplysia californica* neurons using this 3D DP-FISP are also presented here.

8.2 Sequence design

The diffusion preparation consisted in a driven equilibrium module previously described (Figure 29, page 99): non-selective ($90_x - 180_y - 90_{-x}$) with pulsed diffusion gradients placed in-between. Gradient duration δ and separation Δ were chosen to produce a diffusion time as short as possible, yet still achievable on the standard 3D DW-SE Bruker sequence used for the validation of the 3D DP-FISP. The effective diffusion time was therefore t_{diff} = 9.2 ms. Considering the diffusion coefficient of water at 20°C, $D \approx 2 \cdot 10^{-3}\ mm^2/s$, this gives a mean diffusion distance of 10 µm in a 3D space, which is much shorter than both the objects of interest (*Aplysia* neurons) and the sought spatial resolution (25 µm). Moreover, the ADC in the cells and ganglia is likely to be greatly reduced compared to free water, hence even shorter expected diffusion distances. The diffusion gradient amplitude was adjusted to produce the desired b-value.

From the perspective of T_1 contamination of the diffusion-weighted magnetization, the ultra-high field is beneficial through prolonged T_1 relaxation times. In an attempt to further limit this contamination, the delay between tip-up and acquisition start was minimized in every possible way. A strong gradient spoiler was applied prior to FISP acquisition to rapidly destroy any remaining transverse magnetization: 400 mT/m for 2 ms. Moreover, T_1 contamination was limited through the choice of centric encoding in the FISP acquisition and very short overall timing. The FISP preparation was reduced to the acquisition of four dummy scans. The magnetization had therefore not reached steady state when the actual acquisition was started but this did not compromise results, as will be shown later on. A flip angle of 20° was empirically chosen as a compromise between SNR and signal stability between successive excitations. The total delay between magnetization tip up and the acquisition of the center of k-space was eventually 23 ms, a lot shorter than typical T_1 values in nervous tissue. FISP TE and TR were minimized within

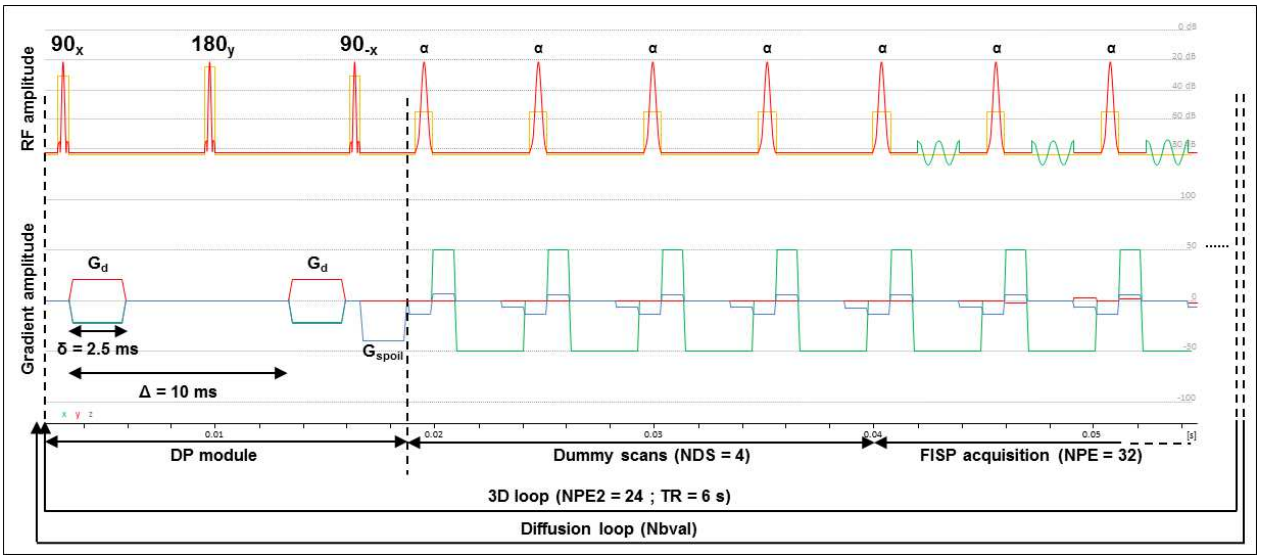

Figure 42. Timeline of the 3D DP-FISP sequence. Diffusion preparation: the diffusion gradients are on all three axes. FISP acquisition: The encoding is centric. Total time between magnetization storing and start of FISP acquisition is 23 ms. Total FISP acquisition time for one k-space plane is 166 ms. The physical axes for the gradients are as follows: x: ro; y: pe; z: slab selection and pe2. Gradient amplitude in % of maximum (1 T/m) and RF amplitude in dB (0 dB ≡ 23.7 W).

the limit of possible A/D sampling rates and gradient duty cycle. The acquisition time for one k-space plane was 166 ms.

The limiting feature of the total acquisition time in a 3D DP-FISP is the long TR between successive planes in k-space. This is required to obtain (almost) complete longitudinal relaxation before the next DP module, and at 17.2 T a global TR of 6 s was chosen.

Figure 42 shows a schematic of the sequence, with set timings.

Artifacts from eddy currents were not visible on the images. This aspect was nonetheless studied in further detail in the following section.

8.3 Phantom validation

Methods

The sequence was tested on phantoms, against a standard DW-SE sequence. Acquisitions were performed at 19°C using the smaller home-built microcoil (700 µm ID) as RF transceiver. The phantoms were 500 µm ID glass capillaries filled with three different solutions: ASW, a saline solution doped with $CuSO_4$, and dodecane (Sigma Aldrich). T_1 was measured in each of the phantoms with a multi-TR RARE

sequence: TE_{eff} = 22 ms / Resolution: 60x30x60 µm³ / 10 TR values ranging from 65 to 15,000 ms for ASW and from 65 to 7500 ms for the other two phantoms.

In a preliminary study, an ASW phantom was scanned using the following DP-FISP parameters: Δ = 10 ms / δ = 2.5 ms / 9 b-values = 10 – 200:200:1600 s/mm² / matrix: 190x32x24 / 25 µm isotropic resolution / flip angle = 20° / TE/TR = 2.6/5.2 ms / TR_{PE2} = 6 s / NA = 2 / TA = 4 min 48 s per b-value. The purpose of this initial scan was to determine the maximum b-value to which it was reasonable to go in terms of SNR and T_1 contamination.

For the subsequent study, the 3D DP-FISP imaging parameters were as follows: Δ = 10 ms / δ = 2.5 ms / 7 b-values = 10 – 100:100:600 s/mm² / matrix: 190x32x24 / 25 µm isotropic resolution / flip angle = 20° / TE/TR = 2.6/5.2 ms / TR_{PE2} = 6 s / NA = 4 / TA = 9 min 36 s per b-value.

The 3D DW-SE parameters were chosen to match those of the DP-FISP, only differing in the following: matrix = 128x32x24 / TE = 18.45 ms / TR = 3 s / NA = 1 / TA = 38 min 24 s per b-value.

The ADC was calculated in each experiment by fitting:

$$\ln S = -b \cdot ADC + constant \tag{8.1}$$

Diffusion prepared sequences produce no cross-terms between the diffusion gradients and the imaging gradients, so the contribution of each is additive for the calculation of the effective b-value. Accounting for the imaging gradients therefore has no impact on the ADC estimate since it does not change the slope of the experimental curve described by Equation (8.1). For simplicity, the effective b-values retained were only those corresponding to the diffusion gradients. For the DW-SE acquisitions, the effective b-values were calculated based on gradient waveforms and timings, using formulas from (Mattiello et al., 1994).

Four features were tested: the accuracy of the ADC estimate compared to DW-SE (taken as the gold standard), the homogeneity of ADC parametric maps across the phantom, the SNR of the images and the presence or absence of T_1 contamination.

Results

Figure 43 shows the signal attenuation curve in ASW. With two averages, the noise level was reached for b ~1400 s/mm². The $\ln(S) = f(b)$ plot reveals a non-linear trend starting from b ~ 1000 s/mm². There are two potential sources to this effect: T_1 contamination and/or a bias related to Rician noise distribution. If caused by T_1

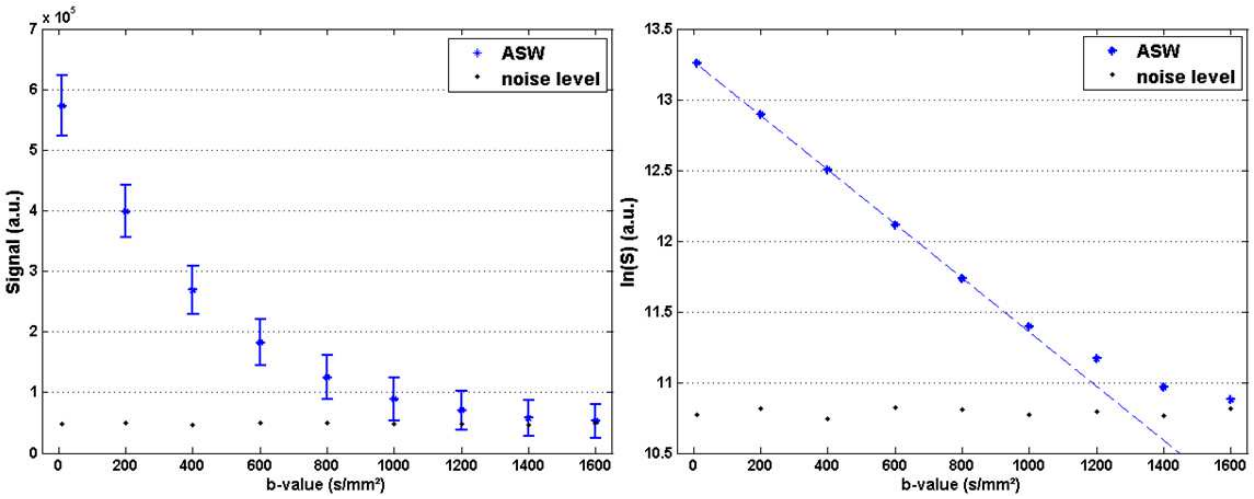

Figure 43. Diffusion signal attenuation curve in an ASW phantom (left: signal, right: ln(signal)). The errorbars represent standard deviation of signal in the homogeneous ROI. The signal reaches noise level for b ~ 1400 s/mm². The ln(S) curve deviates from a linear trend for b ~1000 s/mm².

regrowth, this bias could occur for lower b-values in biological tissue, which has a shorter T_1 than ASW. However, the diffusion coefficient in tissue is also lower, which could balance the effect. If caused by Rician noise distribution, this bias confirms that data should be corrected for this effect at SNR ≤ 3, which was the level reached in our experiment beyond b = 1000 s/mm². A conservative approach was chosen for all the following experiments: b_{max} = 600 s/mm². Higher values are not necessary for ADC estimation. In the *Aplysia*, the SNR is expected to be lower than in ASW due to shorter T_2: the number of averages was therefore increased from 2 to 4. The protocol was set to 7 b-values (10 – 600 s/mm²) and four averages, which added up to a reasonable 1h of acquisition for diffusion measurements.

Table 6 collects T_1 and ADC measurements in phantoms. Each estimate stems from a single fit on the signal averaged over an ROI in the phantom. The T_1 and ADC values of the phantoms are representative of cell survival medium (ASW) and biological samples at 17.2 T (Jelescu et al., 2013; Schoeniger et al., 1994). The 3D DP-FISP sequence was found to produce ADC estimates within 1% of the DW-SE measurements, for b-values up to 600 s/mm².

Figure 44 shows the experimental points and corresponding fits for the three phantoms, using DP-FISP. In this range of diffusion weighting and T_1 values, no curvature of the tail is visible: the data points are well aligned which means that the biases from Rician noise and T_1 are negligible.

Phantom	T_1 (ms)	DW-SE ADC (10^{-3} mm²/s)	DP-FISP ADC (10^{-3} mm²/s)	Error[b] (%)
ASW	2960 ± 21[a]	1.92 ± 0.01	1.91 ± 0.01	-0.5
NaCl, $CuSO_4$	1315 ± 10	2.01 ± 0.01	1.99 ± 0.03	-1.0
Dodecane	1455 ± 15	0.76 ± 0.01	0.76 ± 0.01	< 0.1

Table 6. T_1 values and ADC estimates (from DW-SE and DP-FISP) in each of the three phantoms. [a]The uncertainties represent the standard deviations on the fit parameters. [b]The error is that of the ADC estimate with DP-FISP, compared to DW-SE which is taken to be the gold standard.

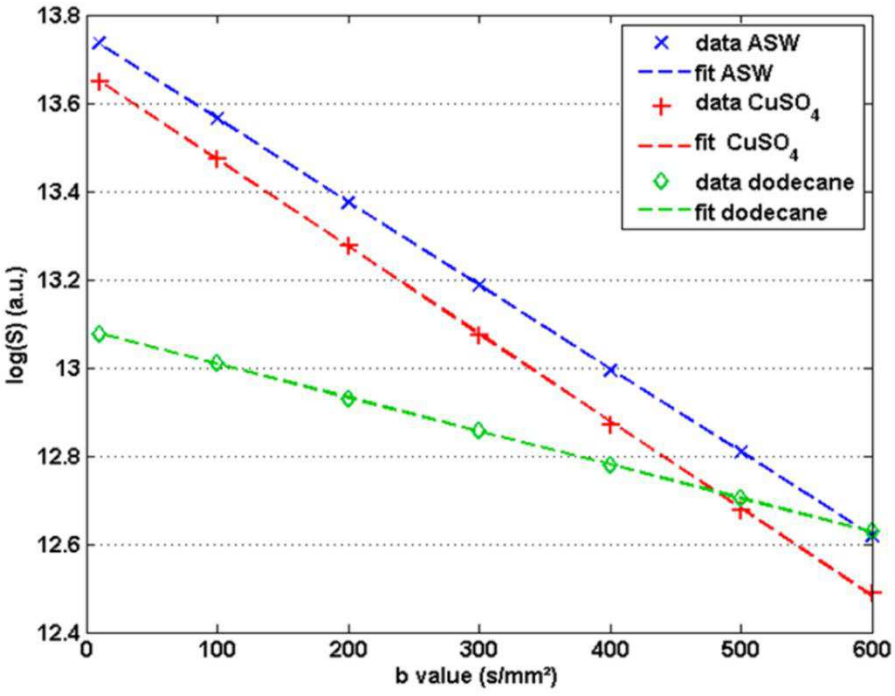

Figure 44. Experimental signal decrease with diffusion weighting, measured with 3D DP-FISP in the three phantoms, and corresponding linear fits. In the b-value range considered, neither of the three solutions (with $T_1 \approx 1.3 - 3$ s and $D \approx 0.8 - 2.2\ 10^{-3}$ mm²/s) suffers from T_1 contamination of the ADC estimate: ln(S) decreases linearly, as expected.

Table 7 provides SNR measurements for DW-SE and DP-FISP for the two extreme b-values (10 and 600 s/mm²). The SNR was estimated from the ratio of mean signal in a central ROI in the phantom over standard deviation in an ROI chosen outside the phantom. The acquisition time of the DW-SE being four times that of DP-FISP, an "equivalent SNR" in terms of acquisition time (SNR_{eq}) was also calculated for DW-SE.

Figure 45 shows a central slice of the ASW phantom and its corresponding ADC and quality of fit (R^2) parametric maps, acquired either with DP-FISP or DW-SE. This time, the fits for ADC extraction are performed on a voxel-by-voxel basis.

Although the DP-FISP image shows an artifact-free central region of 1.8 mm in length, both coil extremities display artifacts in the form of tilted dark bands (see Figure 45). The source of this artifact, visible on the b = 10 s/mm² image only, was briefly explored. The last 90_{-x} flip angle in the preparation was changed to a 90_{-y} in order to image the non-refocused component of the magnetization (Thomas et al., 1998). The resulting image is shown in Figure 46.

		ASW		NaCl, $CuSO_4$		Dodecane	
		SNR	SNR_{eq}[a]	SNR	SNR_{eq}	SNR	SNR_{eq}
b = 10 s/mm²	DW-SE	70	35	98	49	70	35
	DP-FISP	41	41	35	35	20	20
b = 600 s/mm²	DW-SE	21	11	21	11	42	21
	DP-FISP	12	12	11	11	14	14

Table 7. Image SNR with lowest and highest diffusion weighting, for each phantom and modality. [a]The equivalent SNR is calculated for equal acquisition times.

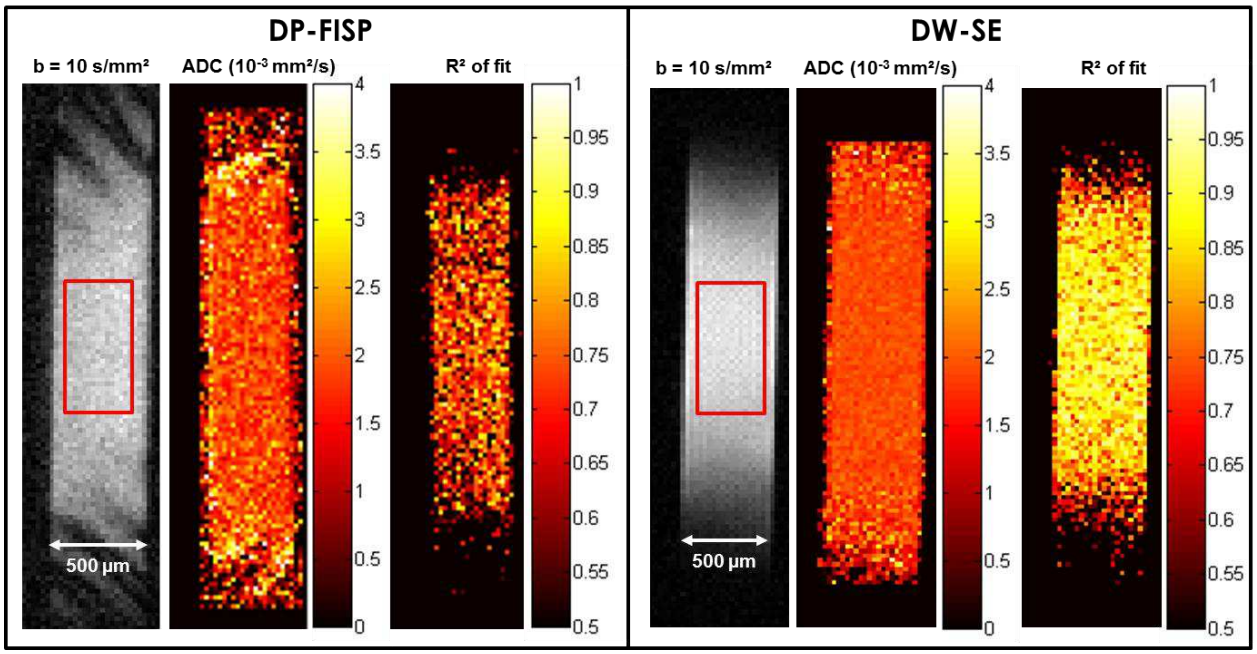

Figure 45. ASW phantom imaged with DP-FISP (left) and DW-SE (right), and parametric maps of ADC and quality of fit (R^2). The resolution is 25 µm isotropic. Statistics over the central square regions: DP-FISP: ADC = 1.9 ± 0.3 10^{-3} mm²/s ; R^2 = 0.7 ± 0.1. DW-SE: ADC = 1.9 ± 0.1 10^{-3} mm²/s ; R^2 = 0.87 ± 0.05.

Discussion and conclusion

The 3D DP-FISP implemented in this work provides rapid ADC measurements for microscopy (25 µm isotropic resolution in 10 min / b-value). Within the range of T_1 values tested here, which are those of interest for cellular imaging at ultra-high field, the DP-FISP sequence outputs ADC values which are within 1% of those obtained with DW-SE. The effect of T_1 recovery is not pronounced enough to disrupt the expected monoexponential behavior for b-values up to 600 s/mm². This conservative upper limit of b-values is nonetheless sufficient for ADC estimation.

The SNR per unit time is comparable to DW-SE and if required, the acquisition time can further be reduced by averaging less (currently NA = 4) or settling for a smaller number of b-values for the fit. However, when performing ADC measurements on living tissue, the acquisition of multiple b-values rather than just the basic minimum of two can be useful to confirm or infirm the stability of the tissue condition from the quality of the data points alignment. For this reason, the acquisition of 7 b-values was maintained for the experiments on *Aplysia*.

Voxel-by-voxel ADC extraction is possible, although the uncertainty is higher than with DW-SE due to noisier data. The signal is homogeneous over the volume of

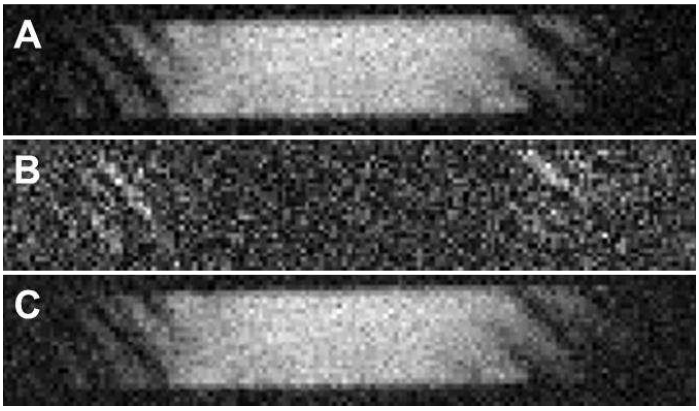

Figure 46. DP-FISP with b = 10 s/mm². A: Preparation pulses: $90_x - 180_y - 90_{-x}$. The magnetization stored is the in-phase component. B: Preparation pulses: $90_x - 180_y - 90_{-y}$. The magnetization stored is the out-of-phase component. The image in B is essentially noise, except for the edges of the coil where signal is the complementary of the banding artifacts in A. The cause is likely breakdown of B_1 homogeneity at the ends of the solenoid. C: Recombining the two images as $I = \sqrt{I^2_{-x} + I^2_{-y}}$ does not remove the artifact completely.

interest of the coil. The artifacts visible at coil ends are likely the result of imperfect refocusing far from the coil center, which is standard for solenoid coils. The "complementary" image of the non-refocused component supports this hypothesis. However, the combination of the two images in the form $I = \sqrt{\left(I_{90_{-x}}\right)^2 + \left(I_{90_{-y}}\right)^2}$ did not permit the elimination of the artifact entirely. Indeed, this correction technique is only effective on phase shifts that are constant from one acquisition to the next. Variable phase changes occurring during the acquisition cannot be corrected for (Thomas et al., 1998). It is unlikely that eddy currents are the source of this artifact for two reasons. First they would be less localized in the coil. Second the coil benefits from a design that greatly limits eddy current circulation in the ground plane, as explained in Chapter 3. These observations also validate *a posteriori* the choice of sequence timings: in spite of the short duration (23 ms) between the end of the preparation and the beginning of acquisition, the images are not corrupted by eddy currents. The short duration on the other hand greatly reduces the bias from T_1 relaxation, which was not detectable in our measurements and therefore required no correction.

Our 3D implementation comes with higher SNR than 2D methods and removes the constraints attached to slice selection (e.g. in (Lu et al., 2012), diffusion preparation slice thickness was three times that of the FISP imaging readout). However, the second phase-encoding direction does not benefit from acceleration, since it is necessary to wait for T_1 relaxation between successive PE2 steps, hence very long global TRs at ultra-high field.

In conclusion, diffusion-prepared FISP, a rapid diffusion MRI technique, has been successfully adapted for 3D imaging at very high isotropic spatial resolution (25 µm). The technique benefits from use at ultra-high field. The sequence produces ADC estimates that are in very good agreement with standard DW-SE in the range of biological diffusion coefficients and T_1 relaxation times. The sequence is much more time efficient than standard DW-SE and less prone to artifacts than EPI, which makes it an ideal candidate for single cell diffusion measurements within the timeframe of cell viability. Phantom studies showed it can be used with confidence in the low b-value range for ADC measurements.

8.4 Application to ADC measurements in neurons

Methods

One *Aplysia* was anesthetized by injection of an isotonic $MgCl_2$ solution. The abdominal ganglion was resected and placed in ASW. The ganglion was mechanically desheathed and neurons were isolated. Cell integrity was verified under the microscope. One cell (~250 µm diameter) was inserted into a glass capillary filled with ASW. It underwent the 3D DP-FISP imaging sequence described in the phantom section.

The cell's nucleus and cytoplasm were manually segmented based on signal intensity on the b = 10 s/mm² image. The data from three ROIs (entire cell, nucleus only, cytoplasm only) were fit to extract mean ADC values. A parametric ADC map was also calculated.

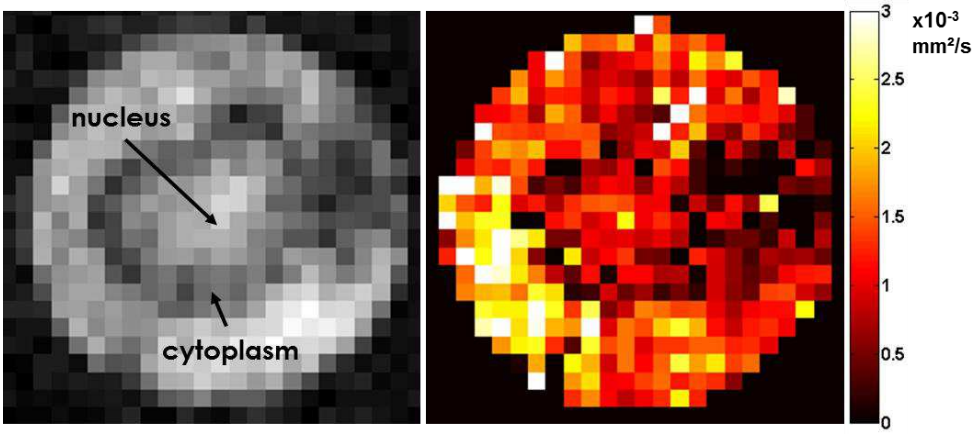

Figure 47. Left: Axial DP-FISP image of an *Aplysia* neuron with b = 10 s/mm². The capillary diameter is 500 µm. Right: associated ADC parametric map. Cytoplasm and nucleus are distinguishable in both images.

Results

Figure 47 shows one b = 10 s/mm² slice of the neuron, as well as the corresponding parametric ADC map. The signal attenuation curves in cytoplasm and nucleus are represented in Figure 48. Cytoplasm and nucleus are fully distinguishable on b = 10 and 100 s/mm² images and then gradually less, as signal in the nucleus decays faster than in the cytoplasm. Figure 49 shows linear fits of ln(S) in the entire cell, nucleus and cytoplasm. The data points are well aligned, with the exception of the first point (b = 10 s/mm²) which was discarded from the fit because the experimental setup had sagged and the images could not be registered satisfactorily. The mean ADCs measured in the cell, cytoplasm and nucleus are (0.68 ± 0.04), (0.57 ± 0.04) and (0.91 ± 0.05) $x10^{-3}$ mm²/s respectively. The nucleus represents 25% of the cell volume. These values are in good agreement with those reported by (Hsu et al., 1996): $0.7x10^{-3}$ and $1.0x10^{-3}$ mm²/s in the cytoplasm and nucleus, respectively. (Schoeniger et al., 1994) reported higher ADC measurements in the nucleus and lower in the cytoplasm ($1.6x10^{-3}$ and $0.23x10^{-3}$ mm²/s, respectively).

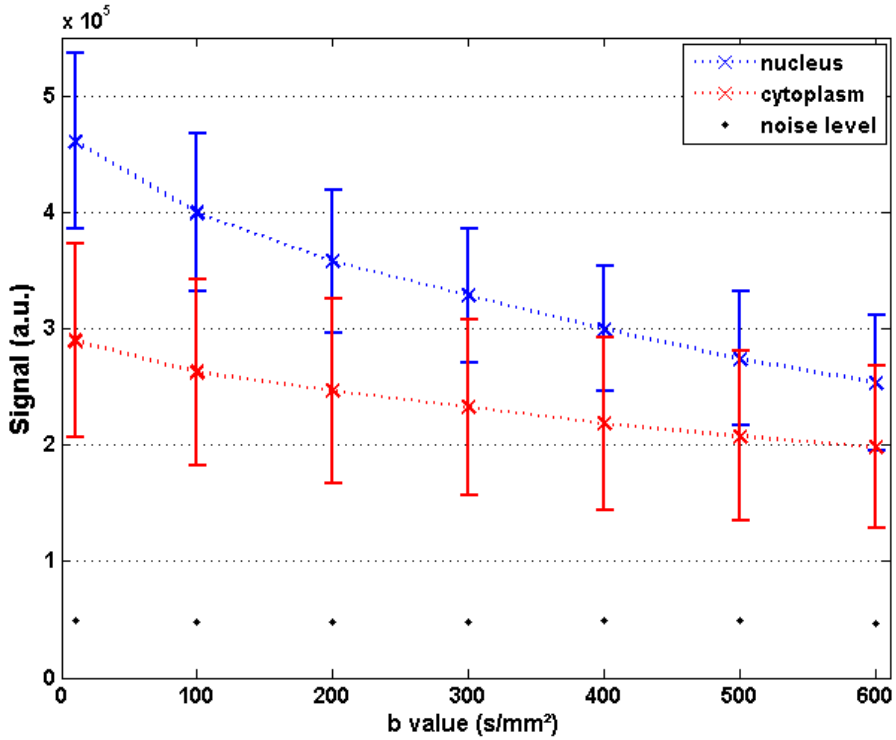

Figure 48. Signal decay in the nucleus and cytoplasm, as a function of b-value. The errorbars represent the standard deviation of signal in the ROIs. The cytoplasm and nucleus are very well distinguished based on signal intensity for b-values up to 100 s/mm². The signal in the nucleus decays faster than in the cytoplasm, but neither reaches the noise level in the b-value range explored.

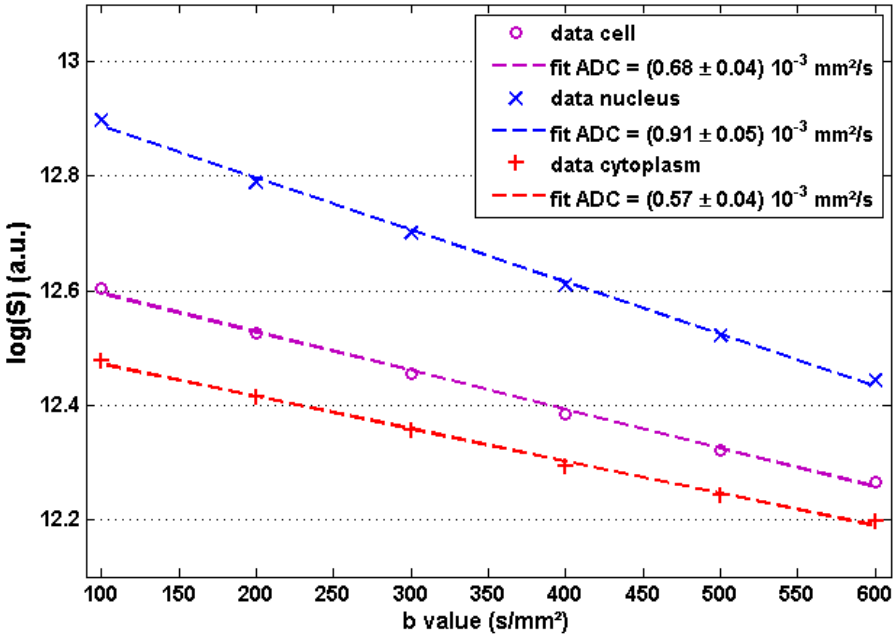

Figure 49. Linear fits of ln(S) over b-value. The slope of the fit is a measurement of the ADC. Mean ADC values in the entire cell, as well as separately in nucleus and cytoplasm can be extracted.

Discussion and conclusion

In terms of single cell diffusion measurements, the 3D DP-FISP sequence brings considerable improvement compared to techniques used previously, which only allowed single slice acquisitions at typical resolutions of 20x20x100 μm^3 within the same acquisition time (Hsu et al., 1996, 1997; Schoeniger et al., 1994). The ADC estimates in the *Aplysia* neuron shown here are consistent with values reported by Hsu *et al*. The source of discrepancy with Schoeniger *et al*. is not clear but in terms of cytoplasmic ADC, a low SNR due to the short T_2 in cytoplasm could lead to less reliable fits.

Although the decay in a cell is likely to be non Gaussian (Grant et al., 2001), the single exponential approximation should still be valid up to b = 600 s/mm². The deviation from a linear relationship was indeed not seen on this dataset.

Additional work is however necessary in order to render the sequence adequate for high b-values, for the purpose of studying non Gaussian behavior in single cells and ganglia.

First, with higher b-values, the effect of T_1 relaxation will likely become non-negligible. As explained earlier, this problem has been addressed in a previous study

that examined diffusion prepared TurboFLASH (Coremans et al., 1997), with the final recommendation being to introduce an additional constant term in the signal equation (e.g. $S = A \cdot \exp(-b \cdot ADC) + B$), which would take on T_1 relaxation effects. However, introducing a larger number of fit parameters is always detrimental for fit robustness. The subtraction method, which consists in tipping the magnetization up (90_{-x}) in one dataset and down (90_x) in another, would probably be worth testing on DP-FISP, in spite of the longer acquisition time associated with this method.

Second, although with a diffusion preparation scheme there are no cross-terms between the diffusion and the imaging gradients, the contribution of imaging gradients to the diffusion weighting should be added. As explained previously, we did not include this contribution in the current application because using $b_{eff} = b_{diff} + b_{imag}$ does not change the slope of the linear fit represented by $\ln(S) = -b \cdot ADC + \ln(S_0)$. However, this is no longer the case if the signal S is to be fit to a nonlinear function (biexponential for instance). We estimated that the contribution of the imaging gradients for the central line in k-space (the first to be acquired) amounted to $b_{imag} \approx 13$ s/mm². However, an accurate estimate of the contribution of the FISP imaging gradients is not straightforward since later echoes have more diffusion weighting than earlier echoes (McNab and Miller, 2010). The accurate estimation of b_{eff} in DP-FISP would therefore also require additional investigation before performing quantitative analyses at higher b-values.

Lastly, additional averaging would probably be necessary to obtain sufficient SNR at higher b-values. As a landmark, with four averages, the SNR at b = 600 s/mm² was 12 in ASW and 8 in the cell.

In conclusion, initial DP-FISP experiments on a large *Aplysia* neuron gave sensible results, with ADC estimates in the cell, cytoplasm and nucleus consistent with previously reported values. The 0 – 600 s/mm² b-value range was sufficient for ADC estimation. The use of the sequence in the high b-value range seems challenging in terms of correction for T_1 contamination and correct assessment of the effective b-value, but would be worth exploring.

8.5 Chapter summary

In this chapter, the various techniques for rapid diffusion measurement were presented and discussed in the light of microscopy needs and issues at ultra-high field. A 3D diffusion-prepared (DP) FISP, suitable for very high spatial resolution (25 μm) and very high magnetic field, was successfully implemented. The sequence performance was tested versus a standard DW-SE on three phantoms with diffusion coefficients and T_1 relaxation times characteristic of biological tissue. The sequence produced ADC estimates in very good agreement with DW-SE, with a much improved temporal efficiency. DP-FISP also proved to be less prone to artifacts than EPI, the only visible artifacts being contained to the solenoid ends and probably related to B_1 inhomogeneity. No eddy current or T_1 contamination was found. Phantom studies therefore showed DP-FISP can be used with confidence in the low b-value range for ADC measurements, making it an ideal candidate for single cell diffusion measurements within the timeframe of cell viability. Initial experiments on a large *Aplysia* neuron gave promising results. The use of the sequence in the high b-value range seems challenging but would be worth exploring.

In the next chapter, the 3D DP-FISP sequence will be used extensively for ADC measurements both in isolated cells and in the buccal ganglia of *Aplysia californica*.

9 Impact of cell swelling on the ADC at different scales

The previous chapter has shown the feasibility of robust ADC measurements in single cells at 25 µm isotropic resolution in about one hour. This methodology will be further used to study the changes in ADC at cellular level, associated with membrane depolarization or cell swelling (similar to the effects of ischemia). These changes will be studied for the first time at two spatial scales on the same animal model: at tissue level by performing ADC measurements in the buccal ganglia, and at soma level by measuring the ADC in single isolated cells. This chapter provides an introduction to the biology and chemistry of cellular response to ischemia and to other conditions associated with membrane depolarization. It also includes a review of the proposed theories that link the tissue ADC decrease to cell swelling. Our results on the *Aplysia* nervous tissue will then be presented and discussed in this light of this review.

The core of the study presented in this chapter has been submitted for publication as: Jelescu IO, Ciobanu L, Geffroy F and Le Bihan D. *Effects of hypotonic stress and ouabain on the apparent diffusion coefficient of water at cellular and tissue levels in the Aplysia.* – manuscript in revision.

Preliminary results were published in the proceedings of the Annual Meeting of the International Society for Magnetic Resonance in Medicine 2013 as: Jelescu IO, Ciobanu L, Geffroy F, Le Bihan D. *Effects of hypotonic stress and ouabain on apparent diffusion coefficient at cellular and tissue levels*.

9.1 Membrane depolarization and cell swelling

As explained earlier, the electrolyte balance between intra- and extracellular spaces is maintained by the ATP pumps and voltage-gated channels in the cellular membrane. There are several physiological and pathological conditions that lead to transient or long-lasting dissipation of the ion gradients across the membrane. For instance, the propagation of an action potential is equivalent to a wave of depolarization and rapid repolarization. In an ischemic event, severely reduced blood flow rates (below 10 mL/min/100g) rapidly lead to ATP depletion and failure of

the ion pumps. The breakdown of Na^+/K^+ pumps leads in turn to membrane depolarization, through lasting exit of K^+ and influx of Na^+ and Ca^{2+} (Heuser and Guggenberger, 1985; Hossmann et al., 1977).

Classically, membrane depolarization is associated with neuronal cell swelling, as a result of excessive Na^+, Ca^{2+} and Cl^- influx accompanied by water content. This water influx is partially associated with maintaining local isotonicity (Lipton, 1973), but more recent data show that water influx has multiple pathways and is quantitatively larger than what ion homeostasis would require (Jourdain et al., 2012; Tasaki and Byrne, 1990).

In direct relation with membrane depolarization, long-lasting cell swelling therefore occurs during ischemia. Proof has been provided that events occurring in the central nervous system during activity could also lead to transient alterations in cellular volumes, both neuronal and glial (Le Bihan, 2007; Lipton, 1973). In Chapter 6, we stressed that several conditions which cause cell swelling have been found to also lead to a decrease in the ADC measured with diffusion MRI, and that there is likely a correlation between the two phenomena. However, the exact mechanism linking them remains to be established. The following section will provide an overview of existing theories. Performing diffusion MR measurements both at cellular and tissue levels could allow us to unveil the precise mechanism that relates cell swelling to overall ADC decrease in tissue. For this purpose, *Aplysia* ganglia and isolated neurons will be exposed to hypotonic solutions or ouabain.

Hypotonic solutions are known to produce cell swelling through ionic equilibration of the cell with the extracellular medium. Although by far not representative of the whole mechanism of cellular stress caused by ischemia, hypotonic media are a simple and robust means of inducing cell swelling, and probing the impact of cell swelling alone on the ADC variation.

Ouabain is a powerful inhibitor of the K^+/Na^+-ATPase and therefore leads to the failure of K^+/Na^+ pumps in the cell membrane, which is similar to the pump breakdown that occurs in ischemia due to ATP depletion. Compared to hypotonic stress, ouabain mimics ischemia-related cellular stress in a closer manner since it causes membrane depolarization and also induces excitotoxicity as a second step (Veldhuis et al., 2003). Indeed, following the initial "pump breakdown – membrane depolarization – cell swelling" scheme, there is also an excessive release of excitatory amino acids (i.e. excitotoxicity). In particular, released glutamate will overactivate N-methyl-D-aspartate (NMDA) receptors and initiate cell death. Unlike ischemia however, the action of ouabain does not lead to complete energy depletion,

but clearly reduces mitochondrial membrane potential and compromises mitochondrial function due to the excess of intracellular Ca^{2+}. Optical microscopy observations of the rat cerebral cortex following injections of ouabain showed a cortical structure characterized by swollen processes and astrocytes, as well as cytoplasmic vacuolation. Neurons are affected by a loss of ribosome configuration and swelling of mitochondria and nucleus (Cornog et al., 1967).

While hypotonic solutions have successfully produced swelling of *Aplysia* neurons, the application of ouabain has been shown to affect the resting membrane potential as expected, but this depolarization was not accompanied by significant swelling (Wheal et al., 1977). A possible hypothesis, put forward to explain the absence of swelling in spite of a rapid net intracellular Na^+ accumulation after pump inhibition by ouabain, was that the accumulated ions would not trigger the expected osmotic activity. This response could be due to an extensive structuring of intracellular water in *Aplysia* neurons, likely related to their extremely high DNA content (among other highly charged molecules) which favors the formation of hydrogen bonds (Carpenter et al., 1973). The two challenges chosen for our experiments should therefore enable us to assess the effect of water intake through osmotic equilibration and of membrane depolarization on the ADC separately.

Let us first analyze the findings from diffusion MRI studies of cell swelling on other tissue models.

9.2 ADC decrease and cell swelling: an overview

The role of the intracellular fraction

One of the most popular views is that the ADC decrease is related to the increase of the intracellular volume fraction, as a result of cell swelling. This hypothesis is based on the assumption that diffusion in the intracellular space is slower than in the extracellular space, due to molecular crowding, cytoplasmic viscosity and restriction effects. Since the measured ADC is a weighted average of various diffusion behaviors within a voxel, this hypothesis is a very sensible one in the absence of more detailed information. This was for instance the conclusion of (Benveniste et al., 1992), who showed a 33% decrease in ADC in the rat brain following either ouabain exposure or acute ischemia, and a more pronounced decrease of 35 – 40% following exposure to either glutamate or NMDA.

The biexponential model described in Chapter 6, which characterized fast and slow pools of water in slow/intermediate exchange, came with the promise of validating this hypothesis. Indeed, initial studies of cell swelling that went to high b-values and performed multi-exponential analysis of the non Gaussian diffusion signal showed that the size of the slow pool increased with ischemic insult, and hypothesized that the slow/fast pools corresponded to intra/extracellular spaces. (Niendorf et al., 1996) studied the diffusion response of rat brain to global ischemia using b-values up to 10,000 s/mm². They found that the slow fraction increased from 17% to 33% following death. However, the fraction of intracellular space is approximately 80% in rat cortex (Sykova and Nicholson, 2008), and increases to 90% following death. So although the evolutions in size of the slow pool and of the intracellular space with global ischemia are similar, quantitatively the two populations do not seem to match at all. The two most serious sources of bias that could explain the discrepancy between the measured slow/fast fractions and the physical sizes of the intracellular and extracellular compartments are either the exchange time compared to the diffusion time, or a significant difference between the transverse relaxation times of each compartment. In their study, Niendorf *et al.* probed diffusion times ranging from 8.4 to 60 ms and found that they did not produce significantly different fraction size estimates. The retained explanation was therefore that the shorter T_2 in the intracellular compartment led to an underestimation of its size. Other subsequent studies on rat hippocampal slices and in the human brain led to diverging conclusions. (Clark and Le Bihan, 2000) showed the independence of the estimated slow fraction on TE, thus ruling out a T_2 effect to explain the discrepancy. (Bui et al., 1999) rightfully suggested that nucleus properties are closer to those of the extracellular space and that hereby associating the nucleus with the extracellular compartment could lead to an underestimation of the intracellular space.

In terms of the diffusion coefficients associated with each pool, Niendorf *et al.* found that D_{fast} and D_{slow} each decreased by 35 – 45% following death. On the contrary, Bui *et al.* found that the diffusion coefficient of each pool was stable with ischemic insult, and that it was only their relative size that changed. The latter observation is more consistent with a view of ischemia as shifting water from a fast to a slow compartment. Studies on perfused human and rat hippocampal slices also concluded to the invariance of D_{fast} and D_{slow} and to a consistent increase in the slow fraction with induced cell swelling (Shepherd et al., 2003a; Shepherd et al., 2003b). The association of the intra/extracellular spaces with these slow/fast pools remained nonetheless greatly unsatisfactory.

Arrest of cytoplasmic streaming and increased cytoplasmic viscosity

This puzzle can perhaps explain the increased motivation to separate the signals arising from the physical intracellular and extracellular compartments. One way of achieving this separation is to resort to imaging non-proton nuclei which are exclusively intra- or extracellular. However, one caution to be taken when interpreting diffusion studies using tracers is that the diffusion properties of the latter may be different from those of water in terms of molecular size, macromolecular binding and exchange properties. ^{133}Cs is an NMR detectable potassium analog that accumulates in the brain intracellular space. The ADC of ^{133}Cs was found to decrease by 30 – 75% in the rat brain within 20 minutes of death (Goodman et al., 2008; Neil et al., 1996). Interestingly, Goodman *et al.* also showed that the ^{133}Cs ADC in muscle tissue did not change significantly in the same conditions, hinting to the tissue-specific nature of the ADC decrease that accompanies global ischemia. The same group performed a similar study using ^{19}F NMR and 2-[^{19}F]luoro-2-deoxyglucose-6-phosphate (2FDG-6P), which can selectively accumulate in the intra- or extracellular space depending on the mode of administration (Duong et al., 1998). Their results showed that the ADCs of 2FDG-6P in the intra- and extracellular space were very similar, and both decreased by about 40% following rat death. This finding challenged the widespread assumption that diffusion in the intracellular space is much slower than in the extracellular space. Given also the similar variation magnitudes, the study did not put forward that one or the other space dominated the tissue ADC behavior. In terms of intracellular ADC decrease with global ischemia, the explanations suggested by the authors were either energy failure leading to a loss of intracellular motion (i.e. breakdown of cytoplasmic streaming) or an increase in the viscosity of the intracellular space due to the dissociation of microtubules, for instance. These hypotheses will be further discussed at the outcome of our study on the *Aplysia* neurons. In terms of extracellular ADC decrease with ischemia, Duong *et al.* suggested that it was related to the increase of extracellular tortuosity caused by cell swelling.

Increased extracellular tortuosity

Extracellular tortuosity is a parameter that quantifies the hindrance of water molecules in the extracellular interstices. It is defined as $\lambda = \sqrt{D/ADC}$, where D is the extracellular free diffusion coefficient and ADC is the extracellular apparent diffusion coefficient. Results on the diffusion of tetramethylammonium in the extracellular space of turtle cerebellum, measured using ion-selective

microelectrodes, supported the contribution of an increased extracellular tortuosity to an overall tissue ADC decrease (Krizaj et al., 1996). They showed that indeed a 20% hypotonic shock produced an increase in the tortuosity of the extracellular medium from 1.70 to 1.79 and was accompanied by a decrease of the extracellular volume fraction from 22% to 12%. Studies on red blood cell suspensions even led to the assumption that the increase in tortuosity of the extracellular space was the main contributor to ADC decrease in tissue (Latour et al., 1994b). However, red blood cell suspensions are perhaps not a valid model for brain tissue. Duong *et al.* for instance argued that in brain tissue the increased tortuosity alone could not account for the overall ADC decrease in tissue, since extracellular space represents only 20% of normal and 10% of ischemic brain tissue volume. This latter view was supported by other studies. For instance, (Silva et al., 2002) studied the effect on ADC of focal cerebral ischemia in the rat, both overall and in the intracellular space. The separation between intra- and extracellular spaces in the second case was achieved by injecting a gadolinium-based contrast agent that remained extracellular and selecting a TE value that completely suppressed the extracellular signal through T_2 decay. This study found a quantitatively similar decrease in ADC with focal ischemia both overall and in the intracellular space. The authors concluded that the ADC drop in the tissue was dominated by the ADC drop in the intracellular space.

The intracellular space: swollen cell bodies and beaded neurites

The choice of tissue model for experimental studies has a great impact on the interpretation of results and it is perhaps important to take some time to explain what hides behind the term “intracellular space”. The mammalian nervous tissue is grossly constituted of neurons and glial cells (mainly astrocytes). The neuronal cell body (soma) is approximately spherical, while axons and dendrites (termed together as neurites) are usually approximated as cylinders. Astrocytes also display numerous processes and arborizations locally characterized by a cylindrical geometry. In the mammalian cortex, the 80% of intracellular space is approximately divided into 10 – 15% of soma and 65 – 70% of neurites and processes (Braitenberg and Schüz, 1998). In response to ischemic insults, cell bodies and astrocytic processes swell, while neurites undergo a shape transformation characterized by focal enlargements separated by constrictions, or “beading” (Li and Murphy, 2008) – see Figure 50.

A recent study on excised rat sciatic nerve – a model where intracellular space is exclusively axonal – showed that beading caused a decrease of the ADC in the axonal intracellular space, mainly attributed to a decrease in diffusion parallel to the neurite (Budde and Frank, 2010). The authors even speculated that the effect of

beading was sufficient to explain the overall ADC decrease in tissue, since it is also expected to affect the tortuosity in the extracellular space. However, the effect of beading should perhaps also be evaluated on a more realistic gray matter model, with coexistence of soma and glial cells, as well as arbitrary orientation of the neurites.

In parallel, studies on spherical cells such as *Xenopus* oocytes showed that the intracellular ADC increased following osmotic stress (Sehy et al., 2002). Similarly, in glial cells that display swelling but no beading (e.g. C6 glioma cell cultures), the intracellular ADC was found to increase with ischemia (Trouard et al., 2008). This ADC increase inside swelling structures is indeed consistent with an overall dilution caused by water influx. Because it appears somewhat contradictory with the ADC decrease measured at tissue level, authors argued that even though intracellular ADC increased, the concomitant increase of the overall intracellular fraction (assumed to have lower diffusion coefficient) and the increased tortuosity of the extracellular space could still produce an overall ADC decrease.

A more valid interpretation would perhaps be that the response is different between soma and neurites: with ischemic insult, the ADC increases inside the soma due to swelling and decreases inside the neurites due to beading. Since the "intracellular space" is mainly constituted of neurites, the ADC decrease is predominant. This is then consistent with the findings of overall intracellular ADC decrease in the rat brain, where "intracellular" is a mixture of soma and neurites, as presented in the previous paragraphs.

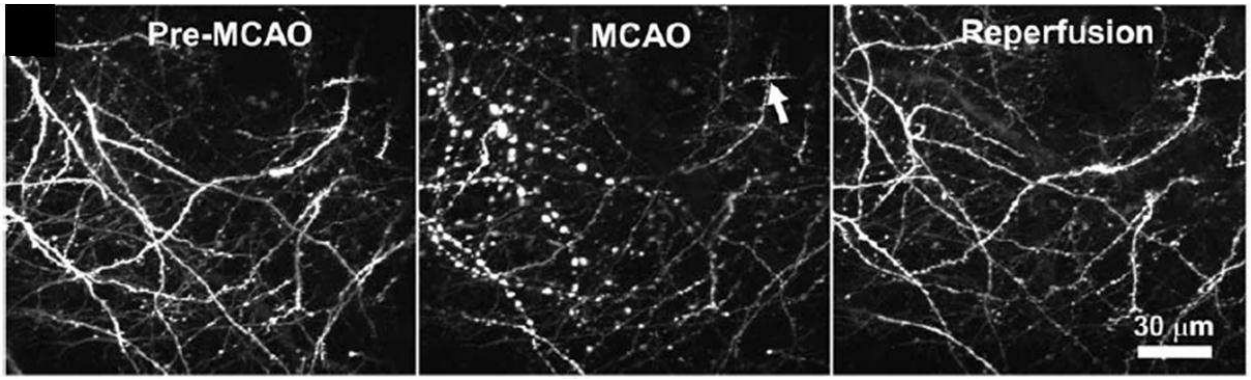

Figure 50. ***Illustration from (Li and Murphy, 2008).*** **Images of dendritic structure in mice. Left: intact structure before middle cerebral artery occlusion (MCAO). Middle: extensive dendritic beading is observed 52 min after MCAO. A small white arrow shows a region in which dendrites were relatively spared, possibly because of residual blood flow. Right: a significant recovery of dendritic structure was observed after animal reperfusion.**

The "intracellular space" therefore does not appear to behave as a single compartment. The distinction between soma and neurites could become important in shedding light on some confounding results. (Li et al., 2002) showed that reperfusion in rats after focal ischemia led to ADC restoration after the initial characteristic drop, but that the reperfusion did not restore cell sizes to their pre-ischemic configuration. Namely, microscopic examinations showed persistently swollen astrocytes and processes. In other words, the initial drop in tissue ADC with acute ischemia did not seem to correlate with cell swelling, since reperfusion restored the ADC value but did not invert the swelling process. The authors then hypothesized that the initial drop in ADC was related to a breakdown of energy metabolism (via a loss of cytoplasmic streaming) rather than to edema. However, it was shown that neurite beading is reversed by reperfusion (Li and Murphy, 2008). Since neurites are the main volumetric constituent of brain tissue, associating the ADC decrease in focal ischemia with neurite beading and its restoration with neurite structure recovery does not seem unreasonable either. Moreover, it is important to bear in mind that an ADC decrease is typically found in multiple conditions that are not necessarily associated with a metabolic breakdown, but always associated with membrane depolarization and therefore cell membrane reconfiguration.

Back to biexponential: no need for physical compartments

Going back to the experimental observation that water diffusion signal in the brain can be well approximated by a biexponential function for b-values between 0 – 10,000 s/mm², there has been increasing evidence that these two pools of water exist at a structural scale smaller than the cell. Indeed, experimental diffusion attenuation curves well modeled by a biexponential function were also found in two types of tissue where intra- and extracellular spaces are undefined: in the cortex of mice exposed to cold injury (with electron microscopy evidence of large missing fractions of cell membrane) and centrifuged human red blood cells with a negligible extracellular space (Schwarcz et al., 2004). This study put forward the idea that the slow and fast diffusing components could be water molecules that are more or less bound to macromolecules, regardless of their position inside or outside the cell. Biexponential fitting was also successfully applied to signal from inside *Xenopus* oocytes and *Aplysia* neurons, showing that slow and fast diffusion components coexist at the intracellular level as well (Grant et al., 2001; Sehy et al., 2002). These results dismissed the identification of the intracellular compartment with the slower pool.

However, much debate exists on what becomes of the D_{fast}, D_{slow} and f_{fast} parameters with cell swelling. Some studies found that only f_{fast} decreased with ischemia, the

other two remaining unchanged (Buckley et al., 1999; Bui et al., 1999; Shepherd et al., 2003a; Shepherd et al., 2003b). Others found that all three parameters decreased in an ischemic context (Niendorf et al., 1996; Schwarcz et al., 2004). And within spherical cell bodies, Sehy *et al*. found that D_{fast} and D_{slow} increased, while their relative fraction was unaltered. At least two factors could be at the origin of such a variety of responses. First, fitting a three-parameter equation to insufficient and/or noisy data leads to poor precision on the fit parameters, as mentioned earlier. Second, as alluded to in Chapter 6, the existence of two pools is not a necessary condition for the diffusion attenuation curve to resemble a biexponential function, in which case we could be wrongly analyzing very different situations with a unique model.

Increased membrane surfaces

Nonetheless, the association of fast and slow pools with water molecules which are far or close to membranes is an interesting concept that could potentially unify all the observations relative to ADC measurements in various tissue models (Le Bihan, 2007). As alluded to earlier, brain tissue water displays diffusion coefficients which are two to ten times smaller than free water diffusion (which is about 2.0 10^{-3} mm²/s at 20°C and 3.0 10^{-3} mm²/s at 37°C). The main factors thought to slow down the diffusion process are high viscosity and macromolecular crowding in the intracellular space, and limited membrane permeability both on the intra- and extracellular sides (Chen and Nicholson, 2000; Hazlewood et al., 1991). In cells, negatively charged surfaces of proteins orient the dipolar water molecules in a first layer, which in turn, may orient a second layer, and so on. Such water structuring was indeed confirmed (Ling, 2003) and could extend up to 50 Å from the protein surface (Clegg, 1984). Water polarization near charged surfaces such as membranes was also shown to build up to influence ranges of up to 200 nm, which would constitute several hundreds of water layers (Xu and Yeung, 1998). Although the extent of this water structuring process has not been quantified in biological tissue, it was suggested that the slow water pool could correspond to highly structured water molecules trapped within a membrane range of influence (Le Bihan, 2007), which could be reinforced by the glyococalyx on the outside and by the cytoskeleton on the inside. Similarly, the fast water pool could correspond to bulk water in fast exchange with the water hydration shell of proteins and macromolecules, thereby producing a diffusion coefficient largely reduced compared to free water, yet higher than the “membrane-trapped” slow fraction. The fast diffusing and slow diffusing protons would therefore correspond to two differently structured water pools, independently of their location in specific functional compartments. Those two pools

are assumed in slow or intermediate exchange on the timescale of the MR experiment, although the residence time of water molecules in one or the other pool would need to be quantitatively assessed. Furthermore, Le Bihan proposed an initial calculation based on a simple spherical cell model which produced a reasonable slow water layer thickness of 50 nm to account for the 30% slow fraction usually estimated in biexponential fits. However, a more realistic model accounting for 65% of neurites versus 15% of spherical soma would be worthwhile investigating.

The implications of such a water distribution on ischemia results are immediate. Any reshaping of the membranes, in the form of cell swelling or neurite beading, would produce a change in the relative fractions of slow and fast diffusing water within a fixed voxel volume. The increase of membrane surface area would thus lead to an increase of the slow water fraction and a decrease in overall ADC. Interestingly, this model could also explain the ADC reduction in tumors or metastases through a higher cell packing and thus larger membrane surface area within a fixed voxel volume.

9.3 How the *Aplysia* model fits in

Given the above state of current knowledge, it appears that the study of diffusion processes at smaller scales, as small as permitted by MR microscopy developments, could help retain the most important processes likely to have an impact on tissue ADC decrease with membrane depolarization and cell swelling. We have chosen to use the *Aplysia* model in order to test the impact of the various effects previously presented. As announced, we will perform diffusion measurements separately within two structures: the region of cell bodies in the buccal ganglia and isolated single neurons. Let us compare the *Aplysia* nervous system to that of mammals, in order to have a better picture of the strengths and weaknesses of this tissue model in its response to physiologic challenges.

As mentioned in Chapter 3, the regions of cell bodies and neuropil are geographically separated in the *Aplysia*, with the cell bodies located in a rind at the outskirts of the ganglion and the neuropil concentrated in the core of the ganglion and in the commissure between symmetrical ganglia. This feature is of paramount importance. Indeed, in mammalian cortex, cell bodies and neuropil are intermingled but they seem to display opposite responses to ischemia, with the ADC increasing in the cell body and decreasing in the neurites. In the *Aplysia* ganglia, we aim to study the response to hypotonic and ouabain stress of the layer of cell bodies only, located

at the rim of the ganglion. It is a fairly reasonable assumption to model this region as constituted of very large neuronal bodies, some glial cells and extracellular space, but almost devoid of neuronal processes.

The *Aplysia* has no astrocytes, and the glial cells in the cell body region are thought to have an essentially nutritive function (Kandel and Kupfermann, 1970). In mammalian systems, it has recently been shown that, while glial cells respond very rapidly to osmotic insults, thus allowing neurons to maintain their electrophysiological stability, it takes a prolonged depolarization such as ischemia for neurons to swell dramatically (Andrew et al., 2007). In the *Aplysia*, the neurons are less "protected" by the glial cells and are themselves endowed with a large capacity to rapidly adapt to external insults. Aside from swelling, beading of neurites in response to insults has also been reported, just like in mammals (Lim et al., 2002).

Another important feature is the extremely large size of neuronal soma in the *Aplysia*. While in mammalian cortex the relative volume fractions are roughly 20% extracellular space, 65% neurites and 15% soma, in the region of cell bodies of the buccal ganglia, the soma fraction was estimated to 41% from our (upcoming) measurements. The regions of cell bodies ("gray matter"), neuropil and axonal tracts in the commissure ("white matter") of buccal ganglia are labeled in Figure 51.

No diffusion anisotropy is expected in the two structures chosen for diffusion measurements. Isotropic diffusion was previously shown in *Aplysia* isolated neuronal soma (Hsu et al., 1997) and the composition of the region of cell bodies selected in the ganglia likely reproduces the same feature. Although *Aplysia* axons are not protected by a myelin sheath, some diffusion anisotropy is expected in the commissure and possibly in the neuropil, but neither of these structures was used for the purpose of the current study.

To sum up, conclusions from diffusion measurements in the *Aplysia* could benefit from the simplicity of the structures under study: either a large spherical neuronal body or a tissue region constituted of large cell bodies, some glial cells and extracellular space *only*, without the confounding mixture of cell bodies and neurites. However, due to this separation between cell bodies and neuropil specific to invertebrates, the extrapolation to diffusion measurements in mammalian cortex will not be straightforward.

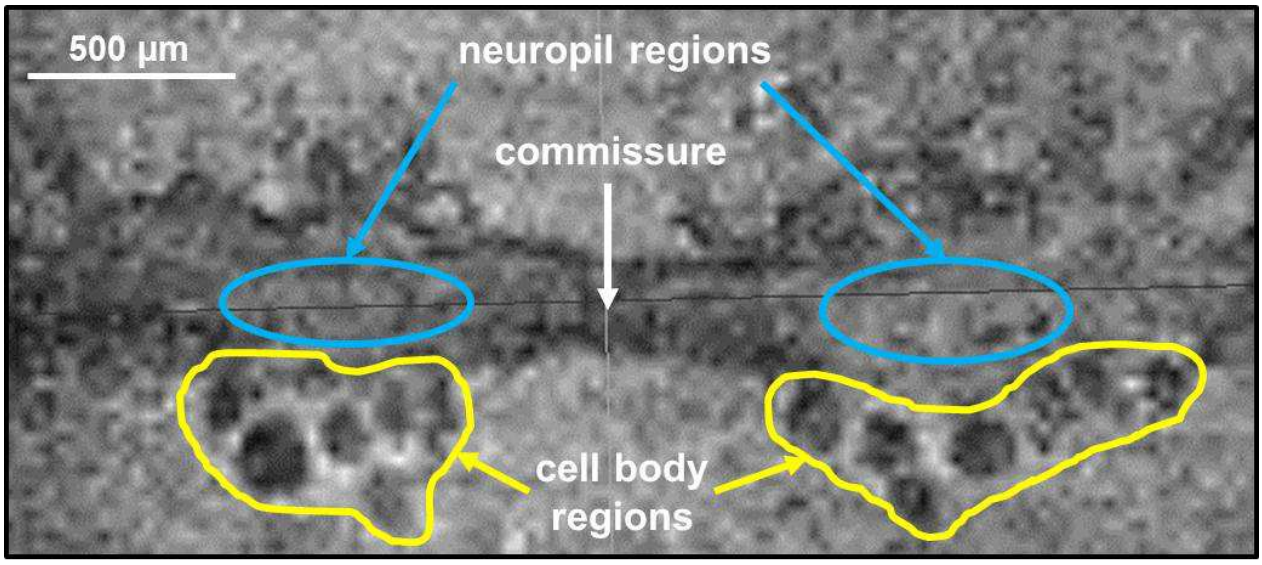

Figure 51. Representative slice from a 3D RARE image of the buccal ganglia (dataset from the MEMRI study in Chapter 5). The bilateral ganglia are connected through a commissure composed of fiber tracts. Each ganglion is organized in a region of cell bodies at the outskirts and a region of processes at the core. This separation is specific to invertebrates.

9.4 ADC measurements in *Aplysia* – Methods

In this study, we aimed to quantify the change in ADC inside mechanically isolated neuronal soma, and inside regions of cell bodies in the buccal ganglia, following exposure to either a hypotonic medium or ouabain.

Experimental

Ten *Aplysia californica* were used in total. Animals were anesthetized by injection of an isotonic $MgCl_2$ solution. The buccal, abdominal and left pleural ganglia were resected and placed in ASW. All experiments were performed at room temperature (19°C).

Single cell MR imaging

The abdominal and left pleural ganglia were desheathed and the larger neurons, with diameters between 150 and 450 µm, were mechanically isolated. These cells were typically R2 and L2 to L11 in the abdominal ganglion, and LPl1 in the left pleural ganglion. Cell integrity was verified under the microscope. Each cell was inserted into a 500 µm ID glass capillary filled with ASW. The sample was then placed inside the 700 µm ID microcoil for imaging.

Each cell underwent the following protocol. An initial (pre-insult) 3D DP-FISP imaging session was performed, as described in the previous chapter. Briefly, diffusion-weighted images were acquired for 7 b-values ranging from 10 to 600 s/mm², at 25 µm isotropic resolution, in about one hour. As discussed in Chapters 6 and 8, the monoexponential diffusion model is expected to be valid in this low b-value range. Following this initial imaging session, the cell was removed from the capillary and placed inside a glass cell culture dish (Cellview, Greiner Bio-One, Courtaboeuf, France) filled with the new medium. This medium was either a 33% hypotonic ASW (obtained by mixing 2/3 ASW and 1/3 distilled water), or ASW containing 1 mM ouabain octahydrate (Sigma Aldrich), or regular ASW (control solution). A previous study of the response to ouabain of *Aplysia* neurons used a concentration of 0.27 mM (Wheal et al., 1977), but in the absence of monitoring of the membrane potential in our study, a higher concentration was chosen, equal to that used in previous studies on a rat model (Benveniste et al., 1992; Buckley et al., 1999). The cell was allowed to equilibrate for 30 minutes inside the new medium, period split into 20 minutes inside the culture dish and 10 minutes inside a glass capillary while setting-up for the post-insult imaging session. Cell integrity was verified under the microscope both at time t = 0 and t = 20 minutes in the culture dish. The second (post-insult) imaging session was identical to the first one.

The total duration of the experiment from initial cell isolation to the end of the post-insult imaging was approximately 3 hours. Earlier studies on *Aplysia* L7 neurons showed that, once isolated and maintained at room temperature in a sealed capillary filled with ASW, cell membrane integrity was lost sometime between 7.5 and 13.5 hours (Schoeniger et al., 1994). The duration of our experiment was consistent with expected cell survival time and the verification of cell aspect under the microscope halfway through the protocol gave good confidence that the cells were intact. Moreover, inspection of the diffusion-weighted images also provided information on potential cell death. Indeed, the contrast between ASW, cytoplasm and nucleus allowed one to determine whether the cell appeared stable or whether it had undergone a process of nucleus expulsion. Data on cells with compromised integrity was not retained.

Buccal ganglia MR imaging

The bilateral buccal ganglia were inserted into a 2.0 mm ID glass capillary filled with ASW. The sample was then placed inside the 2.4 mm ID micro-coil for imaging.

Each pair of ganglia underwent a protocol similar to that for the single cell. A pre-insult 3D DP-FISP imaging session was performed. The imaging parameters that

differed from the single cell experiments were the following: matrix: 128x44x40 / 50 µm isotropic resolution / TE/TR = 1.7/3.4 ms / NA = 2 / TA = 8 min/b-value. Following this initial imaging session, the ganglia were removed from the capillary and placed inside a Petri dish filled with the new medium. This medium was either hypotonic ASW, or ASW with ouabain, or control ASW. The hypotonicity of the solutions varied between 33% and 67% and the ouabain concentration between 1 to 3 mM. The extent of osmotic shock and the ouabain concentration were increased in some of the experiments to evaluate the impact of the protective sheath around the ganglia on tissue response. As for the single cells, the ganglia were allowed 30 minutes of equilibration inside the new medium. The second imaging session was identical to the first one.

The total duration of the experiment from initial ganglia extraction to the end of the post-insult imaging was approximately 3 hours. This duration is well within ganglia survival time, as explained in Chapter 5 for the MEMRI experiments.

Single cell optical microscopy imaging

Additional neurons isolated from the abdominal and pleural ganglia, approximately 100 µm in diameter, were used to quantify cell swelling with absorption and fluorescence microscopy. These measurements were performed only on one cell for each insult in order to provide a rough order of magnitude of the volume change induced.

Each cell was placed inside a cell culture dish filled with ASW. Two types of acquisitions were considered. One used standard light absorption and required no sample preparation. The other used Hoechst staining of the nucleus (through DNA binding) combined with fluorescence acquisition in the blue/cyan range. For the latter, 2 µL of Hoechst 33342 (Life Technologies, Saint-Aubin, France) were added to the 2 mL of ASW in the culture dish, that was then incubated for 5 minutes at room temperature, sheltered from light.

The dish was placed under the microscope (Zeiss Axio Observer Z1, Carl Zeiss, Le Pecq, France), and a z-plane containing cytoplasm and nucleus was brought into focus. For fluorescence imaging, a blue filter (Zeiss filter BP445/50) was used. A snapshot image at t = 0 was taken. The medium of the cell was then changed by simultaneous aspiration of the old medium and injection of the new medium inside the dish. The new medium was either 33% hypotonic ASW, or ASW + 1 mM ouabain, or regular ASW. The acquisition was started immediately, with snapshots acquired every 30 s for one hour, using Zeiss Axio Vision software.

Data analysis

Global ADC change

For every single cell MR dataset, the cell was manually segmented based on signal contrast with ASW in the b = 10 s/mm² image. The voxel count constituted a measurement of cell volume. Signal was averaged over the entire cell ROI, and the natural logarithm of the signal was fit to a linear function of b-value, the slope corresponding to the ADC inside the cell. This type of analysis was sufficient as the data showed no deviation from a monoexponential model in the low b-value range spanned.

Whenever the cell was large enough to enable a reliable segmentation of the nucleus, additional analyses of the volumes and ADCs of the nucleus and the cytoplasm separately were performed.

Structure volumes and ADC values were compared between pre- and post-insult.

For every buccal ganglia MR dataset, a monolateral ROI essentially encompassing cell bodies that send axonal projections into n.2 and n.3 was manually segmented. The size of this ROI was around 300 voxels, corresponding to a volume of 38 µL. Signal was averaged over the entire ROI, and the natural logarithm of the signal was fit to a linear function of b-value, for ADC estimation in the region of cell bodies of the ganglia. ADC values were compared between pre- and post-insult. An illustration of segmentation both in single cells and ganglia is presented in Figure 52.

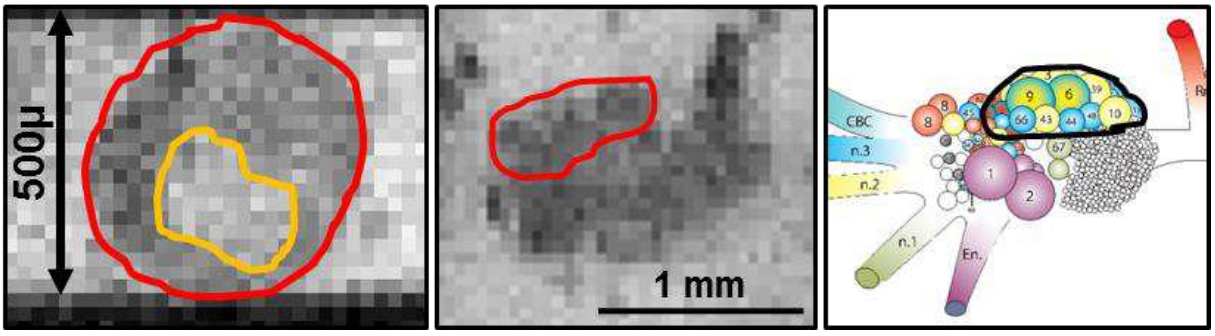

Figure 52. Examples of ROIs for average ADC extraction. Left: Single cell (R2) image. The red contour represents the cell ROI on this slice, and the orange contour the nucleus ROI. The cytoplasm is obtained from the difference of the two. The segmentation of the nucleus was not possible on all cells, only on the largest ones. Middle: Buccal ganglion image. The red contour represents the cluster ROI on this slice. Right: Schematic of the matching buccal ganglion, showing the approximate region chosen for ADC estimation.

Cell volume change

As mentioned previously, the cell volume was assessed with MRI from voxel counts in the cell. The voxel count V was converted into an equivalent cell diameter $d = \sqrt[3]{(6V/\pi)}$. To account for PVE and for the uncertainty associated with manual segmentation, a change in volume between pre- and post-insult was only considered significant if the equivalent diameter varied by at least one voxel.

In the optical microscopy image series, cell and nucleus diameters were estimated at major timepoints. The phases of rapid cell response and subsequent stabilization were determined. The cell and nucleus diameters were compared at t = 0 and t = 30 min pre- and post-insult. For the hypotonic and control media, the Hoechst stained cells displayed a very clear contour of both cell and nucleus membranes on the fluorescence image: the same cell was therefore used to measure the cell and nucleus diameters. For the ouabain experiment, the Hoechst stained cell only displayed clear outlining of the nucleus on the fluorescence image. Standard absorption microscopy was therefore applied on a different cell to measure the change in cell diameter reliably.

Soma fraction in the cell body region

In the MEMRI study, we put forward that T2w images provided excellent contrast between cell bodies and the rest of the medium in the buccal ganglia. Three sets of high resolution RARE images acquired for the MEMRI study were used to obtain an estimate of the volume fraction of cell bodies in the typical ROI selected in the buccal ganglia for ADC measurements. On the RARE images, each side of the buccal ganglia was treated separately, thus producing six independent estimates of soma volume fraction. On each side, an ROI was outlined corresponding to the region shown in Figure 52. A histogram of voxel intensity values in the ROI was plotted and displayed two peaks corresponding to signal levels inside and outside cell bodies, respectively. A signal level threshold was chosen based on this peak separation in the RARE images. Masks for cell bodies within this ROI were generated automatically using the signal level threshold. The soma volume fraction was obtained by comparing the voxel counts of cell body to entire ROI.

9.5 Response to each type of insult – Results

Cells and ganglia are labeled using a 3 symbol code: the first ("c" or "g") refers to cells or ganglia, the second ("c", "h" or "o") refers to the type of insult experienced, control, hypotonic or ouabain, and the last is the number within a same insult group.

Control medium

Three cells and two pairs of ganglia were exposed to the control medium (ASW) in between the two imaging sessions. The purpose of these experiments was to evaluate whether our protocol in itself altered the ADC in the cells and ganglia and/or the cell volume.

Table 8 collects measurements in the cells and Table 9 those in the ganglia.

The ADC changed by less than 3% in the cells and by less than 4% in the ganglia, which was not considered significant compared with measurement uncertainties. A graphical representation of the ADC measurements is provided in Figure 53. The cell volume did not vary significantly as assessed from images with a spatial resolution of 25 µm. Fluorescence microscopy measurements confirmed that the size of the cell did not change in the 30 minutes imparted for equilibration if the new medium was control ASW (Figure 54).

These results altogether confirmed that the chosen protocol did not in itself cause a change in ADC at cell and ganglia level, nor in cell size.

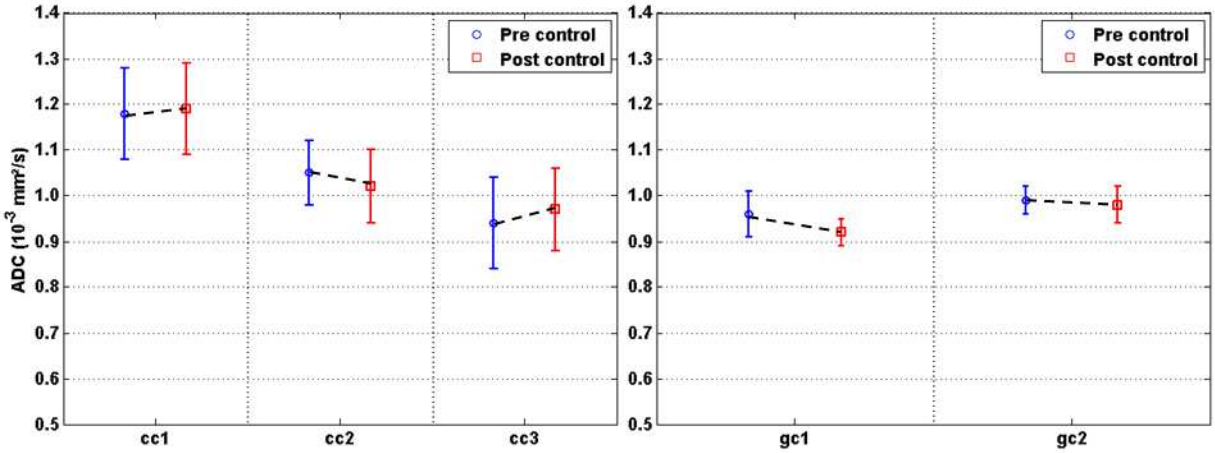

Figure 53. ADC measurements in three soma (left) and in two ganglia (right), pre- and post-exposure to a control ASW solution. The change in ADC is within the measurement uncertainty in all three cell bodies and in both ganglia.

	ADC[a] (x10^{-3} mm²/s)		Cell Volume[b] (# voxels)		Equivalent diameter[b] (# voxels)	
	Pre	**Post**	**Pre**	**Post**	**Pre**	**Post**
cc1	1.18 ± 0.10	1.19 ± 0.10	188 ± 14	198 ± 14	7.1 ± 0.2	7.2 ± 0.2
cc2	1.05 ± 0.07	1.02 ± 0.08	221 ± 15	163 ± 13	7.5 ± 0.2	6.8 ± 0.2
cc3	0.94 ± 0.10	0.97 ± 0.09	268 ± 16	256 ± 16	8.0 ± 0.2	7.9 ± 0.2
mean	*1.06 ± 0.09*	*1.06 ± 0.09*	*226 ± 15*	*206 ± 15*	*7.5 ± 0.2*	*7.3 ± 0.2*

Table 8. ADC and volume measurements in the three cells exposed to a control solution of ASW in-between pre and post imaging sessions. The ADC changed by less than 3% in all cases, and the volume variations were not considered significant given the spatial resolution of 25 µm. [a]The uncertainties represent the standard deviations on the fit parameters. [b]The standard deviations represent the error in counting cell voxels out of the entire useful volume of the coil (22620 voxels).

	ADC[a] (x10^{-3} mm²/s)	
	Pre	**Post**
gc1	0.96 ± 0.05	0.92 ± 0.03
gc2	0.99 ± 0.03	0.98 ± 0.04
mean	*0.98 ± 0.04*	*0.95 ± 0.04*

Table 9. ADC measurements in the two ganglia exposed to a control solution of ASW in-between pre and post imaging sessions. The ADC changed by less than 4% in both cases. [a]The uncertainties represent the standard deviations on the fit parameters.

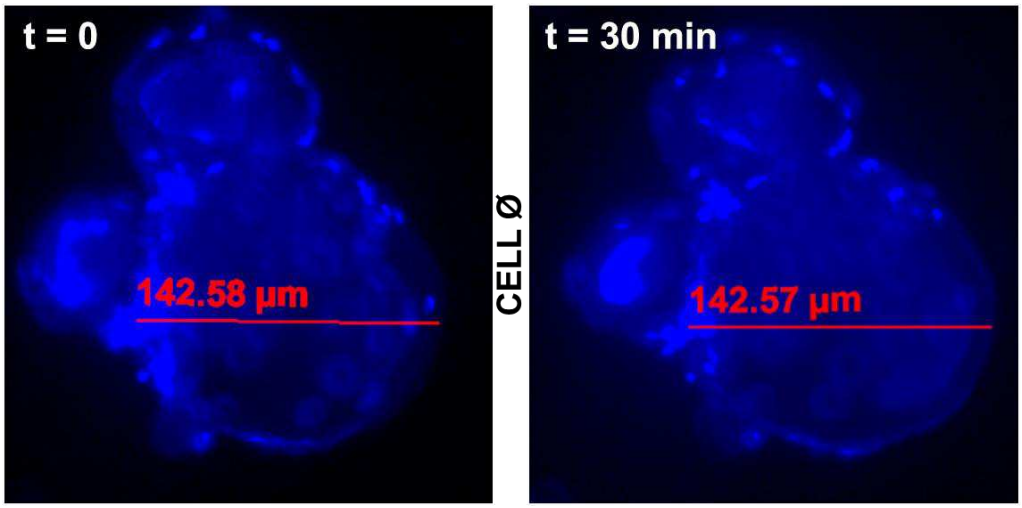

Figure 54. Fluorescence microscopy images of a Hoechst stained neuron, equilibrating with an ASW control medium. The cell diameter did not evolve between timepoints 0 and 30 minutes.

Hypotonic shock

Six cells and four pairs of ganglia were exposed to a hypotonic ASW in between the two imaging sessions.

Table 10 collects measurements in the cells exposed to a 33% hypotonic ASW. Three of the six cells (ch1, ch2 and ch3) were large enough to allow a reliable segmentation of nucleus and cytoplasm. Separate ADC measurements in nucleus and cytoplasm for these cells are collected in Table 11. Measurements in the four ganglia are given in Table 12.

Overall, following exposure to hypotonic ASW, the ADC increased by (32 ± 24)% in the cells and decreased by (12 ± 5)% in the ganglia tissue. A graphical representation of the ADC changes in cells and ganglia is provided in Figure 55. Two-tailed paired Student t-tests were performed on the series of ADC values pre- and post-insult. The pre and post series were found to be statistically different both for the cells ($p < 0.02$) and for the ganglia ($p < 0.005$). The ganglia exposed to 33% and 67% hypotonic ASW responded in a similar fashion and were therefore grouped together.

Separate treatment of nucleus and cytoplasm in the three largest cells showed that hypotonic insult caused an ADC increase both in the nucleus and in the cytoplasm.

	ADC[a] (x10^{-3} mm²/s)		Cell Volume[b] (# voxels)		Equivalent diameter[b] (# voxels)	
	Pre	**Post**	**Pre**	**Post**	**Pre**	**Post**
ch1	0.60 ± 0.02	1.08 ± 0.21	2763 ± 49	3677 ± 55	17.4 ± 0.1	19.1 ± 0.1*
ch2	0.65 ± 0.05	0.80 ± 0.07	2756 ± 49	3365 ± 54	17.4 ± 0.1	18.6 ± 0.1*
ch3	0.66 ± 0.10	0.95 ± 0.03	1655 ± 39	1916 ± 42	14.7 ± 0.1	15.4 ± 0.1
ch4	0.92 ± 0.05	1.14 ± 0.03	204 ± 14	332 ± 18	7.3 ± 0.2	8.6 ± 0.2*
ch5	1.09 ± 0.02	1.23 ± 0.09	119 ± 11	126 ± 11	6.1 ± 0.2	6.2 ± 0.2
ch6	0.93 ± 0.07	1.00 ± 0.04	232 ± 15	239 ± 15	7.6 ± 0.2	7.7 ± 0.2
mean	*0.81 ± 0.05*	*1.03 ± 0.08*	*1288 ± 30*	*1609 ± 33*	*11.8 ± 0.1*	*12.6 ± 0.1*

Table 10. ADC and volume measurements in the six cells exposed to a 33% hypotonic solution of ASW. The ADC increased by (32 ± 24)% on average, accompanied by a volume increase of (24 ± 22)%. An equivalent diameter increase superior to the voxel size was found in three out of six cells (*). [a]The uncertainties represent the standard deviations on the fit parameters. [b]The standard deviations represent the error in counting cell voxels out of the entire useful volume of the coil (22620 voxels).

	ADC[a] (x10^{-3} mm²/s)		Volume[b] (# voxels)		Equivalent diameter[b] (# voxels)	
	Pre	**Post**	**Pre**	**Post**	**Pre**	**Post**
N ch1	0.95 ± 0.12	1.20 ± 0.18	368 ± 19	464 ± 21	8.9 ± 0.2	9.6 ± 0.1
N ch2	0.89 ± 0.07	1.26 ± 0.03	408 ± 20	609 ± 24	9.2 ± 0.1	10.5 ± 0.1*
N ch3	1.01 ± 0.13	1.25 ± 0.05	276 ± 17	332 ± 18	8.1 ± 0.2	8.6 ± 0.2
N mean	*0.95 ± 0.11*	*1.24 ± 0.09*	*351 ± 19*	*468 ± 21*	*8.7 ± 0.2*	*9.6 ± 0.2*
C ch1	0.50 ± 0.02	1.06 ± 0.05	2395 ± 46	3213 ± 53	-	-
C ch2	0.60 ± 0.03	0.66 ± 0.10	2348 ± 46	2756 ± 49	-	-
C ch3	0.58 ± 0.11	0.87 ± 0.03	1379 ± 36	1584 ± 38	-	-
C mean	*0.56 ± 0.05*	*0.86 ± 0.06*	*2041 ± 43*	*2518 ± 47*		

Table 11. ADC and volume measurements in the nucleus (N) and cytoplasm (C) of three cells exposed to a 33% hypotonic solution of ASW. The ADC increased by (31 ± 10)% in the nucleus and by (57 ± 51)% in the cytoplasm. The nucleus swelled by (32 ± 15)% and the cytoplasm by (22 ± 10)%. In the nucleus, an equivalent diameter increase superior to the voxel size was found in one cell only (*). [a]The uncertainties represent the standard deviations on the fit parameters. [b]The standard deviations represent the error in counting cell voxels out of the entire useful volume of the coil (22620 voxels).

		ADC[a] (x10^{-3} mm²/s)	
		Pre	**Post**
33% hypotonic	gh1	0.80 ± 0.03	0.64 ± 0.08
	gh2	1.07 ± 0.03	0.97 ± 0.01
67% hypotonic	gh3	1.05 ± 0.07	0.93 ± 0.06
	gh4	1.06 ± 0.04	0.97 ± 0.05
mean		*1.00 ± 0.04*	*0.88 ± 0.05*

Table 12. ADC measurements in the four ganglia exposed to a hypotonic shock. The ADC decreased by (12 ± 5)% on average. [a]The uncertainties represent the standard deviations on the fit parameters.

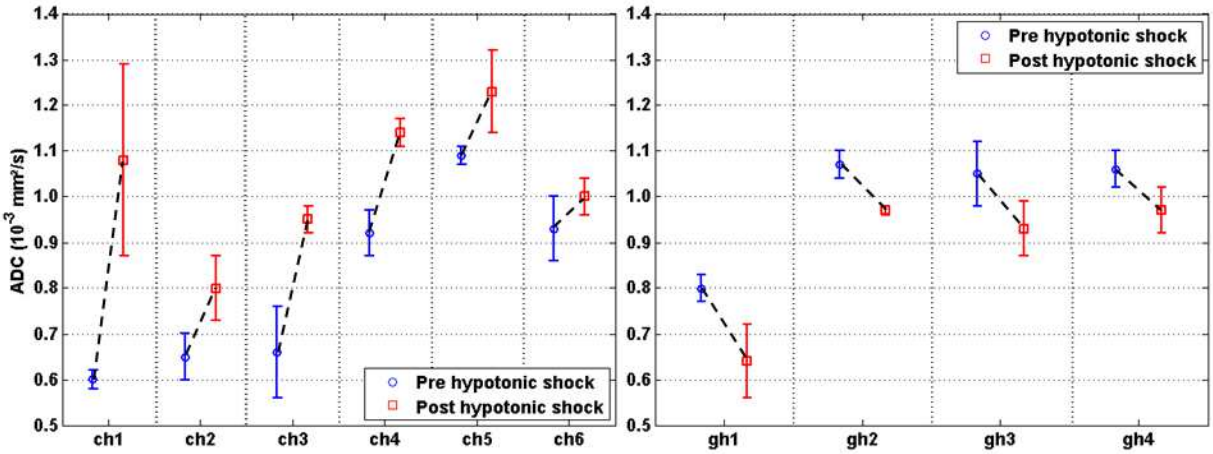

Figure 55. ADC measurements in six soma (left) and in four ganglia (right), pre- and post-exposure to a hypotonic ASW solution. Following this insult, the ADC increased in the soma and decreased in the ganglia tissue.

Hypotonic shock also produced a volume increase of (24 ± 22)% in the cells, (32 ± 15)% in the nuclei and (22 ± 10)% in the cytoplasm. The swelling was above the voxel size (in terms of equivalent structure diameter) for three out of six cells and for one out of three nuclei.

Fluorescence microscopy images of a ~100 µm neuron exposed to a 33% hypotonic insult are shown in Figure 56. Within 30 minutes, cell and nucleus diameter increased by about 12 and 10 µm (corresponding to volume increases of 37% and 51%) respectively and stabilized. Extrapolating to the size of the cells used for MR imaging (150 – 450 µm; nuclei 200 – 230 µm), the diameter increase would be within the 17 – 50 µm range for the cell and 28 – 33 µm range for the nuclei. This is fully

consistent with the fact that our MR measurements sometimes yielded diameter changes below spatial resolution (25 µm) and sometimes above. Swelling measurements with fluorescence microscopy and with MRI are therefore in agreement.

These results underline the high sensitivity of ADC measurements: while physical cell swelling was not always detectable with the MR spatial resolution, the ADC variations permitted to ascertain that a change was occurring in the cell.

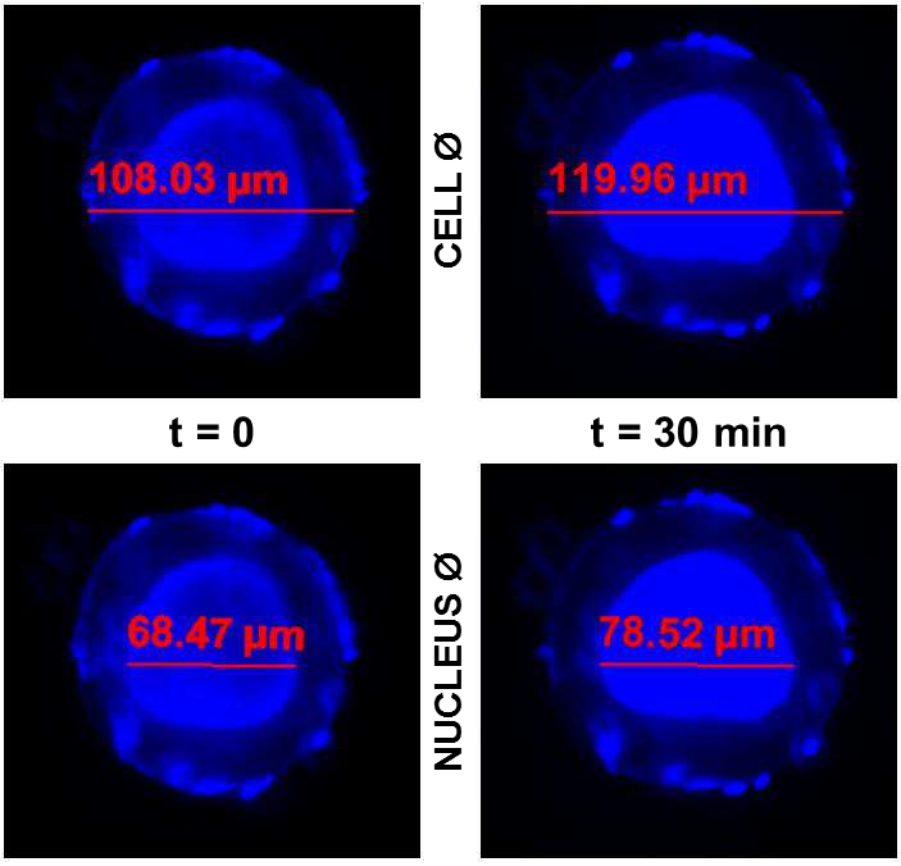

Figure 56. Fluorescence microscopy images of a Hoechst stained neuron, equilibrating with a 33% hypotonic medium. In 30 minutes, the cell diameter increased by 12 µm and that of the nucleus by 10 µm.

Exposure to ouabain

Six cells and four pairs of ganglia were exposed to ouabain in between the two imaging sessions.

Table 13 collects measurements in the cells exposed to 1 mM ouabain. Two of the six cells (co1 and co4) were large enough to allow a reliable segmentation of nucleus and cytoplasm. Separate ADC measurements in nucleus and cytoplasm are collected in Table 14. Results for the ganglia are given in Table 15.

Overall, following exposure to ouabain in ASW, the ADC increased by (30 ± 11)% in the cells and decreased by (18 ± 8)% in the ganglia tissue. A graphical representation of the ADC changes in cells and ganglia is provided in Figure 57. Two-tailed paired Student t-tests showed that the pre and post series were statistically different both for the cells ($p < 5x10^{-4}$) and for the ganglia ($p < 0.05$). As with hypotonic shock, the ganglia exposed to 1 mM versus 3 mM ouabain responded in a similar fashion and were grouped together.

Separate treatment of nucleus and cytoplasm in the two largest cells showed that ouabain caused an ADC increase both in the nucleus and in the cytoplasm.

	ADC[a] ($x10^{-3}$ mm²/s)		**Cell Volume[b] (# voxels)**		**Equivalent diameter[b] (# voxels)**	
	Pre	**Post**	**Pre**	**Post**	**Pre**	**Post**
co1	0.68 ± 0.04	0.84 ± 0.02	1419 ± 36	1452 ± 37	13.9 ± 0.1	14.0 ± 0.1
co2	0.94 ± 0.03	1.20 ± 0.12	498 ± 22	421 ± 20	9.8 ± 0.1	9.3 ± 0.1
co3	0.72 ± 0.09	1.07 ± 0.12	654 ± 25	640 ± 25	10.8 ± 0.1	10.7 ± 0.1
co4	0.78 ± 0.08	1.07 ± 0.01	3280 ± 53	3591 ± 55	18.4 ± 0.1	19.0 ± 0.1
co5	1.03 ± 0.09	1.24 ± 0.05	131 ± 11	164 ± 13	6.3 ± 0.2	6.8 ± 0.2
co6	0.91 ± 0.04	1.10 ± 0.14	332 ± 18	292 ± 17	8.6 ± 0.2	8.2 ± 0.2
mean	*0.84 ± 0.06*	*1.09 ± 0.08*	*1052 ± 28*	*1093 ± 28*	*11.3 ± 0.1*	*11.3 ± 0.1*

Table 13. ADC and volume measurements in the six cells exposed to a solution of 1 mM ouabain in ASW. The ADC increased by (30 ± 11)% on average. The volume change was (1 ± 15)%. No cell showed an equivalent diameter change superior to the voxel size. [a]The uncertainties represent the standard deviations on the fit parameters. [b]The standard deviations represent the error in counting cell voxels out of the entire useful volume of the coil (22620 voxels).

	ADC[a] (x10^{-3} mm²/s)		Volume[b] (# voxels)		Equivalent diameter[b] (# voxels)	
	Pre	**Post**	**Pre**	**Post**	**Pre**	**Post**
N co1	0.91 ± 0.05	0.99 ± 0.04	363 ± 19	344 ± 18	8.9 ± 0.2	8.7 ± 0.2
N co4	0.83 ± 0.08	1.34 ± 0.03	836 ± 28	974 ± 31	11.7 ± 0.1	12.3 ± 0.1
N mean	*0.87 ± 0.07*	*1.17 ± 0.04*	*600 ± 24*	*659 ± 25*	*10.3 ± 0.2*	*10.5 ± 0.2*
C co1	0.57 ± 0.04	0.78 ± 0.03	1056 ± 32	1108 ± 32	-	-
C co4	0.76 ± 0.08	0.98 ± 0.03	2444 ± 47	2617 ± 48	-	-
C mean	*0.67 ± 0.06*	*0.88 ± 0.03*	*1750 ± 40*	*1863 ± 40*		

Table 14. ADC and volume measurements in the nucleus (N) and cytoplasm (C) of two cells exposed to 1 mM ouabain. In the nucleus, the ADC increased by 9% in co1 and by 61% in co4. In the cytoplasm, the ADC increased by 37% in co1 and by 29% in co4. None of the structures showed significant volume change. [a]The uncertainties represent the standard deviations on the fit parameters. [b]The standard deviations represent the error in counting cell voxels out of the entire useful volume of the coil (22620 voxels).

		ADC[a] (x10^{-3} mm²/s)	
		Pre	**Post**
1 mM ouabain	go1	1.23 ± 0.05	1.01 ± 0.05
	go2	0.97 ± 0.05	0.90 ± 0.03
3 mM ouabain	go3	0.96 ± 0.04	0.73 ± 0.02
	go4	1.17 ± 0.08	0.90 ± 0.09
mean		*1.08 ± 0.06*	*0.89 ± 0.05*

Table 15. ADC measurements in the four ganglia exposed to ouabain. The ADC decreased by (18 ± 8)% on average. [a]The uncertainties represent the standard deviations on the fit parameters.

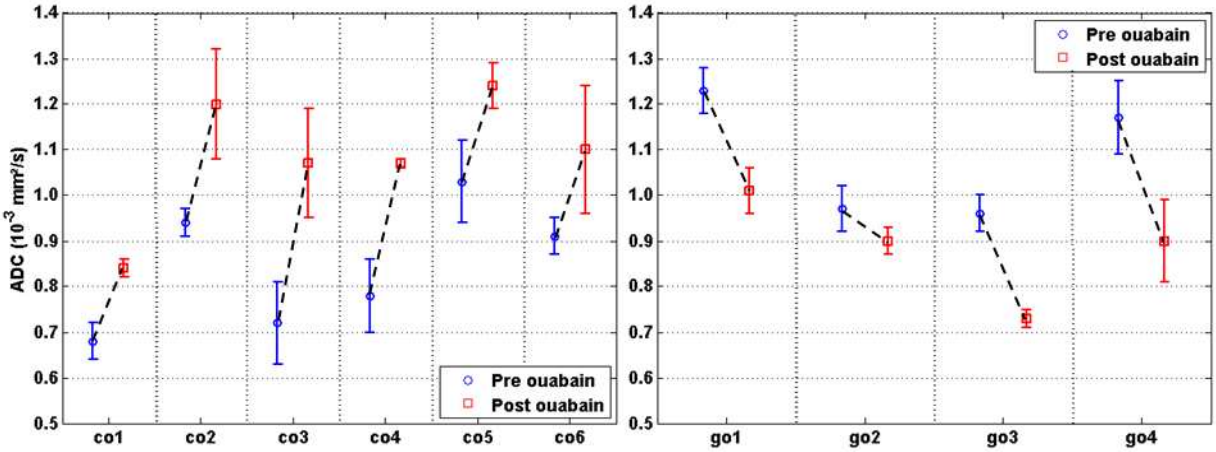

Figure 57. ADC measurements in six soma (left) and in four ganglia (right), pre- and post-exposure to ouabain. Following this insult, the ADC increased in the soma and decreased in the ganglia tissue.

However, the increase in soma ADC caused by ouabain was not accompanied by a significant swelling. The changes in equivalent structure diameter were below the voxel unit for all cells and nuclei.

Optical microscopy images of a ~100 µm neuron exposed to 1 mM ouabain are shown in Figure 58. Within 30 minutes, cell and nucleus diameter increased by about 3.5 and 5.5 µm (corresponding to a volume increase of 12% and 21%) respectively and stabilized. Thus for the size of the cells used for MR imaging (160 – 460 µm; nuclei 220 – 290 µm), we would expect a diameter increase within the 6 – 17 µm range for the cell and 14 – 18 µm range for the nuclei. This is fully consistent with the fact that our MR measurements yielded no diameter changes above the spatial resolution (25 µm). Swelling measurements from optical microscopy therefore agree with volume changes measured with MRI.

These results highlight even more strongly the sensitivity of the ADC measurement: in spite of a very small change in cell size, undetectable with the resolution of MRI, a large change in ADC occurred, indicating that the cell was responding to an environmental insult.

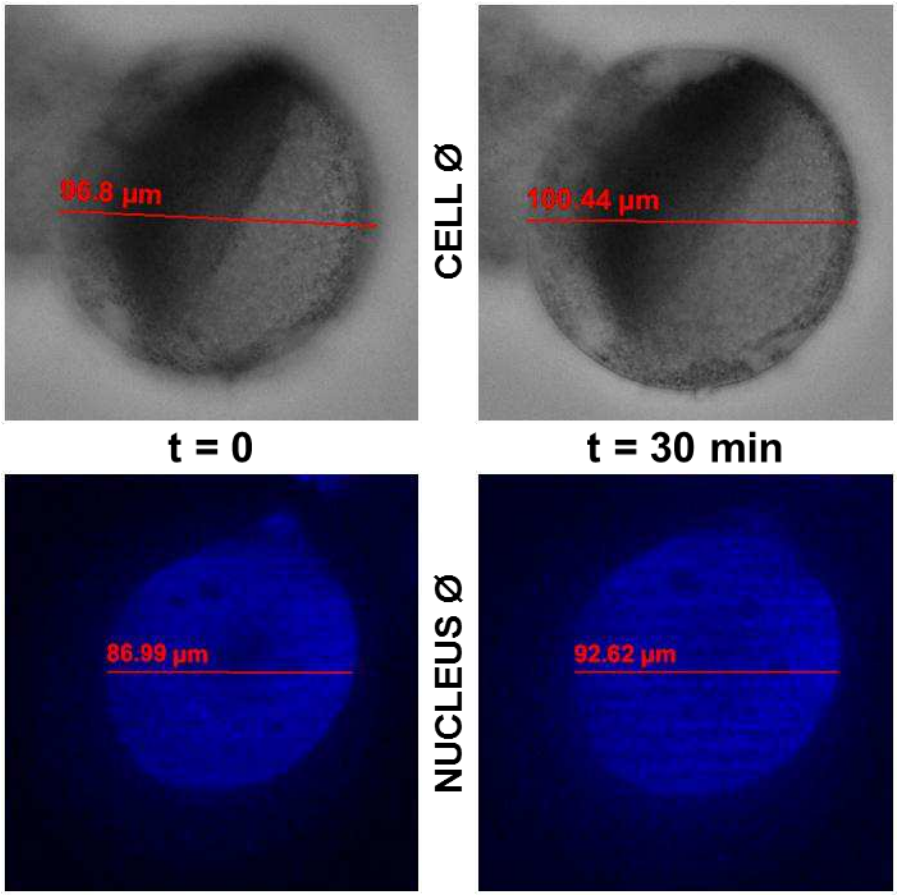

Figure 58. Absorption microscopy image of a neuron (top) and fluorescence microscopy image of a Hoechst stained neuron (bottom), equilibrating with a 1 mM ouabain solution. In 30 minutes, the cell diameter increased by 3.5 µm and that of the nucleus by 5.5 µm.

9.6 Native nervous tissue characteristics – Results

In this section, we will present some relevant results on the intrinsic characteristics of the nervous tissue of *Aplysia californica* which stem from our experiments, prior to any insult.

Typical ADC in cytoplasm and nucleus

Combining the pre-insult ADC measurements in the five large cells on which nucleus segmentation was feasible (ch1, ch2, ch3, co1 and co4), the nucleus and cytoplasm appear to have very distinct ADC values: (0.9 ± 0.1) and (0.6 ± 0.1) $x10^{-3}$ mm^2/s, respectively. The values were consistent across cells and also with values previously reported in the literature (Hsu et al., 1996).

Cell size and ADC

When looking at all the cells scanned pre-insult (15 in total), there appears to be a correlation between cell ADC and volume: larger cells have lower ADC than smaller cells. The correlation coefficient between ADC and cell diameter pre-insult was -0.86 ($p < 5x10^{-5}$). This correlation was also tested on cells post-hypotonic insult and post-ouabain separately (six cells in each group). Following hypotonic shock, the correlation coefficient dropped to -0.65 and became insignificant ($p = 0.16$). Following ouabain exposure, the correlation coefficient dropped to -0.56 thus also becoming insignificant ($p = 0.25$). Figure 59 shows a representation of ADC versus cell diameter pre- and post-insult.

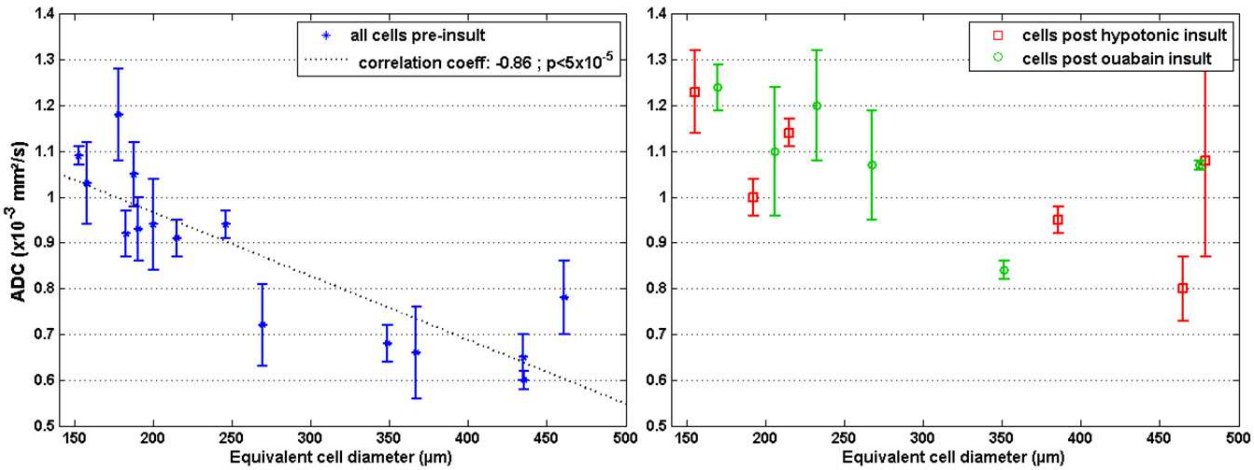

Figure 59. ADC versus cell diameter. Pre-insult (left), there is a significant correlation between ADC and cell diameter. Post-insult (right), the correlation is substantially weakened.

Volumetric fraction of soma in the cell body region

The volumetric fraction of soma calculated using an automatic segmentation procedure based on signal intensity is given in Table 16 for each ganglion used. Figure 60 gives an example of a drawn ROI and of the automatically extracted mask of cell bodies within the ROI.

The average fraction of cell bodies in the ROI typically used for diffusion measurements in the ganglia was found to be (41 ± 3)%. As expected, this value is much larger than in mammalian gray matter (15%).

Ganglion	1 Left	1 Right	2 Left	2 Right	3 Left	3 Right
Soma fraction (%)	41	45	38	38	41	42

Table 16. Soma fraction in the cell body region of the buccal ganglia, estimated from an automatic segmentation procedure, in each of the six ganglia inspected.

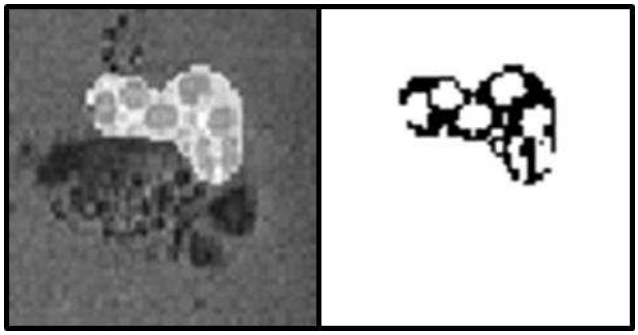

Figure 60. Left: Representative slice from a RARE image of a ganglion (TE_{eff} = 18.4 ms / 25 µm isotropic resolution – see Chapter 5); superimposed in light gray is the manually drawn ROI, similar to the ROIs drawn for diffusion measurements. Right: Automatic segmentation of cell bodies (white) within the manually drawn ROI. The RARE image confirms that the automatic segmentation selects cell bodies reliably.

9.7 Discussion

The main result that stands out from these experiments is that exposure to both a hypotonic solution and to ouabain produced an ADC *increase* inside the soma while causing an ADC *decrease* at the tissue level.

ADC decrease in the tissue

The ADC decrease at tissue level is fully consistent with many previous studies that used hypotonic solutions or ouabain on a variety of tissues.

Osmotic manipulations of turtle cerebellum led to a 25% decrease in ADC when exposed to a 33% hypotonic solution (O'Shea et al., 2000). Similarly, the application of a 20% hypotonic medium to perfused rat hippocampal slices led to a signal increase of 16% on diffusion-weighted images, synonymous of an ADC decrease (Blackband et al., 1997). The latter was however not quantified. The ADC decrease in the buccal ganglia was found to be 12% on average, somewhat milder than the response reported on other tissue models. There are several factors that could potentially explain this discrepancy. One is the large fraction of soma in the region of cell bodies segmented, with a soma ADC that increases with hypotonic challenge. Another contributor is the absence of neurites from the region of cell bodies, as opposed to mammalian gray matter with 65% of neuropil. Both these considerations will be discussed into more detail further on. Lastly, the sheath around the ganglia could partially hinder the access of the insult medium to the underlying tissue. However, since the varying osmolarities did not lead to a significant difference in the level of ADC decrease, this latter factor is expected to be marginal.

With 1 mM ouabain solutions, the ADC was shown to decrease by 33% in the rat brain (Benveniste et al., 1992), by 18% in perfused rat hippocampal slices (Buckley et al., 1999) and by 40% in neo-natal rat brain (Veldhuis et al., 2003). The ADC decrease in the buccal ganglia was found to be 18% on average after ouabain exposure. Once again, the less pronounced ADC decrease in the *Aplysia* buccal ganglia compared with that in the rat brain can be attributed to the difference in tissue model. However, the very similar 18% ADC decrease found in rat hippocampal slices also highlights the potential variability associated with such experimental results. In the *Aplysia*, the similar tissue response to two different concentrations of ouabain (1 mM and 3 mM) could indicate a threshold effect, where further increasing the ouabain concentration is ineffective as all the Na^+/K^+-ATPase is already inhibited. This threshold hypothesis also further rules out the role of the sheath as a major protector from the outside medium.

In the study on neo-natal rat brain, the systemic injection of MK-801 (an NMDA-receptor antagonist that will prevent glutamate from overactivating these receptors) prior to ouabain exposure significantly reduced the lesion volume, as assessed from ADC maps, but did not prevent ADC changes completely (Veldhuis et al., 2003). These results highlighted the two-step effect of ouabain: cell swelling followed by excitotoxicity. The more marked effect of ouabain on the ADC versus hypotonic ASW on *Aplysia* ganglia tissue is also consistent with this mechanism.

ADC increase in the soma

Following a 33% hypotonic shock, the ADC increased in individual isolated neuronal bodies by 32% concomitantly with a cell swelling of 24 – 37% (measured with MRI and optical microscopy). These trends are consistent with cell swelling causing an overall dilution inside the cell. In the largest cells, the volume and ADC increase were found to occur within the cytoplasm and nucleus individually.

Quantitatively, cellular equilibration with a 33% hypotonic outside medium was expected to produce a 50% increase in volume, on the basis of intracellular medium dilution (assuming the protein mass is constant and the cell is a perfect osmometer). Cell size measurements with optical microscopy are expected to be more accurate than with MRI via higher spatial resolution. The 37% volume increase recorded with optical microscopy is close to the expected 50%. Moreover, previous optical microscopy studies on *Aplysia* neurons exposed to a 50% hypotonic solution reported an equivalent volume increase of 31%, underlining the response variability across cells, which are eventually never perfect osmometers (Wheal et al., 1977). The average 32% ADC increase measured with MRI is also consistent with a dilution of protein concentration, although the quantitative relationship between ADC and volume increase remains to be determined.

Our results are in agreement with previous findings on *Xenopus* oocytes analyzed in the light of a two-compartment model (Sehy et al., 2002). The study showed that following a 30% hypotonic shock, the oocyte swelled by 16% and that the ADCs of the "slow" and "fast" compartments identified by the biexponential model increased by 40% and 19% respectively, with their relative fraction unaltered (f_{slow} = 11%). However, an earlier study of the response of *Aplysia* neurons to a 20% hypotonic shock reported no change in ADC in the cytoplasm or in the nucleus (Hsu et al., 1996). The reason for the conflicting results between the latter study and the one performed in this thesis work is not fully clear. Surprisingly, Hsu *et al.* do not present ADC values over the entire the cell, but systematically separated cytoplasm and nucleus. Given their spatial resolution (25x25x150 μm^3) it is very likely each

compartment was severely corrupted by PVE, rendering the interpretation difficult. This issue is somewhat apparent in their reported mean ADC values for cytoplasm and nucleus (0.7 $x10^{-3}$ mm^2/s for both) that do not reproduce the well-accepted higher ADC in the nucleus and lower in the cytoplasm. Moreover, given the high resistance of *Aplysia* neurons to non-ideal conditions, a 20% hypotonic shock might have been too mild to trigger a response.

Following exposure to ouabain, the ADC increased by 30% in isolated neuronal bodies, and separate treatment of cytoplasm and nucleus in the largest cells showed that an ADC increase occurred in both these structures individually. The cellular ADC increase was important in spite of a fairly limited increase in volume (0 – 12% from MRI and optical microscopy measurements). Different mechanisms from a simple dilution could therefore play a role in the ADC response to ouabain. To our knowledge, this is the first report measuring this response so direct comparison with previous findings cannot be performed.

Nonetheless, as explained earlier, ouabain is known to cause swelling of nucleus and mitochondria, as well as loss of ribosome configuration in neurons (Cornog et al., 1967). The latter can eventually lead to a disorganization of the cytoplasmic and membranes structure through the breakdown of protein synthesis. A non-MR technique was previously used to show that the disorganization of the cytoplasmic structure causes the diffusion coefficient of macromolecules to increase inside the cytoplasm (Wojcieszyn et al., 1981). In that study, the diffusion coefficient of fluorescent macromolecules injected inside the cytoplasm of fibroblasts was measured with the FRAP technique (Fluorescence Recovery After Photobleaching (Axelrod et al., 1976)). The measurement was repeated after addition of colchicine, known to disorganize microtubules, and the cytoplasmic diffusion was found to increase. The authors concluded to a diffusion coefficient dominated by cytoplasmic structure rather than by viscosity, which did not change during the experiment. However, once again, the diffusion of water molecules could evolve differently from that of macromolecules, and neurons could also have a distinct behavior compared to fibroblasts. The results of the FRAP study disagree for instance with an MR study on *Xenopus* oocytes (Sehy et al., 2004). In the latter, while confirming that the ADC evolution with hypotonic media is correlated with cell swelling, the authors showed that water ADC was altered neither by microtubule polymerization and depolymerization, nor by nuclear breakdown. The impact of the cytoskeleton on the ADC was thus presented as minimal in their study.

Our results on *Aplysia* neurons exposed to ouabain show a large ADC increase in a context of only mild (or absence of) cell swelling. As mentioned in the introduction of

this chapter, the lack of swelling of *Aplysia* neurons in the presence of ouabain and in spite of a measured membrane depolarization through pump inhibition had been reported previously using optical microscopy (Wheal et al., 1977). Our volume measurements are therefore consistent with this report. Interestingly, the intracellular conductivity of *Aplysia* neurons has been shown to be surprisingly low (5% of external ASW) in spite of high ionic concentration and activity (Carpenter et al., 1973). The authors hypothesized that the low conductivity is related to the structuring of cellular water caused by hydrogen bond formation with polar and charged groups of macromolecules. Wheal *et al*. suggested that the absence of cell swelling in spite of a substantial entry of Na^+ ions could also be due to the structuring of intracellular water. In the current study, we measured a substantial intracellular ADC increase in a context of Na^+ influx yet absence of osmotic activity. A possible – speculative – explanation could be that the partial breakdown of intracellular macromolecular structure caused by ouabain returns water molecules to their free state (hence ADC increase) and insures solvation of incoming Na^+ ions (hence no water influx from the outside). Further studies are however needed in order to conclude on this matter (e.g. does the intracellular conductivity increase after exposure to ouabain?) but our results tend to favor changes in cellular structuring as the main contributor to ADC change.

The existence of a significant correlation between neuron diameter and ADC in the initial state of the cell is worthwhile discussing. Given the cell sizes versus the image spatial resolution, it seems unlikely that the higher ADC in the smaller cells would only result from larger PVE with surrounding ASW voxels, although this effect cannot be completely ignored. Another potential explanation could be the larger relative fraction of nucleus vs cytoplasm in smaller cells. Since the ADC is larger in the nucleus than in the cytoplasm, a large fraction of nucleus in the cell would lead to an overall increased cell ADC. However, no quantification of this parameter was found in the literature. Lastly, larger cells potentially require a strengthened cytoskeleton: an increased structure within the cytoplasm could lead to more important hindrance and membrane binding effects that decrease the ADC in these cells. The correlation is attenuated for cells exposed to hypotonic stress or ouabain because the ADC change is not correlated with the size change in a fixed fashion.

How do we reconcile ADC increase in the soma with ADC decrease in the tissue?

We have shown that individually, each trend is consistent with earlier results in the field: both ADC increase in the soma and ADC decrease in nervous tissue were

reported previously. In this study, we show for the first time that these phenomena occur within the same tissue type: namely that the ADC of neuronal cell bodies increases with hypotonic shock or ouabain, while the ADC of the *region* of cell bodies in the ganglion decreases with these same insults. How can the tissue ADC decrease in spite of substantial ADC increase inside the soma?

The cell body region in the ganglion can be modeled as 40% neuronal cell bodies, the remaining 60% representing extracellular space, glial cells and start of axons and other processes going into the central neuropil region. Averaged over all 15 cells and 10 ganglia used in this study, the ADC pre-insult is around 0.87 (10^{-3} mm²/s) in cell bodies and 1.03 in ganglion tissue. These values are not extremely different one from the other and therefore we can assume that, for b-values 0 – 600 s/mm², the relative contribution of cell bodies and of "the rest" to the diffusion weighted MR signal is similar. There is likely a bias from shorter T_2 relaxation in the cells, previously measured to be about 30 ms in the cytoplasm and 85 ms in the nucleus at 11.7 T (Bowtell et al., 1995). In the DP-FISP preparation, we used a TE of 13 ms for which images of the ganglion (b = 10 s/mm²) did not display significant signal differences between the cell bodies and the rest of the tissue (see for example Figure 52 page 151). The impact of this bias is therefore not expected to be dramatic.

If we consider neuronal cell bodies (40% volumetric fraction) and "the rest of the tissue" (extracellular space, glial cells and negligible processes – 60% volumetric fraction) as two compartments, neither of the two is expected to clearly dominate at low b-values, given the above considerations on ADC and T_2 values. Moreover, little mixing from proton mobility is likely to occur because the typical diffusion distance over the experiment diffusion time (9 ms) is around 7 µm, much smaller than the size of the neuronal bodies and their spacing. Let us then provisionally assume that the diffusion weighted signal at the tissue level arises from these two separate compartments. Using the experimental observation that the tissue signal appears to decay as a single exponential in the low b-value range, we could make the following approximation (valid only for b < 600 s/mm²):

$$\exp(-b \cdot ADC_{tissue}) \approx f\exp(-b \cdot ADC_{soma}) + (1-f)\exp(-b \cdot ADC_{non\ soma}) \qquad (7.1)$$

where f is the cell body volume fraction. Inputting average values for f, ADC_{soma} and ADC_{tissue} and the respective evolutions of all three parameters with hypotonic and ouabain insult, it turns out that the average $ADC_{non\text{-}soma}$ pre-insult in the non-soma tissue space would be around 1.14 10^{-3} mm²/s and the latter would need to drop by

42% with hypotonic shock and 45% with ouabain to account for the tissue ADC decrease.

This back-of-the-envelope calculation is of course very crude but the result is only meant to illustrate that given the high ADC increase within the cell body, a dramatic decrease would need to occur elsewhere in order to explain the overall ADC decrease in tissue. Let us then examine the expected response in extracellular space, glial cells and neurites.

Although it is expected to contribute, the increase in extracellular tortuosity alone cannot account for the effect. This is very simply demonstrated by the fact that the tissue ADC decrease was more pronounced with ouabain than with hypotonic shock, although cell swelling (and therefore increase in extracellular tortuosity) was less marked and the ADC increase inside the cells was comparable.

The relative weight and response of *Aplysia* glial cells was not assessed, but previous studies on mouse astrocytes showed their cell bodies and processes swell in response to hypoosmolarity and ischemia (Risher et al., 2009). The ADC of glial cells in the region of cell bodies is therefore likely to behave in the same way as that of the neuronal soma.

While an ADC decrease is expected in beading neurites, their volumetric fraction inside the selected ROIs was very small due to the spatial separation between cell bodies and neuropil in the *Aplysia*. Since the ROIs were manually drawn, the incorporation of a small volume of the neuropil region in the ganglion core cannot however be completely excluded, but its contribution is expected to be negligible.

So far, we have considered the response of neuronal bodies, extracellular space, glial cells, some contribution of neurites… so what are we leaving out? One important contributor that we have not mentioned so far is membrane surface area. Indeed, as explained earlier in this chapter, there is increasing evidence that membranes could be responsible for a "slow" water layer in their close vicinity. The term "membrane" does not necessarily refer to the cellular membrane only, but could encompass subcellular membranes or even large macromolecular structures that could have a local binding effect on water molecules. Within a fixed volume, an increase of membrane surface area through swelling or reconfiguration could thus provoke an overall decrease of the ADC.

Here is the crux: when looking at a single cell under hypotonic stress, we were tracking the ADC in a variable volume of radius R. Because the volume scales with R^3 and the surface area with R^2, the dilution effect dominated, i.e. the "slow" pool

was likely increasing because of membrane surface increase, but the "fast" pool was increasing faster due to large water intake by the cell. This argument would remain valid even when accounting for intracellular membranes, assuming the structures they encompass experience a homogeneous dilation with respect to that of the cell. When looking at ganglion tissue, the overall water volume was essentially fixed, and the increase of membrane surfaces within that fixed volume due to swelling caused an increase in the population of "bound" water, causing ADC decrease. This difference in viewpoint is illustrated in Figure 61.

However, it is not fully clear how this phenomenon could explain the ouabain results. Indeed, swelling was much milder than following hypotonic shock and the substantial ADC increase inside the soma was largely attributed to a loss of cytoplasmic structure. Although possibly consistent with the fact that bits of membrane and macromolecules have less of a binding effect on protons than fully structured membranes (that also contribute more to motion hindrance), this does not help the interpretation of an 18% ADC decrease at tissue level. One possibility would be that, while membranes within the soma were slightly swollen and largely disrupted, the membrane binding effect experienced by extracellular water and glial cell water was substantially increased. This hypothesis remains in the realm of speculation for now. It is also worthwhile reminding that the excitotoxic damage

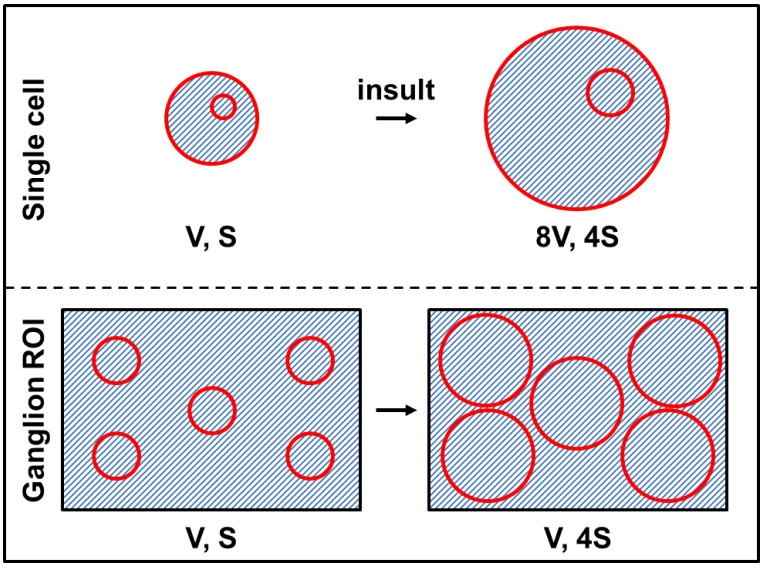

Figure 61. Schematic of the evolution of water volume (hatched) and membranes surface area (red contours) with hypotonic insult, in the single cell experiment (top) and in the ganglion experiment (bottom). In the single cell example, the radii of the cell and of the intracellular structure are assumed to double. The total volume is multiplied by 8 and the total membrane surfaces by 4. In the observation of ganglion tissue, the volume is constant while the total membrane surface area is multiplied by 4. For simplicity, only the cellular membranes were illustrated in the ganglion example.

associated with ouabain causes further ADC changes, the mechanisms of which still need to be addressed.

Sources of tissue ADC decrease in ischemia

In the light of these results let us review the factors that are most often evoked to explain the ADC decrease in tissue with ischemia. It is important to underline that the challenges used in this study are not an exact match to the cellular stress experienced during ischemia. Nonetheless, the effects of cell swelling were probed via a hypotonic stress and that of membrane depolarization via exposure to ouabain.

First of all, our results do not support the hypothesis that the tissue ADC decrease is caused by an increase of the intracellular fraction. Indeed, the intracellular ADC was not found to be substantially lower than overall in the tissue while it increased post-insult to become higher than the tissue ADC.

Similarly, the single cell measurements in this study are in disagreement with a suggested increase in cytoplasmic viscosity and the arrest of cytoplasmic streaming to explain the ADC decrease. Indeed, both effects are expected to produce a decrease in cytoplasmic ADC. On the contrary, the latter was found to increase in all five cells where cytoplasm could be reliably separated from nucleus.

The increase in extracellular tortuosity caused by swelling certainly has an impact on tissue ADC. However, it cannot alone account for the ADC decrease. This was underlined in previous studies on mammals where the extracellular space is small (Duong et al., 1998; Silva et al., 2002) and is supported by our ouabain experiments, where tissue ADC decrease was more pronounced than with hypotonic shock in spite of more limited cell swelling. The effect of extracellular tortuosity could be included in an overall effect of membrane reshaping, which increases hindrance and expands the membrane bound water fraction.

Neurite beading caused by ischemia was recently shown to have a dramatic impact on the tissue ADC, as a result of ADC decrease both in the intracellular (neurite) and extracellular space (Budde and Frank, 2010). The authors claimed that this effect was sufficient to account for the overall ADC decrease in nervous tissue. While its impact is perhaps of great importance in mammalian cortex, where neurites account for 65% of the space, our results show that in a tissue model quasi void of neurites, and in spite of ADC increase inside cell bodies, an ADC decrease was still recorded at tissue level in a context of membrane depolarization or cell swelling. Again, the effect of neurite beading could be incorporated in a more general explanation of increased water hindrance and binding via membrane reshaping. It

should however be noted that the results of Budde *et al*. were obtained using a beading model with conservation of membrane surface (i.e. only reshaping, no expansion). It is not fully clear to what extent this assumption is realistic and what the effect of a beading model without membrane surface conservation would be.

There would be great interest in performing an additional study in the *Aplysia* buccal ganglia, this time looking at the changes in ADC in the neuropil core of each ganglion, as well as in the commissure. These regions indeed correspond to a complementary tissue model almost void of cell bodies and mainly constituted of axons and dendrites. Unfortunately, information in these regions cannot be derived reliably from our current data due to expected anisotropy effects. Indeed, in the current study a single diffusion orientation was used (equal gradients on all three axes), given the isotropy of the soma and of the cell body region. Diffusion in the commissure certainly has different longitudinal and transverse values since the axonal orientation is along left to right. In the neuropil cores, it is likely that the neurite orientation is not random either, since axons come from the rind of cell bodies, like a bunch of balloons tied together. Reliable ADC estimates in these regions should therefore make use of multiple diffusion directions or at least a direction chosen with respect to actual ganglia orientation, and not to physical axes. The acquisition of multiple diffusion directions should perhaps be performed at the expense of less b-values, in order to keep within a reasonable acquisition time.

One potential bias that has not been mentioned yet is the response of the cell bodies inside the ganglion versus the mechanically isolated ones. To address this issue, higher spatial resolution data is required, in order to segment cell bodies within the ganglia and verify that indeed the ADC decreases in a large tissue ROI while increasing inside individual, but not isolated, soma. The issue of much longer acquisition times would however need to be addressed for such an experiment.

9.8 Conclusion and perspectives

We have studied the evolution of ADC with two types of challenges leading to cell swelling or membrane depolarization, hypotonic shock and exposure to ouabain, at two structural levels: inside neuronal soma isolated from the abdominal and pleural ganglia, and in the region of cell bodies of the buccal ganglia, mainly composed of soma, extracellular space and some glial cells. Results showed that a hypotonic shock caused an increase both in volume and in ADC inside the cell, consistent with a dilution phenomenon, but caused an ADC decrease at the tissue level. Similarly,

exposure to ouabain led to a substantial intracellular ADC increase, possibly related to a loss of intracellular structure and disruption of structured water molecules, but caused an ADC decrease at the tissue level. The reconciliation of the two phenomena is possible if considering that water diffusion in the nervous tissue is governed by the distance of molecules to a polarized membrane or macromolecular structure: the surface of the latter slows the molecules down. The expansion and reshaping of membrane surfaces (cellular and subcellular) in response to physiologic challenge could lead to an ADC decrease in tissue through an increase of the membrane-bound water pool. The strength of this model lies is its ability to explain the results obtained on a wide variety of tissue types and structural scales: whether neurites are predominant or absent, whether the intra- or extracellular compartment is considered, whether a tissue or subcellular scale is adopted.

Four major experimental paths can (and should) be followed in continuation. First, higher spatial resolution data should be acquired on the ganglia, in order to segment cell bodies within the ganglia and compare the ADC change in a large tissue ROI with the ADC in soma still present inside. Such an experiment would remove the bias of measurements on isolated cells. Second, even higher spatial resolution in single cell images could eventually demonstrate the existence of the slow water layers close to biological membranes. Third, going to higher b-values would certainly bring interesting information on the evolution of non Gaussian diffusion inside the cell or the ganglia, and on the validity of the "slow/fast pools = bound/unbound protons" model. Additional sequence improvements are however necessary for this purpose. Last, the buccal ganglia of *Aplysia californica* appear as a good tissue model, since they permit the separation of cell bodies from neurites: a similar study in the neuropil and commissure could potentially be of great interest.

9.9 Chapter summary

In this chapter, we described the mechanisms that relate ischemia, membrane depolarization and cell swelling. The different mechanisms put forward to explain how cell swelling causes a decrease in the ADC of brain tissue were presented and discussed. The polemic revealed the need for ADC measurements at spatial resolutions pertaining to MR microscopy. We introduced two types of insults – hypotonic shock and exposure to ouabain – that mimic cause cell swelling and membrane depolarization in *Aplysia* neurons, respectively. Diffusion microscopy measurements were thus performed pre- and post-insult (hypotonic shock or ouabain) in the region of cell bodies of *Aplysia* buccal ganglia (50 μm isotropic resolution) and inside large soma isolated from the abdominal and pedal ganglia of the *Aplysia* (25 μm isotropic resolution). Both challenges caused an ADC increase inside the cell body, while causing an ADC decrease at tissue level. These opposite trends can be reconciled by a membrane-effect explanation of ADC decrease with these types of physiologic challenges. Indeed, soma swelling, neurite beading and reshaping of subcellular structures (nucleus, mitochondria...) could lead to an overall increase of a "slow water" pool at membrane proximity and an overall decreased ADC in the tissue. In order to confirm this effect, higher spatial resolution is necessary to measure diffusion at soma- and tissue-level at once in the ganglia, as well as diffusion close to membranes in isolated cells.

Conclusion

The objective of this work was to combine the potential of MR microscopy and the practicality of the *Aplysia* nervous system in order to bring insight into issues raised by MR neuroimaging at macroscopic scales.

The implementation of MR microscopy comes with important technological challenges related to ultra-high field magnets and strong static field gradients. Additionally, transceiver probes are usually custom-made to optimize sensitivity and homogeneity for a given sample size and application. In spite of these improvements, the sensitivity of MR microscopy remains relatively poor: the highest isotropic resolutions achieved to date are 3 μm on structured phantoms, 4.7 μm on fixed biological tissue, and some 20 – 25 μm on living tissue. For comparison, the resolution of optical microscopy is typically limited by the wavelength and can achieve 200 nm or even less with new sub-diffraction techniques (Neice, 2010). Moreover, optical microscopy can be associated with a wide variety of cellular markers for improved identification of specific structures or molecules. Atomic force microscopy is also particularly suited to biological samples and provides 3D renderings of surfaces with an in-plane resolution of a few nanometers and a sub-atomic vertical resolution (< 1 Å) (Binnig et al., 1986). Combinations of the two techniques (optical and atomic force) are beginning to develop and have led to interesting correlations between cellular surface topography and internal structural information from fluorescence, or to a refined technique for genetic and proteomic manipulation of individual cells (Geisse, 2009).

Nonetheless, MR microscopy withholds very specific and precious advantages compared with other microscopy techniques, which make the effort worthwhile. MR microscopy allows the imaging of small *living and unaltered* samples, without causing tissue deterioration. Studies of dynamic processes are also possible through this feature. This is not always the case for instance of irreversible chemical staining techniques common in fluorescence microscopy. Because it relies on radiofrequencies, MRM also offers the possibility of a genuine isotropic resolution of intact 3D structures such as the neuronal network in the buccal ganglia of *Aplysia*, without the typical penetration issues associated with short wavelengths or the tomographic approach of projection techniques. For the assessment of cellular response to an environmental challenge, digital holographic microscopy for instance can measure the change in optical path across the cell and thereby quantify trans-membrane water and ionic fluxes with great accuracy, without compromising cell viability (Marquet et al., 2005). Unlike diffusion MRM however, the technique can only be applied to mono-layer cell cultures. In terms of *in vivo* micro-imaging, optical coherence tomography has certainly opened many possibilities for imaging

superficial biological structures such as the anterior eye or the retina, with resolution better than 10 μm and 1 – 2 mm penetration (Izatt et al., 1994). However, the technique is not suited for *in vivo* imaging of deep structures. MRM is for now limited to imaging a small – and therefore often *ex vivo* – volume, given the acquisition times at stake. In the future, improved coil designs combined with parallel transmission could eventually make "zoom MRM" of deep structures *in vivo* possible. Last but not least, thanks to the diversity of its contrast mechanisms, MRM gives access to the quantification of a large panel of parameters that almost no other modality can provide today. MRI is still for instance the only tool capable of measuring the self-diffusion coefficient of water.

The compromise resides for now in imaging biological systems for which a resolution of 20 – 25 μm is sufficient. In the project presented here, we have chosen the *Aplysia californica* as a model of nervous system. Its ganglia constitute simple networks of large identified neurons, which can also be individually isolated and are more resistant to non-ideal experimental conditions. Nonetheless, many of their functional properties are transposable to vertebrate models.

Dedicated microcoils were built to accommodate the size of *Aplysia* buccal ganglia and isolated neurons. The experiments naturally also benefitted from the existing Bruker hardware: a 17.2 T magnet equipped with 1 T/m gradients. Importantly, the coil design effectively counterbalanced the issues typically associated with strong gradients (eddy current circulation) and with ultra-high magnetic field (deteriorated field homogeneity through magnetic susceptibility mismatches and operation at high radiofrequencies).

We performed, for the first time, MEMRI within a fully determined neuronal network, at an isotropic spatial resolution of 25 μm that allowed individual neuron identification. Compared to other system models (e.g. rodents) where MEMRI serves to identify the presence of Mn^{2+} in structural regions of the nervous system, in the *Aplysia* buccal ganglia Mn^{2+} is tracked at neuronal level with "ME-MRM". This study served to confirm, on living tissue, the axonal projections of motor neurons into the peripheral nerves of the buccal ganglia. This map of projections had been previously obtained using a destructive staining with cobalt or nickel and optical microscopy. The Mn^{2+} concentrations required for MEMRI were below the toxicity threshold and did not impair neuronal function. Additionally, ganglia stimulation with dopamine was found to produce inter-neuronal Mn^{2+} transport which dominated over the natural washout mechanism. The major perspectives springing from this study are the direct proof of Mn^{2+} synaptic transport from identified pre-synaptic to post-synaptic neurons, and the study of differentiated Mn^{2+}

accumulation in neurons with identified functions, under various conditions of animal stimulation.

In the perspective of performing diffusion measurements inside single cells at microscopic resolution, we examined the potential of 2D DESIRE to yield images with unprecedented diffusion contrast. The sequence was implemented at 17.2 T and tested on homogeneous phantoms of water and silicone oil. The enhancement obtained experimentally was consistent with theoretical predictions but was too low to provide a real advantage for the imaging of biological samples. Possible improvements include the use of stronger gradients and/or of parallel transmission and the design of better performing pulse shapes. We also implemented a 3D DP-FISP, a rapid diffusion technique sequence suitable for the needs of microscopy and ADC quantification. The sequence performance was highly satisfactory for our purposes. Diffusion weighted acquisitions of isolated neurons were available at 25 µm isotropic resolution in less than 10 minutes per b-value, which constituted a considerable improvement compared with previously reported MR single cell images.

We studied, for the first time, the change in ADC with cell swelling and membrane depolarization at two structural scales within the same tissue model: in the region of cell bodies of the buccal ganglia and inside isolated soma. While diffusion measurements in *Aplysia* isolated neurons had been performed before, this was the first report to also study the region of cell bodies as a nervous tissue model. The comparison of results in these two structures was interesting precisely because the cell body region is almost devoid of neurites, which is not the case of mammalian cortex. The ADC was found to substantially increase inside the soma following a hypotonic shock or exposure to ouabain, and yet decrease at the tissue level. The various theories linking ADC decrease in tissue to cell swelling were examined in the light of this finding, with the most pertinent hypothesis being the increase in the amount of "slow water" bound to membranes as a result of membrane expansion and reshaping. The substantial changes in ADC with ouabain in spite of changes in cellular volume also favor the structuring of water molecules as the determining factor, more so than cell size. While this mechanism remains to be confirmed, the results obtained significantly narrowed the list of potential explanations by discarding several of them: the increase of intracellular versus extracellular space, increase of cytoplasmic viscosity and arrest of cytoplasmic streaming. This study has also shown how the combination of information from MRM and fluorescence microscopy can provide a more complete assessment of cell response to a challenging environment. The focus of future works should be the acquisition of diffusion data

with even higher spatial resolution, in order to validate the existence of a slow-diffusing water layer close to membranes or to large macromolecular structures. Other regions of the buccal ganglia, such as the central neuropil regions and the commissure, which are mainly constituted of neurites and devoid of soma, could be used as complementary tissue models to the region of cell bodies for the study of ADC response to the same physiologic challenges.

Overall, the current work demonstrated the usefulness of the *Aplysia* model for MR microscopy studies, with an increased appeal for the imaging of full neuronal networks and not just of isolated large cell bodies. The results presented throughout laid several bricks in the wall of understanding Mn^{2+} transport in the nervous system and the diffusion changes associated with cell swelling or membrane depolarization, but many more studies in both these directions are possible and needed in order to get a full picture of the mechanisms at stake.

List of publications

Peer-reviewed journals:

- **IO Jelescu**, R Nargeot, D Le Bihan and L Ciobanu, *Highlighting manganese dynamics in the nervous system of Aplysia californica using MEMRI at ultra-high field*, NeuroImage 2013; 76:264-271.
- **IO Jelescu**, N Boulant, D Le Bihan and L Ciobanu, *Experimental demonstration of diffusion signal enhancement in 2D DESIRE images*. J Magn Reson 2012; 218:44-8.

Conference proceedings:

- **IO Jelescu**, F Geffroy, D Le Bihan and L Ciobanu, *3D Diffusion Prepared FISP for single cell MR microscopy*, Proc. of the ICMRM 2013 – **oral**.
- **IO Jelescu**, L Ciobanu, F Geffroy and D Le Bihan, *Effects of hypotonic stress and ouabain on apparent diffusion coefficient at cellular and tissue levels*, Proc. of the ISMRM 2013 – **oral**.
- **IO Jelescu**, D Le Bihan and L Ciobanu, *3D DP-FISP for diffusion measurements in MR microscopy at ultra-high field*, Proc. of the ISMRM 2013 – e-poster.
- G Radecki, **IO Jelescu**, R Nargeot, D Le Bihan and L Ciobanu, *Manganese enhanced MRI reveals stimulus-evoked neuronal activation in Aplysia californica*, Proc. of the ISMRM 2013 – poster.
- G Radecki, **IO Jelescu**, R Nargeot, D Le Bihan and L Ciobanu, *Toward in vivo functional neuroimaging of Aplysia using manganese enhanced MRI*, Proc. of the ESMRMB 2012 – e-poster ("certificate of merit" award).
- **IO Jelescu**, R Nargeot, D Le Bihan and L Ciobanu, *Highlighting manganese transport mechanisms in the nervous system with MEMRI in Aplysia californica*, Proc. of the ISMRM 2012 – **oral ("summa cum laudae" award)**.
- **IO Jelescu**, N Boulant, D Le Bihan and L Ciobanu, *Experimental demonstration of diffusion signal enhancement in 2D DESIRE images*, Proc. of the ISMRM 2012 – poster.

- **IO Jelescu**, R Nargeot, D Le Bihan and L Ciobanu, *Tracking dopamine-induced manganese translocation in the nervous system of Aplysia californica*, Proc. of the ENC 2012 – **oral**.
- **IO Jelescu**, R Nargeot, B Djemai, D Le Bihan and L Ciobanu, *Manganese enhanced MRI highlighting neuronal pathways of the buccal ganglion in Aplysia californica*, Proc. of the ICMRM 2011 – **oral**.
- **IO Jelescu**, N Boulant, D Le Bihan and L Ciobanu, *Two-dimensional DESIRE implementation at ultra high field*, Proc. of the ICMRM 2011 – poster.

Nomenclature

1D / 2D / 3D	One / Two / Three dimensional
γ	Gyromagnetic ratio
A/D	Analog-to-digital
ADC	Apparent Diffusion Coefficient
ATP	Adenosine triphosphate
ASW	Artificial Sea Water
b / b_{eff}	Amount of diffusion weighting / Effective b-value
$\mathbf{B_0}$	Main magnetic field
$\mathbf{B_1}$	Excitation field
BW	Bandwidth
D	Diffusion coefficient
DA	Dopamine
DESIRE	Diffusion Enhancement of SIgnal and REsolution
DP	Diffusion prepared (or preparation)
DTI	Diffusion Tensor Imaging
DW	Diffusion-weighted
E.n.	Esophageal nerve
EPI	Echo-planar imaging
FA	Flip angle
FC-40	Fluorinert®
FID	Free induction decay
FISP	Fast Imaging with Steady-state free Precession
FLASH	Fast Low Angle SHot
FOV	Field-of-view

FSE	Fast spin echo
FT	Fourier transform
FWHM	Full width at half maximum
G	Magnetic field gradient
ID	Inner diameter
M_0	Equilibrium magnetization
MEMRI	Manganese Enhanced Magnetic Resonance Imaging
MR / MRI	Magnetic Resonance / Magnetic Resonance Imaging
MRM	Magnetic Resonance Microscopy
MT	Magnetization Transfer
M_z / M_{xy}	Longitudinal / Transverse magnetization
n.2 / n.3	Nerve 2 / Nerve 3
NA	Number of averages
NMDA	N-methyl-D-aspartate
NMR	Nuclear Magnetic Resonance
OD	Outer diameter
OGSE	Oscillating Gradient Spin Echo
PD	Proton density
PE (or pe)	Phase-encoding
ppm	Particles per million
PVE	Partial volume effects
PGSE	Pulsed Gradient Spin Echo
Q	Quality factor
r_1 / r_2	Longitudinal / Transverse relaxivity
ROI	Region of interest
RARE	Rapid Acquisition with Refocused Echoes
RF	Radiofrequency
RO (or ro)	Read-out

Rx	Reception
SE	Spin echo
SNR	Signal-to-noise ratio
SSFP	Steady State Free Precession
T_1 / T_2	Longitudinal / Transverse relaxation time
T1w / T2w	T_1 weighted / T_2 weighted
T_2*	Apparent transverse relaxation time
TA	Acquisition time
TE	Echo time
TR	Repetition time
Tx	Transmission

Bibliography

Aguayo, J.B., Blackband, S.J., Schoeniger, J., Mattingly, M.A., Hintermann, M., 1986. Nuclear magnetic resonance imaging of a single cell. Nature 322, 190-191.

Ahn, C.B., Cho, Z.H., 1991. Analysis of eddy currents in nuclear magnetic resonance imaging. Magn Reson Med 17, 149-163.

Ahn, C.B., Kim, J.H., Cho, Z.H., 1986. High-speed spiral-scan echo planar NMR imaging-I. IEEE Trans Med Imaging 5, 2-7.

Aiken, N.R., Hsu, E.W., Horsman, A., Blackband, S.J., 1996. Maturation effects on the NMR microimaging characteristics of single neurons. Am J Physiol 271, C1295-1302.

Andrew, R.D., Labron, M.W., Boehnke, S.E., Carnduff, L., Kirov, S.A., 2007. Physiological evidence that pyramidal neurons lack functional water channels. Cereb Cortex 17, 787-802.

Aoki, I., Wu, Y.J., Silva, A.C., Lynch, R.M., Koretsky, A.P., 2004. In vivo detection of neuroarchitecture in the rodent brain using manganese-enhanced MRI. NeuroImage 22, 1046-1059.

Assaf, Y., Cohen, Y., 1998. Non-mono-exponential attenuation of water and N-acetyl aspartate signals due to diffusion in brain tissue. J Magn Reson 131, 69-85.

Assaf, Y., Freidlin, R.Z., Rohde, G.K., Basser, P.J., 2004. New modeling and experimental framework to characterize hindered and restricted water diffusion in brain white matter. Magn Reson Med 52, 965-978.

Axelrod, D., Koppel, D.E., Schlessinger, J., Elson, E., Webb, W.W., 1976. Mobility measurement by analysis of fluorescence photobleaching recovery kinetics. Biophys J 16, 1055-1069.

Badea, A., Johnson, G.A., 2012. Magnetic resonance microscopy. Anal Cell Pathol (Amst) 35, 205-227.

Bearer, E.L., Falzone, T.L., Zhang, X., Biris, O., Rasin, A., Jacobs, R.E., 2007. Role of neuronal activity and kinesin on tract tracing by manganese-enhanced MRI (MEMRI). NeuroImage 37 Suppl 1, S37-46.

Beaulieu, C.F., Zhou, X., Cofer, G.P., Johnson, G.A., 1993. Diffusion-weighted MR microscopy with fast spin-echo. Magn Reson Med 30, 201-206.

Bennett, K.M., Schmainda, K.M., Bennett, R.T., Rowe, D.B., Lu, H., Hyde, J.S., 2003. Characterization of continuously distributed cortical water diffusion rates with a stretched-exponential model. Magn Reson Med 50, 727-734.

Benveniste, H., Blackband, S.J., 2006. Translational neuroscience and magnetic-resonance microscopy. The Lancet Neurology 5, 536-544.

Benveniste, H., Hedlund, L.W., Johnson, G.A., 1992. Mechanism of detection of acute cerebral ischemia in rats by diffusion-weighted magnetic resonance microscopy. Stroke 23, 746-754.

Binnig, G., Quate, C.F., Gerber, C., 1986. Atomic Force Microscope. Physical Review Letters 56, 930-933.

Blackband, S.J., Bui, J.D., Buckley, D.L., Zelles, T., Plant, H.D., Inglis, B.A., Phillips, M.I., 1997. MR microscopy of perfused brain slices. Magn Reson Med 38, 1012-1015.

Bottomley, P.A., 1987. Spatial localization in NMR spectroscopy in vivo. Ann N Y Acad Sci 508, 333-348.

Boulant, N., Hoult, D.I., 2012. High tip angle approximation based on a modified Bloch–Riccati equation. Magnetic Resonance in Medicine 67, 339-343.

Bowtell, R.W., Brown, G.D., Glover, P.M., McJury, M., Mansfield, P., Pope, J.M., Ratcliffe, R.E., Waterton, J., Timms, W.E., 1990. Resolution of Cellular Structures by NMR Microscopy at 11.7 T [and Discussion]. Philosophical Transactions of the Royal Society of London. Series A: Physical and Engineering Sciences 333, 457-467.

Bowtell, R.W., Peters, A., Sharp, J.C., Mansfield, P., Hsu, E.W., Aiken, N., Horsman, A., Blackband, S.J., 1995. NMR microscopy of single neurons using spin echo and line narrowed 2DFT imaging. Magn Reson Med 33, 790-794.

Braitenberg, V., Schüz, A., 1998. Cortex: statistics and geometry of neuronal connectivity. Springer.

Brinkley, C.K., Kolodny, N.H., Kohler, S.J., Sandeman, D.C., Beltz, B.S., 2005. Magnetic resonance imaging at 9.4 T as a tool for studying neural anatomy in non-vertebrates. J Neurosci Methods 146, 124-132.

Buckley, D.L., Bui, J.D., Phillips, M.I., Zelles, T., Inglis, B.A., Plant, H.D., Blackband, S.J., 1999. The effect of ouabain on water diffusion in the rat hippocampal slice measured by high resolution NMR imaging. Magn Reson Med 41, 137-142.

Budde, M.D., Frank, J.A., 2010. Neurite beading is sufficient to decrease the apparent diffusion coefficient after ischemic stroke. Proc Natl Acad Sci U S A 107, 14472-14477.

Bui, J.D., Buckley, D.L., Phillips, M.I., Blackband, S.J., 1999. Nuclear magnetic resonance imaging measurements of water diffusion in the perfused hippocampal slice during N-methyl-D-aspartate-induced excitotoxicity. Neuroscience 93, 487-490.

Butterworth, S., 1926. Effective resistance of inductance coils at radio frequency. Experimental Wireless and the Wireless Engineer 3, 203, 267, 417 and 483.

Callaghan, P.T., 1993. Principles of Nuclear Magnetic Resonance Microscopy. Clarendon Press.

Callaghan, P.T., Eccles, C.D., 1988. Diffusion-limited resolution in nuclear magnetic resonance microscopy. Journal of Magnetic Resonance 78, 1-8.

Carew, T.J., Walters, E.T., Kandel, E.R., 1981. Classical conditioning in a simple withdrawal reflex in Aplysia californica. J Neurosci 1, 1426-1437.

Carpenter, D.O., Hovey, M.M., Bak, A.F., 1973. Measurements of intracellular conductivity in Aplysia neurons: evidence for organization of water and ions. Ann N Y Acad Sci 204, 502-533.

Carr, D.H., 1984. The use of iron and gadolinium chelates as NMR contrast agents: animal and human studies. Physiol Chem Phys Med NMR 16, 137-144.

Carr, H.Y., 1958. Steady-State Free Precession in Nuclear Magnetic Resonance. Physical Review 112, 1693-1701.

Carr, H.Y., Purcell, E.M., 1954. Effects of Diffusion on Free Precession in Nuclear Magnetic Resonance Experiments. Physical Review 94, 630-638.

Chen, K.C., Nicholson, C., 2000. Changes in brain cell shape create residual extracellular space volume and explain tortuosity behavior during osmotic challenge. Proc Natl Acad Sci U S A 97, 8306-8311.

Chenevert, T.L., Brunberg, J.A., Pipe, J.G., 1990. Anisotropic diffusion in human white matter: demonstration with MR techniques in vivo. Radiology 177, 401-405.

Chien, D., Edelman, R.R., 1991. Ultrafast imaging using gradient echoes. Magn Reson Q 7, 31-56.

Chin, C.L., Wehrli, F.W., Fan, Y., Hwang, S.N., Schwartz, E.D., Nissanov, J., Hackney, D.B., 2004. Assessment of axonal fiber tract architecture in excised rat spinal cord by localized NMR q-space imaging: simulations and experimental studies. Magn Reson Med 52, 733-740.

Chmurny, G.N., Hoult, D.I., 1990. The Ancient and Honourable Art of Shimming. Concepts in Magnetic Resonance 2, 131-149.

Cho, Z.H., Ahn, C.B., Juh, S.C., Lee, H.K., Jacobs, R.E., Lee, S., Yi, J.H., Jo, J.M., 1988. Nuclear magnetic resonance microscopy with 4-microns resolution: theoretical study and experimental results. Med Phys 15, 815-824.

Church, P.J., Lloyd, P.E., 1991. Expression of diverse neuropeptide cotransmitters by identified motor neurons in Aplysia. J Neurosci 11, 618-625.

Church, P.J., Lloyd, P.E., 1994. Activity of multiple identified motor neurons recorded intracellularly during evoked feedinglike motor programs in Aplysia. J Neurophysiol 72, 1794-1809.

Ciobanu, L., Boulant, N., Le Bihan, D., 2010. Design and Implementation of 2D DESIRE Experiments. EUROMAR, Florence, Italy.

Ciobanu, L., Seeber, D.A., Pennington, C.H., 2002. 3D MR microscopy with resolution 3.7μm by 3.3μm by 3.3μm. Journal of Magnetic Resonance 158, 178-182.

Ciobanu, L., Webb, A.G., Pennington, C.H., 2003. Magnetic resonance imaging of biological cells. Progress in Nuclear Magnetic Resonance Spectroscopy 42, 69-93.

Ciobanu, L., Webb, A.G., Pennington, C.H., 2004. Signal enhancement by diffusion: experimental observation of the "DESIRE" effect. Journal of Magnetic Resonance 170, 252-256.

Clark, C.A., Le Bihan, D., 2000. Water diffusion compartmentation and anisotropy at high b values in the human brain. Magn Reson Med 44, 852-859.

Clegg, J.S., 1984. Properties and metabolism of the aqueous cytoplasm and its boundaries. Am J Physiol 246, R133-151.

Colvin, D.C., Loveless, M.E., Does, M.D., Yue, Z., Yankeelov, T.E., Gore, J.C., 2011. Earlier detection of tumor treatment response using magnetic resonance diffusion imaging with oscillating gradients. Magn Reson Imaging 29, 315-323.

Conturo, T.E., Lori, N.F., Cull, T.S., Akbudak, E., Snyder, A.Z., Shimony, J.S., McKinstry, R.C., Burton, H., Raichle, M.E., 1999. Tracking neuronal fiber pathways in the living human brain. Proc Natl Acad Sci U S A 96, 10422-10427.

Coremans, J., Spanoghe, M., Budinsky, L., Sterckx, J., Luypaert, R., Eisendrath, H., Osteaux, M., 1997. A comparison between different imaging strategies for diffusion measurements with the centric phase-encoded turboFLASH sequence. J Magn Reson 124, 323-342.

Cornog, J.L., Gonatas, N.K., Feierman, J.R., 1967. Effects of intracerebral injection of ouabain on the fine structure of rat cerebral cortex. Am J Pathol 51, 573-590.

Darquie, A., Poline, J.B., Poupon, C., Saint-Jalmes, H., Le Bihan, D., 2001. Transient decrease in water diffusion observed in human occipital cortex during visual stimulation. Proc Natl Acad Sci U S A 98, 9391-9395.

Deoni, S.C., Peters, T.M., Rutt, B.K., 2004. Quantitative diffusion imaging with steady-state free precession. Magn Reson Med 51, 428-433.

Does, M.D., Parsons, E.C., Gore, J.C., 2003. Oscillating gradient measurements of water diffusion in normal and globally ischemic rat brain. Magn Reson Med 49, 206-215.

Duong, T.Q., Ackerman, J.J., Ying, H.S., Neil, J.J., 1998. Evaluation of extra- and intracellular apparent diffusion in normal and globally ischemic rat brain via 19F NMR. Magn Reson Med 40, 1-13.

Duong, T.Q., Silva, A.C., Lee, S.P., Kim, S.G., 2000. Functional MRI of calcium-dependent synaptic activity: cross correlation with CBF and BOLD measurements. Magn Reson Med 43, 383-392.

Edelstein, W.A., Glover, G.H., Hardy, C.J., Redington, R.W., 1986. The intrinsic signal-to-noise ratio in NMR imaging. Magnetic Resonance in Medicine 3, 604-618.

Einstein, A., 1905. Über die von der molekularkinetischen Theorie der Wärme geforderte Bewegung von in ruhenden Flüssigkeiten suspendierten Teilchen. Annalen der Physik 322, 549-560.

Eroglu, S., Gimi, B., Roman, B., Friedman, G., Magin, R.L., 2003. NMR spiral surface microcoils: Design, fabrication, and imaging. Concepts in Magnetic Resonance Part B: Magnetic Resonance Engineering 17B, 1-10.

Farzaneh, F., Riederer, S.J., Pelc, N.J., 1990. Analysis of T2 limitations and off-resonance effects on spatial resolution and artifacts in echo-planar imaging. Magn Reson Med 14, 123-139.

Flint, J.J., Hansen, B., Portnoy, S., Lee, C.H., King, M.A., Fey, M., Vincent, F., Stanisz, G.J., Vestergaard-Poulsen, P., Blackband, S.J., 2012. Magnetic resonance microscopy of human and porcine neurons and cellular processes. NeuroImage 60, 1404-1411.

Flint, J.J., Lee, C.H., Hansen, B., Fey, M., Schmidig, D., Bui, J.D., King, M.A., Vestergaard-Poulsen, P., Blackband, S.J., 2009. Magnetic resonance microscopy of mammalian neurons. NeuroImage 46, 1037-1040.

Frahm, J., Haase, A., Matthaei, D., 1986. Rapid three-dimensional MR imaging using the FLASH technique. J Comput Assist Tomogr 10, 363-368.

Fukushima, E., Roeder, S.B.W., 1993. Experimental Pulse Nmr: A Nuts and Bolts Approach. Addison-Wesley Publishing Company, Advanced Book Program.

Gardner, D., 1971. Bilateral symmetry and interneuronal organization in the buccal ganglia of Aplysia. Science 173, 550-553.

Gardner, D., 1977. Interconnections of identified multiaction interneurons in buccal ganglia of Aplysia. J Neurophysiol 40, 349-361.

Geisse, N.A., 2009. AFM and combined optical techniques. Materials Today 12, 40-45.

Glover, P., Mansfield, S.P., 2002. Limits to magnetic resonance microscopy. Reports on Progress in Physics 65, 1489.

Golay, M.J.E., 1958. Field Homogenizing Coils for Nuclear Spin Resonance Instrumentation. Review of Scientific Instruments 29, 313-315.

Golay, X., Stuber, M., Pruessmann, K.P., Meier, D., Boesiger, P., 1999. Transfer insensitive labeling technique (TILT): Application to multislice functional perfusion imaging. Journal of Magnetic Resonance Imaging 9, 454-461.

Goodman, J.A., Ackerman, J.J., Neil, J.J., 2008. Cs + ADC in rat brain decreases markedly at death. Magn Reson Med 59, 65-72.

Grant, S.C., Buckley, D.L., Gibbs, S., Webb, A.G., Blackband, S.J., 2001. MR microscopy of multicomponent diffusion in single neurons. Magnetic Resonance in Medicine 46, 1107-1112.

Grissom, W.A., Yip, C.-Y., Wright, S.M., Fessler, J.A., Noll, D.C., 2008. Additive angle method for fast large-tip-angle RF pulse design in parallel excitation. Magnetic Resonance in Medicine 59, 779-787.

Gruetter, R., 1993. Automatic, localized in vivo adjustment of all first- and second-order shim coils. Magn Reson Med 29, 804-811.

Gudbjartsson, H., Patz, S., 1995. The Rician distribution of noisy MRI data. Magn Reson Med 34, 910-914.

Haacke, E.M., Brown, R.W., Thompson, M.R., Venkatesan, R., 1999. Magnetic Resonance Imaging: Physical Principles and Sequence Design. Wiley.

Hashemi, R.H., Bradley, W.G., Lisanti, C.J., 2012. MRI: The Basics. Wolters Kluwer Health.

Hazlewood, C.F., Rorschach, H.E., Lin, C., 1991. Diffusion of water in tissues and MRI. Magn Reson Med 19, 214-216.

Hennig, J., Nauerth, A., Friedburg, H., 1986. RARE imaging: a fast imaging method for clinical MR. Magn Reson Med 3, 823-833.

Herberholz, J., Mims, C.J., Zhang, X., Hu, X., Edwards, D.H., 2004. Anatomy of a live invertebrate revealed by manganese-enhanced Magnetic Resonance Imaging. J Exp Biol 207, 4543-4550.

Herberholz, J., Mishra, S.H., Uma, D., Germann, M.W., Edwards, D.H., Potter, K., 2011. Non-invasive imaging of neuroanatomical structures and neural activation with high-resolution MRI. Front Behav Neurosci 5, 16.

Heuser, D., Guggenberger, H., 1985. Ionic changes in brain ischaemia and alterations produced by drugs. Br J Anaesth 57, 23-33.

Hodgkin, A.L., Huxley, A.F., 1952. A quantitative description of membrane current and its application to conduction and excitation in nerve. J Physiol 117, 500-544.

Hossmann, K.A., Sakaki, S., Zimmerman, V., 1977. Cation activities in reversible ischemia of the cat brain. Stroke 8, 77-81.

Hoult, D.I., Richards, R.E., 1976. The signal-to-noise ratio of the nuclear magnetic resonance experiment. Journal of Magnetic Resonance (1969) 24, 71-85.

Hsu, E.W., Aiken, N.R., Blackband, S.J., 1996. Nuclear magnetic resonance microscopy of single neurons under hypotonic perturbation. Am J Physiol 271, C1895-1900.

Hsu, E.W., Aiken, N.R., Blackband, S.J., 1997. A study of diffusion isotropy in single neurons by using NMR microscopy. Magn Reson Med 37, 624-627.

Hsu, E.W., Schoeniger, J.S., Bowtell, R., Aiken, N.R., Horsman, A., Blackband, S.J., 1995. A modified imaging sequence for accurate T2 measurements using NMR microscopy. J Magn Reson B 109, 66-69.

Hu, T.C., Pautler, R.G., MacGowan, G.A., Koretsky, A.P., 2001. Manganese-enhanced MRI of mouse heart during changes in inotropy. Magn Reson Med 46, 884-890.

Huang, S., Liu, C., Dai, G., Kim, Y.R., Rosen, B.R., 2009. Manipulation of tissue contrast using contrast agents for enhanced MR microscopy in ex vivo mouse brain. NeuroImage 46, 589-599.

Izatt, J.A., Hee, M.R., Swanson, E.A., Lin, C.P., Huang, D., Schuman, J.S., Puliafito, C.A., Fujimoto, J.G., 1994. Micrometer-scale resolution imaging of the anterior eye in vivo with optical coherence tomography. Arch Ophthalmol 112, 1584-1589.

Jackson, J.D., 1975. Classical electrodynamics. Wiley.

Jelescu, I.O., Nargeot, R., Le Bihan, D., Ciobanu, L., 2013. Highlighting manganese dynamics in the nervous system of Aplysia californica using MEMRI at ultra-high field. NeuroImage 76, 264-271.

Jensen, J.H., Helpern, J.A., Ramani, A., Lu, H., Kaczynski, K., 2005. Diffusional kurtosis imaging: the quantification of non-gaussian water diffusion by means of magnetic resonance imaging. Magn Reson Med 53, 1432-1440.

Jeong, E.K., Kim, S.E., Parker, D.L., 2003. High-resolution diffusion-weighted 3D MRI, using diffusion-weighted driven-equilibrium (DW-DE) and multishot segmented 3D-SSFP without navigator echoes. Magn Reson Med 50, 821-829.

Jespersen, S.N., Kroenke, C.D., Ostergaard, L., Ackerman, J.J., Yablonskiy, D.A., 2007. Modeling dendrite density from magnetic resonance diffusion measurements. NeuroImage 34, 1473-1486.

Jezzard, P., Barnett, A.S., Pierpaoli, C., 1998. Characterization of and correction for eddy current artifacts in echo planar diffusion imaging. Magn Reson Med 39, 801-812.

Jin, J.M., 1999. Electromagnetic analysis and design in magnetic resonance imaging. CRC Press.

Jourdain, P., Boss, D., Rappaz, B., Moratal, C., Hernandez, M.-C., Depeursinge, C., Magistretti, P.J., Marquet, P., 2012. Simultaneous Optical Recording in Multiple Cells by Digital Holographic Microscopy of Chloride Current Associated to Activation of the Ligand-Gated Chloride Channel $GABA_A$ Receptor. PLoS One 7, e51041.

Kabotyanski, E.A., Baxter, D.A., Cushman, S.J., Byrne, J.H., 2000. Modulation of fictive feeding by dopamine and serotonin in aplysia. J Neurophysiol 83, 374-392.

Kanayama, S., Kuhara, S., Satoh, K., 1996. In vivo rapid magnetic field measurement and shimming using single scan differential phase mapping. Magn Reson Med 36, 637-642.

Kandel, E.R., 2001. The molecular biology of memory storage: a dialogue between genes and synapses. Science 294, 1030-1038.

Kandel, E.R., Kupfermann, I., 1970. The Functional Organization of Invertebrate Ganglia. Annual Review of Physiology 32, 193-258.

Keevil, S.F., 2006. Spatial localization in nuclear magnetic resonance spectroscopy. Physics in Medicine and Biology 51, R579.

Kehoe, J., 1972. Three acetylcholine receptors in Aplysia neurones. J Physiol 225, 115-146.

Kohn, D.F., Wixson, S.K., White, W.J., Benson, G.J., 1997. Anesthesia and Analgesia in Laboratory Animals. Elsevier Science.

Krizaj, D., Rice, M.E., Wardle, R.A., Nicholson, C., 1996. Water compartmentalization and extracellular tortuosity after osmotic changes in cerebellum of Trachemys scripta. J Physiol 492 (Pt 3), 887-896.

Krombach, G.A., Saeed, M., Higgins, C.B., Novikov, V., Wendland, M.F., 2004. Contrast-enhanced MR delineation of stunned myocardium with administration of MnCl(2) in rats. Radiology 230, 183-190.

Kupfermann, I., Carew, T.J., Kandel, E.R., 1974. Local, reflex, and central commands controlling gill and siphon movements in Aplysia. J Neurophysiol 37, 996-1019.

Kupfermann, I., Kandel, E.R., 1969. Neuronal controls of a behavioral response mediated by the abdominal ganglion of Aplysia. Science 164, 847-850.

Latour, L.L., Hasegawa, Y., Formato, J.E., Fisher, M., Sotak, C.H., 1994a. Spreading waves of decreased diffusion coefficient after cortical stimulation in the rat brain. Magn Reson Med 32, 189-198.

Latour, L.L., Svoboda, K., Mitra, P.P., Sotak, C.H., 1994b. Time-dependent diffusion of water in a biological model system. Proc Natl Acad Sci U S A 91, 1229-1233.

Lauterbur, P.C., 1973. Image Formation by Induced Local Interactions: Examples Employing Nuclear Magnetic Resonance. Nature 242, 190-191.

Lauterbur, P.C., Hyslop, W.B., Morris, H.D., 1992. NMR microscopy: old resolutions and new desires. XI International Society of Magnetic Resonance Conference, Vancouver, B.C.

Le Bihan, D., 1988. Intravoxel incoherent motion imaging using steady-state free precession. Magn Reson Med 7, 346-351.

Le Bihan, D., 2007. The 'wet mind': water and functional neuroimaging. Physics in Medicine and Biology 52, R57.

Le Bihan, D., Breton, E., Lallemand, D., Grenier, P., Cabanis, E., Laval-Jeantet, M., 1986. MR imaging of intravoxel incoherent motions: application to diffusion and perfusion in neurologic disorders. Radiology 161, 401-407.

Le Bihan, D., Johansen-Berg, H., 2012. Diffusion MRI at 25: exploring brain tissue structure and function. NeuroImage 61, 324-341.

Le Bihan, D., Mangin, J.F., Poupon, C., Clark, C.A., Pappata, S., Molko, N., Chabriat, H., 2001. Diffusion tensor imaging: concepts and applications. J Magn Reson Imaging 13, 534-546.

Le Bihan, D., Urayama, S., Aso, T., Hanakawa, T., Fukuyama, H., 2006. Direct and fast detection of neuronal activation in the human brain with diffusion MRI. Proc Natl Acad Sci U S A 103, 8263-8268.

Lee, H., Price, R.R., 1994. Diffusion imaging with the MP-RAGE sequence. J Magn Reson Imaging 4, 837-842.

Lee, S.-C., Kim, K., Kim, J., Lee, S., Han Yi, J., Woo Kim, S., Ha, K.-S., Cheong, C., 2001. One Micrometer Resolution NMR Microscopy. Journal of Magnetic Resonance 150, 207-213.

Li, F., Liu, K.F., Silva, M.D., Meng, X., Gerriets, T., Helmer, K.G., Fenstermacher, J.D., Sotak, C.H., Fisher, M., 2002. Acute postischemic renormalization of the apparent diffusion coefficient of water is not associated with reversal of astrocytic swelling and neuronal shrinkage in rats. AJNR Am J Neuroradiol 23, 180-188.

Li, P., Murphy, T.H., 2008. Two-Photon Imaging during Prolonged Middle Cerebral Artery Occlusion in Mice Reveals Recovery of Dendritic Structure after Reperfusion. The Journal of Neuroscience 28, 11970-11979.

Li, T.Q., Kim, D.H., Moseley, M.E., 2005. High-resolution diffusion-weighted imaging with interleaved variable-density spiral acquisitions. J Magn Reson Imaging 21, 468-475.

Lim, C.S., Lee, J.C., Kim, S.D., Chang, D.J., Kaang, B.K., 2002. Hydrogen peroxide-induced cell death in cultured Aplysia sensory neurons. Brain Res 941, 137-145.

Lin, C.P., Tseng, W.Y., Cheng, H.C., Chen, J.H., 2001. Validation of diffusion tensor magnetic resonance axonal fiber imaging with registered manganese-enhanced optic tracts. NeuroImage 14, 1035-1047.

Lin, Y.J., Koretsky, A.P., 1997. Manganese ion enhances T1-weighted MRI during brain activation: an approach to direct imaging of brain function. Magn Reson Med 38, 378-388.

Ling, G.N., 2003. A new theoretical foundation for the polarized-oriented multilayer theory of cell water and for inanimate systems demonstrating long-range dynamic structuring of water molecules. Physiol Chem Phys Med NMR 35, 91-130.

Lipton, P., 1973. Effects of membrane depolarization on light scattering by cerebral cortical slices. J Physiol 231, 365-383.

Lodish, H.F., 2003. Molecular Cell Biology. Macmillan Higher Education.

Lu, L., Erokwu, B., Lee, G., Gulani, V., Griswold, M.A., Dell, K.M., Flask, C.A., 2012. Diffusion-prepared fast imaging with steady-state free precession (DP-FISP): a rapid diffusion MRI technique at 7 T. Magn Reson Med 68, 868-873.

Marquet, P., Rappaz, B., Magistretti, P.J., Cuche, E., Emery, Y., Colomb, T., Depeursinge, C., 2005. Digital holographic microscopy: a noninvasive contrast imaging technique allowing quantitative visualization of living cells with subwavelength axial accuracy. Opt Lett 30, 468-470.

Massin, C., Boero, G., Vincent, F., Abenhaim, J., Besse, P.A., Popovic, R.S., 2002. High-Q factor RF planar microcoils for micro-scale NMR spectroscopy. Sensors and Actuators A: Physical 97–98, 280-288.

Mattiello, J., Basser, P.J., Le Bihan, D., 1997. The b matrix in diffusion tensor echo-planar imaging. Magn Reson Med 37, 292-300.

Mattiello, J., Basser, P.J., Lebihan, D., 1994. Analytical Expressions for the b Matrix in NMR Diffusion Imaging and Spectroscopy. Journal of Magnetic Resonance, Series A 108, 131-141.

McNab, J.A., Miller, K.L., 2010. Steady-state diffusion-weighted imaging: theory, acquisition and analysis. NMR Biomed 23, 781-793.

Medhurst, R.G., 1947. H.F. resistance and self-capacitance of single-layer solenoids. Experimental Wireless and the Wireless Engineer 24, 35-43, 80-92.

Meme, S., Joudiou, N., Szeremeta, F., Mispelter, J., Louat, F., Decoville, M., Locker, D., Beloeil, J.C., 2013. In vivo magnetic resonance microscopy of Drosophilae at 9.4 T. Magn Reson Imaging 31, 109-119.

Mendonca-Dias, M.H., Gaggelli, E., Lauterbur, P.C., 1983. Paramagnetic contrast agents in nuclear magnetic resonance medical imaging. Semin Nucl Med 13, 364-376.

Minard, K.R., Wind, R.A., 2001a. Solenoidal microcoil design—Part II: Optimizing winding parameters for maximum signal-to-noise performance. Concepts in Magnetic Resonance 13, 190-210.

Minard, K.R., Wind, R.A., 2001b. Solenoidal microcoil design. Part I: Optimizing RF homogeneity and coil dimensions. Concepts in Magnetic Resonance 13, 128-142.

Minard, K.R., Wind, R.A., 2002. Picoliter (1)H NMR spectroscopy. J Magn Reson 154, 336-343.

Mohmmadzadeh, M., Baxan, N., Badilita, V., Kratt, K., Weber, H., Korvink, J.G., Wallrabe, U., Hennig, J., von Elverfeldt, D., 2011. Characterization of a 3D MEMS fabricated micro-solenoid at 9.4 T. J Magn Reson 208, 20-26.

Morton, D.W., Chiel, H.J., Cohen, L.B., Wu, J.Y., 1991. Optical methods can be utilized to map the location and activity of putative motor neurons and interneurons during rhythmic patterns of activity in the buccal ganglion of Aplysia. Brain Res 564, 45-55.

Moseley, M.E., Cohen, Y., Mintorovitch, J., Chileuitt, L., Shimizu, H., Kucharczyk, J., Wendland, M.F., Weinstein, P.R., 1990. Early detection of regional cerebral ischemia in cats: comparison of diffusion- and T2-weighted MRI and spectroscopy. Magn Reson Med 14, 330-346.

Mulkern, R.V., Haker, S.J., Maier, S.E., 2009. On high b diffusion imaging in the human brain: ruminations and experimental insights. Magn Reson Imaging 27, 1151-1162.

Muller, R.N., 1996. Contrast agents in whole body magnetic resonance: operating mechanisms. In: Grant, D.M., Harris, R.K. (Eds.), Encyclopedia of Nuclear Magnetic Resonance. John Wiley & Sons, New York, pp. 1438-1444.

Murayama, Y., Weber, B., Saleem, K.S., Augath, M., Logothetis, N.K., 2006. Tracing neural circuits in vivo with Mn-enhanced MRI. Magn Reson Imaging 24, 349-358.

Nargeot, R., Simmers, J., 2012. Functional organization and adaptability of a decision-making network in aplysia. Front Neurosci 6, 113.

Nayak, K.S., Lee, H.L., Hargreaves, B.A., Hu, B.S., 2007. Wideband SSFP: alternating repetition time balanced steady state free precession with increased band spacing. Magn Reson Med 58, 931-938.

Neice, A., 2010. Chapter 3 - Methods and Limitations of Subwavelength Imaging. In: Peter, W.H. (Ed.), Advances in Imaging and Electron Physics. Elsevier, pp. 117-140.

Neil, J.J., Duong, T.Q., Ackerman, J.J., 1996. Evaluation of intracellular diffusion in normal and globally-ischemic rat brain via 133Cs NMR. Magn Reson Med 35, 329-335.

Niendorf, T., Dijkhuizen, R.M., Norris, D.G., van Lookeren Campagne, M., Nicolay, K., 1996. Biexponential diffusion attenuation in various states of brain tissue: implications for diffusion-weighted imaging. Magn Reson Med 36, 847-857.

Niendorf, T., Norris, D.G., Leibfritz, D., 1994. Detection of apparent restricted diffusion in healthy rat brain at short diffusion times. Magn Reson Med 32, 672-677.

Nishimura, D.G., 1996. Principles of magnetic resonance imaging. Stanford University.

Norris, D.G., Bornert, P., Reese, T., Leibfritz, D., 1992. On the application of ultra-fast RARE experiments. Magn Reson Med 27, 142-164.

O'Shea, J.M., Williams, S.R., van Bruggen, N., Gardner-Medwin, A.R., 2000. Apparent diffusion coefficient and MR relaxation during osmotic manipulation in isolated turtle cerebellum. Magn Reson Med 44, 427-432.

Olson, D.L., Peck, T.L., Webb, A.G., Magin, R.L., Sweedler, J.V., 1995. High-Resolution Microcoil 1H-NMR for Mass-Limited, Nanoliter-Volume Samples. Science 270, 1967-1970.

Østergaard, L., Sorensen, A.G., Chesler, D.A., Weisskoff, R.M., Koroshetz, W.J., Wu, O., Gyldensted, C., Rosen, B.R., 2000. Combined Diffusion-Weighted and Perfusion-Weighted Flow Heterogeneity Magnetic Resonance Imaging in Acute Stroke. Stroke 31, 1097-1103.

Pauly, J., Nishimura, D., Macovski, A., 1989. A k-space analysis of small-tip-angle excitation. Journal of Magnetic Resonance (1969) 81, 43-56.

Pautler, R.G., Mongeau, R., Jacobs, R.E., 2003. In vivo trans-synaptic tract tracing from the murine striatum and amygdala utilizing manganese enhanced MRI (MEMRI). Magn Reson Med 50, 33-39.

Pautler, R.G., Silva, A.C., Koretsky, A.P., 1998. In vivo neuronal tract tracing using manganese-enhanced magnetic resonance imaging. Magn Reson Med 40, 740-748.

Peck, T.L., Magin, R.L., Lauterbur, P.C., 1995. Design and analysis of microcoils for NMR microscopy. J Magn Reson B 108, 114-124.

Pennington, C.H., 2003. Prospects for diffusion enhancement of signal and resolution in magnetic resonance microscopy. Concepts in Magnetic Resonance Part A 19A, 71-79.

Pfeuffer, J., Provencher, S.W., Gruetter, R., 1999. Water diffusion in rat brain in vivo as detected at very large b values is multicompartmental. MAGMA 8, 98-108.

Pipe, J.G., Farthing, V.G., Forbes, K.P., 2002. Multishot diffusion-weighted FSE using PROPELLER MRI. Magn Reson Med 47, 42-52.

Quicke, D.L., Brace, R.C., 1979. Differential and staining of cobalt-and nickel-filled neurones using rubeanic acid. J Microsc 115, 161-163.

Radecki, G., Jelescu, I.O., Nargeot, R., Le Bihan, D., Ciobanu, L., 2013. Manganese enhanced MRI reveals stimulus-evoked neuronal activation in Aplysia californica. International Society of Magnetic Resonance in Medicine, Salt Lake City, USA.

Risher, W.C., Andrew, R.D., Kirov, S.A., 2009. Real-time passive volume responses of astrocytes to acute osmotic and ischemic stress in cortical slices and in vivo revealed by two-photon microscopy. Glia 57, 207-221.

Saleem, K.S., Pauls, J.M., Augath, M., Trinath, T., Prause, B.A., Hashikawa, T., Logothetis, N.K., 2002. Magnetic resonance imaging of neuronal connections in the macaque monkey. Neuron 34, 685-700.

Schachter, M., Does, M.D., Anderson, A.W., Gore, J.C., 2000. Measurements of Restricted Diffusion Using an Oscillating Gradient Spin-Echo Sequence. Journal of Magnetic Resonance 147, 232-237.

Schick, F., 1997. SPLICE: sub-second diffusion-sensitive MR imaging using a modified fast spin-echo acquisition mode. Magn Reson Med 38, 638-644.

Schoeniger, J.S., Aiken, N., Hsu, E., Blackband, S.J., 1994. Relaxation-time and diffusion NMR microscopy of single neurons. J Magn Reson B 103, 261-273.

Schwarcz, A., Bogner, P., Meric, P., Correze, J.L., Berente, Z., Pal, J., Gallyas, F., Doczi, T., Gillet, B., Beloeil, J.C., 2004. The existence of biexponential signal decay in magnetic resonance diffusion-weighted imaging appears to be independent of compartmentalization. Magn Reson Med 51, 278-285.

Sehy, J.V., Ackerman, J.J., Neil, J.J., 2001. Water and lipid MRI of the Xenopus oocyte. Magn Reson Med 46, 900-906.

Sehy, J.V., Ackerman, J.J., Neil, J.J., 2002. Evidence that both fast and slow water ADC components arise from intracellular space. Magn Reson Med 48, 765-770.

Sehy, J.V., Zhao, L., Xu, J., Rayala, H.J., Ackerman, J.J., Neil, J.J., 2004. Effects of physiologic challenge on the ADC of intracellular water in the Xenopus oocyte. Magn Reson Med 52, 239-247.

Serrano, F., Deshazer, M., Smith, K.D., Ananta, J.S., Wilson, L.J., Pautler, R.G., 2008. Assessing transneuronal dysfunction utilizing manganese-enhanced MRI (MEMRI). Magn Reson Med 60, 169-175.

Shepherd, T.M., Thelwall, P.E., Blackband, S.J., Pike, B.R., Hayes, R.L., Wirth, E.D., 3rd, 2003a. Diffusion magnetic resonance imaging study of a rat hippocampal slice model for acute brain injury. J Cereb Blood Flow Metab 23, 1461-1470.

Shepherd, T.M., Wirth, E.D., 3rd, Thelwall, P.E., Chen, H.X., Roper, S.N., Blackband, S.J., 2003b. Water diffusion measurements in perfused human hippocampal slices undergoing tonicity changes. Magn Reson Med 49, 856-863.

Sigmund, E.E., Halperin, W.P., 2003. Hole-burning diffusion measurements in high magnetic field gradients. Journal of Magnetic Resonance 163, 99-104.

Silva, A.C., Bock, N.A., 2008. Manganese-enhanced MRI: an exceptional tool in translational neuroimaging. Schizophr Bull 34, 595-604.

Silva, A.C., Lee, J.H., Aoki, I., Koretsky, A.P., 2004. Manganese-enhanced magnetic resonance imaging (MEMRI): methodological and practical considerations. NMR Biomed 17, 532-543.

Silva, M.D., Omae, T., Helmer, K.G., Li, F., Fisher, M., Sotak, C.H., 2002. Separating changes in the intra- and extracellular water apparent diffusion coefficient following focal cerebral ischemia in the rat brain. Magn Reson Med 48, 826-837.

Sinha, U., Sinha, S., 1996. High speed diffusion imaging in the presence of eddy currents. J Magn Reson Imaging 6, 657-666.

Solomon, I., 1955. Relaxation Processes in a System of Two Spins. Physical Review 99, 559-565.

Stehling, M.K., Turner, R., Mansfield, P., 1991. Echo-planar imaging: magnetic resonance imaging in a fraction of a second. Science 254, 43-50.

Stejskal, E.O., Tanner, J.E., 1965. Spin Diffusion Measurements: Spin Echoes in the Presence of a Time-Dependent Field Gradient. The Journal of Chemical Physics 42, 288-292.

Sukstanskii, A.L., Ackerman, J.J., Yablonskiy, D.A., 2003. Effects of barrier-induced nuclear spin magnetization inhomogeneities on diffusion-attenuated MR signal. Magn Reson Med 50, 735-742.

Sukstanskii, A.L., Yablonskiy, D.A., Ackerman, J.J., 2004. Effects of permeable boundaries on the diffusion-attenuated MR signal: insights from a one-dimensional model. J Magn Reson 170, 56-66.

Sundgren, P.C., Dong, Q., Gomez-Hassan, D., Mukherji, S.K., Maly, P., Welsh, R., 2004. Diffusion tensor imaging of the brain: review of clinical applications. Neuroradiology 46, 339-350.

Sykova, E., Nicholson, C., 2008. Diffusion in brain extracellular space. Physiol Rev 88, 1277-1340.

Takeda, A., Ishiwatari, S., Okada, S., 1998. In vivo stimulation-induced release of manganese in rat amygdala. Brain Res 811, 147-151.

Tasaki, I., Byrne, P.M., 1990. Volume expansion of nonmyelinated nerve fibers during impulse conduction. Biophys J 57, 633-635.

Thomas, D.L., Pell, G.S., Lythgoe, M.F., Gadian, D.G., Ordidge, R.J., 1998. A quantitative method for fast diffusion imaging using magnetization-prepared TurboFLASH. Magn Reson Med 39, 950-960.

Trouard, T.P., Harkins, K.D., Divijak, J.L., Gillies, R.J., Galons, J.P., 2008. Ischemia-induced changes of intracellular water diffusion in rat glioma cell cultures. Magn Reson Med 60, 258-264.

Tyszka, J.M., Fraser, S.E., Jacobs, R.E., 2005. Magnetic resonance microscopy: recent advances and applications. Current Opinion in Biotechnology 16, 93-99.

Van der Linden, A., Van Meir, V., Tindemans, I., Verhoye, M., Balthazart, J., 2004. Applications of manganese-enhanced magnetic resonance imaging (MEMRI) to image brain plasticity in song birds. NMR Biomed 17, 602-612.

Van der Linden, A., Verhoye, M., Van Meir, V., Tindemans, I., Eens, M., Absil, P., Balthazart, J., 2002. In vivo manganese-enhanced magnetic resonance imaging reveals connections and functional properties of the songbird vocal control system. Neuroscience 112, 467-474.

Veldhuis, W.B., van der Stelt, M., Delmas, F., Gillet, B., Veldink, G.A., Vliegenthart, J.F., Nicolay, K., Bar, P.R., 2003. In vivo excitotoxicity induced by ouabain, a Na+/K+-ATPase inhibitor. J Cereb Blood Flow Metab 23, 62-74.

Walters, E.T., Bodnarova, M., Billy, A.J., Dulin, M.F., Diaz-Rios, M., Miller, M.W., Moroz, L.L., 2004. Somatotopic organization and functional properties of mechanosensory neurons expressing sensorin-A mRNA in Aplysia californica. J Comp Neurol 471, 219-240.

Watanabe, T., Natt, O., Boretius, S., Frahm, J., Michaelis, T., 2002. In vivo 3D MRI staining of mouse brain after subcutaneous application of MnCl2. Magn Reson Med 48, 852-859.

Webb, A.G., Grant, S.C., 1996. Signal-to-noise and magnetic susceptibility trade-offs in solenoidal microcoils for NMR. J Magn Reson B 113, 83-87.

Weiger, M., Schmidig, D., Denoth, S., Massin, C., Vincent, F., Schenkel, M., Fey, M., 2008a. NMR microscopy with isotropic resolution of 3.0 µm using dedicated hardware and optimized methods. Concepts in Magnetic Resonance Part B: Magnetic Resonance Engineering 33B, 84-93.

Weiger, M., Zeng, Y., Fey, M., 2008b. A closer look into DESIRE for NMR microscopy. Journal of Magnetic Resonance 190, 95-104.

Wheal, H.V., Horn, N.M., Austin, G.M., 1977. The effect of sodium pump inhibitors on Aplysia neuronal cell volume. Comp Biochem Physiol C 57, 139-141.

Williams, R.W., Herrup, K., 1988. The control of neuron number. Annu Rev Neurosci 11, 423-453.

Wind, R.A., Minard, K.R., Holtom, G.R., Majors, P.D., Ackerman, E.J., Colson, S.D., Cory, D.G., Daly, D.S., Ellis, P.D., Metting, N.F., Parkinson, C.I., Price, J.M., Tang, X.W., 2000. An integrated confocal and magnetic resonance microscope for cellular research. J Magn Reson 147, 371-377.

Wojcieszyn, J.W., Schlegel, R.A., Wu, E.S., Jacobson, K.A., 1981. Diffusion of injected macromolecules within the cytoplasm of living cells. Proc Natl Acad Sci U S A 78, 4407-4410.

Wright, A.C., Wehrli, S.L., Zhang, G., Takahashi, M., Hackney, D.B., Selzer, M.E., Wehrli, F.W., 2002. Visualization of individual axons in excised lamprey spinal cord by magnetic resonance microscopy. J Neurosci Methods 114, 9-15.

Xu, X.H., Yeung, E.S., 1998. Long-range electrostatic trapping of single-protein molecules at a liquid-solid interface. Science 281, 1650-1653.

Yablonskiy, D.A., Bretthorst, G.L., Ackerman, J.J., 2003. Statistical model for diffusion attenuated MR signal. Magn Reson Med 50, 664-669.

Yablonskiy, D.A., Sukstanskii, A.L., 2010. Theoretical models of the diffusion weighted MR signal. NMR Biomed 23, 661-681.

Yamashita, N., 1982. Enhancement of ionic currents through voltage-gated channels in the mouse oocyte after fertilization. J Physiol 329, 263-280.

Zheng, W., Ren, S., Graziano, J.H., 1998. Manganese inhibits mitochondrial aconitase: a mechanism of manganese neurotoxicity. Brain Res 799, 334-342.

Zhong, J., Petroff, O.A., Prichard, J.W., Gore, J.C., 1993. Changes in water diffusion and relaxation properties of rat cerebrum during status epilepticus. Magn Reson Med 30, 241-246.

Zur, Y., Wood, M.L., Neuringer, L.J., 1991. Spoiling of transverse magnetization in steady-state sequences. Magnetic Resonance in Medicine 21, 251-263.